RECONSTRUCTION, CHARACTERIZATION, MODELING AND VISUALIZATION OF INHERENT AND INDUCED DIGITAL SAND MICROSTRUCTURES

A Dissertation
Presented to
The Academic Faculty

by

Ye Lu

In Partial Fulfillment
of the Requirements for the Degree
Doctor of Philosophy in the
School of Civil and Environmental Engineering

Georgia Institute of Technology
December 2010

RECONSTRUCTION, CHARACTERIZATION, MODELING AND VISUALIZATION OF INHERENT AND INDUCED DIGITAL SAND MICROSTRUCTURES

Approved by:

Dr. J. David Frost, Advisor
School of Civil and Environmental Engineering
Georgia Institute of Technology

Dr. Susan Burns
School of Civil and Environmental Engineering
Georgia Institute of Technology

Dr. Carlos Santamarina
School of Civil and Environmental Engineering
Georgia Institute of Technology

Dr. Arun Gokhale
School of Materials Science and Engineering
Georgia Institute of Technology

Dr. Glenn Rix
School of Civil and Environmental Engineering
Georgia Institute of Technology

Date Approved: November 1, 2010

To My Family

ACKNOWLEDGEMENTS

The past four and a half year marks a milestone. I can feel myself grow in the ways seeing, thinking, and solving problems. But this could not happen without my advisor, Dr. David Frost. His advice, guidance and patience helped me overcome the research challenges, and his genius and creative vision of geotechnical engineering inspired and encouraged me to continue on this path. Thank you for giving me the great opportunity to pursue this research presented here.

I would like to thank my committee members, Dr. Susan Burns, Dr. Glenn Rix, Dr. Carlos Santamarina, and Dr. Arun Gokhale for offering valuable comments and suggestions.

Dr. David Potyondy from Itasca Consulting Group, Inc., and Dr. Brent Lindquist of University of Stony Brooke provided immediate and helpful answers to my questions regarding their softwares, and their help are gratefully acknowledged.

I would like to thank Dr. Carlos Santamarina for his great comments during the course of this research. I also benefit a lot from taking his innovative geotechnical courses.

The biaxial device and the data acquisition system were very complicated to use. I was fortunate to have Dr. Matt Evans to come to the lab and teach me how to use it. His help is gratefully acknowledged.

I would like to thank the fellow geosystem students, Catherine, Mesut, Andew, Topraj and Duhwan, who offered me their help and their friendship over the past years. I will never forget those discussions about family and life with Catherine and Mesut.

I would like to thank my parents for their love and supports over the years. They never stopped me from pursuing my dream and I cannot go this far without them standing behind me.

Finally, Yong, thank you for your love and support.

TABLE OF CONTENTS

LIST OF TABLES

LIST OF FIGURES

SUMMARY

Strain localization, the phenomenon of large shear deformation within thin zones of intensive shearing, commonly occurs both in-situ and in the laboratory tests on soils specimens. The intriguing mechanism of strain localization and how it will affect the general behavior of soil specimens have been investigated by many researchers. Some of the efforts have focused on finding the links between material properties (void space, fabric tensor) and mechanical behavior (stress, strain, volumetric strain). In the last ten years, several extensive studies have been conducted at Georgia Tech to investigate the mechanism of strain localization and link the microstructural properties with the engineering behavior of Ottawa sands. These studies have included 2-D and 3-D characterization of soil microstructures under either triaxial or biaxial shearing conditions. To extend and complement these previous studies, the current study focuses particularly on 3-D reconstruction, analysis and modeling of specimens of Ottawa sand subject to triaxial or biaxial loading. The 3-D microstructure of biaxial specimens was reconstructed using an optical microscopy based montage and serial sectioning technique. Based on the reconstructed 3-D digital volumes, a series of 2-D and 3-D characterizations and analyses, including local void ratio distributions, extent of shear bands, influence of soil fabrics and packing signature effects, were conducted. In addition to the image analysis based reconstruction and characterization, the 3-D discrete element method (DEM) code, PFC3D, was used to explore both biaxial and triaxial shear related soil behaviors at the global and particulate scale. Void ratio distributions, coordination numbers, particle rotations and displacements, contact normal distributions and normal

contact forces as well as global stress and strain responses were investigated and analyzed to help understand the mechanism of strain localization. The microstructures of the numerical specimens were also characterized in the same way as the physical specimens and similar strain localization patterns were identified. Combined with the previous related studies, the current study provides new insights into the strain localization phenomenon of Ottawa sands subject to triaxial and biaxial loading. In addition, the reconstructed digital specimens were subject to a series of dissection studies which revealed exciting new insights into “microstructure signatures” which exist at both meso and micro scales within the real and simulated specimens.

CHAPTER 1

INTRODUCTION

1.1. Research Purpose

The mechanisms behind the response of a soil mass subject to shearing have been of interest to researchers for a long time. In the early years, many research efforts focused on the global behavior of sheared soil masses. However, since the 1970s, more and more researchers have recognized that strain localization plays an important role in shear-induced failure cases. Consequently, interpretation of the shear behavior of soil specimens from a global perspective is not sufficient. As a result, a number of more recent experimental studies including triaxial and/or plane strain tests have been devoted to the study of strain localization (e.g., Arthur et al., 1977; Vardoulakis, 1979; Desrues et al., 1985; Tatsuoka et al., 1990; Desrues et al., 1996; Finno et al., 1996; Rechenmacher, 2005; Evans and Frost, 2010) and have concluded that the critical state may only be achieved inside the shear bands or shear zones. As the localized areas are much smaller in scale than the soil specimen, examinations on those areas should be performed at a microstructural level. In order to link the microstructural properties to the engineering behavior of the soils, different measurement and characterization technologies have emerged (e.g., X-ray CT, MRI, optical microscopy). These techniques are able to permit characterization as well as visualization of the internal structure in 2-dimensional (2-D) and 3-dimensional (3-D) space at the micro-level. Other than the direct testing and measurements performed in the laboratory, the advent of computer-based numerical modeling, especially the discrete element method (DEM), provides complementary tools for investigations at the particle level.

1.2. Research Scope

In the last ten years, several extensive studies were completed at Georgia Tech to investigate the mechanism of strain localization and link the microstructural properties with the engineering behavior of Ottawa sands (Yang, 2005; Evans, 2005). These studies focused on soil behavior under either triaxial or plane strain (biaxial) loading conditions. The microsturctural properties (e.g., particle size, pore size, pore throat size and tortuosity) were characterized through image analysis of high resolution optical images captured from laboratory specimens. Testing of some of the specimens was simulated using 2-D DEM modeling to provide supplementary insight into the particulate structures inside the strain localization zone. This current study extends and complements these previous studies and in particular focuses on 3-D reconstruction, analysis and modeling (Table 1.1). The combined insight provided by the previous and current studies will provide new insights into the strain localization phenomenon of Ottawa sands subject to triaxial and biaxial loading.

1.3. Organization of the Thesis

The thesis is composed of 8 chapters. The chapters are organized as follows:

- Chapter 2 gives a brief overview of relevant previous works on strain localization, characterization and visualization of soil microstructures, and numerical modeling of soil specimens;
- Chapter 3 provides a more detailed summary of on the previous related microstructural work on triaxial and biaxial testing, 2-D and 3-D characterization and visualization of soil microstructures, and some numerical modeling of Ottawa sands that was noted in Table 1.1;
- Chapter 4 presents the 3-D DEM modeling of triaxial specimens, the related parametric studies, and the assessment of the global and microstructural behavior of the numerical specimens;

- Chapter 5 introduces the serial sectioning technique employed in the current study to reconstruct 3-D coupons obtained from biaxial specimens;
- Chapter 6 presents the 3-D DEM modeling of biaxial specimen coupons, the related parametric studies, and the assessment of the global and microstructural behaviors of the numerical specimens;
- Chapter 7 provides a summary of the 2-D and 3-D analysis and 3-D visualization of the physical and simulated microstructures; and
- Chapter 8 summarizes the findings of the present study and provides some recommendations for future work.

Table 1.1 Overview of research elements for investigation of strain localization in triaxial and biaxial specimens

Triaxial Shear Studies	**Biaxial Shear Studies**
Device development	Device development
Physical experiments (global) Ottawa 30-50 (AP and MT[1])	Physical experiments (global) Ottawa 20-30 (AP[1])
Structure impregnation (single phase) unsheared / sheared	Structure impregnation (2 phase) unsheared / sheared
Serial sectioning Reconstruction of physical specimen	Serial sectioning Reconstruction of physical specimen
2-D microstructure characterization	2-D microstructure characterization
2-D DEM modeling	2-D DEM Modeling
3-D microstructure characterization	3-D microstructure characterization
3-D particle and pore visualization	3-D particle and pore visualization
3-D DEM modeling (AP and MT[1])	3-D DEM modeling (AP[1])
Digital specimen dissection	Digital specimen dissection
Medial axis – 3-D analysis	Medial axis – 3-D analysis
Membrane effect studies	Membrane effect studies

Note: [1] AP – air pluviation, MT – moist tamping

Shading Legend:

Yang (2005)

Current study

Evans (2005)

N/A

CHAPTER 2

LITERATURE REVIEW

2.1. Strain Localization

The failure of soils is one of the perpetual interests in geotechnical engineering, and a significant amount of research has been dedicated to exploring the mechanisms behind failure. Over the past four decades, researchers have recognized that localized deformations commonly occur both in-situ (slopes, retaining walls, embankments, foundations) and in the laboratory tests (triaxial and biaxial tests). Strain localization, or shear banding, manifests itself in large shearing deformation within thin zones of intensive shearing (Drescher et al., 1990; Finno et al., 1996). Once strain localization initializes, these thin zones usually feature volumetric dilation and higher void ratios. Consequently, the assumption that the soil masses are treated as continua is no longer valid and the material behavior should be viewed as a bifurcation problem.

The axisymmetric triaxial compression test is one of the most commonly used and studied laboratory tests in soil mechanics. It was believed in the past that the failure pattern of a soil specimen in a triaxial compression test was either 'brittle' (with some prominent shear planes) or 'soft' (with no clearly defined shear planes but a barrel-like shape) depending on the test material, initial void ratio, confining pressure, and other factors. However, even for the barrel-like failure pattern, strain localization may still exist. Through a breakthrough research study using X-ray computed tomography, Desrues et al. (1996) discovered a turbine-like internal structure for triaxial sand specimens. This overall structure is composed of two kinds of sub-structures: a cone centered on the axis of the specimen, with the tip outside the specimen and its contour matching exactly the specimen's bottom section; and a set of shear planes radially

aligned, see Figure 2.1. Desrues et al. (1996) concluded that the turbine structure developed for both loose and dense sands. In another summarized study, Desrues and Chambon (2002) mentioned that in axisymmetric tests, strain localization may remain more or less hidden inside the specimen, especially when improved test conditions are used, with reduced slenderness and refined anti-friction devices. The same shear pattern was confirmed by Alshibli et al. (2000), who used computed tomography to investigate the internal structures of sand specimens subject to axisymmetric triaxial tests in a microgravity environment aboard the Space Shuttle during the NASA STA-79 mission.

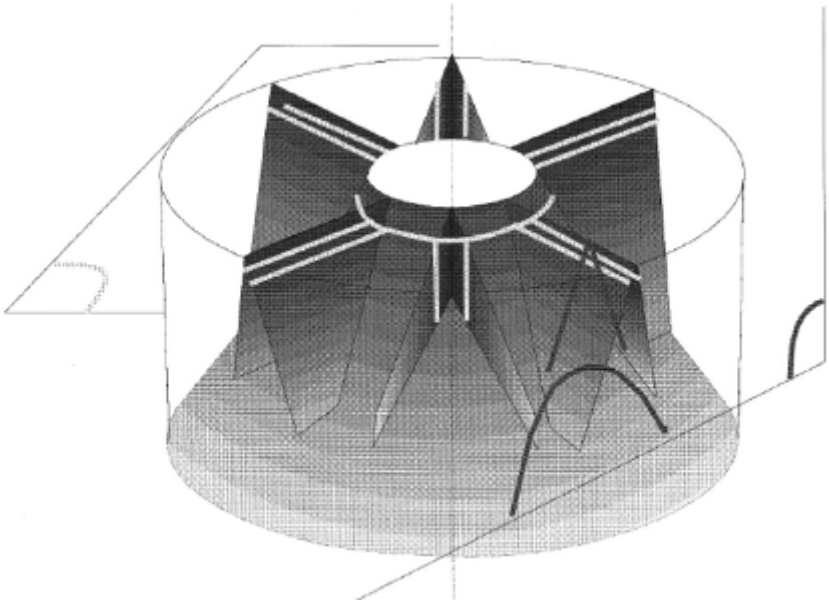

Figure 2.1 Idealized representation of the shear pattern in triaxial sands (Desrues et al., 1996)

One of the factors that lead to prominent presence of strain localization is the 3-D stress condition. Therefore, strain localization or shear banding can be observed in most of the true triaxial compression tests, in which intermediate principal stress can be controlled separately from minor principal stress. Desrues et al. (1985) tested dry sands in a rigid-platen true triaxial apparatus. The sand specimens were wrapped in painted rubber membranes which helped highlighting the localized zones of shear deformation

(Figure 2.2). Wang and Lade (2001) performed a series of true triaxial tests on dense, medium and loose Santa Monica Beach sand. The shear bands were usually observed on the minor principal stress surface when the strength of the specimens was decreasing at the highest rate, and shear bands became well defined when the strength reached its residual state. By testing dense Toyoura sand using a rigid-platen true triaxial apparatus, Sun et al. (2008) concluded that strain localization resulted in a sharp peak in the stress ratio strain curve with a sudden drop of shear strength and a sudden change in volumetric deformation rate.

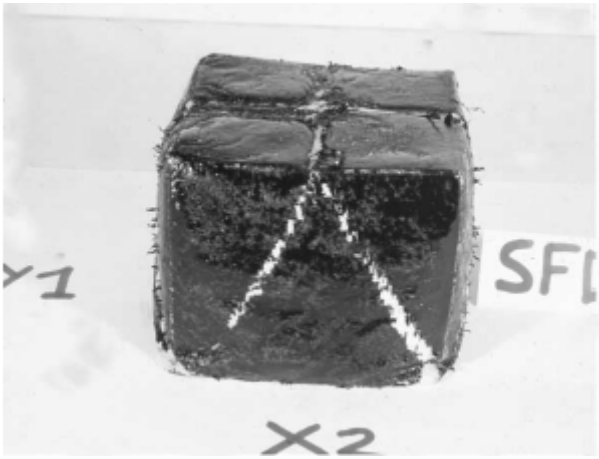

Figure 2.2 Strain localization in a cubical specimen tested in a rigid-platen true triaxial apparatus (Desrues et al., 1985)

In plane strain (biaxial) compression tests, strain localization is the dominant failure pattern due to the configuration of the tests – strain is restricted in one horizontal direction and not restricted in the orthogonal direction. Normally, shear bands initialize around the peak and become more clearly defined as shearing proceeds. Therefore, plane strain tests have been heavily investigated by researches for the phenomenon of strain localization. Since the first documented case in 1936 (Kjellman, 1936), many researchers have reported experimental and theoretical works on plane strain tests on soils (e.g., Bishop, 1961; Duncan and Seed, 1966; Lee, 1970; Vardoulakis, 1980; Drescher et al.,

1990; Tatsuoka et al., 1990; Han and Vardoulakis, 1991; Peric et al., 1992; Finno et al., 1996; Rechenmacher, 2005; Frost and Evans, 2009; Evans and Frost, 2010). Most of the experimental work indicated the occurrence of single or multiple shear bands. Figure 2.3 shows the shear band that developed at different strain levels for Ottawa sand under biaxial compression.

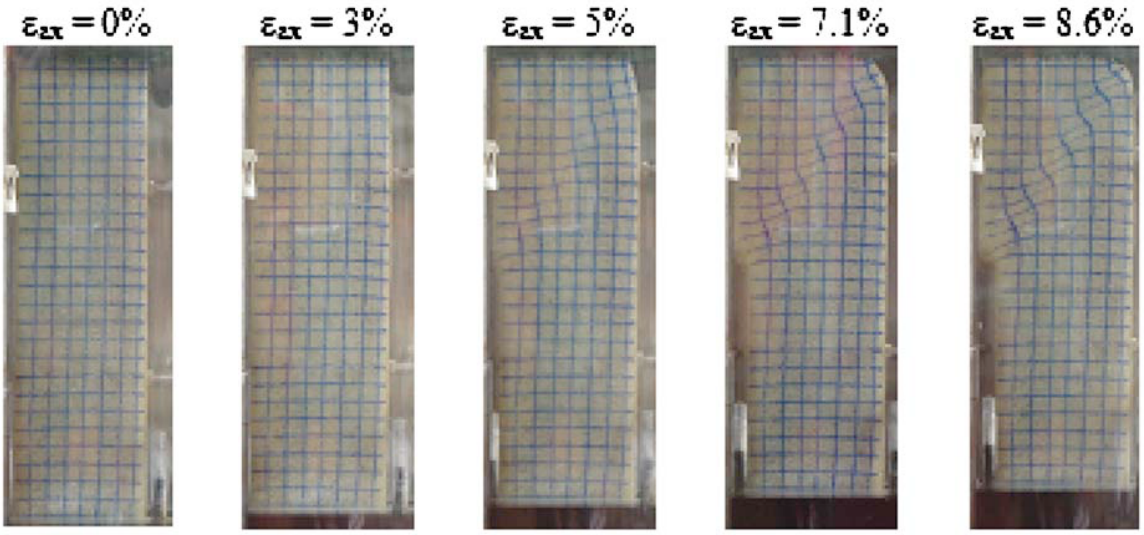

Figure 2.3 Shear banding of Ottawa sand under biaxial compression (Frost and Evans, 2009)

By summarizing previously published research works, Desrues and Chambon (2002) reached the conclusion that strain localization in shear band mode can be observed in most, if not all, laboratory tests leading to rupture in geomaterials, at least at sufficiently low temperature and pressure. Therefore, it is necessary to further investigate the intriguing mechanism of strain localization and how it affects the general behavior of soil specimens.

2.2. 3-D Characterization and Visualization of Soil Microstructures

As strain localization is closely related to the failure behavior of soils, some researchers have tried different approaches to find the link between the two mechanisms.

One of these approaches is to characterize the material behavior (void ratio, distribution of voids, particle size, particle orientation, etc.) as well as the mechanical behavior (shear strain, volumetric strain, and etc) of the strain localization zones. Since the strain localization zones are relatively thin (usually about 10~20 particle size wide for sands), characterization of the zones needs to be conducted at the sub-particle scale. For strain localization in clay, the behavior is somewhat different from that in sand and its characterization won't be discussed further herein. The technologies used to characterize soil microstructure have evolved reapidly especially in the last decade, from rudimentary 2-D optical image methods to the currently available 3-D methods based on X-ray CT, MRI and high resolution optical microscopy. The current trend of imaging technologies for soil microstructure studies can be summarized as: three-dimensional (3-D), rapid generation of images, and availability and affordability to researchers. In the following sections, some of the most frequently used imaging technologies will be reviewed and summarized, including Digital Image Correlation (DIC), X-ray Computed Tomography (CT), and microscopy based serial sectioning.

2.2.1. Digital Image Correlation

Before discussing Digital Image Correlation, a parallel technique called False Relief Stereophotogrammetry (FRS) is noted. Both FRS and DIC are predominantly used for tracking displacement fields in a specimen. The first known documented use of FRS in soil mechanics was Butterfield et al. (1970). Later, FRS was applied in plane strain tests to detect non-homogeneous deformation (Desrues, 1984; Viggiani and Desrues, 2004). The major principles of FRS are based on the analyses of successive analog photographs taken from a fixed viewpoint at different time intervals during loading. With the help of some markers (drawn grid or paints) on the specimen surface, a matrix of incremental displacements can be created and the values can be computed by comparing two photos at different time intervals. However, an assumption of FRS is that the

deformations captured by the photographs are planar, and hence FRS is best suited for plane strain tests. With the rapid development of digital photography and relevant computation techniques in recent years, the FRS method has been gradually superseded by DIC. Similar to FRS, DIC computes displacement fields by correlating successive digital images taken at different times. However, instead of manually-instrumented markers, DIC tracks the grey-scale values within pre-defined subsets. A digital image is composed of arrays of pixels and each pixel reflects a grey-scale number representing brightness. As noted by Rechenmacher (2005), pixel subset sizes used in the analyses have to be large enough to encompass a unique gray level pattern (to avail a unique mathematical pattern for matching), but also small enough to limit subsets to only affine straining over a deformation increment (an assumption in the DIC matching algorithm). In addition to 2-D space, the technique of DIC has already been extended to 3-D space. By positioning two cameras, which take photos from two different viewpoints, the 3-D shape of the object and 3-D displacements (X-, Y-, Z- plane) can be established. Therefore, DIC is no longer restricted to plane strain tests (Rechenmacher and Finno, 2004; Rechenmacher et al., 2010), but can be applied to other laboratory tests such as triaxial tests (Rechenmacher, 2005). By studying the evolution of strain localization with time in the plane strain tests using DIC, Rechenmacher (2005) and Rechenmacher et al. (2010) concluded that multiple and conjugate shear bands were seen to initiate their formation in the hardening regime, while the fate of the persistent shear band clearly was not decided until softening.

Compared with FRS, DIC is more affordable and available to researchers as no special equipment other than digital cameras and some software algorithms to perform DIC correlation are required. However, there are some limitations of DIC:

- Displacement within sub-regions is the only one direct measurement;

- Resolution of the measurements is affected by the resolution of the digital images, which will be more than 30 μm/pixel if the image of a typical plane strain specimen (140 mm in height) is taken by a 10-Megapixel digital camera; and
- Only surface displacements can be measured with very limited knowledge of the internal structures.

An alternative to the last limitation is to combine DIC with X-ray CT to illustrate the displacements of the internal structures. This will be discussed further in the next section.

2.2.2. X-Ray Computed Tomography

The early application of X-ray in geotechnical engineering was measuring strain fields in soils using X-ray radiography in 1960s (Roscoe et al., 1963). X-ray radiography is an image capturing technique based on X-ray attenuation according to different densities and compositions of objects. The system usually is composed of a source and a detector (film sensitive to X-ray or digital detector). The source projects X-rays into the targeted object, and the detector that is positioned behind the object captures the X-rays that pass through the object. Ultimately, X-ray radiography gives a 2-D presentation of superimposed internal structures. For soil masses, this technique is able to detect although not quantify the heterogeneity of soil density in 2-D space. With the advancement of technologies, 3-D representation of objects can now be achieved by X-ray computed tomography (CT). For X-ray CT, the source and detector are not fixed but rotate around the object. A series of 2-D images of the targeted object are taken at different angles and later correlated by computer programs to construct a 3-D representation of the structure. The 3-D images can be dissected in different directions for characterization and analysis. So far, X-ray CT has been used in a wide range of fields – medical, manufacturing, and petroleum amongst other. One of the pioneering applications of X-ray CT in soil testing is measuring the void ratio evolution inside shear bands in triaxial sand specimens by Desrues et al. (1996). Desrues and his coworkers performed a series of axisymmetric

triaxial compression tests on dry Hostun RF sand with different material densities (loose and dense), boundary conditions (lubricated and non-lubricated), specimen dimensions (long and short), and induced imperfections. The specimens were scanned by X-ray scanners at the initial, final, and some intermediate stages of loading. By examining the X-ray CT images of the specimens similar to those shown in Figure 2.4, Desrues et al. (1996) proposed a complex localization pattern for triaxial specimens (introduced in Section 2.1 and Figure 2.1). In addition to the localization model, Desrues et al. (1996) was able to link local X-ray attenuation value to local density of the sand, and concluded that the limit-state void ratio is measured not globally but inside the shear bands. After Desrues et al. (1996), many researches have utilized X-ray CT to study soil behavior (e.g., Shi et al., 1999; Alshibli et al., 2000; Otani et al., 2000; Ngan-Tillard et al., 2005; Kneafsey et al., 2007; Alshibli and Hasan, 2008; Thomson and Wong, 2008; Hall et al., 2010). Some of these researches even realized in-field measurements (scanning the specimens while performing the soil tests). Consequently, the testing results are not affected by interruptions to scan the specimen. With the ability to obtain images at different times, X-ray CT can be combined with DIC to produce a true 3-D displacement field for the specimen (Hall et al., 2010). The image resolution of X-ray CT images are normally a few hundred micrometers per pixel (e.g., 2 mm/pixel for Desrues et al., 1996, 0.2 mm/pixel for Alshibli et al., 2000, 0.48 mm/pixel for Thomson and Wong, 2008) based on energy intensity of regular X-ray sources. Considering the size range for sand (0.075 mm to 2 mm), such resolution is sufficient for characterizing shear band thickness (roughly 10~20 mean particle size) but not individual sand particles or a segmented void. In other words, characterization using X-ray CT does not reach microstructural level, but rather an average over the region that spans a few particle diameters. In the past few years, a newer higher-energy X-ray source has been available through synchrotron radiation which produces images with high resolution. Such technique has been implemented to characterize the shear bands with a resolution of a few micrometers per

pixel (9 μm/pixel for a cylindrical volume with 9 mm in diameter and 1.8 mm in height from Oda et al., 2004; 15 μm/pixel for cylindrical cores with 8 mm in diameter and 50 mm in height from Hasan and Alshibli, 2010; 14 μm/pixel for cylindrical specimens with 11 mm in diameter and 22 mm in height from Hall et al., 2010). As the result, microstructural behaviors, like particle rotation, particle orientation, coordination number, etc. have been characterized, and some interesting findings about strain localization have been reported. Oda et al. (2004) studied the particle arrangement within the shear bands in the plane strain tests, and proposed the large void in the shear band is surrounded by linked particles (so-called columns). The existence of those columns explains why large voids can exist in shear bands where large shear deformation is accumulating. Hasan and Alshibli (2010) characterized the material behaviors of sand particles under plane strain tests using high-resolution X-ray CT, and indicated most particles inside the shear band orient themselves perpendicular to the shear band, while particles outside the shear band have no preferred orientations in the horizontal plane. Hall et al. (2010) reported that for the triaxial tests of sands, a clear correspondence can be established between the zones of the specimen experiencing localization of shear strain and the zones where grain rotations are more intense.

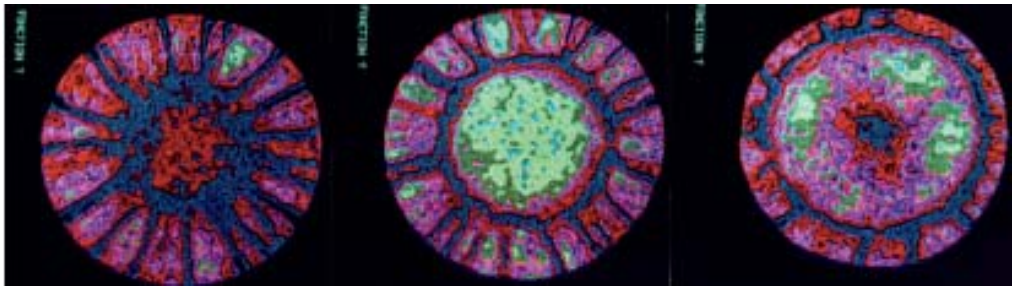

Figure 2.4 Horizontal slices through an X-ray CT image volume of a triaxial compression specimen of dry dense Hostun sand near the end of test (Viggiani and Hall, 2008)

2.2.3. Microscopy Based Serial Sectioning

Although characterization of soil microstructures based on microscopic images is not a new technique (e.g., Jongerius et al., 1972; Michelland et al., 1989; Yudhbir and Abedinzadeh, 1991), its application to soil laboratory testing has been more recent. Over the past twenty years, different soil specimens have been tested, preserved or impregnated under various test conditions, and imaged under microscopes for microstructural characterization and analysis. Some relevant works are Bhatia and Soliman (1990), Ibrahim and Kagawa (1991), Kuo and Frost (1995), Kuo et al. (1998), Frost and Jang (2000), Evans and Frost (2010), Wang et al. (2010). Compared with the aforementioned DIC and X-ray tomography, the optical microscopic images provides short-range images (sub-particle level), which enables a more comprehensive characterization of the soil microstructure (particle size, fabric tensors, coordination number, void space, etc.).

With the advent of serial sectioning, microscopy based image analysis can be used to create 3-D microstructures. Serial sectioning technique was developed in the 1970s in the field of material science (Rhines and Craig, 1976). Such techniques involve taking successive images of the specimens while gradually removing the materials and stacking the images in order to create a 3-D representation. Serial sectioning was later improved by image montage and surface removing/preparation techniques. Image montage relates to the capturing of small field-of-view images in a grid pattern and then stitching those images into a large field-of-view image. With image montage, a large field of interest, can be investigated while not losing image resolution required for small particles. New developments in surface grinding/polishing allow for the fast removal of material and the production of high-quality surfaces for subsequent imaging. Fast removal of the materials reduces the time to complete hundreds of section slices, while surface preparation can substantially affect image quality and consequent image processing needs. If the images are generated in low quality, processing of the images

before they can be characterized requires complicated procedures and can take a long time. Compared with other 3-D characterization techniques (X-ray CT and MRI), serial sectioning is inexpensive and easy to operate yet produces high-resolution large area images. Therefore, it has been used widely in material science (e.g., Bystrzycki and Prezetakiewicz, 1992; Li et al., 1998; Tewari and Gokhale, 2000; Singh and Gokhale, 2005), biomedical (e.g., Fiala and Harris, 2001; Hoffpauir et al., 2007) and many other fields. The application of serial sectioning in soil testing is relatively novel and not much work has been completed to date (Yang, 2005). Compared with other 3-D characterization techniques that have been used in soil testing, such as DIC and X-ray CT, serial sectioning has the advantage of being able to capturing both short-range (particle-wise) and long-range features (localized zones). Reconstruction of a specimen >10 mm in dimension with the resolution of a few micrometers can be easily achieved using affordable and commercially available preparation apparatus and an optical microscope. Such resolution can only be achieved by high-energy X-ray source (Oda et al., 2004; Hasan and Alshibli, 2010; Hall et al., 2010). Those high-energy X-ray sources are expensive and not easily accessible to most researchers in geotechnical engineering. The disadvantage of serial sectioning is that it is a destructive technique.

2.3. Numerical Modeling of Soil Laboratory Testing

Among the numerical modeling methods available for soil laboratory testing, the finite element method (FEM) and the discrete element method (FEM) are the most widely used ones.

2.3.1. Finite Element Method

Finite Element Method (FEM) emerged as a numerical tool to model continua in the middle of the last century and the term “The Finite Element Method” was first proposed by Clough (1960). In FEM, the continua are discretized into meshes which are

the basic elements for simulation. The elements are connected by points (also called nodes), and interactions between the elements are solved by a series of differential equations. Generally, finer meshes with more nodes yield more accurate predictions. Since its introduction into the field of geotechnical engineering by Clough and Duncan (1971) to model soil-structure-interaction, FEM has been used to model various geotechnical problems (e.g., Clough and Hansen, 1971; Borja and Lee, 1990; Ou et al., 1996; Griffiths and Lane, 1999; Seo et al., 2009). The basic principles of FEM are elasticity and plasticity. However, classical theorems of elasticity and plasticity like Hooke's Linear Law of elasticity are too simple to capture the behaviors of different geomaterials (rock, sand, and clay). To compensate for this, various constitutive models (e.g., Mohr-Coulomb model, Cam-Clay model and Duncan-Chang Hyperbolic Model) were proposed and are still the subject of an ongoing research. Applications of FEM to laboratory soil testing are relatively fewer than in other problems. Some of the case histories are modeling triaxial tests on sands by Macari-Pasqualino et al. (1994), triaxial tests on clay by Sheng et al. (1997), and triaxial tests on clay by Liyanapathirana et al. (2005). A number of issues are related to modeling soil tests with FEM, one of which is that FEM is unable to handle large-deformation problems since they will result in the collapse of the discretized mesh. Another issue is that once localized zones appear which is true for most cases, the soil mass can no longer be treated as a continuum. In addition, modeling sand with FEM is relatively less appropriate than modeling rock or clay, as sand is usually considered to have little or even no cohesion.

2.3.2. Discrete Element Method

The discrete element method (DEM) was pioneered by Cundall (1971) in rock mechanics and is currently one of the preferred numerical techniques to model geomaterials. DEM assumes the soil mass is composed of distinct particles which can displace independently from one another and interact only at contact points (Cundall and

Strack 1979). The major principles behind DEM are fairly simple – the motion of each particle is calculated by Newton's second law, and the force of each particle is updated by a force-displacement law. Although the interactions between particles are basically elastic, an assembly of particles can undergo large strain, display plastic behaviors, and exhibit localized strains. Except for the mechanical behavior, DEM provides for better simulations of material behavior at a microscopic scale than FEM. Since the basic elements in 2-D DEM are circular particles (or disks) which can be bonded or detached, they can maneuver in different ways: contact, detach, shear, slip, etc. Therefore, DEM is a useful tool studying the microstructural behaviors of geomaterials. DEM has been used by many researchers to model both laboratory (e.g., Cundall, 1989; Iwashita and Oda, 1998; Bertrand et al., 2005; Cheng et al., 2008; Yan, 2009; Wang and Gutierrez, 2010) and field (e.g., Maynar and Rodríguez, 2005; Vardakos et al., 2006; Lobo-Guerrero and Vallejo, 2007; Shoda et al., 2009) works in the last decade. Most of the early research work was completed using two-dimensional (2-D) models due to various reasons, one of which is computational capabilities. However, as soil masses are subject to 3-D loading in most laboratory or field conditions, 2-D modeling is not sufficient for simulation. One example is the role that intermediate principal stress plays in strain localization during triaxial and plane strain tests. Although some insights could be gained through 2-D DEM simulations (e.g., Huang et al., 2008; Wang and Leung, 2008; Mahmood and Iwashita, 2010), nevertheless, 3-D DEM simulation can yield a better solution. Recently, 3-D DEM was used by a number of researchers to study the mechanical and microstructural behaviors of soils subject to triaxial and biaxial shearing (e.g., Thornton, 2000; Powrie et al., 2005; Salot et al., 2007; Cheung and O'Sullivan, 2008; Belheine et al., 2009; O'Sullivan and Cui, 2009; Zhao and Evans, 2009).

Compared with FEM, although DEM is highly capable of simulating particle-wise behaviors of geomaterials, it does have several drawbacks. One of them is the boundary conditions. For many of the physical laboratory soil tests, the soil masses are bound with

flexible membranes. Such boundary conditions are continuum in nature and conform to the law of elasticity. Thus, they cannot be fully realized in DEM provided the major principles are Newton's second law and a force-displacement law. Another drawback is that with current computational capability, a full-scale simulation of soil mechanics problems is still impossible. One example is that for a regular plane strain laboratory test on Ottawa 20-30 sand specimens, such as those analyzed in his study, the number of particles contained in the specimen is approximately 1.4 million. Nevertheless, performing a DEM test with this number of particles is computationally expensive, and most of time the particles are scaled several times to substantially reduce the computation load. Consequently, the simulation results will encounter some scaling problems and the validity of using DEM in large-domain problems, especially field works, is limited. In recent years, some researchers have proposed combining DEM and FEM to solve the drawbacks of both numerical methods while not losing their advantages: Kaneko et al. (2003) developed a global-local analysis to model biaxial tests on sands; Fakhimi (2009) used a hybrid discrete-finite element model to simulate triaxial tests on sands; Elmekati and El Shamy (2010) coupled FEM and DEM programs to model axially loaded piles embedded in granular media. However, those attempts require either appropriate coupling techniques to handle FEM and DEM programs or compiling specific in-house programs.

2.4. Summary and Conclusions

Strain localization is the phenomenon of extensive large shearing induced deformations concentrating within thin zones of shearing. This phenomenon has been widely observed in many in-situ geo-structures and most laboratory soil tests. Some researchers have proved that even under a testing condition favoring symmetry (i.e., asymmetric triaxial test), strain localization still occurs in the internal structure. As strain localization eventually leads to the shear failure of geomaterials, investigations into the intriguing mechanism of strain localization, the development of the microstructural

properties inside the localized zones, and their link to the general engineering behavior will facilitate the understanding of the shear failure behavior of soils.

As the localized zones are usually very thin (10~15 particle diameters wide for sands), the characterization on the microstructural properties needs to be conducted at the sub-particle scale. Some of the available technologies that can do this are: digital image correlation, X-ray (micro) computed tomography and microscopy based serial sectioning. Among those technologies, both X-ray micro CT and serial sectioning can provide 3-D reconstruction of the specimens with sufficient resolution (i.e., a few micrometers). However, compared to X-ray micro CT, serial sectioning can nominally extend the reconstructed specimen size using image montage and image stacking techniques. As the apparatus for serial sectioning is commercially available and affordable, microscopy based serial sectioning is widely accessible to researchers in geotechnical engineering.

For soil lab tests, the finite element method and the discrete element method are the most frequently used numerical modeling techniques. However, applications of FEM in modeling soil lab tests are limited because large deformations, bifurcation problems and the discrete nature of granular materials are difficult to accommodate in FEM. On the contrary, the discrete element method solves these problems by using distinct particles as the basic model elements. Although DEM has its own drawbacks such as difficulty in modeling a continuum and the fact that particle scaling is normally needed to control computational effort, it is currently one of the preferred numerical techniques to model geomaterials.

Some of the techniques introduced in this chapter have already been implemented in the studies on strain localization of sheared Ottawa sand at Georgia Tech over the past ten years. These previous studies along with the findings will be introduced in the next chapter.

CHAPTER 3

COMPLEMENTARY RELATED STUDIES

3.1. Introduction

The current study extends and complements two previous studies on strain localization in laboratory specimens of Ottawa sand subject to triaxial and biaxial loading (see Table 1.1). Therefore, it is appropriate to review the scope and findings of the previous related studies in some detail before presenting the findings from the current study. Those studies are triaxial tests related works fulfilled by Yang (2005) and biaxial tests related works completed by Evans (2005), and they are introduced sequentially in the following sections.

3.2. Triaxial Related Researches

Yang (2005) performed triaxial compression tests on Ottawa sands. Some of the specimens were later impregnated and 3-D digital structures were reconstructed by montage generation and serial sectioning. A series of 2-D and 3-D characterizations were completed based on the reconstructed structures.

3.2.1. Testing and Reconstruction of Triaxial Specimens

The material tested was dry Ottawa 30-50 sands, composed of poorly graded, sub-rounded quartz sands with median particle size of 0.35 mm. A standard sieve analysis that conformed to ASTM D422-63 was performed, and the grain size distribution is shown in Figure 3.1. Some index properties of the sand are listed in Table 3.1. Two preparation methods, air pluviation (AP) and moist tamping (MT), were used to create specimens of different soil fabrics with close initial void ratios. The prepared specimens were nominally 140 mm in height and 70 mm in diameter and were sheared to a global

axial strain of about 14% under an initial effective confining stress of 50 kPa using a CKC automated triaxial system manufactured by Soil Engineering Equipment Company. After shearing was completed, the specimens were impregnated with Epo-Tek 301 epoxy resin from Epoxy Technology. The epoxy resin was selected for its low viscosity, optical transparency and low shrinkage. In order to compare the sheared microstructures with unsheared microstructures, two extra specimens that were not sheared were prepared with AP and MT and impregnated using the same epoxy resin technique as the sheared specimens. Information on four specimens used to compare inherent and induced microstructures in triaxial specimens is listed in Table 3.2.

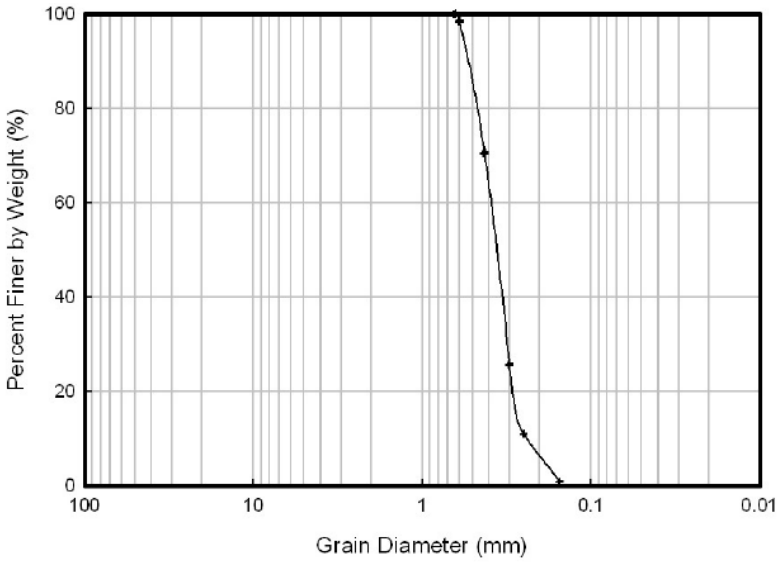

Figure 3.1 Grain size distribution of Ottawa 30-50 sands (Yang, 2005)

Table 3.1 Index properties of Ottawa 30-50 sands (based on Yang, 2005)

Material Property	Tested Sands
Median Grain Size, D_{50} (mm)	0.35
Coefficient of Uniformity, C_u	1.65
Coefficient of Curvature, C_c	1.06
Specific Gravity, G_s	2.67
Maximum Void Ratio, e_{max}	0.82
Minimum Void Ratio, e_{min}	0.50

Table 3.2 Specimen information (based on Yang, 2005)

Sample ID	Shearing State	Preparation Method	Initial Void Ratio
AP0	Unsheared	Air pluviation	0.582
AP14	Sheared to 14% axial strain	Air pluviation	0.579
MT0	Unsheared	Moist tamping	0.580
MT14	Sheared to 14% axial strain	Moist tamping	0.583

A coupon, 19 mm x 11 mm x 5 mm in size, was cut from each resin impregnated specimen. For all specimens, the coupons were extracted from central portion of the specimens and thus for the sheared specimens contained the microstructures induced by shearing. The four extracted coupons were then serial sectioned to generate stacks of imaged slices that were later volume rendered into 3-D digital geo-structures. The laboratory procedure for serial sectioning was:

- The coupon was placed in a cylindrical mounting cup and impregnated with epoxy resin. This step yielded a specimen of appropriate shape and size for the preparation machine;
- The specimen was removed from the mounting cup after the resin had cured. Four cylindrical holes and four conical holes were drilled into the impregnated coupon corners for the purpose of aligning the coupon during image processing and controlling the removal thickness between two adjacent slices, respectively;
- The grinding and polishing MultiPrep^{TM} system from Allied High Tech Products Inc. was calibrated as specified by the manufacturer;
- The specimen was mounted in the MultiPrep^{TM} system, and a layer of materials about 8 μm thick was removed using 6 μm Dia-Grid Diamond Discs;
- The specimen surface was polished with 1 μm Diamond Compound on Gold Label Cloth for about 30 seconds;

- Images of the specimen surface were captured using a Leica DM4000 microscope;
- The last three steps were repeated until the desired number of slices was obtained.

When capturing the images of the specimen under the microscope, the montage technique was applied using QWin software. A large area high-resolution image of each surface was obtained by stitching 20 sub-images in a 5 x 4 grid pattern with an overlap of 20%. As a result, each coupon was digitized into 600 slices with 2465 x 1465 pixels in size. Each slice was imaged with a resolution of 7.83 μm/pixel and each slice was spaced 8 μm away from adjacent slices, which yielded similar resolutions in the x, y, and z directions. The images were aligned using ImageJ from NIH with the plugin RegisterROI by Abràmoff (2004) to correct for any possible rotational and translational movements between slices. The stitched slices were then cropped to a size of 1800 x 1100 pixels for software limitation reasons. After binarization and image processing, the slices were rendered into 3-D structures using the program VoxBlast from Vay Tek, Inc. The typical 3-D structure shown in Figure 3.2 represents a sample size of 14 mm x 9 mm x 5 mm and contained approximately 20,000 sand grains in the volume. This digital volume contains approximately 1.2 billion voxels of side 8 μm.

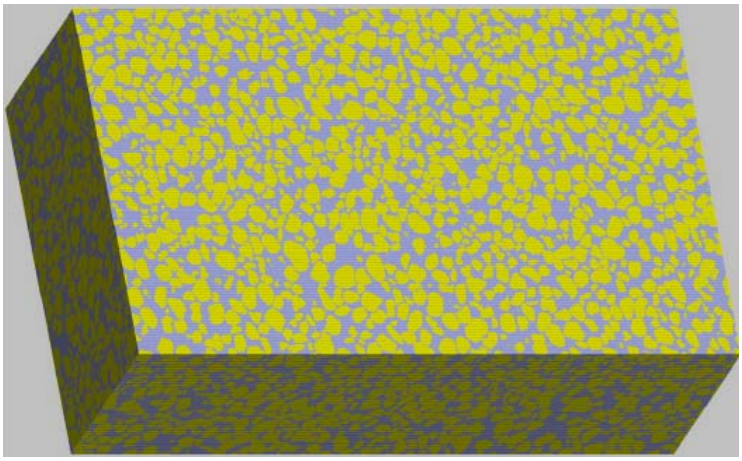

Figure 3.2 3-D reconstructed structure with yellow represents sand grains and blue for pore space (Yang, 2005)

3.2.2. 2-D and 3-D Characterization and Visualization of Triaxial Specimens

2-D characterizations of the triaxial specimens included local void ratio distributions, 2-D pore size measurement and 2-D throat size measurement. 3-D characterizations included 3-D void ratio measurement, 3-D throat size, 3-D pore size and tortuosity. Selected results are summarized below.

The 2-D pores were characterized by local void ratio distributions and pore size distributions. The local void ratio distribution was calculated based on 60 selected slices (every tenth) for each specimen (Figure 3.3). In general, sheared specimens showed a large statistical mean than the unsheared specimens, which indicates more large voids can be found in sheared specimens. The induced pore structures in the sheared specimens were also characterized by pore size distributions in Figure 3.4. The distributions for both AP14 and MT14 were shifted to the right of AP0 and MT0, which indicates dilated internal structures inside AP14 and MT14. The data in Figure 3.4 for sheared specimens does not discriminate between zones of limited/moderate and high shearing within specimens, nevertheless the noted trend is greater for the AP specimens where more extensive shearing occurred than for the MT specimens where stronger localization occurred.

3-D microstructural behavior of the specimens was quantified by a research software package, 3DMA (Lindquist, 1999). The software was initially designed to characterize pores in rocks, most of which are disconnected. When using 3DMA to analyze pore structures of sands, image dilation needs to be applied to the individual slices to create more shared points between particles so that the pores can be segmented. The 3-D void ratios were calculated by voxel count (Table 3.3) and matched well with the 2-D void ratios. The 3-D pore size distributions for both unsheared and sheared specimens are shown in Figure 3.5. Consistent with 2-D pore size distributions, the histogram of AP 14 was shifted to the right of AP0, a sign indicating that larger voids were identified in the sheared specimen. On the contrary, the histogram of MT 14 was

shifted to the left of MT0, which was contradictory to the findings in 2-D analysis. Yang (2005) concluded that the possible causes are the algorithm used in the software (3DMA) to partition the pore space and the 3-D morphological operations performed on the non-uniform structure.

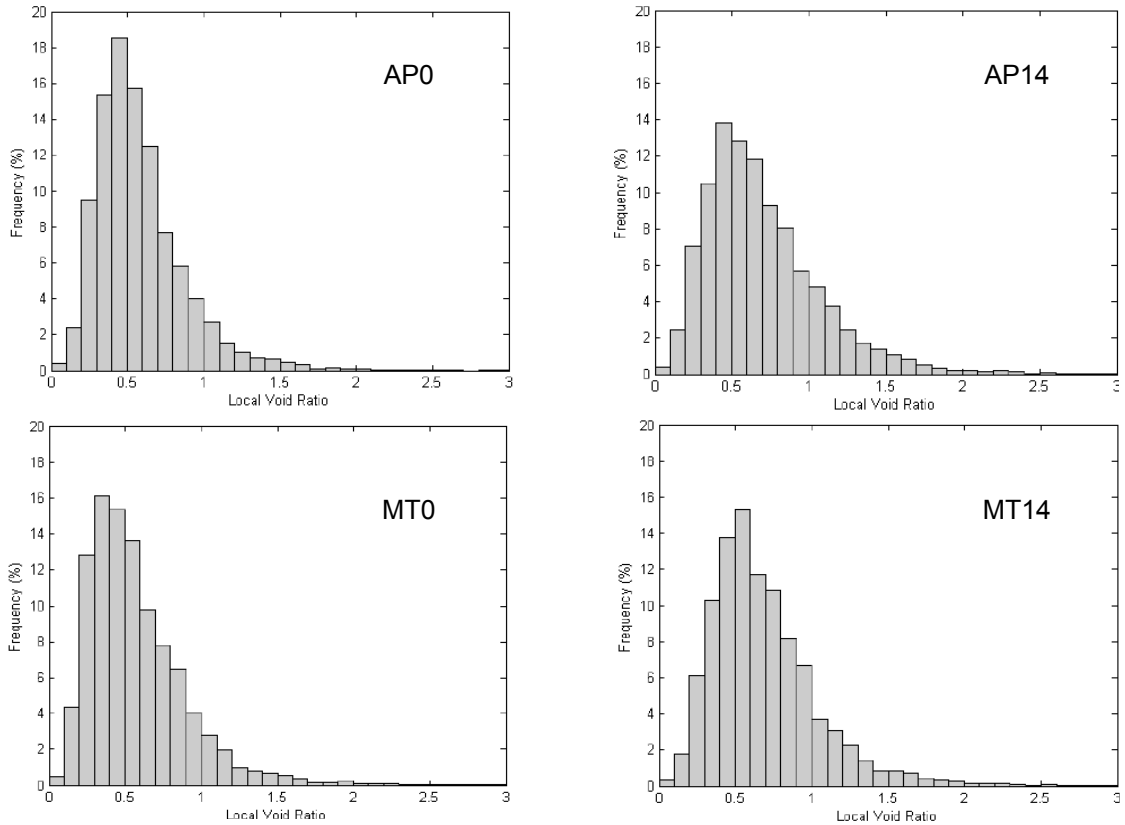

Figure 3.3 Local void ratio distributions of triaxial specimens (Yang, 2005)

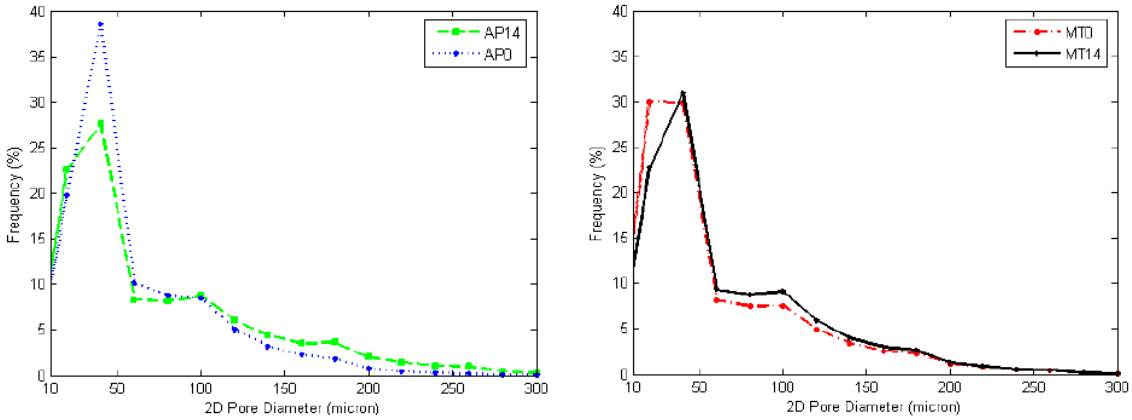

Figure 3.4 Pore size distributions of triaxial specimens (Yang, 2005)

Table 3.3 Porosity and void ratio information for triaxial specimens (Yang, 2005)

Sample	2-D porosity	3-D porosity	2-D Void Ratio	3-D Void Ratio	Experimental Measurement of Void Ratio
AP0	0.365	0.365	0.575	0.576	0.582
AP14	0.417	0.417	0.715	0.716	N/A
MT0	0.365	0.365	0.575	0.575	0.580
MT14	0.413	0.415	0.704	0.709	N/A

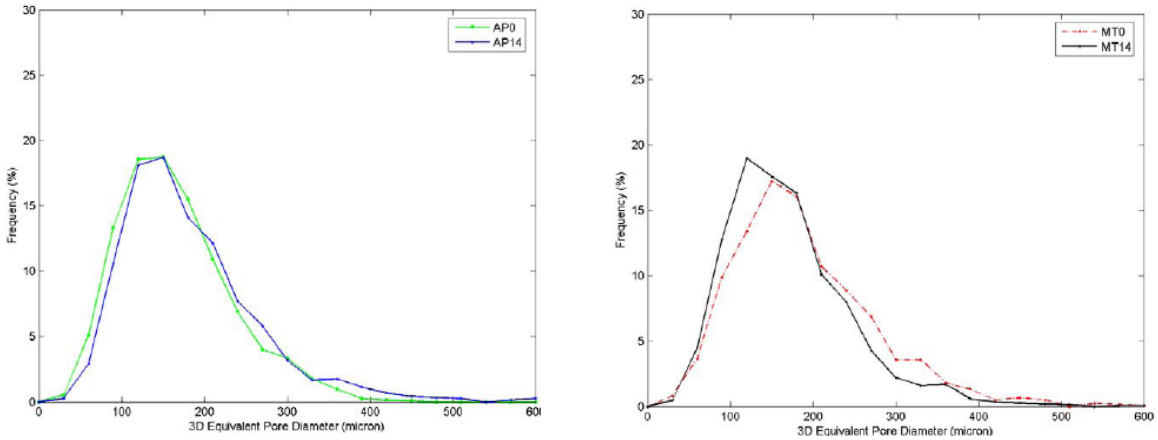

Figure 3.5 3-D pore size distributions for triaxial specimens (Yang, 2005)

One of the key elements in 3DMA is constructing the medial axis of the pore space. Medial axis is defined as the "spine" of the object running along its geometric centers (Lindquist et al., 1996). The medial axis of the pore space reduces the dimensionality of the structure while still preserving the topological and geometrical information. Only after the medial axis is constructed can the pore space be partitioned, the pore bodies identified, and the path length and tortuosity calculated. Tortuosity describes the length of a path an object travels through a set of interconnected pores. In 3DMA, all the connected medial axis paths between the medial axis voxels on two parallel planes can be tracked. The shortest path tortuosity is defined as the ratio between the shortest path length and the Euclindean distance between the voxels (Lindquist, 1999). For the triaxial specimens, the toruosities were estimated in the x, y and z directions using sub-volumes of 600^3 voxels (Table 3.4). The tortuosities in z direction

were always higher than x and y directions, which was due to the 2-D image dilation operation in the x-y planes. Other than that, no obvious anisotropy of tortuosities was observed in those specimens. The mean tortuosities of unsheared specimens were higher than the correlated sheared specimens, which indicate the tortuosity decreases with the increase of pore size.

Table 3.4 Statistics of tuortuosities for triaxial specimens (Yang, 2005)

	Mean				Standard Deviation				Coeff. of Variation (%)			
	AP0	AP14	MT0	MT14	AP0	AP14	MT0	MT14	AP0	AP14	MT0	MT14
X	1.776	1.622	1.690	1.623	0.053	0.034	0.068	0.068	2.98	2.10	4.02	4.19
Y	1.632	1.562	1.697	1.607	0.067	0.032	0.08	0.039	4.11	2.05	4.71	2.43
Z	1.937	1.697	1.839	1.746	0.080	0.051	0.091	0.046	4.13	3.01	4.95	2.63

In addition to the global 3-D volume created by serial sectioning in Figure 3.2, smaller-scale structures (e.g., single particles, pore structures and single pores) could be extracted from the global volume and visualized. Figure 3.6 (a) presents the 3-D view of a single Ottawa sand particle, which exhibits sub-rounded features. Figure 3.6 (b) shows a pore body surrounded by sand particles. Figure 3.6 (c) is a segmented single pore along with its medial axis defined by 3-DMA.

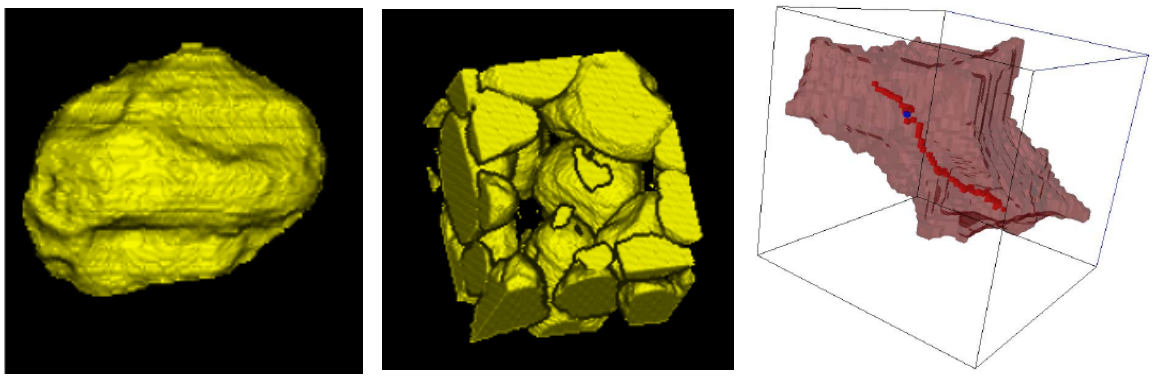

(a) (b) (c)

Figure 3.6 Visualization of (a) single sand particle; (b) a pore body surrounded by sand particles; and (c) a single pore and it medial axis

3.3. Biaxial Related Researches

Evans (2005) performed a series of biaxial shear tests on Ottawa 20-30 sands. The microstructural behaviors of some specimens were characterized using 2-D microscopic images. In addition, 2-D DEM modeling of the biaxial tests was performed to give some supplementary insights into the specimen behaviors under plane strain shearing. The role of membrane in biaxial shear testing was also studies (Evans, 2005; Frost and Evans, 2009).

3.3.1. Biaxial Compression Tests

The laboratory system for biaxial compression tests is comprised of five major parts: air supply, control panel, load frame, specimen chamber and data acquisition system (Figure 3.7). The control panel, load frame and specimen chamber were manufactured by GeoTest Instrument Corporation, and the data acquisition system was developed by Evans (2005). The biaxial device is capable of enforcing plane-strain loading on a prismatic specimen under both drained and undrained conditions. In addition, the base platen rests on a frictionless sled, which can help the shear band to develop once it initializes. Specimens are prepared in a prismatic mold using a manual air pluviator. The nominal dimensions of the prepared specimen are 140 mm in height, 80 mm in length, and 40 mm in width. A series of drained bixial compression tests were performed by Evans (2005) using the system. All tests in the Evans study were performed on dry specimens and the confining stress was applied through air pressure. After shearing, two specimens were impregnated by a two-stage procedure, and were designated as slightly dilatant (BT-2030-13) and highly dilatant (BT-2030-16) according to their initial void ratio, confining stress, and stress-strain response. The two-stage impregnation procedure involved two steps: (1) flushing the specimen while it was still in the biaxial device with a dilute solution of Elmer’s Carpenter Glue to provide initial high cementation; and (2) impregnating the specimen with Epo-Tek 301 epoxy resin after it

was extracted from the biaxial device. In order to provide comparisons between sheared and unsheared specimens, two additional unsheared samples, correlating to slightly dilatant (BT-2030-U2) and highly dilatant (BT-2030-UN), were impregnated and solidified. The test parameters of the four specimens are listed in Table 3.5. For each of the specimen, the middle portion of the specimen was dissected to produce five coupons of size 40 mm x 40 mm x 16 mm. Four of the five coupons were used for analysis by Evans and identified as -20, -40, -60, and -80 according to their locations as a percentage of total sample width. One surface of the -20, -40, -60, and -80 coupons was then ground and polished using a Buehler Metaserve table from Buehler Ltd. After the surfaces were polished, images of the surfaces were captured using a Leica DM4000 microscope. These images were 6791 x 5869 pixels in size and had a 7.83 μm/pixel resolution. Each of these large images was created by stitching 460 sub-images (23 columns and 20 rows) together with an overlap of 50%. The images were then cropped into a final image size of 4400 x 4400 pixels, converted to binary images, and processed to remove noise for later image-based characterization and analysis. The tested material was Ottawa 20-30 sands from the U.S. Silica Company. The sands are poorly graded, sub-rounded, quartz sands with a D_{50} of 0.74 mm. The grain size distribution of the sand is shown in Figure 3.8, and key index properties are listed in Table 3.6.

3.3.2. 2-D Analyses of Biaxial Specimens

2-D analyses of biaxial specimens included local void ratio distributions, subregional void ratios and mean free paths, spatial averaging along pre-determined inclined strips, virtual surface analysis and membrane effects. Some of the results are summarized in the below.

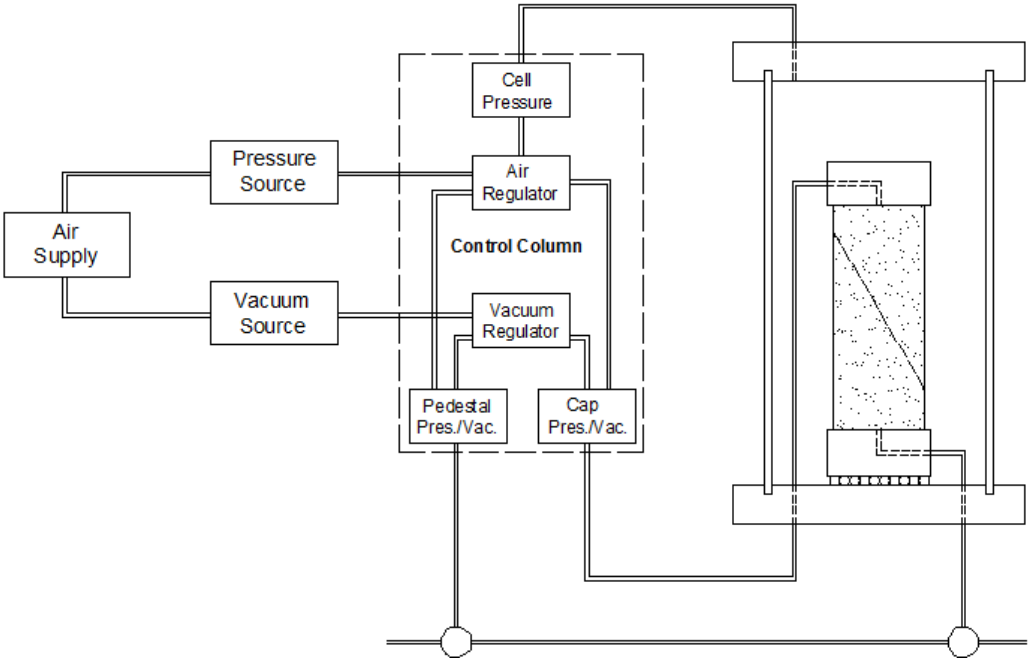

Figure 3.7 Schematic of experimental biaxial system

Table 3.5 Test parameters for the resin-impregnated biaxial specimens (based on Evans, 2005)

	Slightly Dilatant (BT-2030-13)	Unsheared (BT-2030-U2)	Highly Dilatant (BT-2030-16)	Unsheared (BT-2030-UN)
Initial Void Ratio	0.60	0.60	0.56	0.57
Confining Stress	20 psi	20 psi	10 psi	10 psi
Shear Band Inclination Angle	59°	N/A	61°	N/A

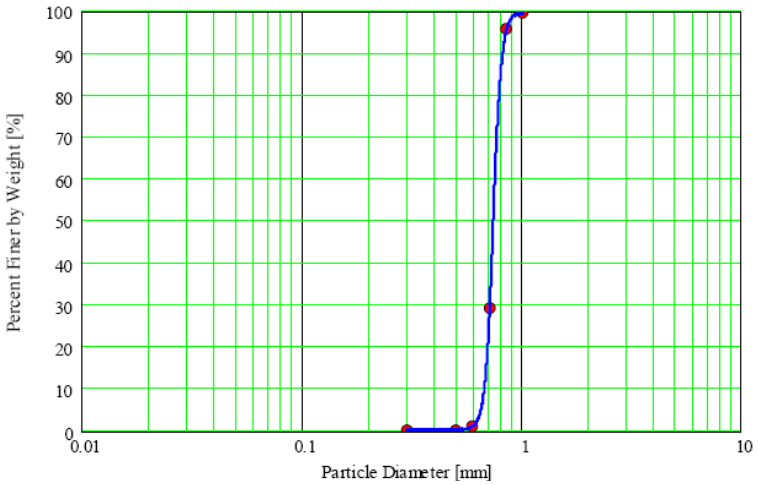

Figure 3.8 Grain size distribution for Ottawa 20-30 sands (Evans, 2005)

Table 3.6 Index properties of Ottawa 20-30 sands (based on Evans, 2005)

Property	Value
Median Grain Size, D_{50} (mm)	0.74
Coefficient of Uniformity, C_u	1.12
Coefficient of Curvature, C_c	1.00
Specific Gravity, G_s	2.65
Maximum Void Ratio, e_{max}	0.742
Minimum Void Ratio, e_{min}	0.502

Spatial averaging calculations along pre-determined inclined strips were performed on the microscopic images to define the extent of shear bands. Each image was divided into 200-pixel (1.57 mm, approximately 2 x D_{50}) wide strips that were oriented along the shear bands. Void ratios were calculated inside each strip and plotted as a function as distance along a transect that is normal to the shear band (Figures 3.9 and 3.10). In unsheared specimens, the strips were inclined as the same angle as the corresponding sheared specimens. The demarcation lines for shear band extent were determined by plotting accumulated area void ratios from the left and the right on the same axes as the incremental void ratios. Locations where the slope of the accumulated void ratios changed in sign were selected as the boundary of shear band. Figures 3.9 clearly indicates the presence and extent of the localized zone within the sheared specimens, and Figure 3.10 shows the void ratios are relatively constant along the transect in the unsheared specimens.

The local void ratio distribution was estimated from all four surfaces for a specimen. Figure 3.11 shows that shearing tends to shift the histograms of sheared specimens to the right of the unsheared specimens. With the extent of shear band defined from spatial averaging analysis, local void ratio distributions were calculated inside and outside shear band (Figure 3.12). The local void ratios inside the shear band increased

dramatically relative to the local void ratios outside the shear band by showing a right-shifted and flattened histogram.

The membrane effects on the stress and strain of the specimens were investigated for the biaxial compression tests using DIC technology. A grid with nominal point spacings of four to five millimeters was drawn on the side of the membrane prior to testing. An image of the specimen was captured by a 3.2-megapixel Canon PowerShot A75 digital camera every two minutes during testing. The positions of the grid points in the images taken at different times were correlated to create displacement fields for the specimen. Figure 3.13 shows the membrane deformation contours for a typical biaxial test and indicates the occurrence of localization between 5% and 6% axial strain. The stress tensor of the membrane was then calculated from the strain tensor (converted from displacement tensor) by Hooke's Linear Law and applied to correct in-plane stresses after localization. Evans (2005) found that the overall normal stress correction should be on the order of 1 kPa for the entire length of displacement along the shear band. This amounts to an average correction of approximately 0.5% in the slightly dilatant specimen and 1% in the highly dilatant specimen. For the shear stress, membrane effects amount to approximately 9% of the total shear stress in the slightly dilatant specimen and 18% in the highly dilatant specimen.

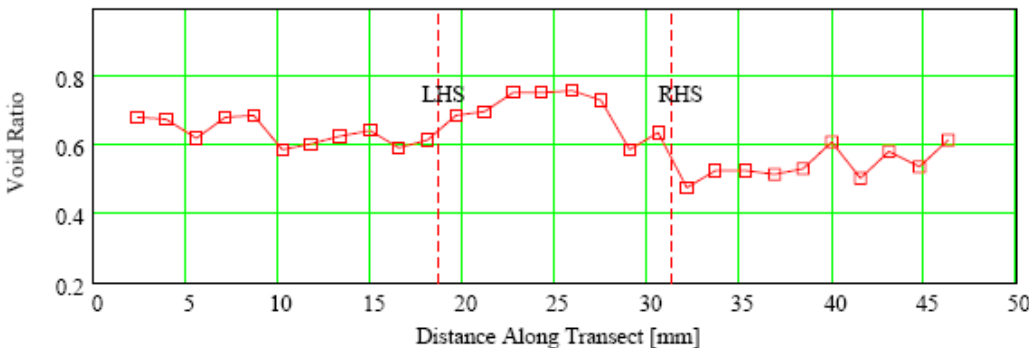

Figure 3.9 Incremental void ratio transects for surface -60 of highly dilatant sheared specimen (Evans, 2005)

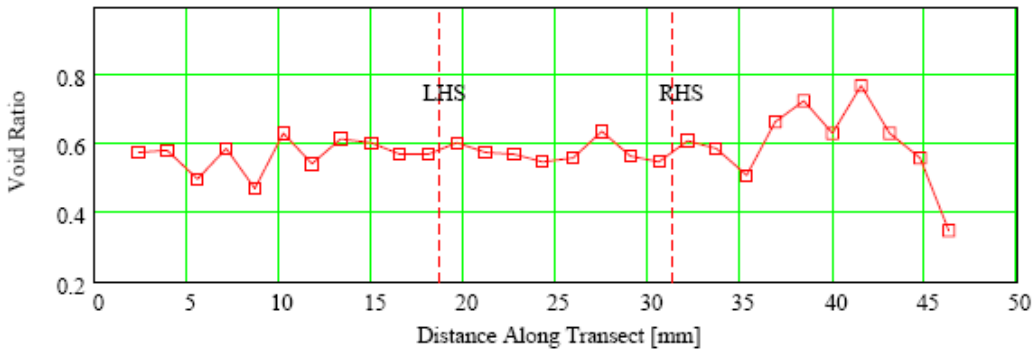

Figure 3.10 Incremental void ratio transects for surface -60 of highly dilatant unsheared specimen (Evans, 2005)

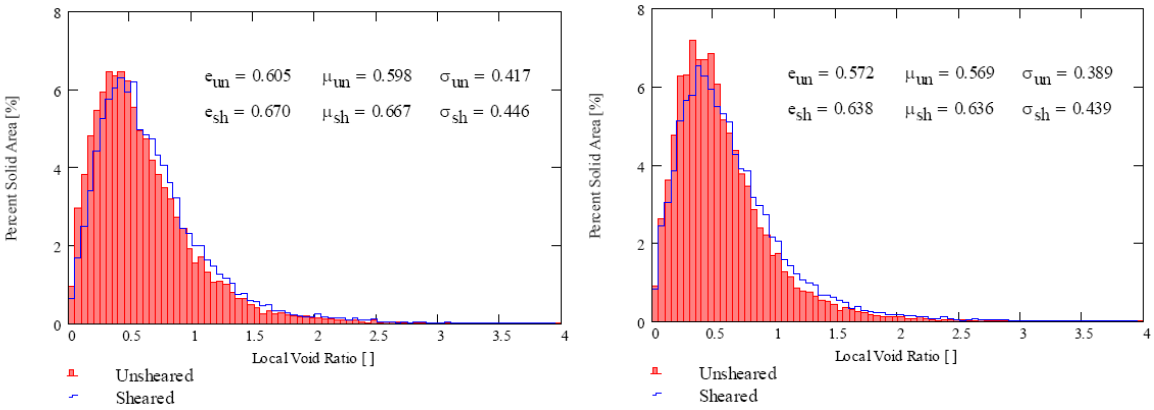

Slightly dilatant Highly dilatant

Figure 3.11 Local void ratio distributions for biaxial specimens (Evans, 2005)

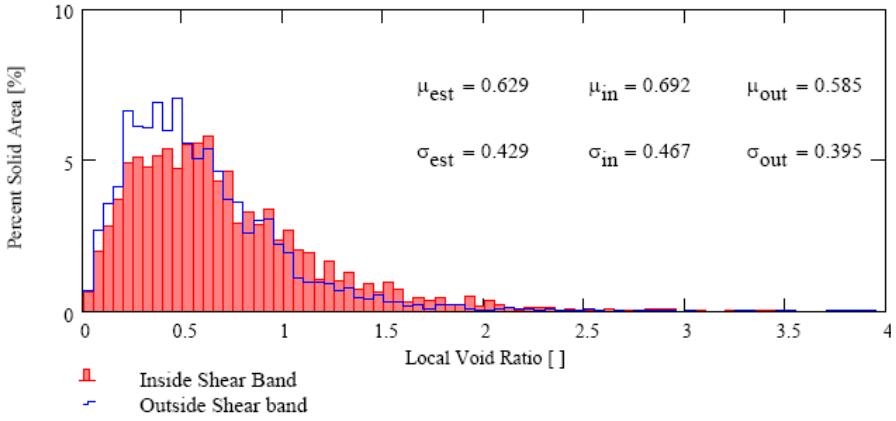

Figure 3.12 Local void ratio distributions inside and outside shear band of surface -60 for highly dilatant specimen (Evans, 2005)

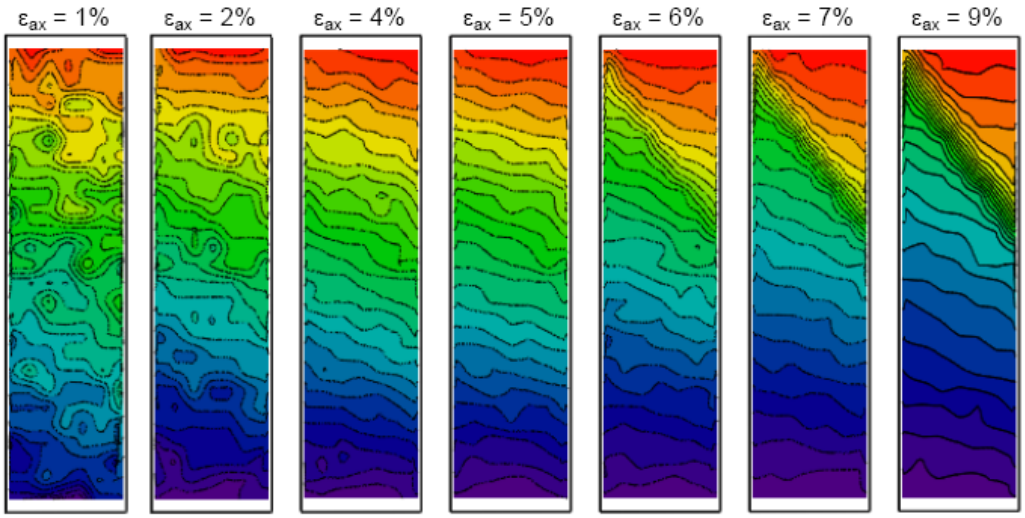

Figure 3.13 Membrane deformation contours for a biaxial specimen (Evans, 2005)

3.3.3. 2-D DEM Modeling of Biaxial Specimens

A series of numerical biaxial tests were performed by Evans using the commercially available 2-D DEM code PFC2D, *Particle Flow Code in Two Dimensions v3.00* (Itasca, 2003). The numerical model was 12 m x 6 m in dimension and comprised of approximately 5000 particles with mean ball diameter of 0.05 m. The model dimension was scaled relative to the physical specimens to speed up calculation time. Two-ball clumps instead of single balls were used for the particles to create more complex geometries and reduce the magnitude of particle rotations. Each clump was comprised of two identically-sized balls overlapping by 50% (by diameter). The numerical specimen was confined by two rigid platens in the vertical directions and two flexible membranes along the horizontal directions. The top and bottom platens also served as loading platens over the course of testing. The lateral flexible membrane was simulated by a string of bonded balls that were velocity controlled. To ensure the membrane could stretch and contract, relative vertical positions between end platens and membrane endpoints were closely monitored so that more balls would be added or removed if the membrane was too short or too long. The properties of the numerical setup

are summarized in Table 3.7. In addition to evaluating the mechanical behavior of the numerical models, the same 2-D image analyses, including subregional void ratios and mean free paths, local void ratio distributions, inclined spatial averaging, and virtual surface analysis, were performed to characterize the microstructures of the numerical biaxial specimens. Figure 3.14 presents some of the analysis results for the highly dilatant numerical specimens at 10% strain, and it clearly indicates the strain localization initialized and developed in the numerical modeling similar to what was observed in the physical experiments

Table 3.7 Model properties and material properties for PFC2D simulations of biaxial tests (based on Evans, 2005)

Parameters	Experimental	Numerical
Specimen height	140 mm	12 m
Specimen width	40 mm	6 m
Mean particle size (long axis)	0.74 mm	0.75 m
Mean particle size (short axis)	-	0.05 m
Particle normal stiffness	-	10^8 N/m
Particle shear stiffness	-	10^7 N/m
Particle friction coefficient	-	0.31
Particle specific gravity	2.65	2.65
Membrane stiffness	-	10^7 N/m
Platen/membrane friction coefficient	-	0.31
Membrane specific gravity	-	1.50

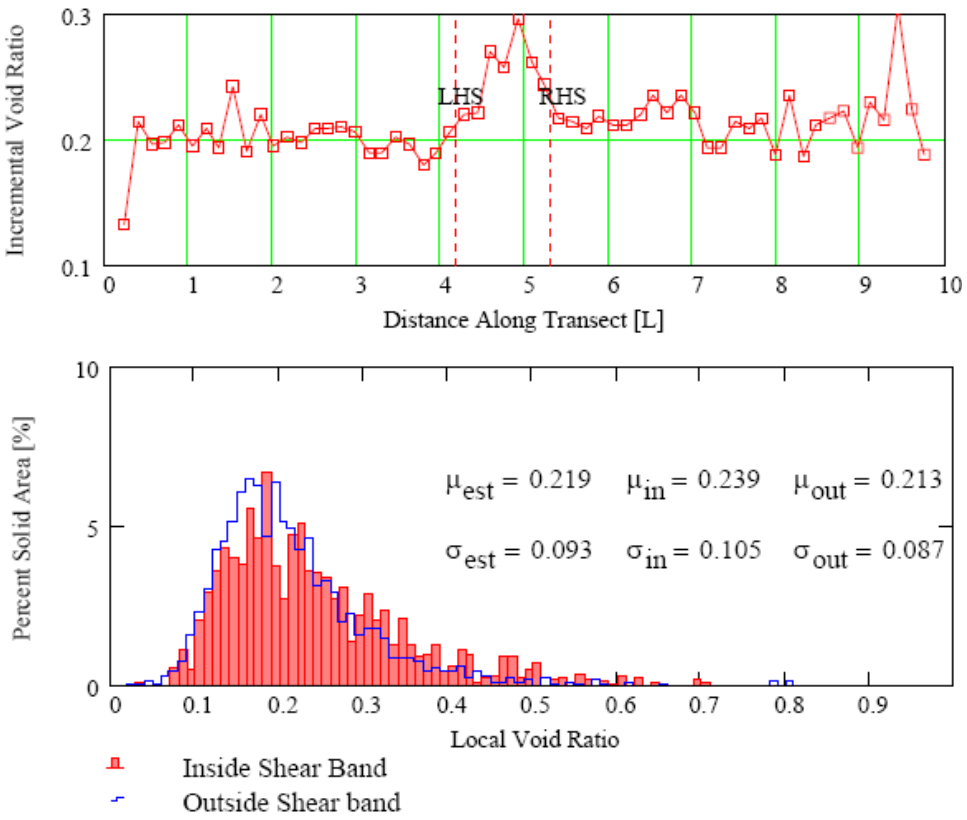

Figure 3.14 Incremental void ratios of strips parallel to the shear band (upper) and local void ratio distributions inside and outside the shear band (lower) for highly dilatant specimen at 10% global axial strain (Evans, 2005)

3.4. Summary and Conclusions

The two previous studies on strain localization in sheared Ottawa sand focused on triaxial shear tests and biaxial shear tests.

For the triaxial related studies, an optical microscopy based montage and serial sectioning technique was developed to reconstruct the 3-D microstructures of sheared and unsheared triaxial specimens prepared by air-pluviation and moist-tamping. The reconstructed volumes were characterized both in 2-D and 3-D for microstructural properties and behavior. The characterization results indicated that the different soil fabrics prepared by air-pluviation and moist-tamping resulted in different microstructural behaviors (e.g., larger pore size and throat size) as well as mechanical behavior.

The biaxial related studies focused on 2-D characterization and numerical modeling of the biaxial sheared specimens subjected to different initial states (i.e., initial void ratio and confining pressure). A number of 2-D microscopic images were captured from the selected surfaces of the specimen, and the spatial averaging calculations along pre-determined inclined strips performed on the images clearly defined the extent of the shear band. The digital image correlation technology was utilized to investigate the membrane effects on the stress and strain response of the specimens. It was found the membrane effect accounted for 0.5% to 1.0% of the normal stress and 9% to 18% of the shear stress measured in the specimen. The biaxial tests were simulated using the 2-D DEM code PFC2D. The particles were modeled by two-ball clumps and the lateral flexible membrane was modeled by a string of bonded balls. The modeling results mimicked the initialization and development of the shear band inside the specimen.

CHAPTER 4

3-D NUMERICAL MODELLING OF TRIXIAL SPECIMENS

4.1. Introduction of PFC3D

As introduced in Section 2.3, numerical simulation, and in particular the discrete element method, has been widely used in studies on laboratory soil tests. With the advancement of computational capabilities, 3-D discrete element method (DEM) which computes particle interactions in 3-D space has been implemented by various researchers.

The 3-D DEM code used in this research is PFC3D: *Particle Flow Code in 3 Dimensions v4.0* (Itasca, 2008). This commercial code was chosen because of its robust performance and wide use. In addition, as the 2-D version of the code, PFC2D, was used in previous related studies (Evans, 2005) to model biaxial tests, the 3-D version was selected here to ensure consistent evaluation on soil performance from 2-D to 3-D. The basic assumptions and mathematical formulations of PFC3D follow those of PFC2D, except for the inclusion of forces and displacements in the 3rd dimension. A brief introduction on PFC2D was presented in Evans (2005). Detailed description of the theory involved in PFC3D can be found in the user's manual (Itasca, 2008). As with PFC2D, two types of objects can be modeled in PFC3D, "balls" and "walls". However, in PFC3D, balls are modeled as spheres instead of discs, and walls are in the form of planes instead of lines. Another advantage of PFC3D is that non-planar walls, such as cylindrical, spherical, spiral, and ring-shaped elements, can be modeled. Two logics, clump logic and measurement logic, are essential to the numerical simulation in this research and they are introduced in the following sections.

4.1.1. Clump Logic

Considering the irregular shape of natural soils, sometimes spheres may not be an appropriate simulation of soil particles, and more complex particle shapes are needed. One way to achieve this in PFC3D is using clump logic. A clump is a group of slaved particles that behave as a rigid body (with a deformable boundary) that will not break apart, regardless of the forces acting upon it (Itasca, 2008). Although both are comprised of multiple particles, clumps differ from bonded particles by: (1) particles within a clump can be overlapped to any extents; and (2) contact forces between particles within a clump are not generated during computation. The simplest form of a clump is created by overlapping two identical spheres to different extents, which creates different aspect ratios. Figure 4.1 shows such clumps with aspect ratios equal to 2, 1.5, and 1.25. The aspect ratio is defined as the length over the width of an ellipsoid. Clumps can also be formed by using more spheres and/or spheres of different radii.

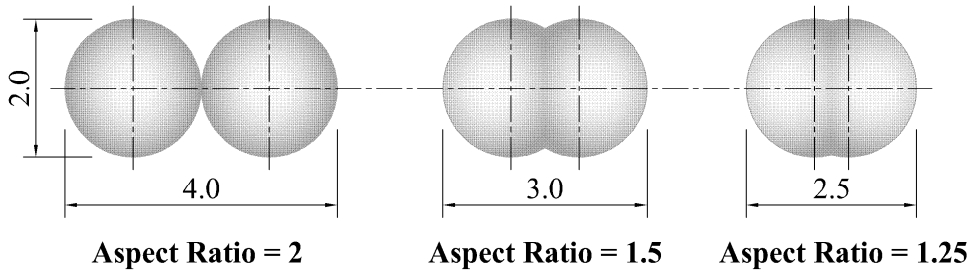

Figure 4.1 Clumps with different aspect ratio

The basic mass properties of a clump are total mass, location of the center of mass, moments and products of inertia. The total mass is the sum of the masses of spheres within a clump. Therefore, when replacing a sphere with a clump while keeping the total mass unchanged, the density of the spheres within the clumps should be multiplied by certain reduction coefficient to count for the overlapped portions. The moments and products of inertia are defined within the local coordinates of the clump. As long as the mass properties are defined, the force and motion of the clump can be

updated. Since it is treated as a rigid body, the calculation of the force and motion of a clump does not change a lot from the calculation of a single sphere.

Other than providing a better simulation of the real soil particle shape, application of clumps to 3-D DEM models can reduce large-magnitude rotations and enhance interlocking between particles (Yan, 2009). Interlocking plays an important role in helping effective particle chains to develop, which consequently enable the specimen to withstand larger applied forces. Effects of applying clumps instead of spheres will be discussed in later sections.

4.1.2. Measurement Logic

In PFC3D, a number of properties, such as porosity, coordination number as well as stress and strain rate can be measured within a specified volume during calculation cycles. Such volume is a circle in PFC2D and a sphere in PFC3D. Therefore, the volume will be referred as a "measurement sphere" in later sections. As porosity and coordination number are the properties of interest in this study, the assumptions and equations used by the measurement logic are briefly described here (the following definitions and equations come from Itasca, 2008, but are included here for completeness).

The coordination number of a soil can be estimated by the average number of contacts per particle. In PFC3D, the coordination number, *cn*, is the average number of active contacts per body, where a body can be either a single particle or a clump, and is computed as:

$$cn = \frac{\sum_{N_p} n_c^{(p)} + \sum_{N^l} n_c^{(l)}}{N_p + N_l} \tag{4.1}$$

where N_p is the number of spheres; N_l is the number of clumps with centroids in the measurement region; $n_c^{(\phi)}$ is the number of active contacts of body ϕ with $\phi = \{p, l\}$. An active contact is one that is either carrying a nonzero normal force or has a parallel bond.

According to the definition, contacts between the spheres that compose a clump won't be included in the coordination number calculation.

The porosity, n, is the ratio of total void volume, V^{void}, within the measurement region to measurement-region volume, V^{reg}:

$$n = \frac{V^{void}}{V^{reg}} = 1 - \frac{V^{mat}}{V^{reg}} \tag{4.2}$$

where V^{mat} is the volume of material in the measurement region. Computation of V^{mat} should exclude particle overlaps arising from compressive contact forces and particle overlaps within the clumps.

4.2. DEM Modeling of Triaxial Tests

4.2.1. Modeling Algorithm

Two numerical triaxial tests, representing an air-pluviated specimen and a moist-tamped specimen were performed. The numerical tests were completed in four stages: (1) sample preparation; (2) clump creation; (3) consolidation; and (4) sample shearing.

The first stage, sample preparation, built up the preliminary frame for the numerical experiments. In the beginning, a specimen compartment was constructed using a cylindrical wall and two horizontal walls at the ends. The two horizontal walls were assigned with large stiffness of 1 x 10^8 N/m to serve as loading platens in the subsequent stages. The stiffness of the cylindrical wall was 1/10 the stiffness of the two end platens, and was designed to serve as the confining membrane for the specimen. The cylindrical wall was assigned with smaller stiffness to create a flexible confining membrane in the sense of stress, whereas it was still rigid in the sense of strain. The compartment was 70 mm in diameter and 140 mm in height, exactly the same as its physical counterpart. Particles were generated in the compartment using two methods. One was to generate particles randomly inside the compartment which approximately simulated the physical

preparation method of air pluviation, and the other was to generate particles layer by layer with different relative densities which approximately simulated the physical preparation method of moist tamping (see Figure 4.2). It should be noted here that neither of the numerical preparation methods yield perfect simulations of physical preparation methods, as the generated particles were not subject to any gravitational fields. However, they were still designated as air-pluviated and moist-tamped to indicate different specimen fabrics (homogeneous versus heterogeneous) and for the ease of comparison with physical specimens as well. Variation of relative densities within each layer for the physical moist-tamped specimen was measured by Yang (2005) and shown in Figure 4.2. According to Frost and Park (2003), the relative density within a (tamped) layer typically increases by about 15% from bottom to top. In order to account for such density variation, each tamped layer was divided into three sub-layers, and the relative density increased linearly from the bottom sub-layer to the top sub-layer. Both preparation methods generated particle assemblies with the same initial global void ratio. As the numerical specimen was prepared to the initial void ratio of 0.580, it was in the dense state. To maintain the dense state for shear, the inter-particle friction was set to zero until the last stage.

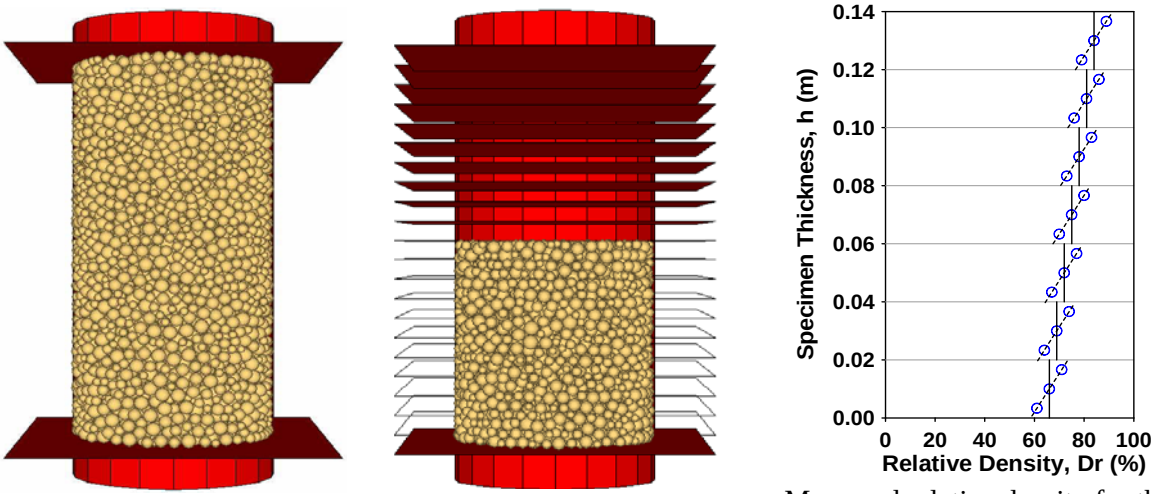

Air pluviation

Moist tamping

Measured relative density for the physical moist-tamped specimen

Figure 4.2 Preparation methods simulating air pluviation and moist tamping

The second stage, clump creation, was to replace every single sphere with an arbitrarily oriented two-sphere clump, while keeping the volume, centroidal position and material properties unchanged. The two-sphere clump was composed of two identical spheres overlapping each other to achieve certain aspect ratio. Nominally, the aspect ratio of a particle affects its rotation when the specimen is subject to loading. Selection of an aspect ratio for the modeling depends on the aspect ratio of the tested sand and some other factors. Lee (1998) measured the aspect ratio of Ottawa 20-30 sand from 2-D microscopic images and found a wide distribution range (1.0 ~ 1.9) with the mean value of 1.28. Considering particle rotations would not be fixed in the modeling, the aspect ratio value was set as 1.5:1, a bit higher than the mean value but still within a reasonable range of Lee's (1998) measurement to impose additional restrictions on particle rotations. The clumps were set as unbreakable, which means all the constituent particles of a clump were forced to stick together throughout any calculation cycle. To take a closer look at the particles and their arrangement, three cubes, about 5 times the particle size in width, length, and height, were cut from the assemblies of single spheres, 2-sphere clumps and real soil particles (see Figure 4.3). Based on a visual analysis, the 2-sphere clumps yield a better representation of real soil microstructures than single spheres. After the single spheres were replaced with clumps, the specimen was equilibrated to remove particle overlaps resulting from the replacement procedure.

The next test stage was to isotropically consolidate the specimen under 50 kPa stress, comparable to the consolidation stage of the physical laboratory triaxial test. In order to reach the isotropic loading state, a servo-controlled mechanism was applied to both the cylindrical wall and horizontal upper and lower walls. For each calculation cycle, the servo mechanism computed the difference between the measured and required stresses, and then adjusted wall velocities to reduce the stress difference. After the desired consolidation loads were reached, inter-particle friction was assigned to the

clumps. Then, the system was ready for the final stage – shearing to a global axial strain of 14%.

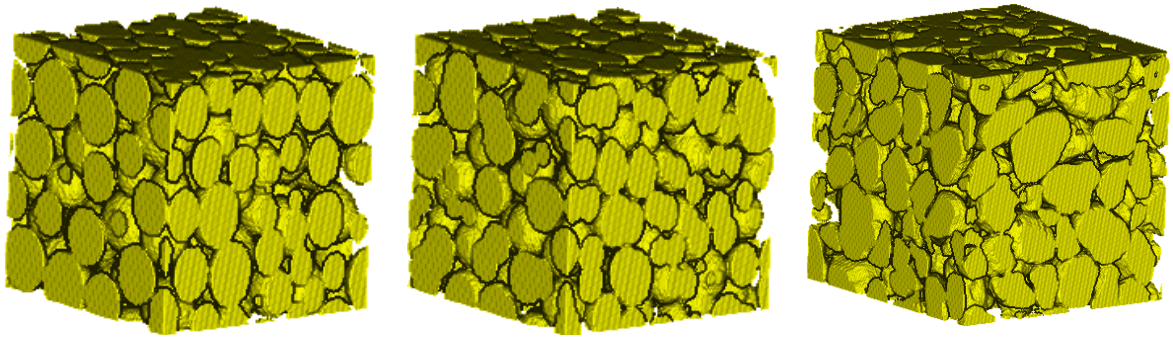

(a) (b) (c)

Figure 4.3 Particle cubes, about 5 times the mean particle size in width, length, and height, composed of: (a) single spheres; (b) 2-sphere clumps; and (c) real soil particles

4.2.2. Material Properties

In order to set up a reasonable numerical model, the parameters should be selected with caution so that they do not deviate far from the material properties of real soils. In this section, how key model parameters including particle size, contact stiffness and inter-particle friction were determined is presented.

The most common ways to generate particles in DEM are either defining one universal particle size or several discrete particle sizes. A better approximation used in the current research was to assume that the grain size conforms to a uniform distribution. The size range was chosen based on the linear portion of the grain size distribution curve in Figure 3.1, and consequently the minimum particle size would be 0.25 mm and the maximum 0.45 mm. The selected range of the uniform distribution should be appropriate for the following reasons: (1) the median particle size ended up being 0.35 mm, which was equivalent to D_{50}; (2) 80% of the experimental soil specimen by weight was finer than the maximum particle size while 15% of the experimental soil specimen by weight was finer than the minimum particle size. Considering that the dimensions of the

numerical specimen would be 140 mm in height and 70 mm in width, particle size between 0.25-0.45 mm meant that more than 10,000,000 particles would be needed to fill in the specimen compartment. This heavily multiplied the calculation time, and Ni et al. (2000) pointed out that increasing the number of particles beyond 15,000 in a 3-D DEM simulation had relatively little effect on results. Accordingly, the particle size was scaled 12 times to reduce the number of particles generated in the numerical model (see Table 4.1). A total of 8791 spheres for AP and 8804 spheres for MT were generated to fill in the specimen compartments with the desired initial void ratio. After each sphere generated in the sample preparation stage was replaced with an unbreakable 2-sphere clump, the system contained the same number of particles, with mean particle size of 5.3 mm in the long axis and 3.5 mm in the short axis, while the void ratio remained as 0.580 (see Table 4.2).

Table 4.1 Model properties of the numerical triaxial tests for stage (1)

Parameters	Experimental		Numerical	
	AP	MT	AP	MT
Specimen Height (mm)	140	140	140	140
Specimen Width (mm)	70	70	70	70
Particle Size Range (mm)	-	-	3.0~5.4	3.0~5.4
Mean Particle Size (mm)	0.35	0.35	4.2	4.2
Initial Void Ratio	0.579	0.583	0.580	0.580
Particle Normal Stiffness, k_n (N/m)	-	-	1.5×10^6	1.5×10^6
Particle Shear Stiffness, k_s (N/m)	-	-	1.5×10^5	1.5×10^6
Particle Friction Coefficient	-	-	0.27	0.31
Specific Gravity	2.67	2.67	2.67	2.67
Platen Stiffness (N/m)	-	-	1×10^8	1×10^8
Membrane Stiffness (N/m)	-	-	1×10^7	1×10^7
Number of Particles	-	-	8791	8804

In PFC3D, basic component behaviors at contacts consist of stiffness, slip and bonding. The bonding model was not used in the triaxial simulation, and thereby not

discussed further here. PFC3D provides two contact-stiffness models: a linear model and a simplified Hertz-Mindlin model. The first of these models linearly relates the force and relative displacement through constant contact stiffness, while the second one non-linearly relates the force and relative displacement by non-constant contact stiffness. The non-constant contact stiffness is a function of the geometric and material properties of the two contacting entities as well as the current value of the normal force. According to PFC3D manual (Itasca, 2008), the simplified Hertz-Mindlin model is appropriate when modeling assemblies with no bonds, experiencing small-strain conditions and exclusively compressive stresses; for all but few highly specialized situations, the linear model should be adequate. As the assemblies used in this research were un-bonded particles which would experience large-strain conditions, the linear contact-stiffness model was adopted. The linear model is defined by the normal stiffness and shear stiffness. The normal stiffness of the particles, k_n, is a secant stiffness. If assuming that particles at contact conform to Hertzian contact, the relationship between the contact force and displacement can be expressed as (Santamarina et al., 2001):

$$\delta = \frac{1}{2 \cdot R^{1/3}} \left[\frac{3 \cdot \left(1 - \nu_g\right)}{G_g} \cdot N \right]^{2/3} \tag{4.3}$$

where δ is the displacement of particle due to contact; N is the normal load transferred through the contact; R is the particle radius; ν_g is the Poisson's ratio of the material that makes the grains, which is 0.31 for quartz; and G_g is the shear stiffness of the material that makes the grains, which is 29 GPa for quartz. Substituting the mean equivalent spherical radius of the clumps, which equals to 2.1 mm, into equation 4.3, the non-linear relationship is plotted and shown in Figure 4.4. As the normal stiffness equals to normal force over displacement, it increases with the normal force. Considering the possible magnitudes of the contact forces for the assemblies generated in this research, the normal stiffness at the load of 1 N which equals to 1.5 x 10^6 N/m was selected for the numerical

simulation. It should be noted here that the determination of normal stiffness involved approximation and estimation. The shear stiffness of the particles, k_s, is a tangent stiffness and correlates to shear forces. So far, there is no unanimous agreement on how to choose k_s for soils. In the current research, k_s was constrained to vary between k_n and $k_n/10$. The stiffness parameters for the simulation are listed in Tables 4.1 and 4.2.

Table 4.2 Model properties of the numerical triaxial tests for stage (2)

Parameters	Experimental		Numerical	
	AP	MT	AP	MT
Aspect Ratio of Clumps	-	-	1.5:1	1.5:1
Mean Particle Size in Long Axis (mm)	0.35	0.35	5.3	5.3
Mean Particle Size in Short Axis (mm)	-	-	3.5	3.5
Initial Void Ratio	0.579	0.583	0.580	0.580
Particle Normal Stiffness, k_n (N/m)	-	-	1.5×10^6	1.5×10^6
Particle Shear Stiffness, k_s (N/m)	-	-	1.5×10^5	1.5×10^6
Particle Friction Coefficient	-	-	0.27	0.31
Specific Gravity	2.67	2.67	2.67	2.67
Number of Spheres	-	-	17582	17608
Number of Clumps	-	-	8791	8804

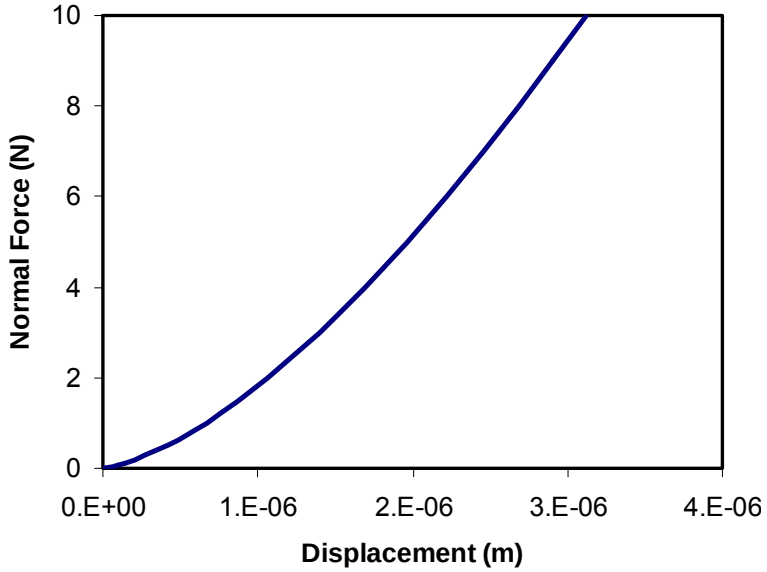

Figure 4.4 Non-linear force-displacement response for particles at contact

Slip behavior actually depicts the relation between the shear and normal forces when two entities are at contact, and it is defined by the friction coefficient, μ. When the shear force exceeds the maximum allowable shear contact force, which is the product of friction coefficient and normal force, slip will take place and the shear force is maintained as the maximum allowable shear contact force. Proctor and Barton (1974) performed a series of laboratory tests to measure the angle of inter-particle friction, and they concluded that the friction angle of dry quartz is 17.4° which correlates to the friction coefficient of 0.31. However, since the friction angle concluded by Proctor and Barton (1974) was based on the shearing between quartz particles and a quartz plane, some adjustments were made when applying the friction coefficient to the numerical models.

4.2.3. Measuring Scheme

One of the advantages of numerical simulations over lab tests is that both global and local soil behaviors can be monitored throughout the loading process. In PFC3D, local soil behavior can be measured by putting measurement spheres at the locations of interest. The logic of measurement sphere has been introduced in Section 4.1.2.

In the current study, since the development of void ratio is one of the research interests, the rule to determine where to put a measurement sphere is whether that location will undergo drastic change of void ratio. As many as 18 measurement spheres were used to evaluate the entire specimen, and their coordinates within the specimen are illustrated in Figure 4.5. The radius of measurement sphere 8 was 34 mm, and contained more than 2600 clumps. The radii of the remaining 17 measurement spheres were 10 mm, and each of them contained more than 70 clumps. Based on their locations and radii, measurement sphere 8 would yield a generalized evaluation within the middle portion of the specimen while the other measurement spheres would capture local changes. It should be noted that the terminology ‘local’ here refers to a scale between micro-scale and

macro-scale due to the size of the measurement sphere and number of particles encompassed by the measurement sphere. Hence, the 'local' measurements mentioned in this chapter refer to meso-scale.

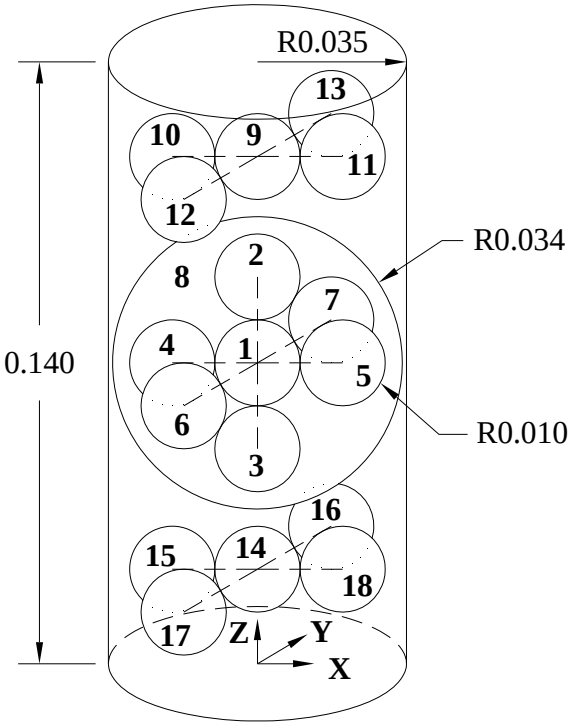

Meas. Sphere	X	Y	Z	R
1	0	0	0.070	0.010
2	0	0	0.100	0.010
3	0	0	0.040	0.010
4	-0.020	0	0.070	0.010
5	0.020	0	0.070	0.010
6	0	-0.020	0.070	0.010
7	0	0.020	0.070	0.010
8	0	0.000	0.070	0.034
9	0	0	0.118	0.010
10	-0.020	0	0.118	0.010
11	0.020	0	0.118	0.010
12	0	-0.020	0.118	0.010
13	0	0.020	0.118	0.010
14	0	0	0.022	0.010
15	-0.020	0	0.022	0.010
16	0.020	0	0.022	0.010
17	0	-0.020	0.022	0.010
18	0	0.020	0.022	0.010

Note: all the dimensions are in meters

Figure 4.5 Coordinates and radii of the measurement spheres

4.3. Parametric Study of the Numerical Model

Before performing any numerical tests, a parametric study was carried out to investigate the influence from some particle parameters. The parameters investigated were normal stiffness, k_n, shear stiffness, k_s, and friction coefficient, μ.

The first investigated parameter was normal stiffness of particles. Three numerical tests were performed with k_n equal to 5.0 x 10^5 N/m, 1.5 x 10^6 N/m, and 1.0 x 10^7 N/m, while keeping k_s of 1.5 x 10^6 N/m and μ of 0.31. The results are plotted in Figure 4.6. It is predictable that the initial modulus, peak strength and residual strength

would increase as the normal stiffness increased. However, peak strain did not change with different k_n.

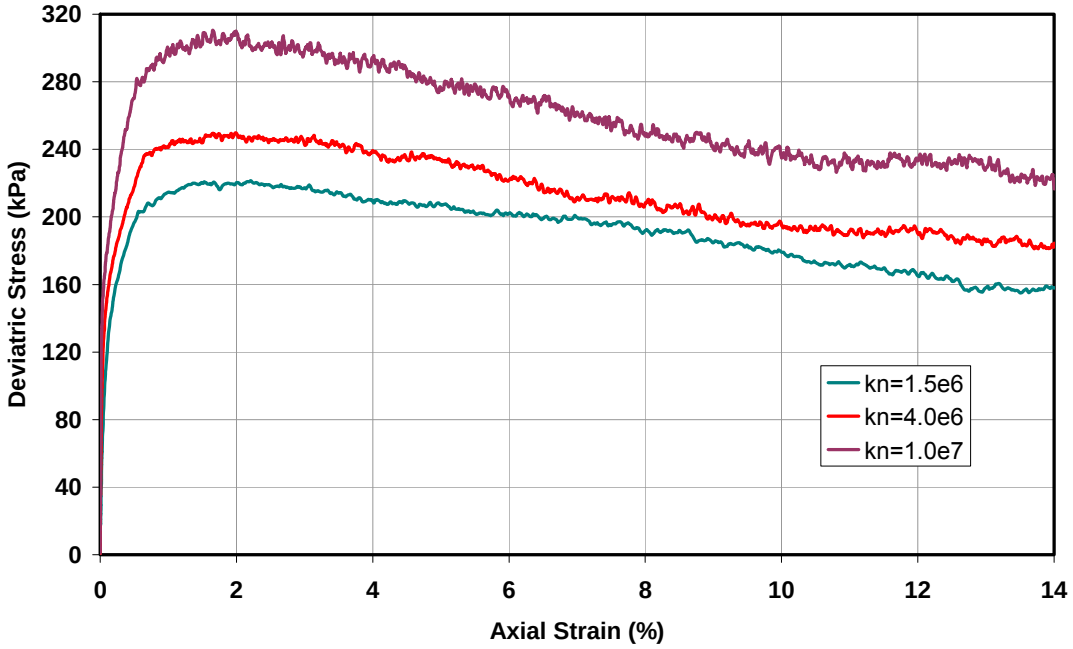

Figure 4.6 Effects of normal stiffness, k_n, on stress-strain response

The second investigated parameter was shear stiffness of particles. A series of numerical tests were performed with k_s equal to 1.0 x 10^5 N/m, 1.5 x 10^6 N/m, and 4.0 x 10^6 N/m, while keeping k_n of 1.5 x 10^6 N/m and μ of 0.31 (see Figure 4.7). In contrast to what was observed with normal stiffness, shear stiffness did not show substantial effects on the initial modulus, peak strength and residual strength. However, smaller shear stiffness did result in larger peak strain.

The last parametric study was performed by varying μ for 0.27, 0.31, and 0.35 whilst k_n and k_s were both kept as 1.5 x 10^6 N/m (see Figure 4.8). The initial modulus and peak strain did not change with friction coefficient, whereas the peak strength and residual strength increased as the friction coefficient increased. This can be explained by the fact that since larger friction means it is more difficult for the particles to slip, the specimen will exhibit greater resistance to applied external force. The residual strengths

of the three numerical tests tended to converge at large strain, which implies the normal stiffness might play a more important role in the residual strength than the inter-particle friction.

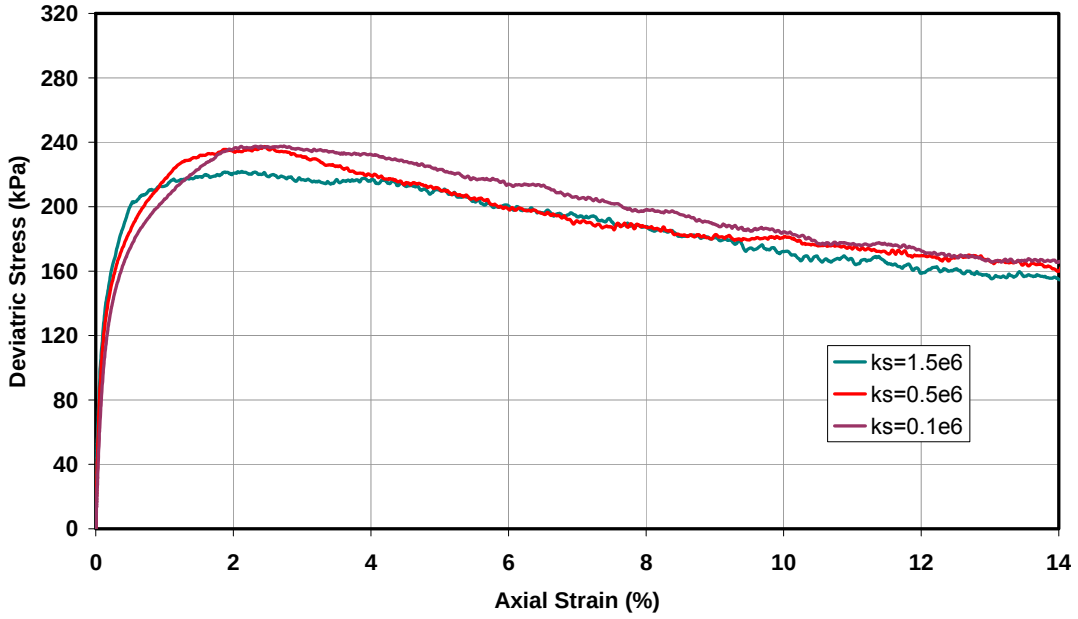

Figure 4.7 Effects of shear stiffness, k_s, on stress-strain response

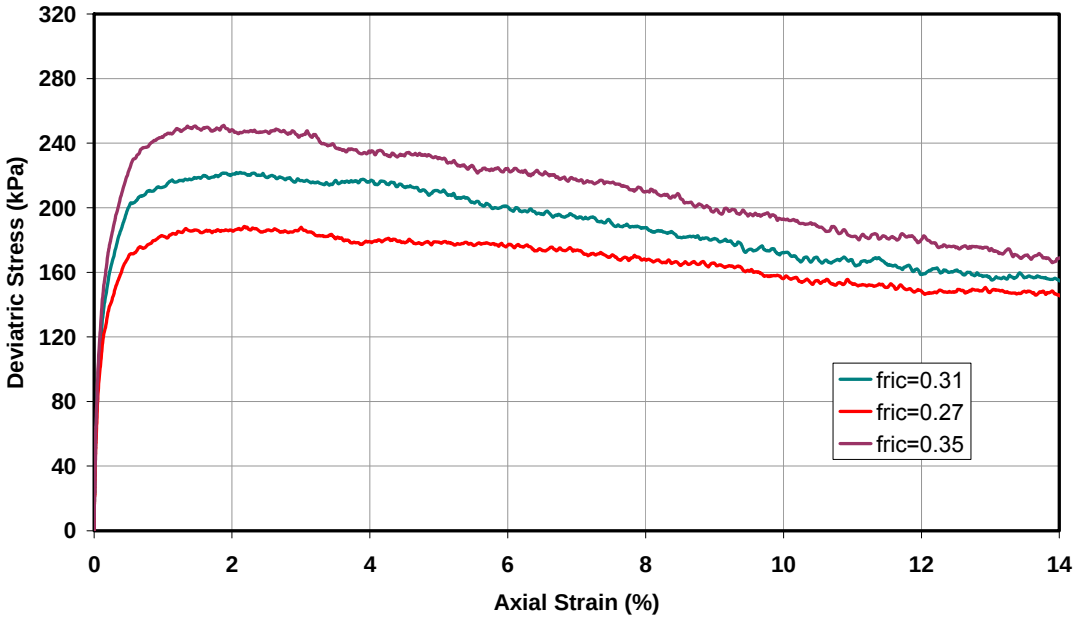

Figure 4.8 Effects of friction coefficient, μ, on stress-strain response

4.4. DEM Simulation Results

Two numerical tests, in which the particles were generated in different ways, were performed to simulate the laboratory triaxial tests. These tests were designated as DEM_AP and DEM_MT, indicating an air-pluviated specimen and a moist-tamped specimen, respectively. The procedures and modeling parameters of the numerical tests have been introduced in Sections 4.2.1 and 4.2.2.

4.4.1. Stress-Strain Response

The stress-strain responses of the numerical tests, along with the laboratory tests, are presented in Figure 4.9. For the laboratory tests, the moist-tamped specimen yielded a higher initial modulus and a higher peak strain than the air-pluviated specimen, which can be explained by the fact that the moist-tamped specimen experienced greater stress than the confining pressure prior to the compression test, i.e. preshearing during preparation (Chen, 2000). The air-pluviated specimen reached the peak stress of 218 kPa at the strain of 3.3%, while the moist-tamped specimen reached a lower peak stress of 189 kPa at 1.8% strain. The stress difference of about 30 kPa between the air-pluviated and moist-tamped specimens was maintained from the peak to the end of the shearing stage. As for the numerical tests, both tests matched well with the laboratory tests until they were sheared to a large axial strain. The residual stress of the numerical test was 3 kPa less than the laboratory test for the air-pluviated specimens, and 10 kPa for the moist-tamped specimens.

4.4.2. Volumetric Strain

The volumetric strains from both the numerical tests and experimental tests are also presented in Figure 4.9. One thing should be noted is that since the radial strains were not monitored during the lab tests, the volumetric strains could only be calculated at 14% axial strain via 2-D image analysis results (Yang, 2005). Overall, the numerical tests

showed a small volumetric contraction in the beginning followed by continuous volumetric dilation. For the numerical tests, the moist-tamped specimen experienced 1% more volumetric dilation than the air-pluviated specimen, which might result from the greater friction coefficient assigned to the particles. However, for the laboratory tests, larger volumetric strain occurred in the air-pluviated specimen than the moist-tamped specimen.

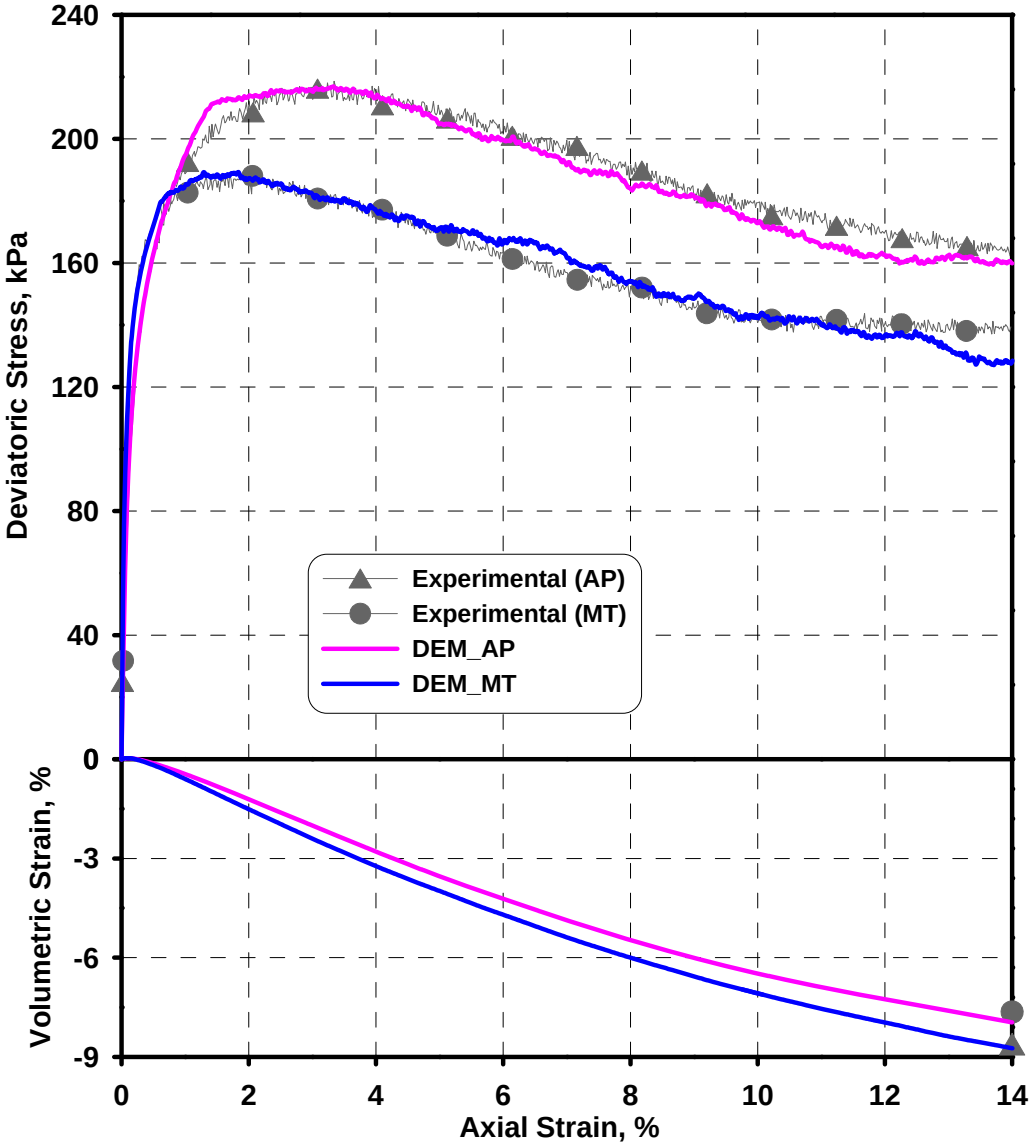

Figure 4.9 Stress-strain response for the numerical tests

4.4.3. Void Ratio

The void ratios of the numerical specimens were measured by measurement spheres and are presented in Figures 4.10 and 4.11. As previously mentioned, measurement sphere 8 yielded generalized void ratio within the middle portion of the specimen, while the other measurement spheres yielded local void ratio changes. For both tests, the generalized change of the void ratio was smooth while the local changes were not, which can be attributed to the shape of clumps. Interlocking and unlocking of clumps is considered to be responsible for the sudden local changes of void ratio in the smaller measurement spheres. Although the generalized void ratios of both specimens were the same prior to shearing, the local void ratio within DEM_MT showed larger range of variation than DEM_AP. The range of local void ratio within DEM_MT increased from 0.06 before shearing to 0.09 after shear, while it increased from 0.04 to 0.06 within DEM_AP. The generalized void ratio of DEM_MT was larger than DEM_AP at large axial strain. In general, the void ratios measured from the two numerical tests illustrate how specimen fabric can affect the local specimen behavior and also suggest that the specimen preparation methods applied in the numerical tests were successful in approximating the physical preparation methods.

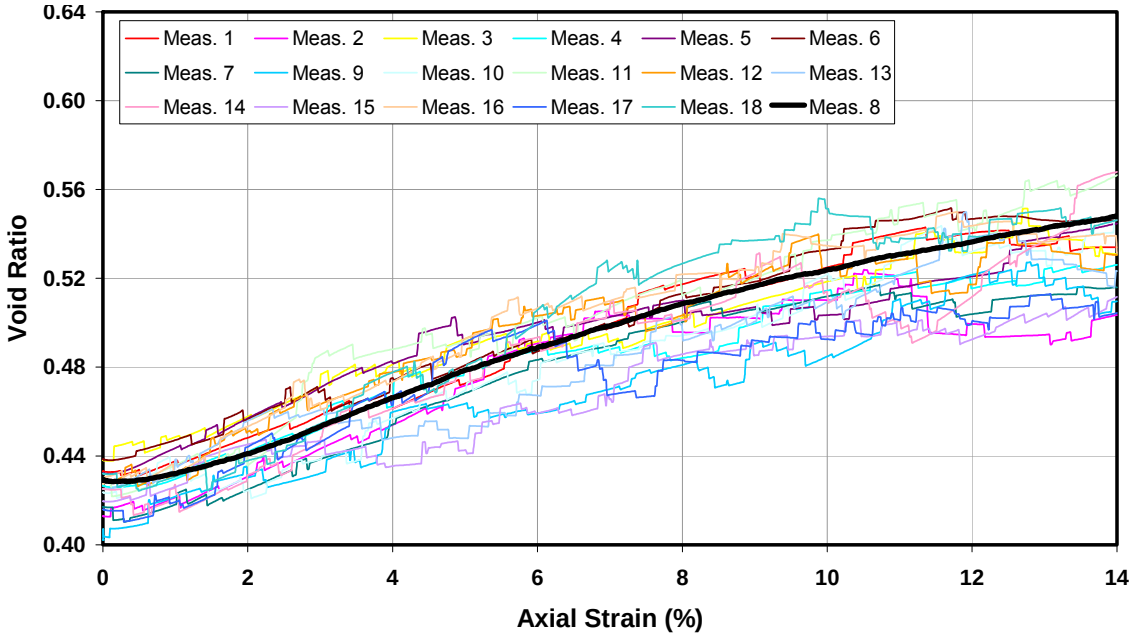

Figure 4.10 Void ratio measurement for DEM_AP

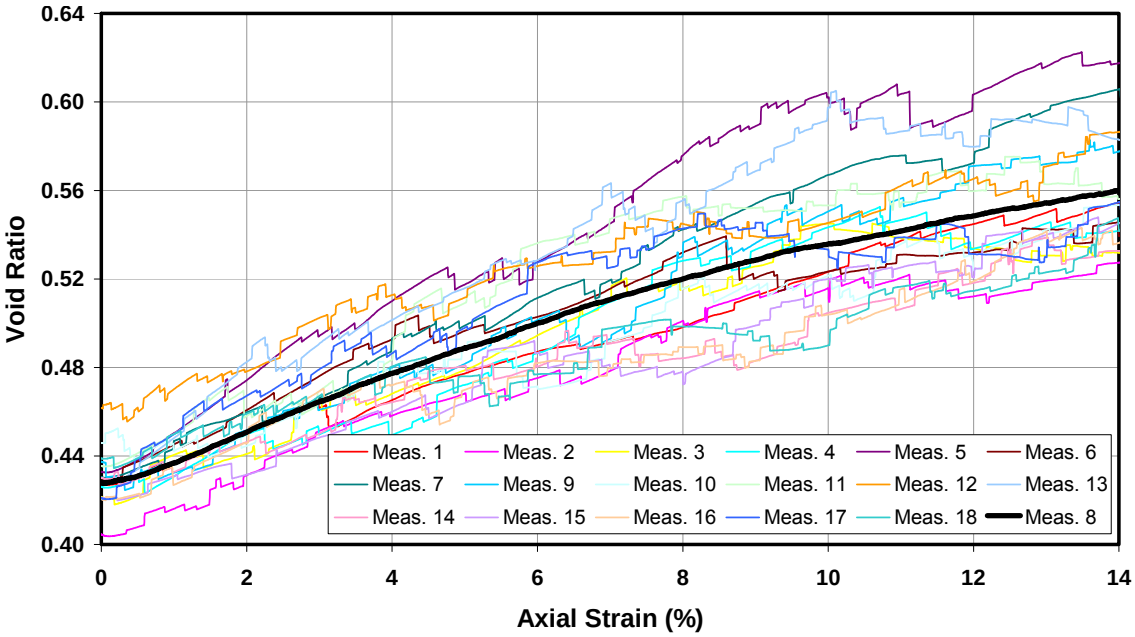

Figure 4.11 Void ratio measurement for DEM_MT

4.4.4. Contact Normals

The polar histogram of contact normals is another indicator of the microstructure of particulate materials. A contact is represented by a vector, oriented normal to the plane of the contact (Santamarina et al., 2001). Figure 4.12 presents the polar histograms of contact normals for DEM_AP at 0%, 1.0%, 3.3%, 5.0% and 14.0% axial strains. Figure 4.13 presents the polar histograms of contact normals for DEM_MT at 0%, 0.5%, 1.9%, 5.0% and 14.0% axial strains. These strains were selected to represent pre-shearing, pre-peak, peak, post-peak, and end of shearing stages, and they were marked on the stress-strain curves for reference. Before the specimens were sheared (0% axial strain), the polar histograms of both DEM_AP and DEM_MT could be fit by an ellipsoid which indicates effective particle chains had not formed yet. At this stage, the number of contact normals was 39946 for the air-pluviated specimen and 40027 for the moist-tamped specimen. When shearing started, the polar histograms tended to shrink in particular along those directions where the elevation angle was close to zero. The development of polar histograms during shear proves the formation of effective particle chains and release of the load from the particles not affiliated with the effective particle chains. At the end of shearing, a large percentage of the contact normals are orientated parallel to the outer surfaces of complementary cones that may or may not intersect and form during shearing with their bases at the upper and lower platens. The number of contact normals was reduced by almost half at the end of shearing for both specimens, which was 26347 for the air-pluviated and 24451 for the moist-tamped. Two facts contribute to such a drastic reduction: (1) volumetric dilation due to shearing; and (2) formation of effective particle chains that sustained most of the load. The polar histograms of DEM_AP and DEM_MT showed slight differences before shearing and after shearing, which might result from different particle deposition. However, configuration of such differences requires further geometric analysis.

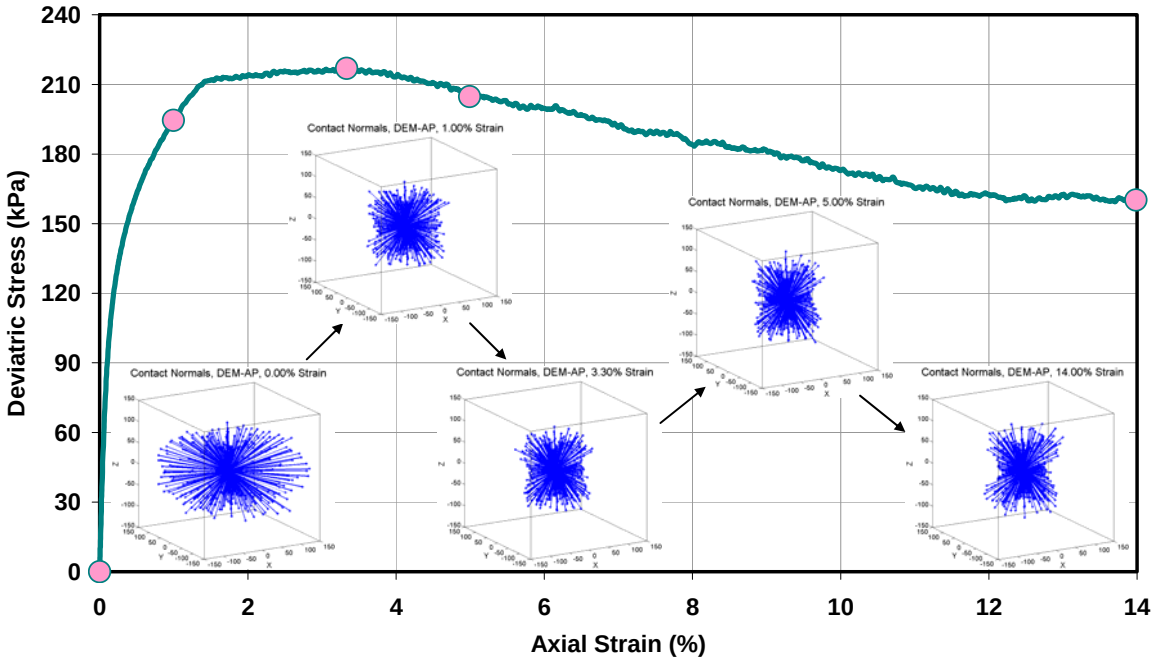

Figure 4.12 Polar histograms of contact normals for DEM_AP

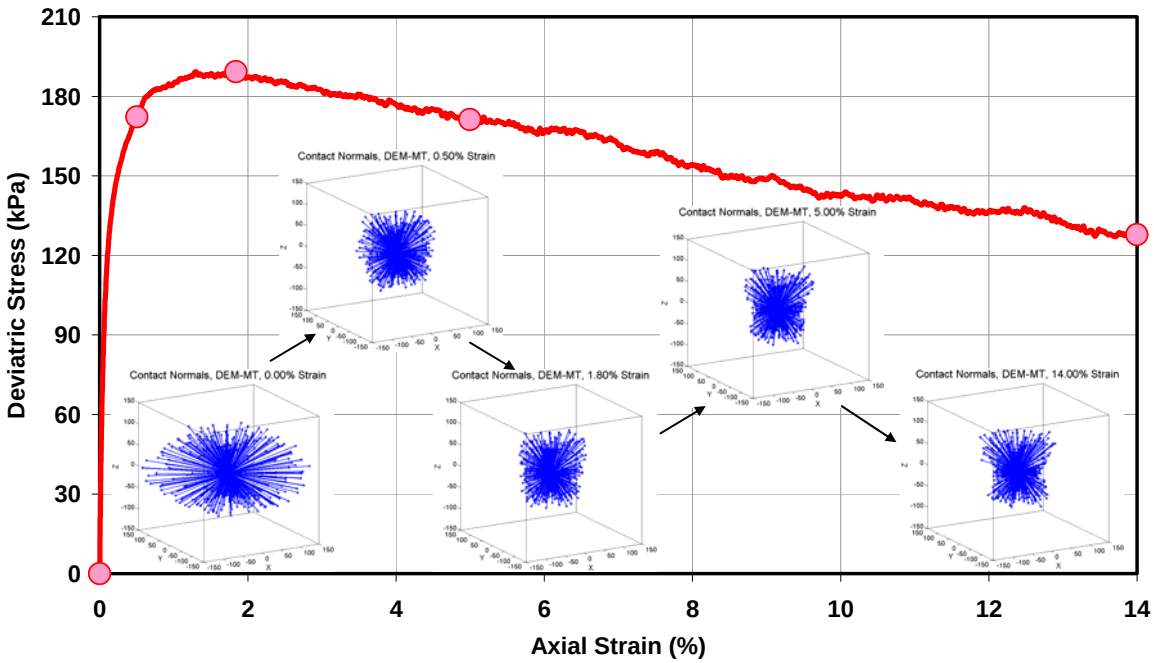

Figure 4.13 Polar histograms of contact normals for DEM_MT

4.4.5 Coordination Number

Coordination number of a soil, *cn*, is the average number of contacts per particle (Santamarina et al., 2001). By its definition, coordination number is correlated with the number of contact normals. Coordination number is an index for packing stability and density. Usually, the greater the coordination number, the denser and more stable the packing. Coordination numbers for the specimens were obtained from the same measurement spheres as void ratios, and they are plotted in Figures 4.14 and 4.15 for DEM_AP and DEM_MT respectively. Again, the curves of generalized measurements are smooth while those of local measurements are not, which resulted from the shape of clumps. The generalized coordination numbers measured by sphere 8 of both tests started around 10 followed by remarkable decrease especially when the specimens were sheared from 0% to 0.5% axial strain. This phenomenon corresponds to the fact that the polar histograms of contact normals shrank quickly during 0% to 0.5% strain also (Figures 4.12 and 4.13). Such sudden decrease of coordination number within small strain change implies effective particle chains initialized and developed once the loading condition changed from isotropic to anisotropic. After the peak axial strain, the generalized coordination numbers stabilized at 6.2 for DEM_AP and 5.7 for DEM_MT. In general, the coordination number of DEM_AP was higher than DEM_MT, which indicates a denser packing in the air-pluviated specimen during and at the end of shearing. The variation of local coordination numbers within DEM_MT was greater than DEM_AP, and is attributed to the specimen fabrics resulting from different deposition methods.

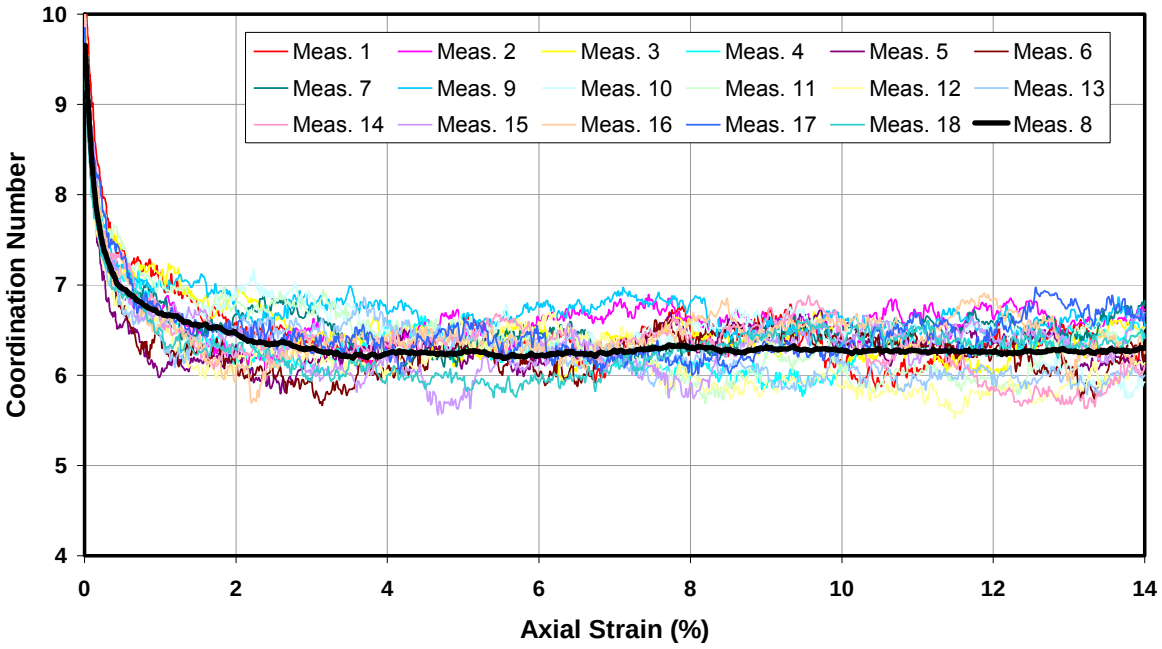

Figure 4.14 Coordination number of DEM_AP

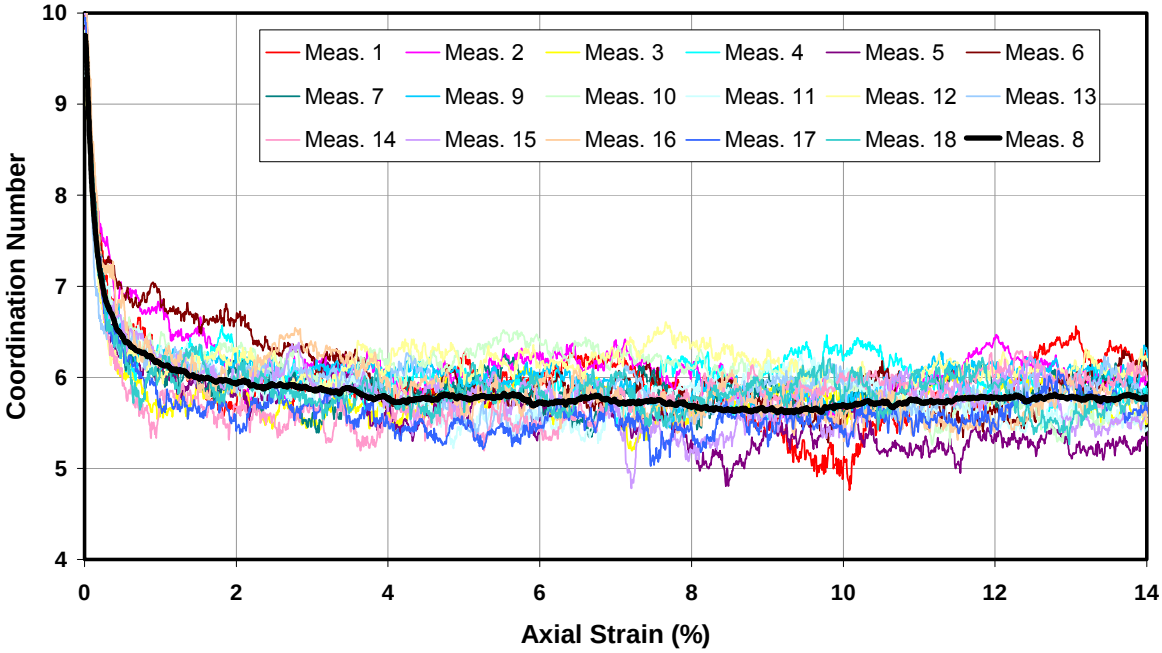

Figure 4.15 Coordination number of DEM_MT

4.4.6. Particle Orientation

As the basic particles used for the numerical tests were clumps, their orientation can be characterized by inclination of the long axes. The polar histograms of particle orientation at the same five axial strains as those selected for contact normals are plotted in Figures 4.16 and 4.17 for DEM_AP and DEM_MT, respectively. Similar to the polar histograms of contact normals, slight differences exist for the polar histograms of particle orientation for DEM_AP and DEM_MT. Such differences are difficult to depict unless further geometric analysis are performed. For both tests, the polar histograms of particle orientation were quite ellipsoidal prior to shearing, however, the histograms could not maintain the ellipsoidal shapes and showed some preferences especially towards the edges of the specimens post shearing. The development of particle orientation from ellipsoidal to non-ellipsoidal can be characterized by the change of shape and size of the polar histograms.

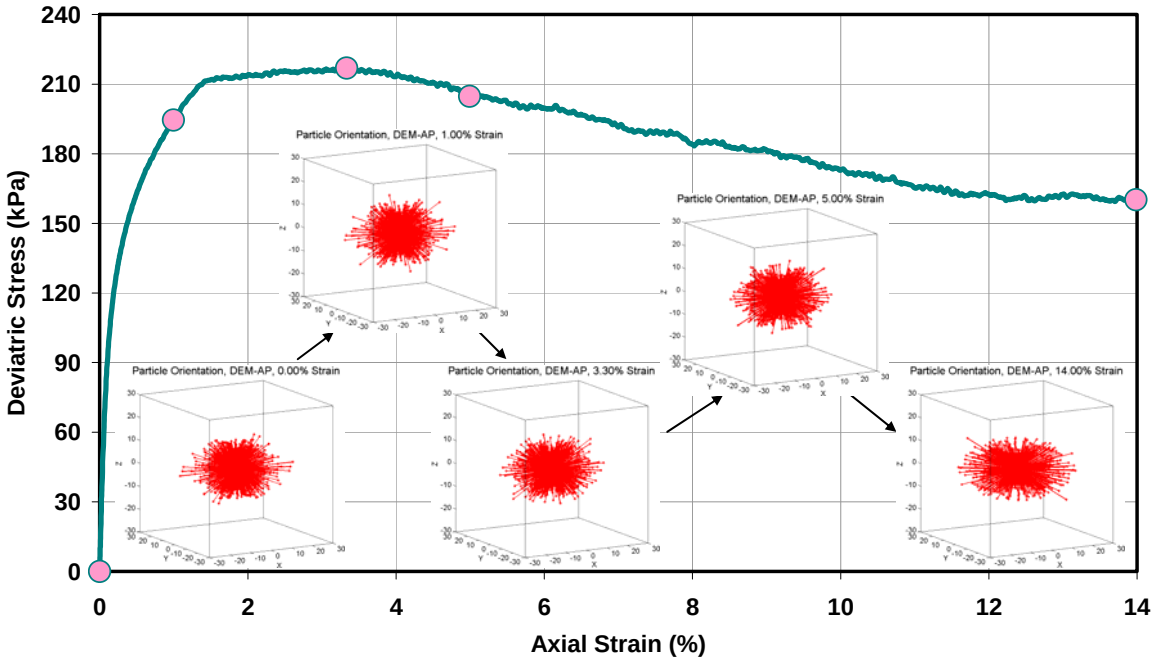

Figure 4.16 Polar histograms of particle orientation for DEM_AP

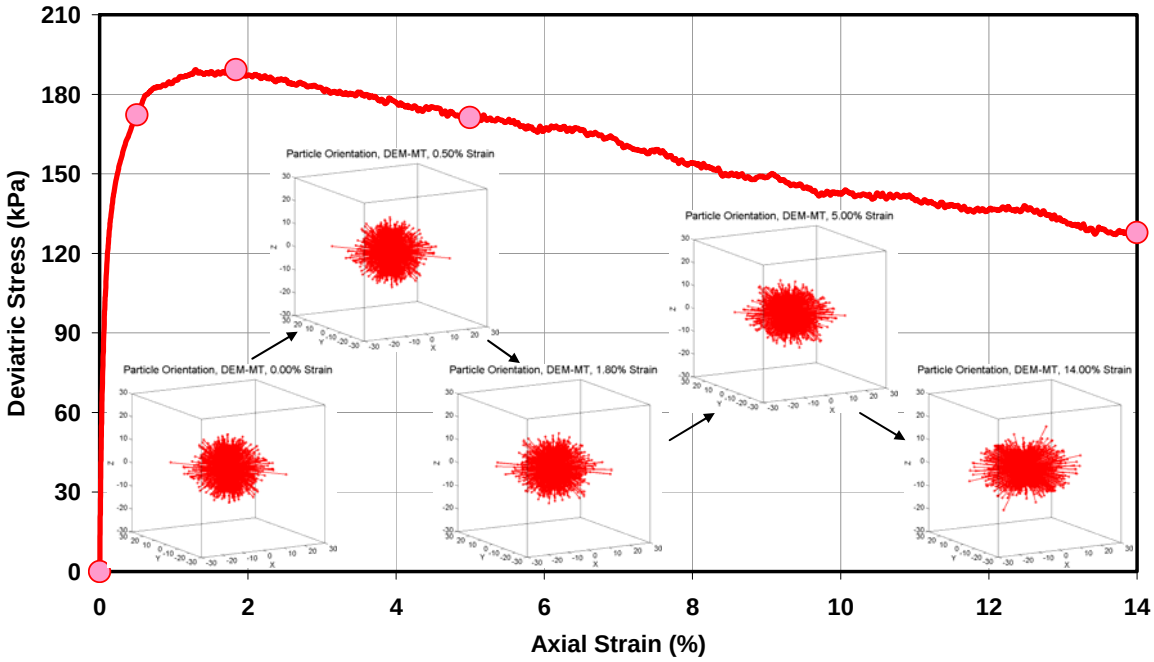

Figure 4.17 Polar histograms of particle orientation for DEM_MT

4.4.7. Particle Rotation and Displacement

For particulate materials, the particles will undergo rotations and displacements if subjected to shearing. Mapping the particle rotations and displacements can facilitate the understanding of shear behavior and location of shear zones. Particle rotations and displacements are 3-D in nature. However, considering the number of particles in the modeling, 3-D presentation will disable a clear observation of the specimen. Therefore, rotations and displacements were decomposed into X-Z, Y-Z, X-Y components and plotted for selected particles. Due to the axisymmetric feature of the tests, only the X-Z components of rotations and displacements of the particles in the center of the specimens are presented in Figures 4.18 and 4.19 for DEM_AP and DEM_MT, respectively. To exclude any effects from the consolidation stage, rotations and displacements were zeroed before shearing was initiated. At the pre-peak strains, both specimens did not show substantial particle rotations. For DEM_AP, the magnitude of displacements was small and uniform throughout the specimen. However, for DEM_MT, the magnitude of

displacements was larger than DEM_AP, and the lower part of the specimen had already moved upwards as a block, which indicates that a major shear zone tended to form within some weak layers created by the moist tamping preparation method in the upper portion of the specimen. At the peak axial strain, two blocks formed within the lower and upper portions of the air-pluviated specimen due to inter-particle friction and interlocking. Still, no apparent shear zone can be discerned at this stage. Some particles experienced rotations of 0.15~0.30 radians, and were evenly distributed throughout the specimen. For the moist-tamped specimen, as the shear zone had already been initiated before peak and the bottom block continued to move upwards, only a few particles experienced rotations of more than 0.15 radians. At 5.0% strain, more particles rotated more than 0.15 radians and moved towards the possible shear zones in both DEM_AP and DEM_MT. When sheared to 14.0% strain, the major shear zone developed in the middle of the air-pluviated specimen, which proves air pluviation created a uniform specimen with no weak layer dominating. At this stage, particles within both the air-pluviated and moist-tamped specimens experienced large-magnitude rotations. Contrary to expectation, no concentration of large-magnitude rotations was found within the major shear zones for both specimens. The main cause for the phenomenon is likely the rigid confining wall that only allows uniform displacements.

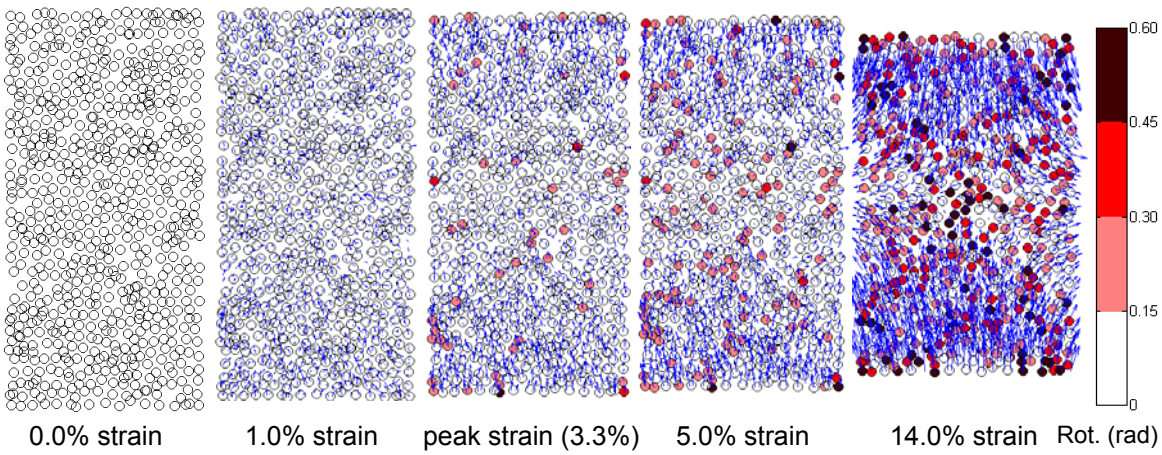

Figure 4.18 Particle rotations and displacements in X-Z plane for DEM_AP

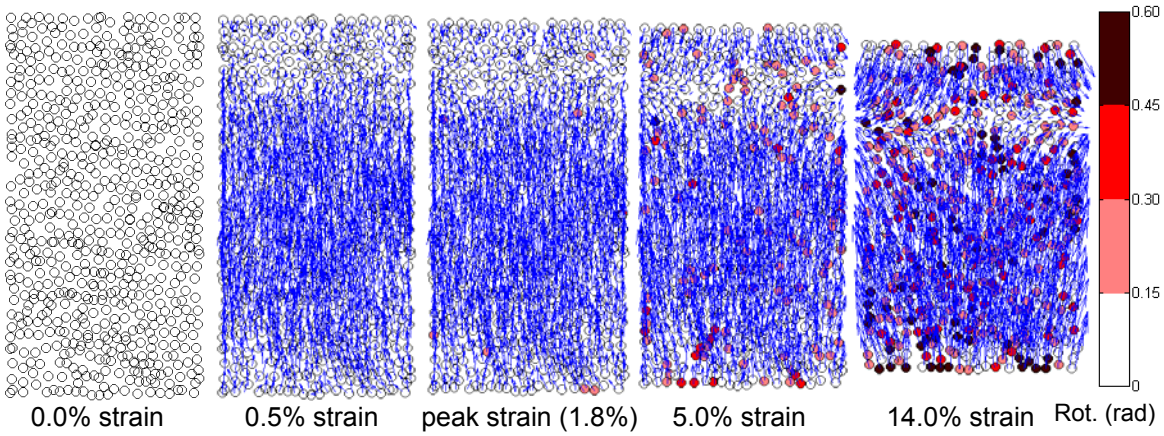

Figure 4.19 Particle rotations and displacements in X-Z plane for DEM_MT

When examining the particle rotations and displacements in the X-Z plane at 14.0% axial strain for both DEM_AP and DEM_MT, it appears that some cone-like structures may form inside specimen. Such cone structures were a part of the turbine-like internal failure structure proposed by Desrues et al. (1996) (an illustration of the structure can be found in Figure 2.1, and images of the cross sections of the sheared triaxial specimens are shown in Figure 2.4). To confirm the existence of the failure structure, the particle rotations and displacements in the X-Y plane were plotted at selected locations, 1/4, 1/2 and 3/4 specimen height, for DEM_AP and DEM_MT in Figures 4.20 and 4.21. For DEM_AP, the 1/4 and 3/4 sections showed smaller particle rotations and displacements within the central region than the 1/2 section, a sign indicating that more particles within the central region were less mobilized. Combining this finding with Figure 4.18, it proves that two cones with their centers on the axis of the specimen and their bases rooted at the end portions of the specimen were formed at the end of shearing. For DEM_MT, the 3/4 section experienced larger particle rotations and displacements within the central region than the 1/4 and 1/2 sections. The cone in the lower half of the specimen should be much larger than the cone in the upper half of the specimen. Unlike the air-pluviated specimen, the cone structure in the moist-tamped specimen did not center on the axis of the specimen. In general, regarding the turbine-like internal

structures, the cone structures were able to be clearly defined in the numerical specimens while the “blade” structures were not. Multiple factors, such as boundary conditions and particle scaling, may be responsible for the missing “blade” structures.

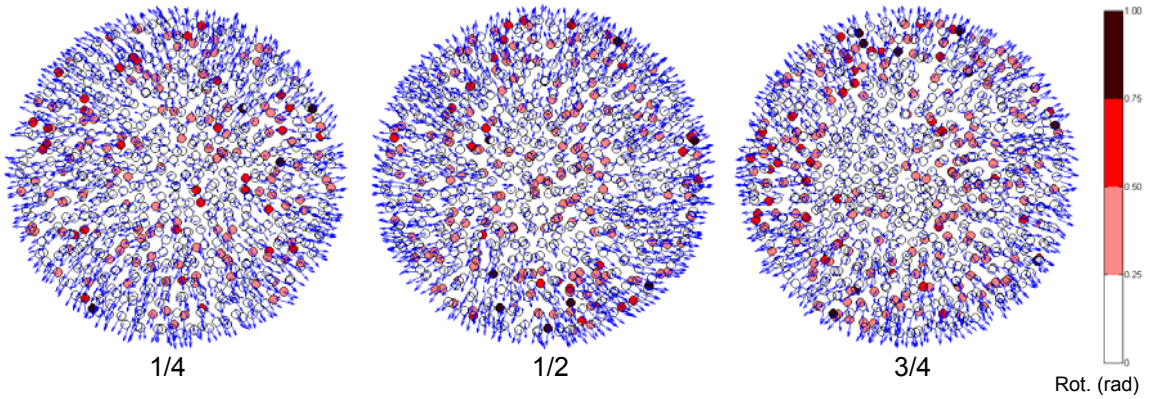

Figure 4.20 Particle rotations and displacements in X-Y plane for DEM_AP at 14% axial strain

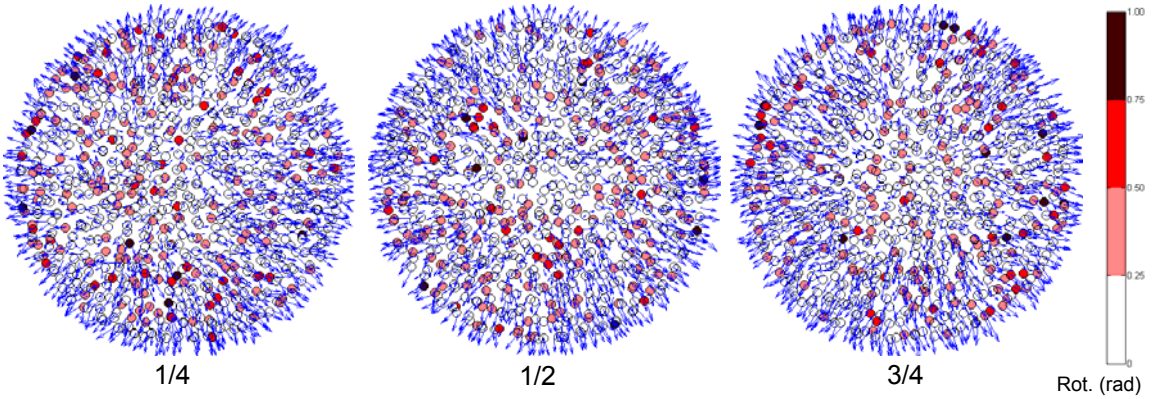

Figure 4.21 Particle rotations and displacements in X-Y plane for DEM_MT at 14% axial strain

4.4.8. Normal Contact Forces

The evolution of normal contact forces is presented in Figures 4.22 and 4.23 for the air-pluviated and moist-tamped specimens, respectively. Since nearly 9000 particles were employed by each 3-D numerical test, it would be difficult to see clearly if all of the normal contact forces were presented. Therefore, only the normal contact forces within

±10 mm from the central plane are included in Figures 4.22 and 4.23. Prior to shearing, the normal contact forces of both the air-pluviated and the moist-tamped specimens were uniform, which indicates an isotropic loading condition. This phenomenon correlates well with the findings from the polar histograms of contact normals. As soon as shearing started, the distribution of the normal contact forces did not maintain uniform any longer, and some major force chains formed along the direction of major principal stress to sustain the increasing vertical loading. The major force chains grew in number and magnitude until the specimen approached the peak state. After the peak, some of the major force chains bent and collapsed. In addition, with the initialization of a dominant shear zone (the middle portion for DEM_AP and upper portion for DEM_MT), they became the least concentrated area for the major force chains.

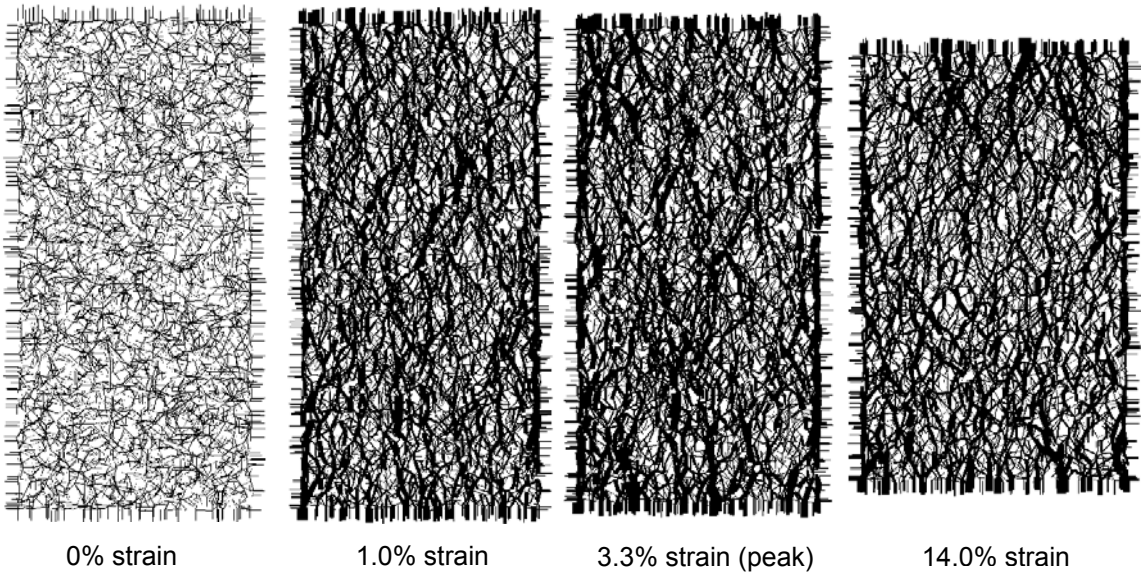

Figure 4.22 Normal contact forces for DEM_AP

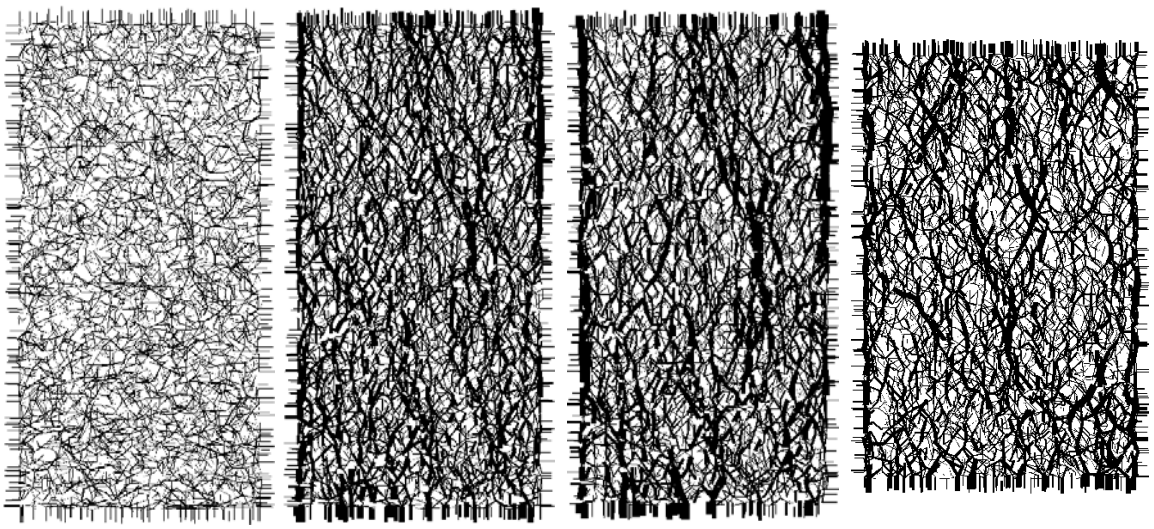

Figure 4.23 Normal contact forces for DEM_MT

4.5. Comparison with Single Sphere Model

Two additional numerical tests, designated as DEM_1B_AP and DEM_1B_MT, were performed using single spheres to compare with the tests using 2-sphere clumps. The material properties and experimental procedures for the single sphere specimens were the same as for the clump specimens, except that the single spheres were not replaced with clumps at stage two.

4.5.1. Stress-Strain Response and Volumetric Strain

Stress and strain responses for the numerical tests using single spheres along with the numerical tests using clumps are presented in Figure 4.24. For the air-pluviated and moist-tamped specimens, the peak stresses of the single sphere specimens were about half of the clump specimens and were reached at larger peak strains. The peak strains were 4% for DEM_1B_AP and 5.8% for DEM_1B_MT. After the peak, the stress in DEM_1B_AP experienced minor but noticeable decrease, but the stress in DEM_1B_MT did not show any apparent decrease. The differential behavior between the single sphere specimens and the clump specimens is attributed to the fact that for single spheres, the

applied pressures were mainly sustained through rolling and slipping, while for clumps interlocking played an additional and substantial role. Because of their irregular shape, one clump can be interlocked with another one, which consequently creates effective particle chains. As a result, the effective particle chains help the specimen to withstand larger applied forces. On the other hand, when the specimen is sheared to large strain, collapse of the particle chains lead to more reduction of stress.

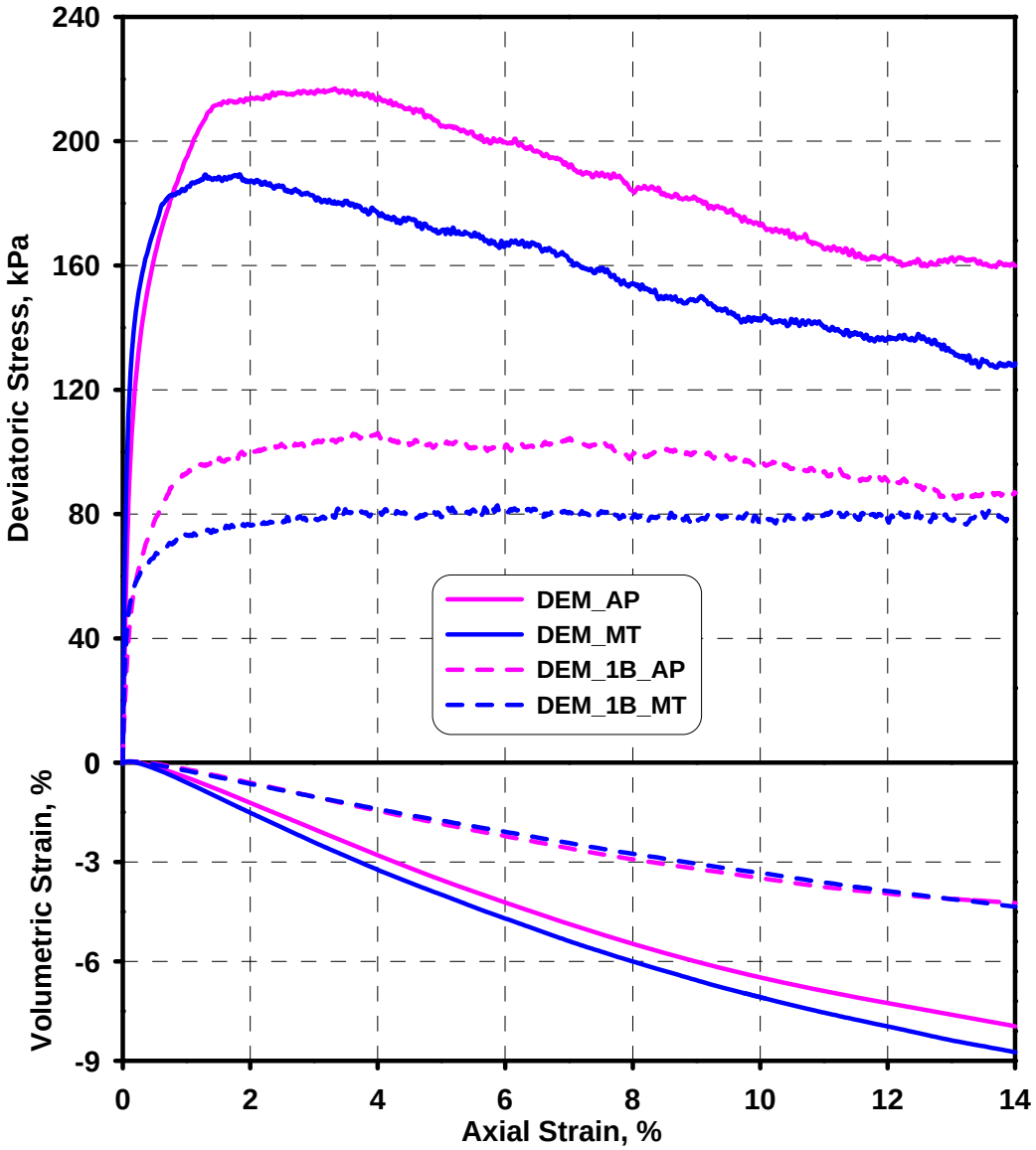

Figure 4.24 Stress-strain response for the numerical tests using single spheres

Volumetric strains of the numerical tests using single spheres are also presented in Figure 4.24. Similar to the stress-strain responses, the volumetric strains of the single sphere specimens were only half of the clump specimens. In general, the volumetric strains of both DEM_1B_AP and DEM_1B_MT did not differ from each other, which indicates that specimen fabrics may not have an effect on the volume change if single spheres are used.

4.5.2. Void Ratio

The void ratios inside the single sphere specimens are shown in Figures 4.25 and 4.26. Prior to shearing, the generalized void ratios of the two single sphere specimens reached 0.56, which were higher than the generalized void ratios of the clump specimens. This was caused by the different particle behaviors of spheres and clumps during the consolidation stage. Other than the generalized void ratios, curves of the local void ratios of the single sphere specimens were much smoother than the clump specimens as no interlocking behaviors occurred among the single spheres. Similar to the test involving clumps, specimen fabric still caused larger local void ratio variations in the moist-tamped single sphere specimen than the air-pluviated single sphere specimen, whereas the generalized void ratios were not affected.

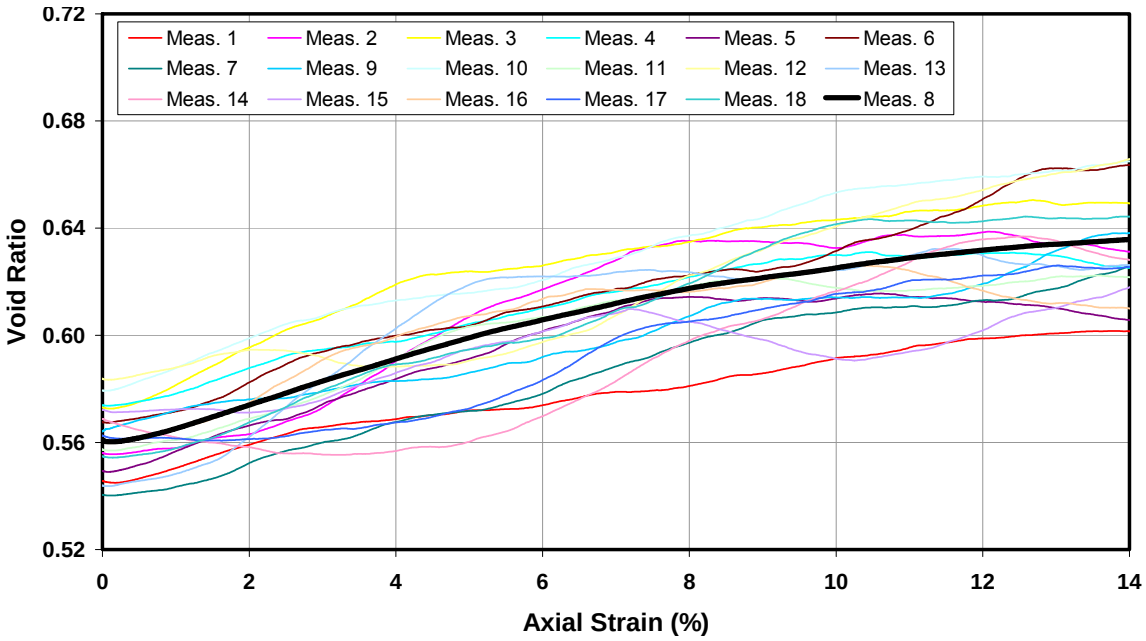

Figure 4.25 Void ratio measurement for DEM_1B_AP

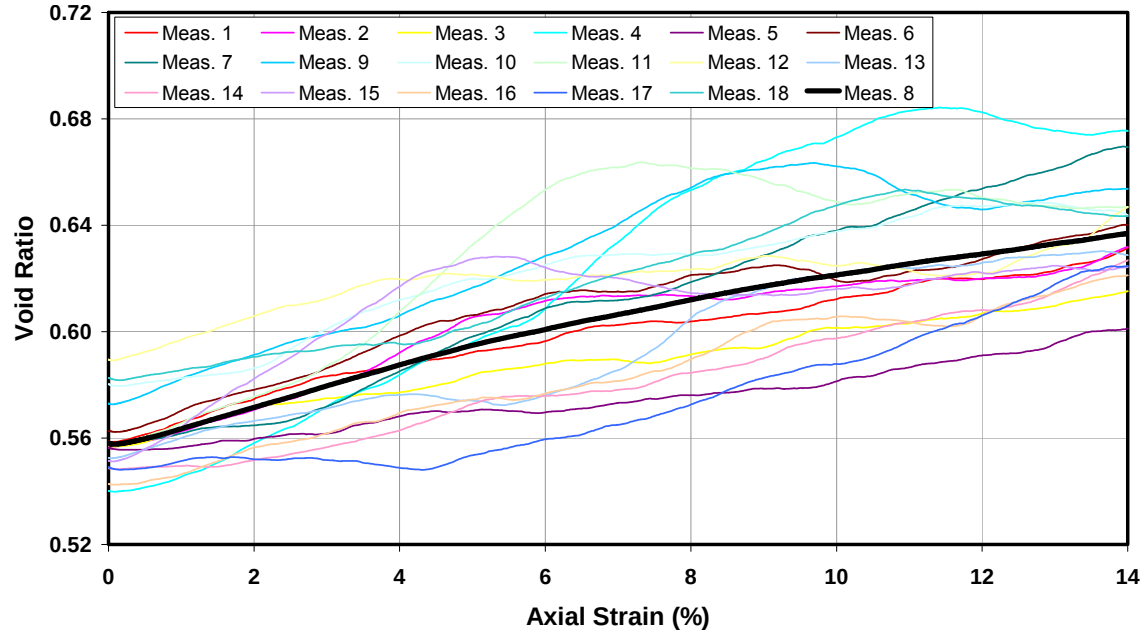

Figure 4.26 Void ratio measurement for DEM_1B_MT

4.5.3. Contact Normals

The polar histograms of contact normals for the numerical tests using single spheres are plotted in Figures 4.27 and 4.28. As with the clump specimens, 5 polar

histograms were chosen to represent different loading stages, i.e., prior to shearing, pre-peak, peak, post-peak, and end of shearing. Prior to shearing, the number of contact normals was 22932 for DEM_1B_AP and 23490 for DEM_1B_MT, which were about half the number of contact normals for the clump specimens. The shapes of polar histograms before shearing were quite spherical, which indicates an isotropic loading state. During the stress-hardening stage, the polar histograms shrank quickly though not as much as the clump specimens. The shape of the polar histograms remained nearly spherical until the stress-softening stage. This proves effective particle chains are more difficult to initialize with only particle rolling and slipping than with particle interlocking involved. At the end of shearing, the number of contact normals was reduced to 18817 for DEM_1B_AP and 18149 for DEM_1B_MT. Finally, specimen fabric caused the distribution of contact normals to be more anisotropic in DEM_1B_MT than in DEM_1B_AP. However, such difference needs some mathematical tools to be characterized.

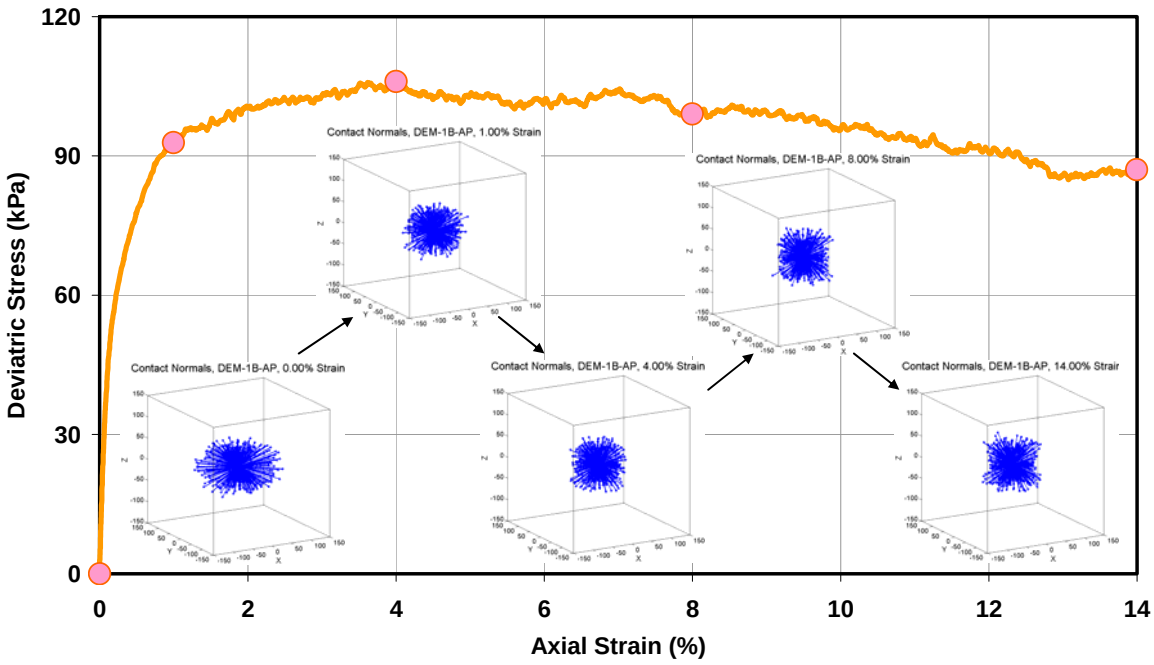

Figure 4.27 Polar histogram of contact normals for DEM_1B_AP

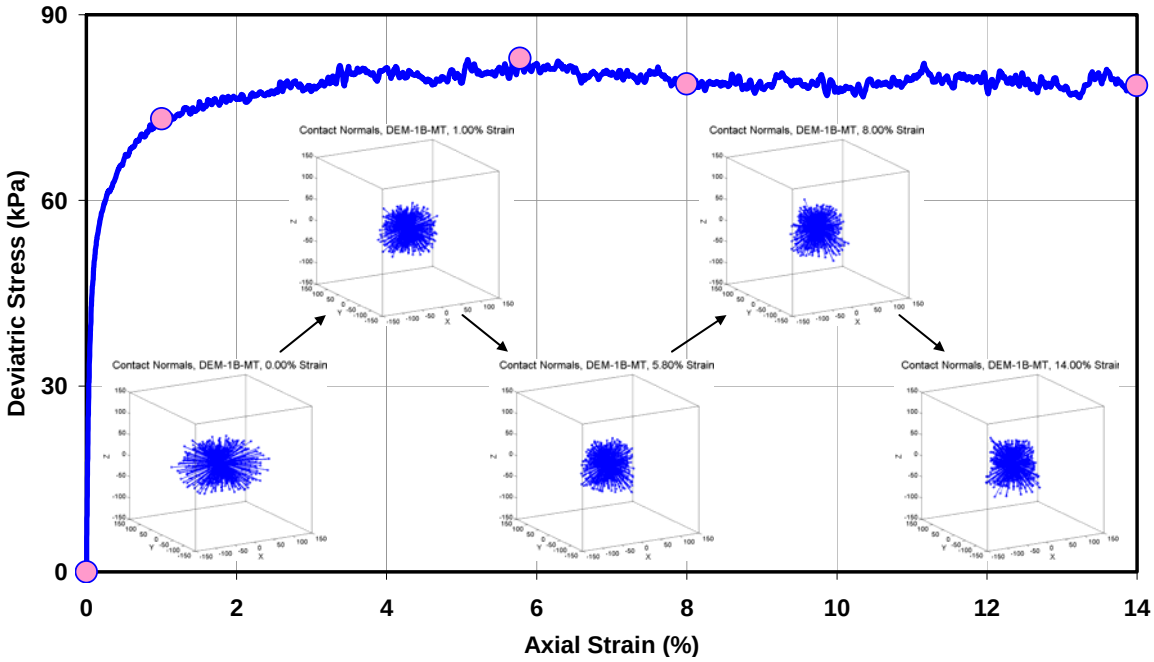

Figure 4.28 Polar histogram of contact normals for DEM_1B_MT

4.5.4. Coordination Number

Development of coordination numbers within the specimens using single spheres was measured by the same measurement spheres previously mentioned and is presented in Figures 4.29 and 4.30. Due to the shape of particles, the coordination number of the single spheres was much less than the clumps. Once shearing started, *cn* decreased rapidly from 5.6 to 4.7 for DEM_1B_AP and from 5.7 to 4.6 for DEM_1B_MT prior to 0.5% axial strain. Such rapid decrease is more related to the change of loading conditions (isotropic to anisotropic) than particle shape or specimen fabrics. After 2% axial strain, *cn* stabilized at around 4.5 for DEM_1B_AP and 4.3 for DEM_1B_MT. Larger variation of local coordination number measurements could be found in the moist-tamped specimen than in the air-pluviated specimen, which resulted from the larger degree of heterogeneity inside the moist-tamped specimen.

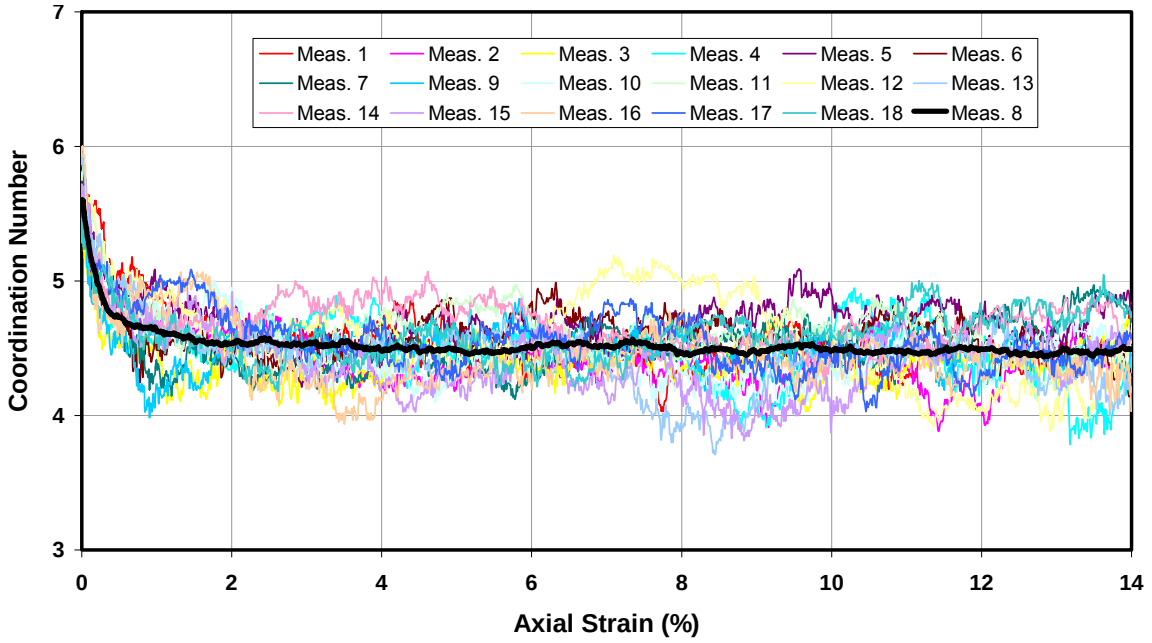

Figure 4.29 Coordination number of DEM_1B_AP

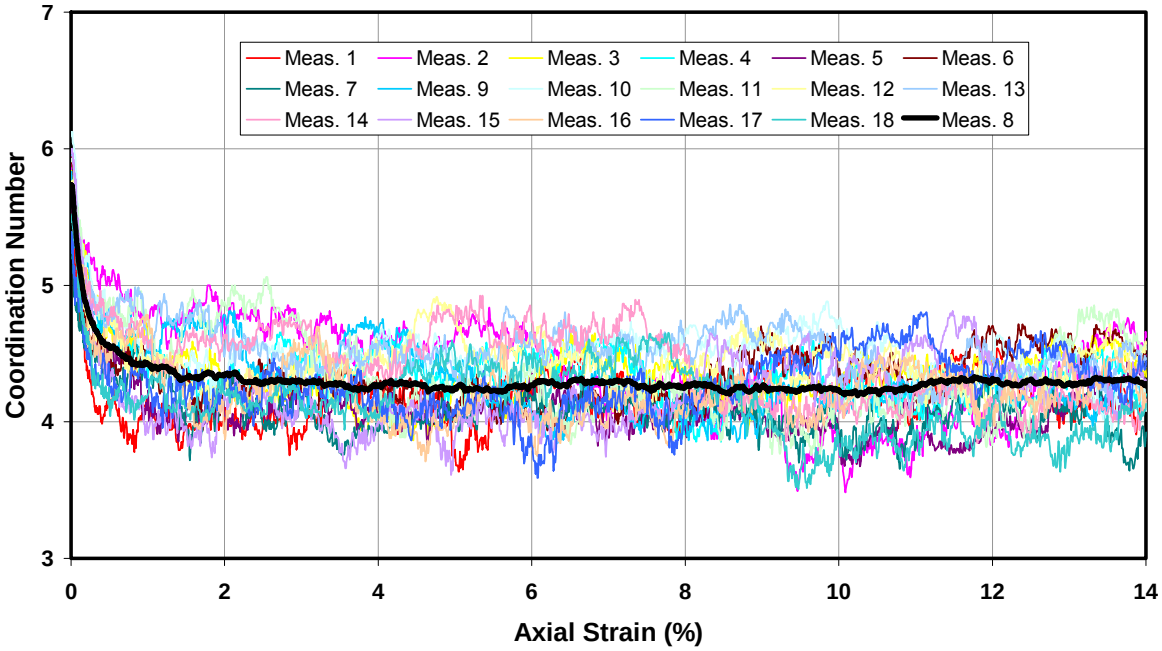

Figure 4.30 Coordination number of DEM_1B_MT

4.5.5. Particle Rotation and Displacement

The X-Z components of particle rotations and displacements at pre-peak, peak, post-peak, and end of shearing are presented in Figures 4.31 and 4.32 for DEM_1B_AP and DEM_1B_MT. Compared with the clump specimens (Figures 4.18 and 4.19), the development of particle rotations and displacements was similar for the single sphere specimens. However, some differences exist for these two kinds of particles: (1) the single spheres underwent much larger rotations than the clumps; (2) shear blocks formed later during loading and to a smaller degree for the single spheres than the clumps. The latter resulted from the fact that the single spheres developed lateral displacements towards the confining wall while such a tendency was suppressed in the clump specimens. All these differences came from the particle shape, as single spheres had to rotate more to enforce effective particle chains which in contrast, could be more readily achieved by particle interlocking in the clump specimens. Though not as obvious as for the clump specimens, specimen fabric still caused the shear zones to initialize at different locations for the single sphere specimens – in the middle portion for the air-pluviated and lower portion for the moist-tamped specimens.

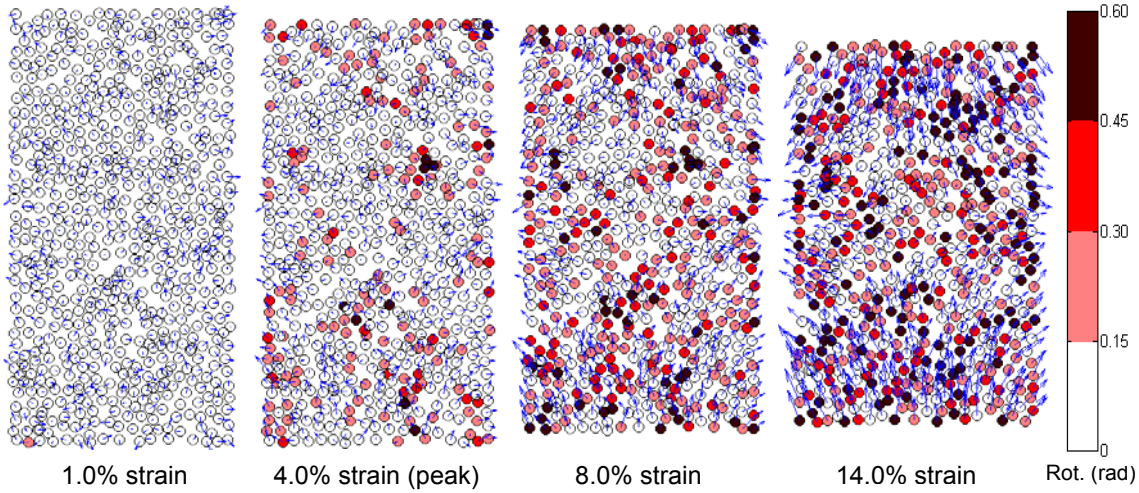

Figure 4.31 Particle rotations and displacements in X-Z plane for DEM_1B_AP

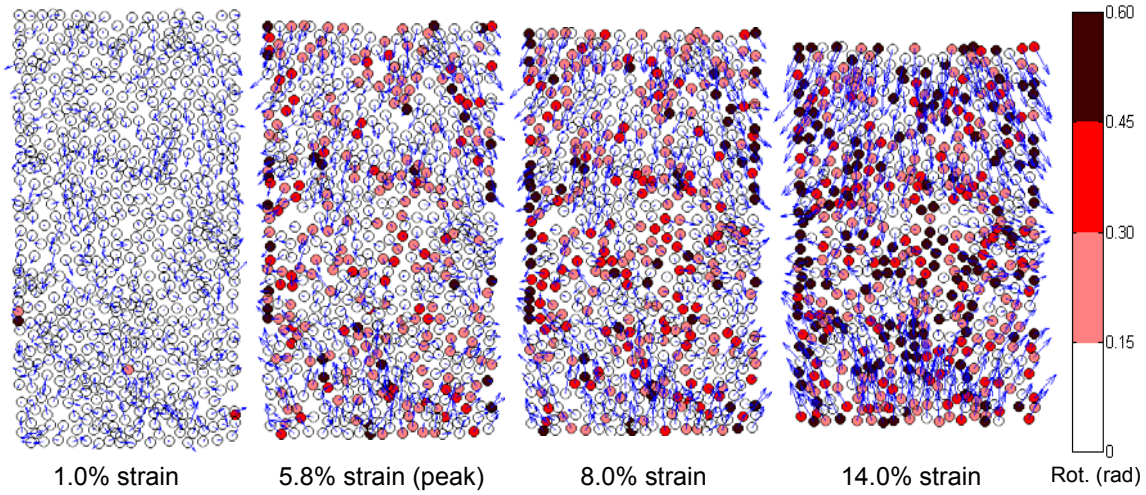

Figure 4.32 Particle rotations and displacements in X-Z plane for DEM_1B_MT

4.5.6. Normal Contact Forces

The evolution of normal contact forces within ±10 mm from the central plane are presented in Figures 4.33 and 4.34 for DEM_1B_AP and DEM_1B_MT. Prior to shearing, the normal contact forces were distributed uniformly throughout the specimens. Once the loading changed from isotropic to anisotropic, the normal contact forces became less diffuse and multiple major force chains came into shape. In general, the normal contact forces inside the single sphere specimens evolved in a similar way as the clump specimens. However, the single sphere specimens differ from the clump specimens that: (1) the arrays of normal contact forces were less dense; and (2) more major force chains could be defined. Finally, the difference between the air-pluviated and moist-tamped is not as obvious for the single spheres as for the clumps.

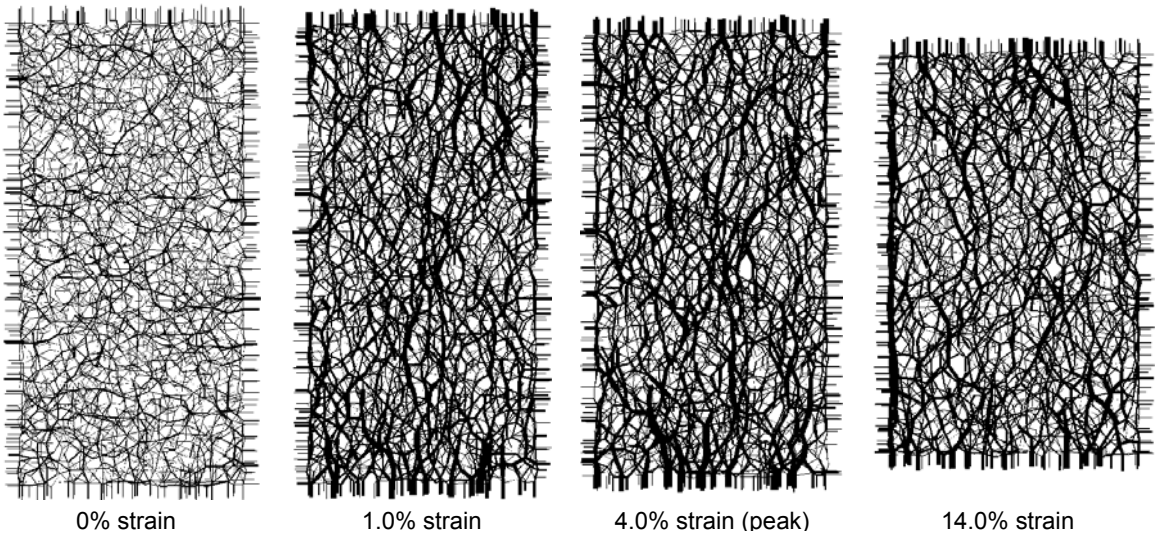

Figure 4.33 Normal contact forces for DEM_1B_AP

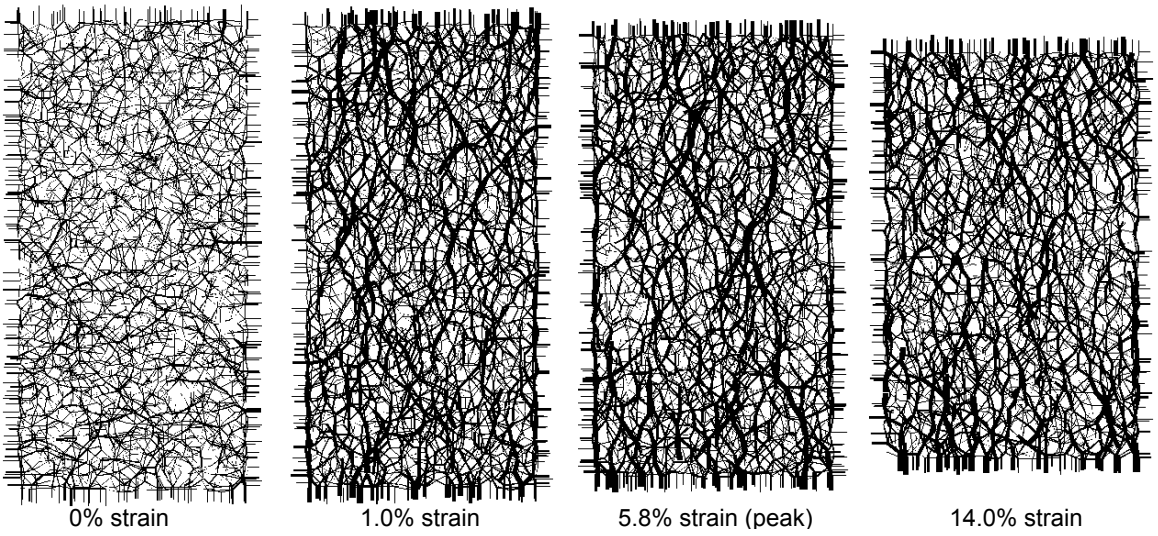

Figure 4.34 Normal contact forces for DEM_1B_MT

4.6. Summary and Conclusions

The triaxial compression tests were modeled using 3-D DEM code PFC3D. A series of parametric studies showed that the normal stiffness and friction coefficient of particles affected the peak stress and residual stress, while the shear stiffness of particles affected the peak strain.

Two preparation methods were used to create two different initial fabrics for the numerical modeling specimens. One of the methods generated homogeneous specimen fabrics and was designated as air-pluviation, while the other method created layered structures and was designated as moist-tamping. The application of the two methods enabled the role of particle fabrics to be investigated in the numerical modeling. However, the two preparation methods did not yield an exact match to their physical counterparts, i.e., air-pluviation and moist-tamping, since the particles did not pluviate from a certain specified height into the specimen compartment under the influence of gravitational field. This needs to be improved in the preparation modeling algorithm for future research.

Numerical tests were performed to simulate the laboratory triaxial tests, and the stress-strain responses and volumetric strains of the simulated tests matched well with the experimental results. Although the typical inclined shear bands found in the physical triaxial tests could not be observed for the simulated specimens, detailed examination on the internal structures showed that some cone-like structures formed inside the simulated specimens. Such cone structures were a part of the turbine-like internal failure structure proposed by Desrues et al. (1996). The cause of the absent “blade” structures may be as a result of the imposed boundary conditions (velocity-controlled rigid cylindrical walls) and particle scaling. Consequently, the microstructures of the simulated triaxial specimens were not characterized and compared to the microstructures of the physical triaxial specimens in Chapter 7. Future works need to be done to create flexible membranes for the numerical triaxial tests.

The particles used for the numerical tests were two-sphere clumps with an aspect ratio of 1.5:1. Additional numerical tests were performed using single spheres. Comparisons on the mechanical behaviors, microstructural properties and visualization of the internal structures between the clump specimens and the single sphere specimens indicated that: (1) particle interlocking among the clumps reduced the particle rotations

and enhanced the strength of the specimens; and (2) the clump specimens yielded a better representation of the real specimens than the single sphere specimens in terms of overall response as well as internal structure evolution.

CHAPTER 5

3-D MICROSTRUCTURE RECONSTRUCTION OF BIAXIAL SPECIMENS

5.1. Serial Sectioning for 3-D Reconstruction of Biaxial Specimens

The 3-D digital structures reconstructed in this study were obtained from the coupons impregnated and extracted from biaxial shear specimens by Evans (2005). When choosing which parameters to use with the 3D reconstruction techniques for the current study, the following factors were considered: size of the particles, scale of the features of interest, and desired resolution of the acquired images. As the impregnated coupons were Ottawa 20-30 sands with D_{50} of 0.74 mm and the features of interest were both the large-scale (shear band) and small-scale (local void ratio and particle size), the optical microscopy based serial sectioning method was utilized.

5.1.1. Experimental Procedures

Optical microscopy based montage and serial sectioning procedures were first implemented by Yang (2005) to construct 3D digital mircrostructures of Ottawa 30-50 sands subject to triaxial shearing. The same techniques were adopted herein to reconstruct Ottawa 20-30 sands subject to biaxial shearing. However, since the targeted materials in the current study were different in particle size and the features of interest were larger in scale, some modifications were implemented to account for these differences. Major experimental procedures for the reconstruction include: cutting and mounting, grinding and polishing, and image capturing and processing.

5.1.1.1. Cutting and Mounting

A highly dilatant biaxial specimen and a corresponding unsheared specimen were selected for 3-D reconstruction. Each of them had been sliced into 5 coupons, representing 0-20%, 20-40%, 40-60%, 60-80% and 80-100% portions of the specimen (Evans, 2005). In order to limit any boundary effect, a 21 mm x 13 mm sub-coupon was cut from the 40-60% coupon of both the highly dilatant and the unsheared specimens (see Figure 5.1). The sub-coupon dimension of 21 mm x 13 mm was chosen based on the size of the 1" diameter mounting cup for the polisher/grinder device. The sub-coupon from the highly dilatant specimen was selected to encompass the shear zone. The apparatus used to cut the coupons was a Buehler Isomet 1000 Precision Saw. The wheel speed was set at 100 rpm and the load weight as 350 gram to minimize possible cutting-induced damage to the specimen surface.

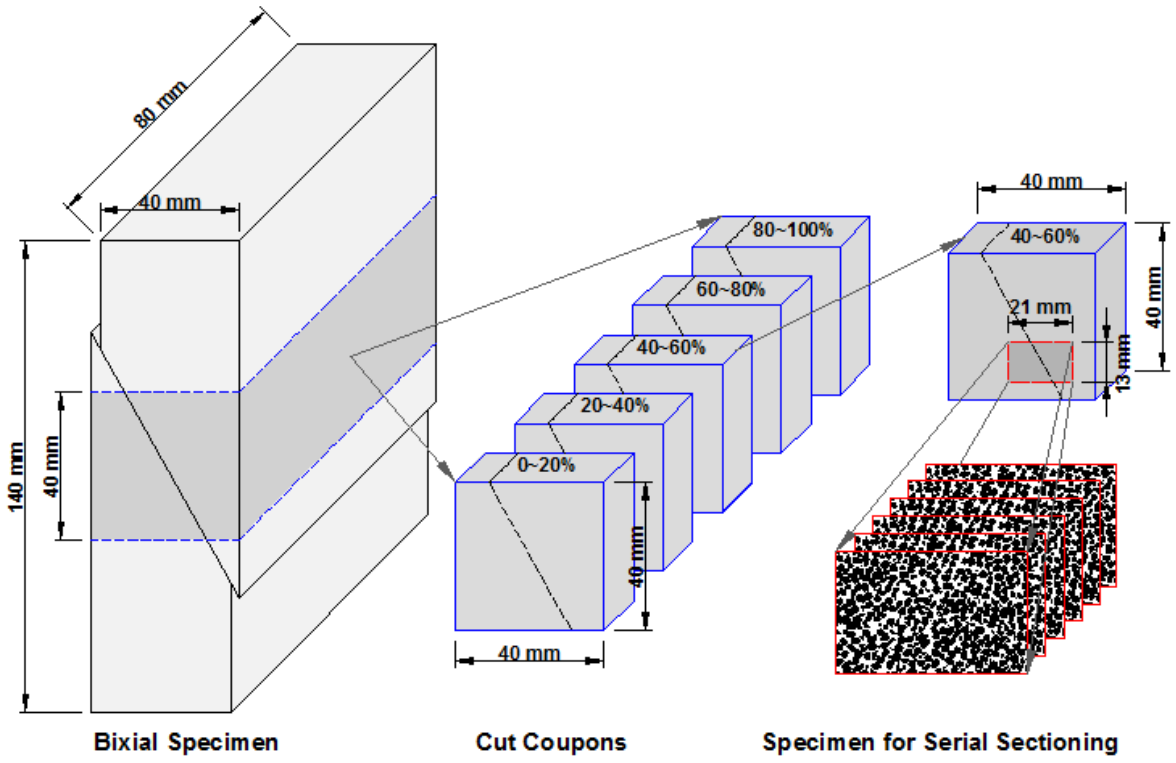

Figure 5.1 Sampling location of serial sectioning specimen

After cutting, the 21 mm x 13 mm sub-coupon was mounted in a 1" diameter mounting cup with epoxy resin to create a desirable shape for the preparation machine. As the epoxy resin was Epo-Tek 301, the same resin used by Evans (2005) to impregnate the biaxial specimens, this mounting process did not cause any disturbance to the sub-coupons. After 24 hours of curing, the specimen was released from the mounting cup, and several cylindrical and conical holes were drilled as previously noted. The cylindrical holes, also called alignment holes, were used for aligning the slices during serial stacking. The conical holes, with a vertex angle of 60°, were used for checking the removed thickness. After these fiduciary marks were drilled, the specimen was ready for grinding and polishing.

5.1.1.2. Grinding and Polishing

The device used for grinding and polishing in the present study was a MultiPrep™ System manufactured by Allied High Tech Products, Inc. Grinding and polishing is critical to producing high-quality images, which in turn greatly reduces the amount of image processing required. The major experimental procedures and parameters followed those used by Yang (2005), however some test parameters needed to be determined by trial tests. The MultiPrep™ System provides three motion options to ensure even surface grinding and polishing: wheel rotation, sample rotation and sample oscillation. The wheel speed depends on the material and size of the sample to be ground and cannot be set either too slow or too fast since this may result in uneven grinding or polishing of the surface. In addition, a slow wheel speed means that long grinding time may be required whereas a fast wheel speed can cause damage to the surface being ground. Through a series of trial tests, the optimum wheel speed for the 1" specimens used in this research was determined to be 80 rpm. A larger 1½" diameter specimen size was also tested. It was found that: 1) the grinding time was more than double the grinding time of 1" specimen; 2) an even grinding surface was very difficult to achieve, especially

in the boundary regions. When the specimen was ground on the wheel, although it experienced the same angular velocity, the linear velocities at different locations changed according to the distances from the wheel axis. Although the MultiPrep^{TM} System allows two additional motion modes (sample rotation and sample oscillation) to minimize the influence, the linear velocity difference is magnified when the specimen size increases. Figure 5.2 shows the ground and polished surface of a 1½" diameter specimen, which shows an uneven surface with a bright middle area and a dark edge area. For comparison, the corresponding image for a 1" diameter specimen is shown in Figure 5.3 and a uniform specimen surface can be observed.

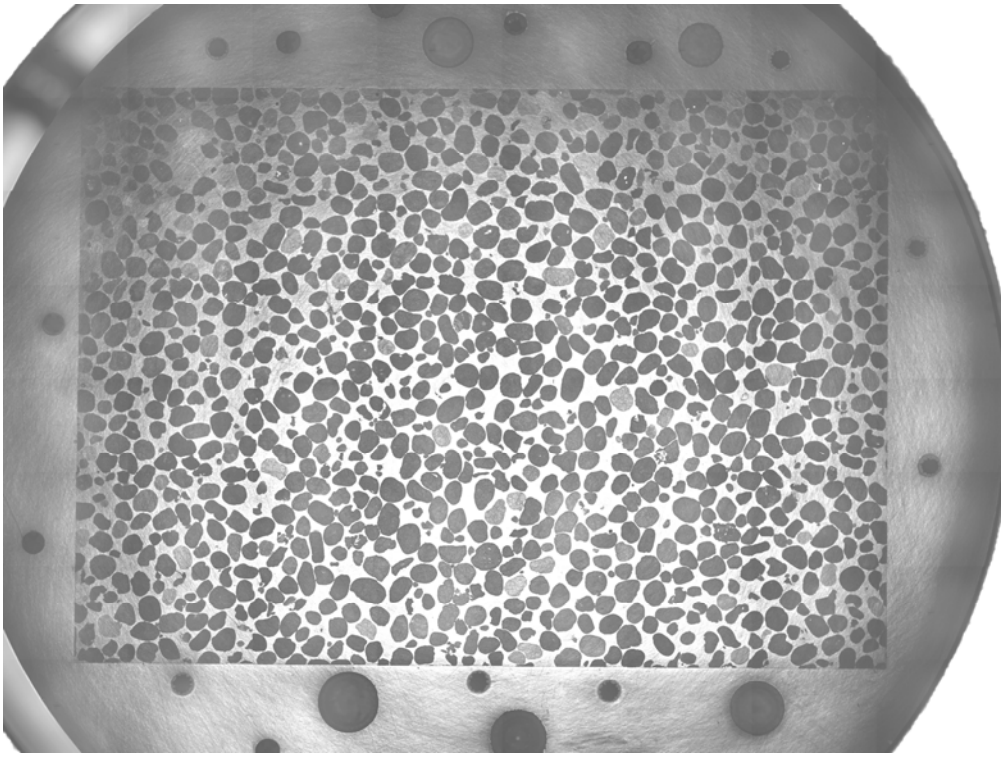

Figure 5.2 Uneven surface of 1½" diameter specimen

For each stage of grinding and polishing, a 14 μm thick layer of material was removed. This was selected as a function of the particle size and the image resolution of the microscope. An image resolution of 14 μm/pixel was determined to be adequate to

illustrate both large and small fields of interest. In order to generate true-to-scale 3-D digital images, 2-D images were captured after every 14-μm of material was removed. Based on the wheel speed, specimen size, removed thickness and condition of the abrasive, the grinding time for each section was between 2 and 3 minutes. The subsequent polishing time was 30 seconds. Using this approach, 600 slices were generated for the highly dilatant sheared specimen and 430 slices were generated for the unsheared specimen by serial grinding and polishing.

5.1.1.3. Imaging and Processing

When each stage of grinding and polishing was completed, a set of images of the section were captured using a Leica DM4000 microscope and Leica QWin 3.0 software. Given the D_{50} of Ottawa 20-30 sands and the scale of the fields of interest, an objective lens 2.5/0.07 was used to provide an appropriate magnification. The microscope was configured with a digital camera capable of capturing color images with high resolution. With the selected magnification and resolution, each image covered an area of 4.47 mm x 3.35 mm. This was only a small portion of a 21 mm x 13 mm specimen. In order to create a larger field of view, a montage technique was applied. This technique involved taking images contiguously in a grid pattern and then stitching the images together. In this manner, images of large features of interest can be created while still maintaining the appropriate resolution for small features of interest. Finally, each surface section of the specimen was represented by a montage image of 1920 x 1440 pixels made up from 6 x 6 sub-images (see Figure 5.3).

Although a steel fixture that can hold the specimen was designed and fabricated (Yang, 2005) to ensure that each image was captured at the same orientation and position, some translational or rotational movements could still take place from slice to slice. This would eventually lead to distortion of the rendered 3D structures. Therefore, the slice images were aligned using the drilled alignment holes with the software ImageJ from

NIH with the plug-in RegisterROI by Abràmoff (2004). After aligning the slices, the grey-scale images were binarized into black and white images and cropped to a size of 1300 x 800 pixels using a batch processing routine. Due to the quality of sample preparation, only a few image processing operations were needed to remove some noise.

The processed images were rendered into 3D structures using the software VoxBlast from VayTek, Inc. For the highly dilatant specimen, the rendered structure represents a true sample size of 18.1 mm x 11.2 mm x 8.4 mm and includes approximately 5100 particles. This volume contained 0.6 billion voxels of side approximately 14 μm. For the unsheared specimen, the rendered structure represents a true sample size of 18.1 mm x 11.2 mm x 6.0 mm and includes approximately 3800 particles. This volume contained 0.45 billion voxels of side approximately 14 μm. The rendered 3D structures will be discussed further in Chapter 7.

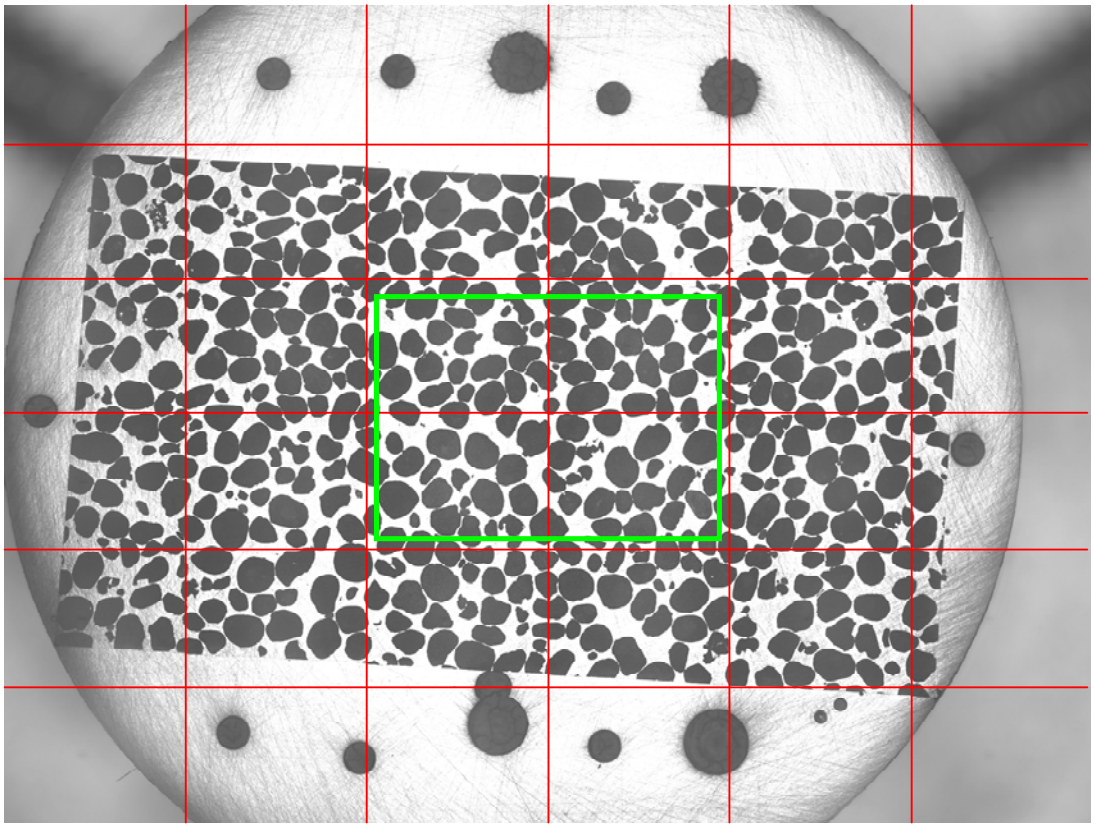

Figure 5.3 Large image created by 6 x 6 sub-images

5.1.2. Stitching Effects

As mentioned previously, the montage technique was used to create a large field of view from multiple smaller fields of view. The software Leica QWin has a built-in function to create a montage by capturing sub-images with a user-defined grid pattern with 0% overlap and stitching the sub-images together. In order to verify whether the montage operation would affect the image quality, a stitched image was compared with an un-stitched image. A sub-region cropped from the center of a stitched image, defined by the green frame in Figure 5.3, was labeled as a stitched image and displayed in Figure 5.4 (a). The middle of the region that is marked by two parallel red lines is where the seams of stitching were located. Another individual image was captured at the central location of the specimen and labeled as un-stitched in Figure 5.4 (b). This image correlates to the pink-framed region in Figure 5.4 (a). By comparing the pink-framed region in Figure 5.4 (a) and Figure 5.4 (b), only minor distortions were discovered at the boundaries of the particles. Those distortions accounted for less than 0.1% difference in grain pixels. It was concluded that stitching with 0% overlap did not impose significant effect on the montage images.

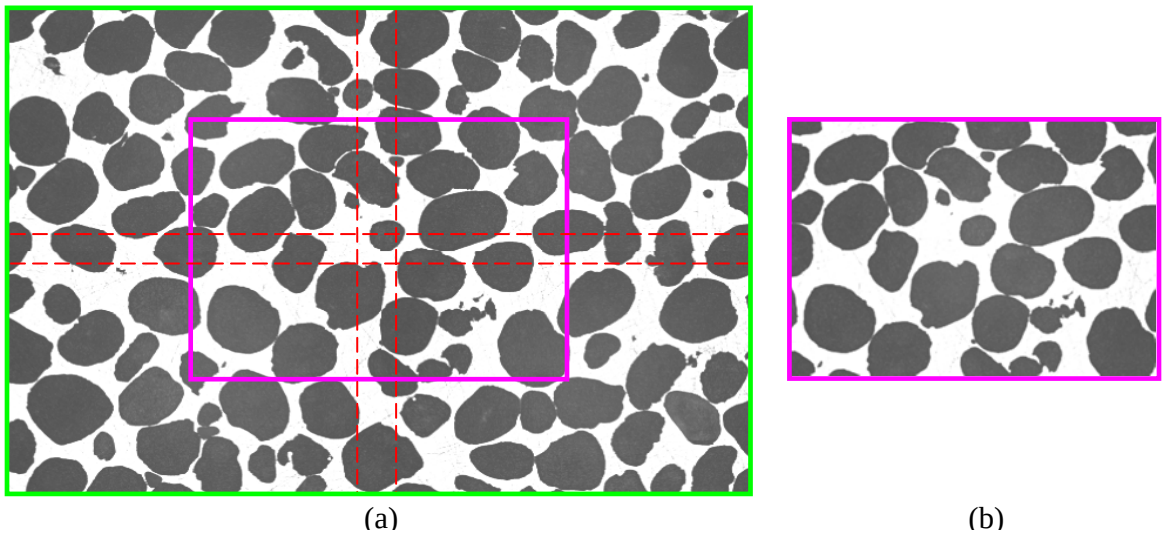

Figure 5.4 Stitching effects: (a) stitched image, and (b) un-stitched image

5.2. Comparisons of Different Surface Preparation Procedures

Two types of surface preparation procedures have been developed for optical microscopy based image analysis and implemented in the previous researches. The effects of the two procedures will be analyzed and compared here. One of the procedures uses the MultiPrep™ System by Allied High Tech Products, Inc. and was adopted for the serial sectioning in the current study. Due to the fact that grinding time for each slice takes about 2~3 minutes, this procedure is given the name of "short-duration" grinding. Another surface preparation procedure implemented by Yang (2002) and Evans (2005) uses the Buehler MetaServe polishing table. Since the grinding of each surface takes 30~60 minutes, the procedure is given the name "long-duration" grinding. Detailed parameters of each procedure are listed in Table 5.1.

Table 5.1 Parameters of two surface preparation procedures

	Long-Duration Grinding		Short-Duration Grinding	
	Grinding Phase	Polishing Phase	Grinding Phase	Polishing Phase
System	Buehler MetaServe		Allied High Tech MultiPrep™	
Abrasive	600-grit SiC powder on cast iron wheel	1000-grit SiC powder	6 µm Dia-Grid diamond discs	1 µm diamond compound
Polishing Cloth	N/A	Temet 1000 cloth on aluminum	N/A	Gold Label
Extender	50g/250 ml Metadi Fluid	50g/250 ml water	BlueLube™	BlueLube™
Overburden Stress	29 kPa (typ.)	23 kPa (typ.)	600 gram	600 gram
Wheel Speed	120 rpm	120 rpm	80 rpm	80 rpm
Duration	30-60 min	10-13 min	2-3 min	30 sec

These two surface preparation procedures created distinctive surface conditions, which lead to sharply different images captured by the microscope. In order to examine

how the preparation procedures would affect the image analysis results, an additional set of serial sectioning tests were performed. In this set of tests, the specimen was first prepared by the long-duration grinding, and an image of the surface was captured. This surface was designated as surface 0. Then, the specimen was ground and polished by the short-duration grinding with a thickness of 5 μm removed for each slice. A total of 10 slices were generated using the short-duration grinding and were designated as surfaces 1 to 10. Images of slices 1 to 10 were captured at the same location as surface 0. To ensure accurate comparisons between surface 0 and surfaces 1 to 10, the microscope settings (illumination, aperture, magnification, resolution, etc) were kept the same. Figure 5.5 presents surface 0 and surface 3 which are 15 μm apart. For surface 0 prepared by the long-duation grinding, the image shows white grain space with black pock marks, grey resin space, and black grain boundaries. For surface 3 prepared by the short-duration grinding, the image shows black grain space and grey resin space. Such distinctive surface conditions resulted from the abrasive and the grinding time. For the long-duration grinding, the resin was ground faster than the grains and thus led to a higher grain surface than the resin surface. Other than a higher grain surface, such a grinding procedure also caused abraded grain boundaries. During the subsequent polishing stage, the higher grain surface was the most polished part and the slanted grain boundary the least. As a result, the grain boundary was the most diffusive part under the microscope and showed a black color ring around the particles in the captured image (Figure 5.6). However, during the short-duration grinding, the grains were ground at same rate or faster than the resin. This caused the grain surface to be level with or lower than the resin surface (Figure 5.6). During the subsequent polishing stage, the higher resin surface was polished to smooth and the grain surface was not polished as much. When the prepared surface was placed under the microscope, the light reflected at the resin surface but diffused at the grain surface, and hence the captured image showed white resin and black grains.

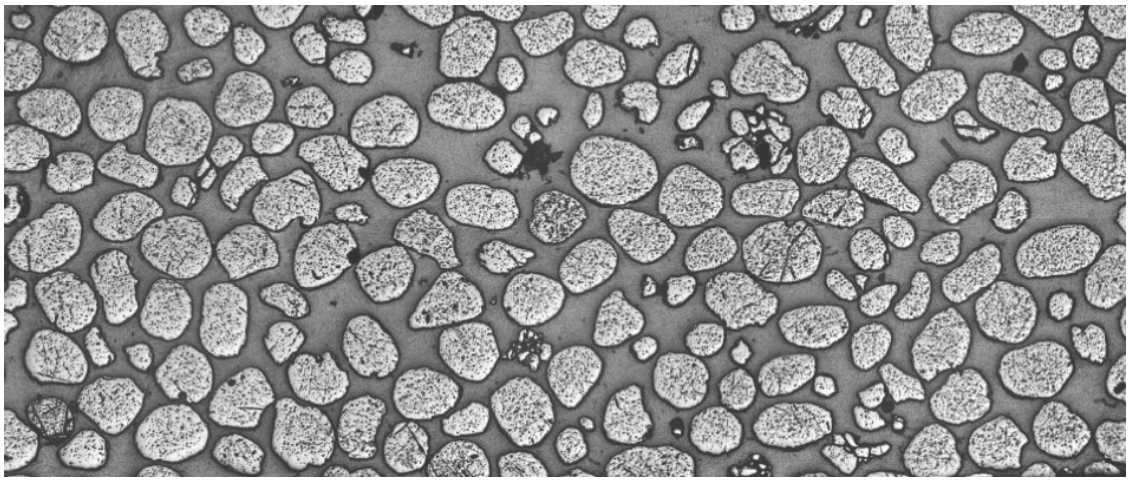

(a)

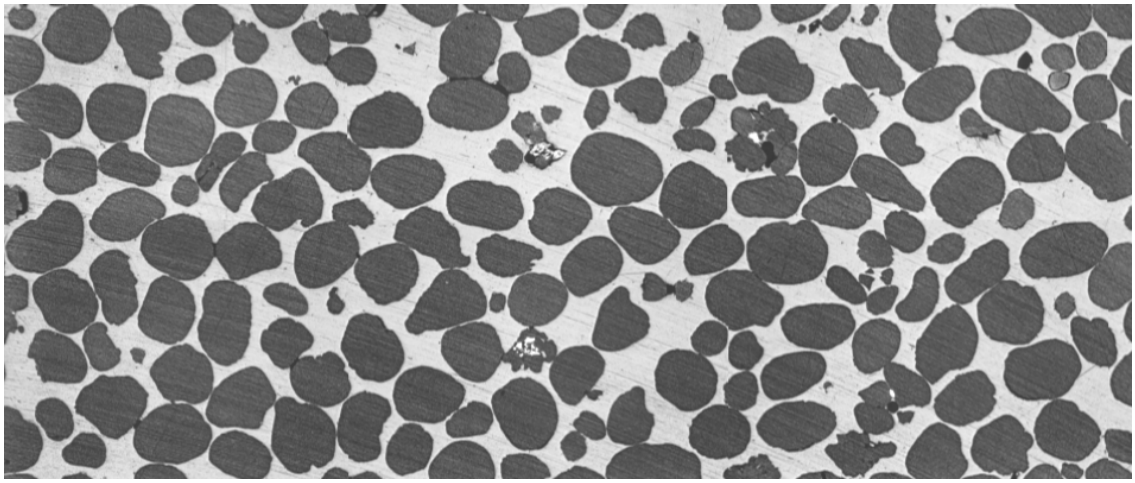

(b)

Figure 5.5 Surfaces prepared by different preparation procedures: (a) surface 0, and (b) surface 3

It is evident that the grey-scale images of surfaces 1 to 10 are easy to binarize by simply thresholding the grey level, while binarization of surface 0 is more complicated. Some morphological operations were necessary to remove the black specks in the grain space and segment the black boundaries into the white grain space. By a close examination on the slice, it was found that the widths of grain boundaries varied between 0 and 3 pixels. Two binarization schemes were performed on the slice, with one segmenting about 1-pixel-wide boundaries into the grain space and another one segmenting about 2-pixel-wide boundaries. After binarizing slices 0 to 10, the void ratio

was calculated for each slice based on simple pixel counting, and the results are plotted in Figure 5.7. It can be seen in the figure that the width of grain boundaries segmented into the grain space substantially affected the calculated void ratio. By including grain boundaries 1 pixel wider, the void ratio decreased from 0.61 to 0.48. This finding agrees well with the grain perimeters which accounted for about 6% of the entire image area. When comparing the void ratios, it is noticed that binarization of slice 0 by segmenting 2-pixel-wide grain boundaries into grain space matches better with the binarized slices 2 to 10.

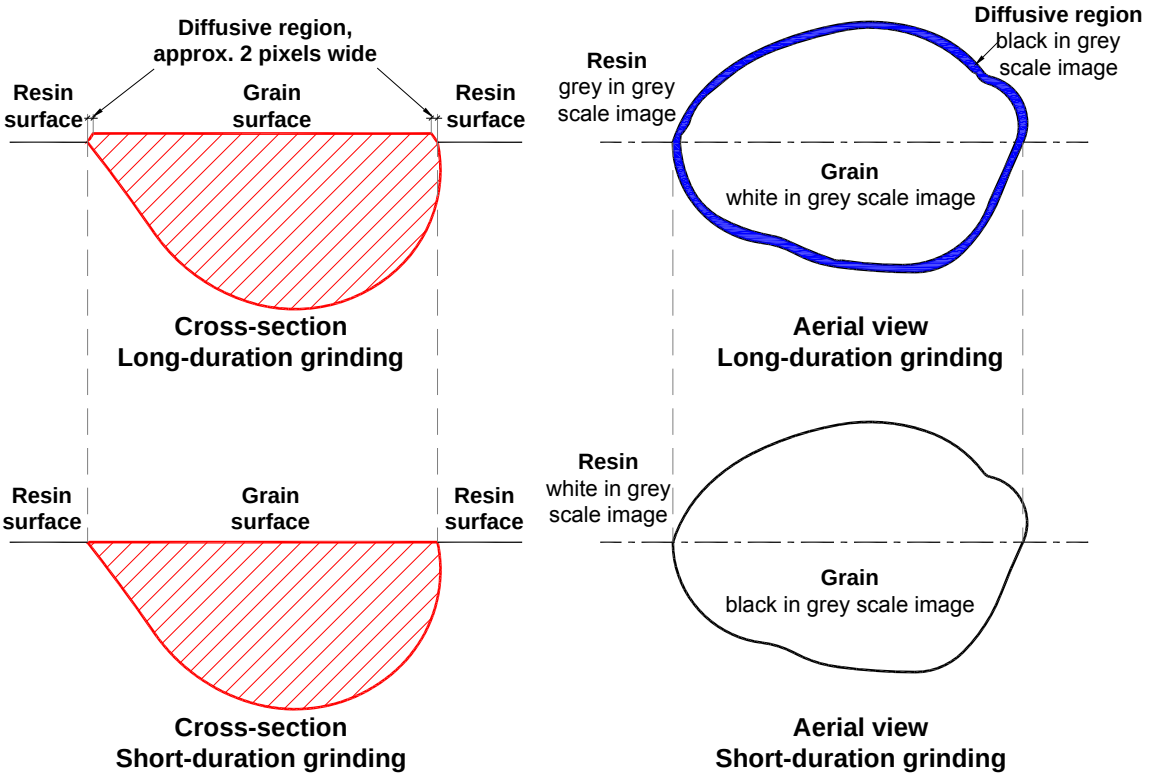

Figure 5.6 Schematic views of specimen surfaces prepared by the long-duration grinding and the short-duration grinding

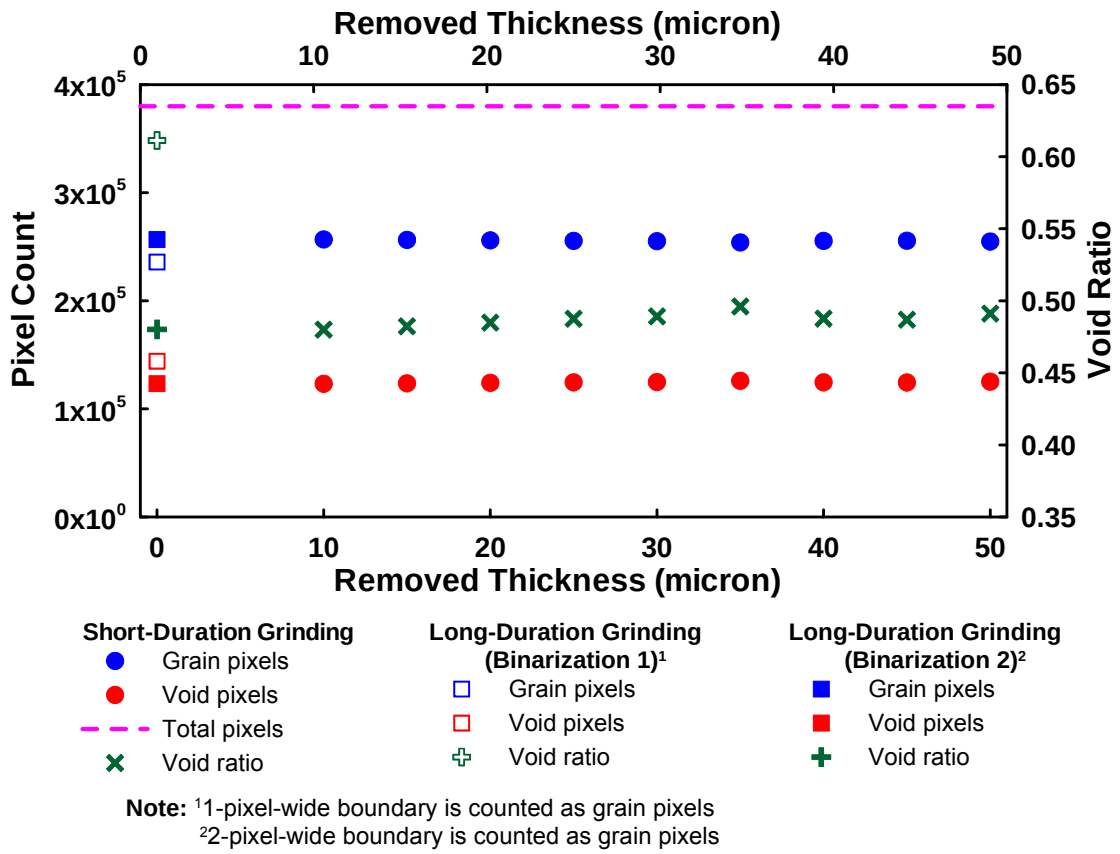

Figure 5.7 Void ratios resulting from two preparation procedures

5.3. Summary and Conclusions

The optical microscopy based image montage and stacking techniques used in the current study are efficient tools to reconstruct 3-D large volume high resolution digital microstructures of sand specimens. The image montage technique is about creating a large field of view image by stitching together a number of small field of view images captured in a grid pattern while not losing image resolution. The image stacking involves 3-D volume rendering using a serial stack of montage slices.

Two types of surface preparation procedures were developed during the previous studies completed at Georgia Tech, one of which is called short-duration grinding and the other is called long-duration grinding. The specimen surfaces prepared by these two procedures showed distinctive image characteristics under the optical microscope, which

were caused by the different abrasives and preparation time used. Through a comparison study, it was shown that the images of the surfaces prepared by the short-duration grinding were easier to binarize and resulted in more consistent image processing and characterization results than the long-duration grinding.

The digital microstructures of two biaxial specimens, a highly dilatants sheared specimen and its corresponding unsheared specimen, were reconstructed using the optical microscopy based serial sectioning method. Characterization of the captured serial slices will be presented and discussed in Chapter 7.

CHAPTER 6

3-D NUMERICAL MODELING OF BIAXIAL SPECIMENS

6.1. Introduction

In the last decade, biaxial shear or plane strain tests have been used by a number of researchers to investigate the onset mechanism of shear banding or strain localization. An introduction to biaxial compression tests can be found in Section 3.3.1. However, due to the limitations of the experimental apparatus and the associated instrumentations, only limited measurements are available for the study of mechanism specifics. Some researchers have used numerical approaches, and in particular the discrete element method (DEM), to facilitate the investigation of shear banding (e.g., Iwashita and Oda, 1998; Tordesillas et al., 2008; Mahmood and Iwashita, 2010), however, most of them have concentrated on 2-dimensional (2-D) modeling. One major issue pertaining to the numerical modeling of biaxial tests is the boundary conditions. It is required that the specimen is able to develop localized strains in the direction of the minor principal stress, which means that the boundaries have to be flexible. Otherwise, it is difficult for shear bands to initialize in the numerical simulations. To date some researchers have solved this issue using one of several approaches: (1) rigid walls (Rothenburg and Bathurst, 1992; Kuhn, 1999; Claquin et al., 2003); (2) boundary particles with applied force (Thomas and Bray, 1999; O'Sullivan et al., 2002); (3) a string of particles that are force-controlled (Tannant and Wang, 2002); and (4) a string of particles that are velocity-controlled (Evans and Frost, 2010). Although 2-D DEM simulations yield good results, they do ignore the influence of the intermediate principal stress. As the result, 3-D DEM potentially provides a superior solution.

In the same manner as for the 2-D simulations, the flexible membranes should be modeled properly in the 3-D DEM simulations of biaxial shear tests. However, creating flexible membranes is even more complex in 3-D DEM than in 2-D DEM, as the degrees of freedom of a rigid body increases from 3 in 2-D space to 6 in 3-D space. Some researchers have tried different approaches to simulating flexible membranes, including using a layer of stress-controlled particles (Powrie, et al., 2005), direct application of pre-defined forces to the boundary particles (Cheung and O'Sullivan, 2008), and utilizing stacks of velocity-controlled rigid walls (Zhao and Evans, 2009). The first approach only allows the membrane particles to move in the direction of the minor principal stress but restrains their movements normal to the rigid side plates. Therefore, deformation of the specimen is limited. The second approach requires frequent updates of the boundary particles and applied forces since the particles that emerge at the boundary keep changing when the soil specimen deforms. As a result, it is difficult to independently control the material properties of the boundary particles. The last approach creates flexible membranes by using stacks of rigid walls that only have 3 degrees of freedom in 3-D space, and thus the membranes can only be called semi-flexible. In the current study, a different approach was applied to simulate the flexible membranes, which enable the shear band to initialize and develop in 3-D space.

The 3-D DEM code used to model the biaxial tests is PFC3D, which was introduced in Section 4.1.

6.2. DEM Modeling of Biaxial Tests

A series of laboratory biaxial tests were performed on Ottawa 20-30 sand by Evans (2005) and have been summarized in Section 3.3. Two tests, BT-2030-13 (slightly dilatant) and BT-2030-16 (highly dilatant), were chosen for numerical simulation.

6.2.1. Modeling Algorithm

The numerical biaxial tests consisted of five stages: (1) sample preparation; (2) clump creation; (3) consolidation; (4) membrane replacement; and (5) sample shearing. The numerical model was built in a 3-D coordinate system, in which specimen width was parallel to the x-axis, specimen length parallel to the y-axis, and specimen height parallel to the z-axis (Figure 6.1).

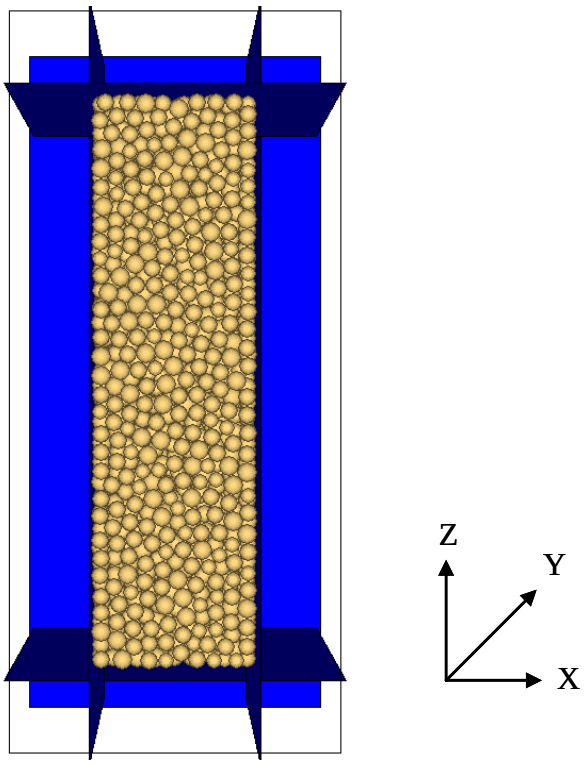

Figure 6.1 Preliminary setup for numerical biaxial tests

The first stage, sample preparation, set up the preliminary frame for the numerical experiments. In order to match the physical tests, a specimen compartment of 140 mm x 80 mm x 40 mm was created by six rigid planar walls (Figure 6.1). The six planar walls were designated as the bottom, top, back, front, left, and right walls according to their relative locations. The bottom and top walls were parallel to the X-Y plane, the back and front walls were parallel to the X-Z plane, and the left and right walls were parallel to the

Y-Z plane. All of the six walls were assigned with a high stiffness value of 1 x 10^8 N/m. Particles were generated inside the compartment according to the desired initial void ratio of 0.600 for slightly dilatant (SD) and 0.560 for highly dilatant (HD) specimens, exactly the same as their physical counterparts. Although the physical biaxial specimens were prepared by a hand pluviator, both air pluviation (AP) and moist tamping (MT) were used to prepare the numerical specimens to investigate how the initial specimen fabric would affect both the global and mircostructural behaviors. When preparing the numerical specimens by moist tamping, the following assumptions were made: (1) the specimen was generated by 7 layers; (2) the relative density of the middle layer (the 4th layer) equaled to the global density; (3) each layer was divided into 3 sub-layers to account for relative density variation within the layer; and (4) for every 3 sub-layers, the bottom one was the loosest and the top one was the densest. This approach was selected to reflect the findings presented by Frost and Park (2003) for physical specimens. The assumed distribution of relative density along the specimen is show in Figure 6.2. To maintain a dense state for the shearing stage, the inter-particle friction was set to zero until stage (4) of the numerical test sequence.

The second stage, clump creation, was the same as stage (2) of the numerical triaxial tests. At this stage, every single sphere was replaced with an arbitrarily oriented two-sphere clump, while keeping the volume, centroidal position and material properties unchanged. The two-sphere clump was set as unbreakable and composed of two identical spheres with the aspect ratio of 1.5:1. After all the replacements were completed, the assigned initial void ratio of the specimen was still maintained.

The third stage was to isotropically consolidate the sample under the designated confining pressure, 137.8 kPa for the slightly dilatant specimen and 68.9 kPa for the highly dilatant specimen. In order to reach the isotropic loading state, a servo-mechanism was applied to the bottom, top, left and right walls so that the wall velocities were adjusted within each calculation cycle to reduce the differences between the measured

and required stresses on the walls. It should be noted that the back and front walls were kept still throughout all five stages.

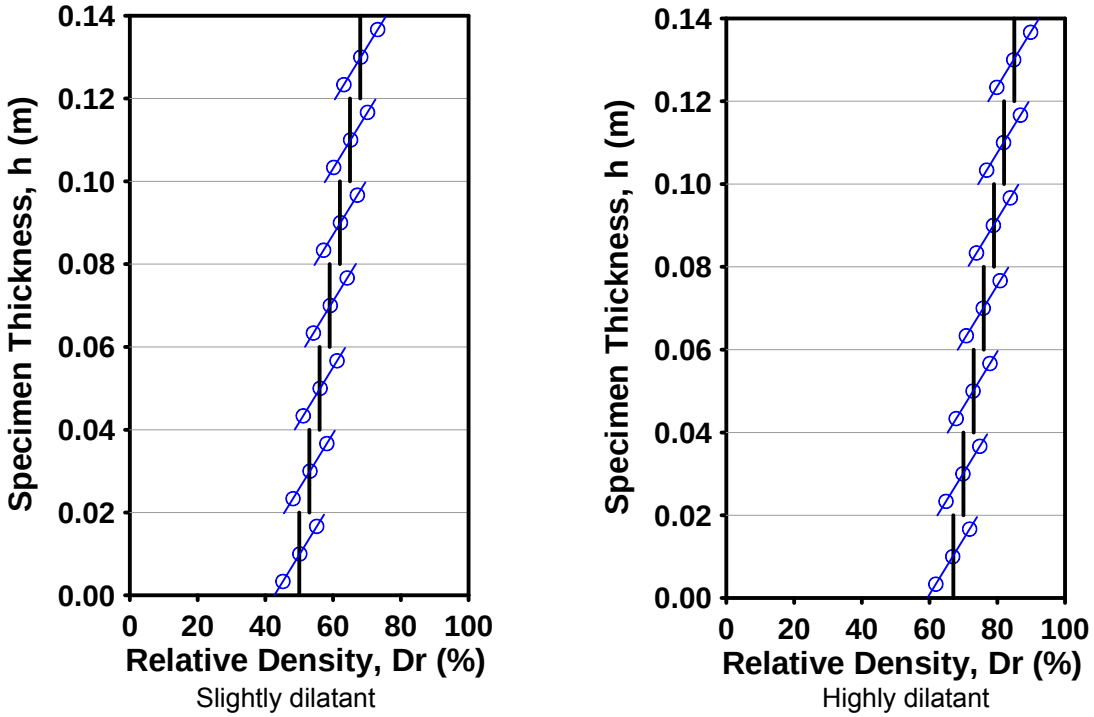

Figure 6.2 Assumed relative density for moist tamping

The fourth stage was to replace the left and right rigid walls with flexible membranes. In physical biaxial test, the specimen is typically bounded by a flexible latex membrane which can be stretched or contracted as specimen volume changes. Evans and Frost (2010) simulated the flexible membrane in 2D modeling using a string of velocity-controlled bonded particles, and the membrane endpoints (top and bottom) were closely monitored so that particles would be added or removed if the membrane was too short or too long. However, this approach is difficult to apply in 3D modeling, as the degree of freedom of membrane particles is 6 in 3D space while only 3 in 2D space. Consequently, an improved version of the algorithm was implemented in the current study. The flexible membrane was modeled by a sheet of simply-packed single spheres (Figure 6.3). The particle size used for the entire membrane was uniform and less than 2.4 times the

minimum specimen particle size in the short axis to prevent any particles from passing through the membrane. Approximately 11,000 particles were needed for two membranes (left-side and right-side). Some requirements should be fulfilled to ensure that the sheet of particles deflects and functions like a flexible membrane: (1) each membrane particle can undergo independent translational and rotational displacements relative to its neighboring membrane particles; and (2) the translational and rotational displacements of each membrane particle should be related to its neighboring membrane particles. PFC3D provides two standard approaches to bond particles, one is contact bond and the other is parallel bond. As indicated by Itasca (2008), the contact bond can transmit only a force, while the parallel bond can transmit both a force and a moment. Considering the possible relative displacements between the membrane particles, contact bonds were assigned. To prevent the contact bonds from breaking when the contact forces exceed the contact bond strengths, both the normal and shear contact bond strengths were set to be 1×10^{10} N/m. A servo-mechanism was required here to maintain a constant confining pressure on the simulated membrane. Since the simulated membranes were composed of almost 11,000 particles, it is unrealistic to implement any of the aforementioned servo-mechanisms. A new servo-mechanism was devised here to fulfill the function. For a typical membrane particle, two types of forces will act on it – contact force and applied force (Figure 6.4). The contact force results from the interaction between a membrane particle and a specimen particle, and it is computed by the DEM code. As the contact force was needed for later calculation of the minor principal stress, the algorithm illustrated in Figure 6.5 was implemented to record the contact force on each membrane particle. The applied force is the result of the confining pressure acting on a membrane particle. When the specimen deforms, both the specimen dimension and the number of membrane particles in contact with the specimen particles keep changing. The servo-mechanism retrieves the information on specimen deformation and membrane deformation and adjusts the applied force on each membrane particle within each calculation cycle. Consequently, how much

each membrane particle moves depends on the summation of the two forces and the particle stiffness. It should be noted here that what the servo-mechanism controls is the force and displacement in X-direction. Forces and displacements in other directions are dependent on the interactions between the membrane particles and specimen particles. To ensure that the membranes could freely stretch while still confining the specimen particles, they were constructed 40 mm longer than the specimen length and 40 mm longer than the specimen height and bounded by 16 walls at the ends (Figure 6.6). During this numerical stage, the bottom, top, back, and front walls were reduced in size to match the actual specimen size. After the left and right rigid walls were replaced by the left and right flexible membranes, inter-particle friction was assigned to the specimen particles and the specimen was consolidated again to reach the isotropic stress state. The modeling results proved that the algorithm introduced here is capable of creating a flexible membrane that enables localized strains (Figure 6.7).

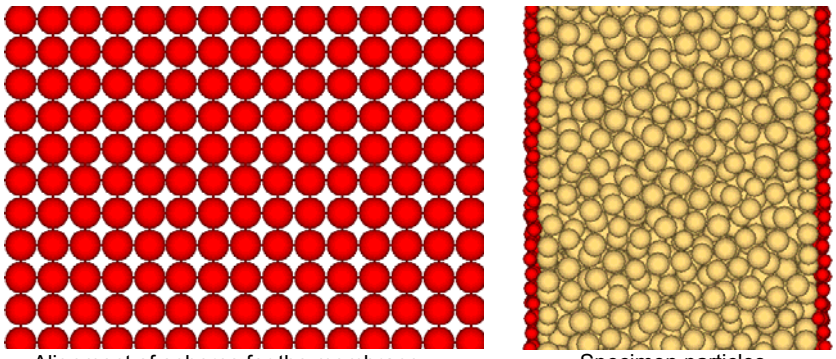

Figure 6.3 Structure of a flexible membrane

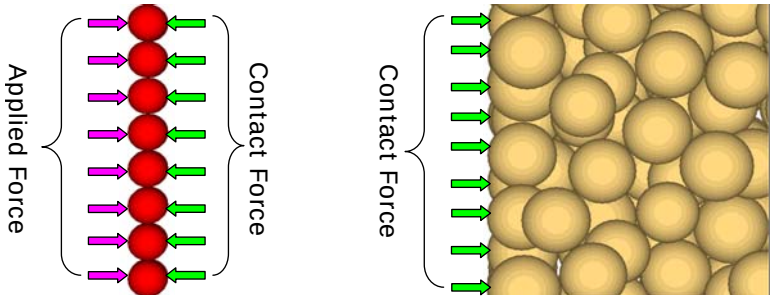

Figure 6.4 Forces acting on the membrane particles

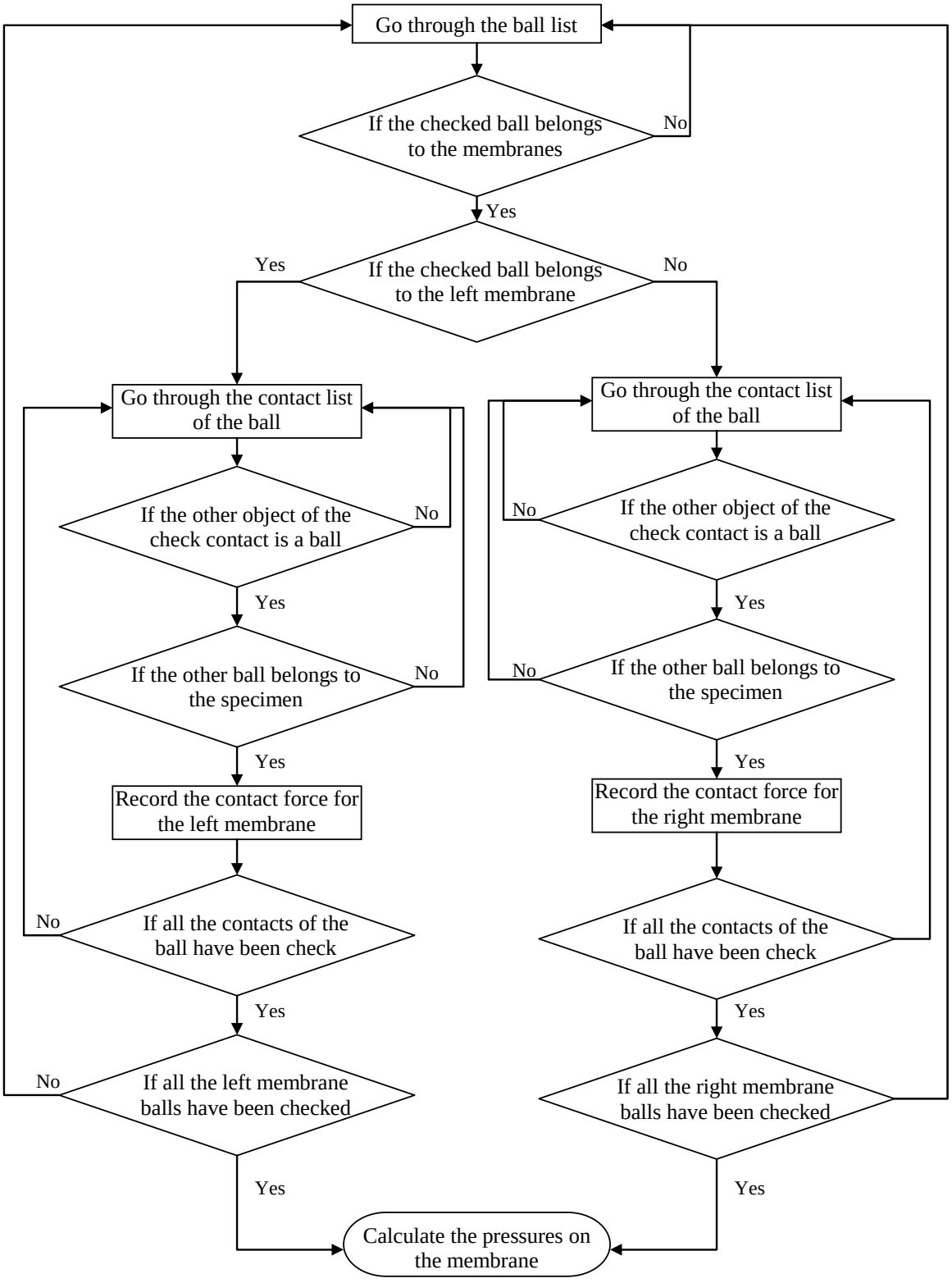

Figure 6.5 Flowchart indicating the steps to record the contact force of the membrane particles

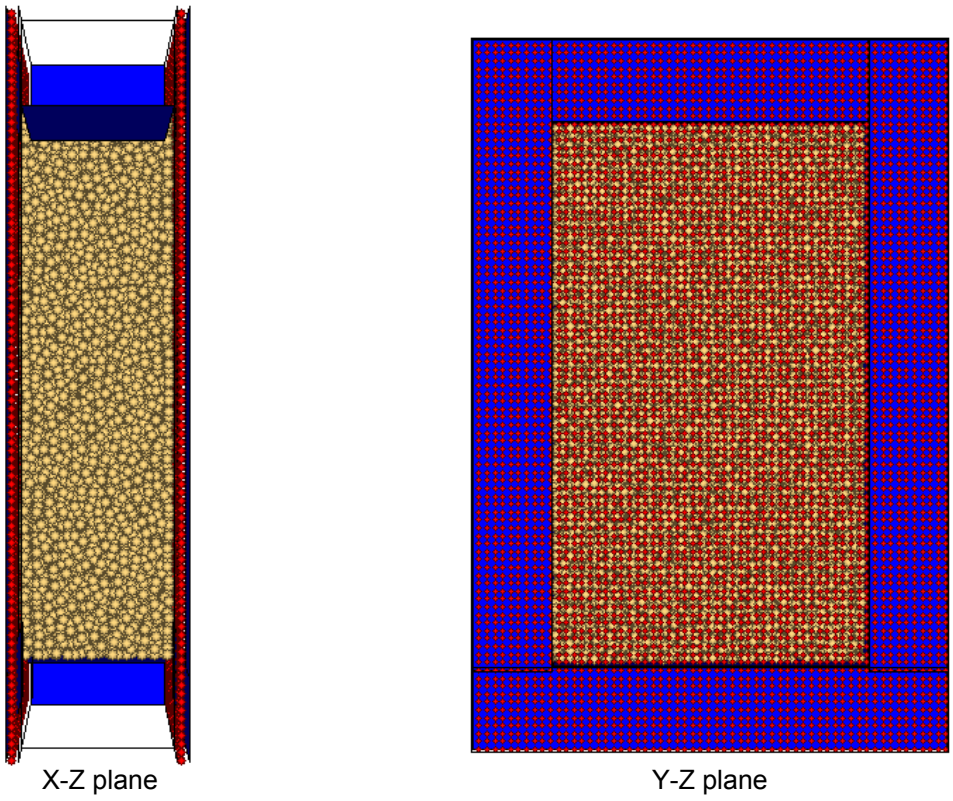

Figure 6.6 Flexible membranes bounded by rigid walls at the boundaries

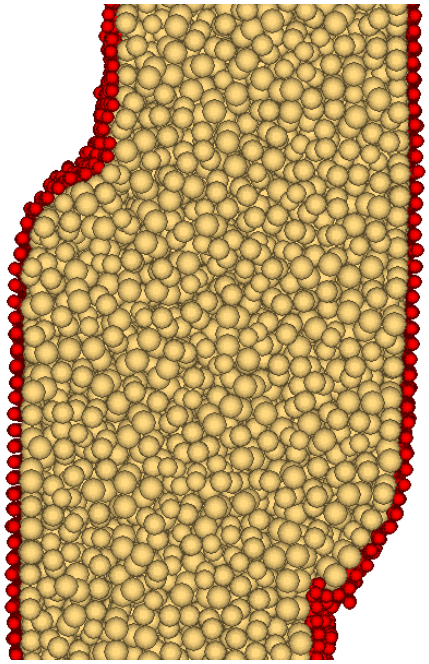

Figure 6.7 Deformed specimen confined by the flexible membranes

The last stage was to shear the specimen to failure. For the numerical biaxial test, it took longer to complete all the testing stages than a numerical triaxial test due to the fact that more particles were involved in the modeling particularly in modeling the membranes.

6.2.2 Material Properties

For the numerical modeling of biaxial tests, material properties of the membrane particles were set independently from the specimen particles. Therefore, material properties are introduced separately for these two types of particles.

When choosing material properties for the specimen particles, such as normal and shear stiffness of the particles and particle friction coefficient, the equations introduced in Section 4.2.2 still apply since both the triaxial and biaxial experimental tests used Ottawa sand. However, the normal stiffness (k_n), the shear stiffness (k_s), and the friction coefficient (μ) used in the modeling were adjusted from the calculated values to fit the stress-strain responses of the physical biaxial shear tests based on a parametric study presented in Section 6.3. Since the Ottawa sands tested by the biaxial device were larger in the median particle size than those tested by the triaxial device, the particle size and size distribution for the numerical biaxial tests differed from that used in the numerical triaxial tests. Again, it was assumed the particle size conformed to a uniform distribution of which the range was determined based on the grain size distribution curve of Ottawa 20-30 sands in Figure 3.7. In the end, the size range of 0.67 mm to 0.81 mm were chosen because: (1) the median particle size was exactly the same as 0.74 mm; and (2) 90% of the sand grains by weight were finer than 0.81 mm while 15% was finer than 0.67 mm. Considering the dimensions of the numerical biaxial specimen, particle size between 0.67 and 0.81 mm means that more than 1,000,000 particles should be generated to fill up the specimen compartment. This would cause the modeling to be computationally expensive.

Thus, the particle size was scaled 5 times to reduce the number of particles generated. The final particle size along with other model parameters is listed in Tables 6.1 and 6.2.

Table 6.1 Model properties of the numerical biaxial tests for stage (1)

Parameters	Experimental		Numerical	
	SD	HD	SD	HD
Specimen Height (mm)	140	140	140	140
Specimen Length (mm)	80	80	80	80
Specimen Width (mm)	40	40	40	40
Confining Pressure (kPa)	137.8	68.9	137.8	68.9
Particle Size Range (mm)	-	-	3.35~4.05	3.35~4.05
Mean Particle Size (mm)	0.74	0.74	3.70	3.70
Initial Void Ratio	0.600	0.560	0.600	0.560
Particle Normal Stiffness, k_n (N/m)	-	-	4×10^5	5×10^5
Particle Shear Stiffness, k_s (N/m)	-	-	5×10^4	5×10^4
Particle Friction Coefficient	-	-	0.23	0.25
Specific Gravity	2.65	2.65	2.65	2.65
Platen Stiffness (N/m)	-	-	1×10^8	1×10^8
Membrane Stiffness (N/m)	-	-	5×10^4	1.5×10^4
Number of Particles	-	-	10557 (AP)	10827 (AP)

Table 6.2 Model properties of the numerical biaxial tests for stage (2)

Parameters	Experimental		Numerical	
	SD	HD	SD	HD
Aspect Ratio of Clumps	-	-	1.5:1	1.5:1
Mean Particle Size in Long Axis (mm)	0.74	0.74	4.65	4.65
Mean Particle Size in Short Axis (mm)	-	-	3.10	3.10
Initial Void Ratio	0.600	0.560	0.600	0.560
Particle Normal Stiffness, k_n (N/m)	-	-	4×10^5	2×10^5
Particle Shear Stiffness, k_s (N/m)	-	-	5×10^4	5×10^4
Particle Friction Coefficient	-	-	0.23	0.25
Specific Gravity	2.65	2.65	2.65	2.65
Number of Spheres	-	-	21114 (AP)	21654 (AP) 21678 (MT)
Number of Clumps	-	-	10557 (AP)	10827 (AP) 10839 (MT)

The membrane particles were essentially single spheres of uniform size. The only requirement on its particle size was that it should be less than 2.4 times the minimum specimen particle size in the short axis. Therefore, the particle size was set as 2 mm. In reality, the specimen membranes are made of latex rubber and very light in weight. Accordingly, the specific gravity of membrane particles was set as 1.0. The normal stiffness, k_n, decides how much a particle moves subjected to the normal forces. As a flexible membrane was desirable here, k_n of the membrane particles should not exceed that of the specimen particles. The shear stiffness, k_s, was set as zero. The friction coefficient of membrane particles was the same as the specimen particles. The normal contact bond strength and shear contact bond strength were assigned values of 1×10^{10} N/m to prevent contact bonds from breaking. The material properties of membrane particles are listed in Table 6.3.

Table 6.3 Material properties of membrane particles

Parameters	SD	HD
Particle Size (mm)	2.0	2.0
Particle Normal Stiffness, k_n (N/m)	5×10^4	1.5×10^4
Particle Shear Stiffness, k_s (N/m)	-	-
Particle Friction Coefficient	0.23	0.25
Normal Contact Bond Strength (N/m)	1×10^{10}	1×10^{10}
Shear Contact Bond Strength (N/m)	1×10^{10}	1×10^{10}
Specific Gravity	1.00	1.00
Number of Particles	10800	10800

6.3. Parametric Study of the Numerical Model

A comprehensive parametric study was performed to investigate the effects on the modeling results from some of the model parameters. The studied parameters can be categorized into two groups. One group of parameters are those relating to the specimen particles and include normal stiffness, k_n, shear stiffness, k_s, and friction coefficient, μ,

while another group of parameters are those relating to the membrane particles and include normal stiffness, k_n, and membrane particle size. The parametric study was carried out using a highly dilatant specimen prepared with moist tamping and assigned with the following parameters: k_n of the specimen particles of 5 x 10^5 N/m, k_s of the specimen particles of 5 x 10^4 N/m, μ of 0.25, k_n of the membrane particles of 1 x 10^5 N/m, and membrane particle size of 2.0 mm. For each set of investigations, one of the parameters was varied within a certain range while other parameters were kept as the original setting. Other than stress-strain response, effects of the parameters on volumetric strain, particle rotations and particle displacements were also examined.

6.3.1. Normal Stiffness of Specimen Particles

The normal stiffness of specimen particles was investigated using 5 x 10^4 N/m, 1 x 10^5 N/m, 5 x 10^5 N/m, and 5 x 10^6 N/m. As the shear stiffness was fixed as 5 x 10^4 N/m, the ratio of k_s/k_n equaled to 1, 1/2, 1/10, and 1/100.

The principal stresses and volumetric strain for different specimen particle normal stiffness values are plotted in Figure 6.8. For the major and intermediate principal stresses, it is expected that higher normal stiffness will result in larger initial modulus and strength. The modeling results shows the initial modulus did increase as the normal stiffness increased. However, it is interesting to find that when the largest k_n of 5 x 10^6 N/m was used, the peak major principal stress was less than the major principal stress when k_n of 5 x 10^5 N/m was used. One possible cause for this is that the k_s/k_n ratio for this case was 1/100. As mentioned in Section 4.2.2, there's no unanimous agreement on how to choose k_s to date, and many researchers have used the ratio of k_s over k_n between 1/10 to 1. In general, the residual stresses did not vary too much with normal stiffness. However, it is believed that when k_n decreased to a value like 5 x 10^4 N/m, the impact of normal stiffness on the residual stress can be substantial. For the volumetric strain, the

smaller the normal stiffness, the larger contraction the specimen experienced at the beginning of shearing.

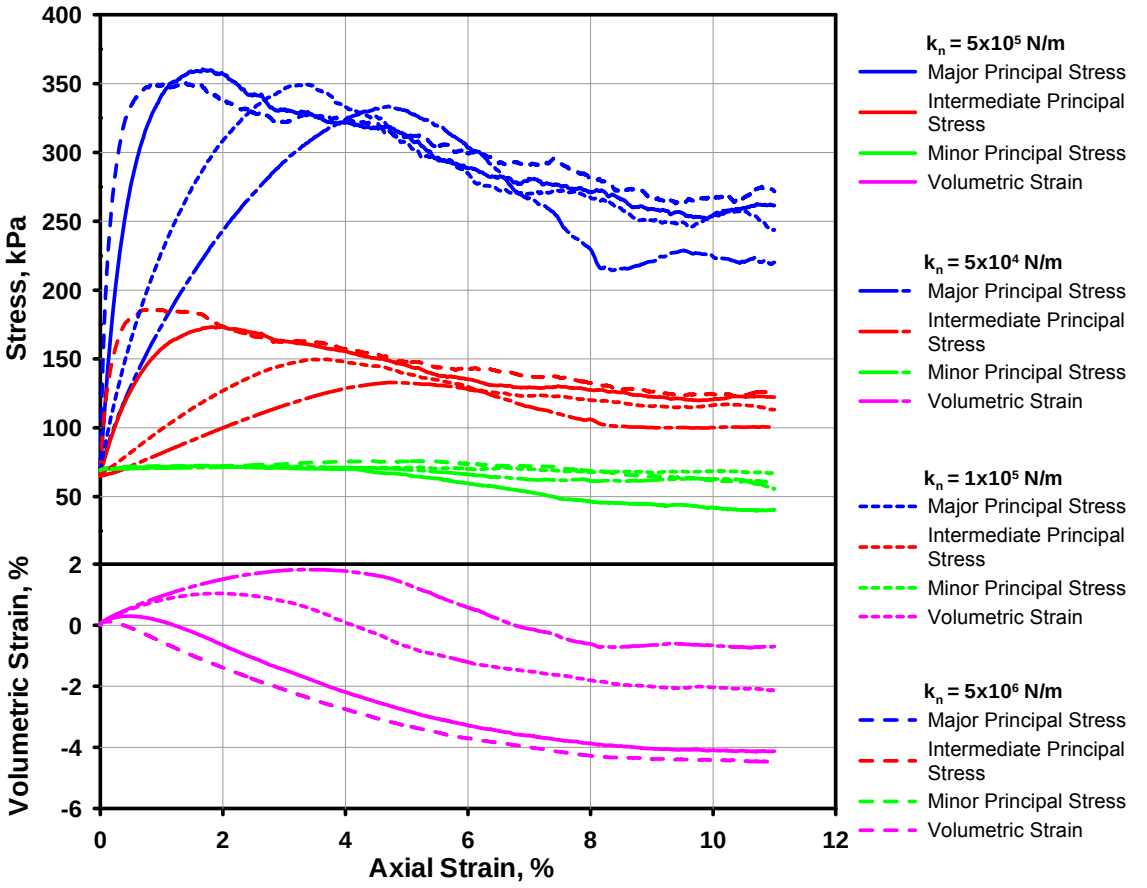

Figure 6.8 Stress-strain response and volumetric strain for different normal stiffness of specimen particles

For the case of the numerical biaxial test, the X-Z components and Y-Z components of particle rotations and displacements were distinctive due to the boundary conditions, and hence particle rotations and displacements were dissected and presented for the X-Z plane and the Y-Z respectively. It should be noted that all the particle rotation and displacement maps presented in this chapter do not include all the particles. Only the particles within the middle X-Z plane or Y-Z plane are presented. The particle rotations and displacements in the X-Z plane for different normal stiffness at 11% global axial

strain are plotted in Figure 6.9. When the normal stiffness increased, the following effects were noticed: (1) evidence of more than one shear band occurred although only one dominated in the end; and (2) the location of the dominant shear band moved up. Figure 6.10 presents the particle rotations and displacements in the Y-Z plane for different normal stiffness. It is interesting to find that the shear band tended to tilt in the Y-Z plane as k_n increased. This phenomenon may result from these factors coupled or not coupled: the normal stiffness of the membrane particles, k_s/k_n ratio of the specimen particles, and specimen fabric (the parametric study was carried out on a numerical specimen prepared by moist-tamping).

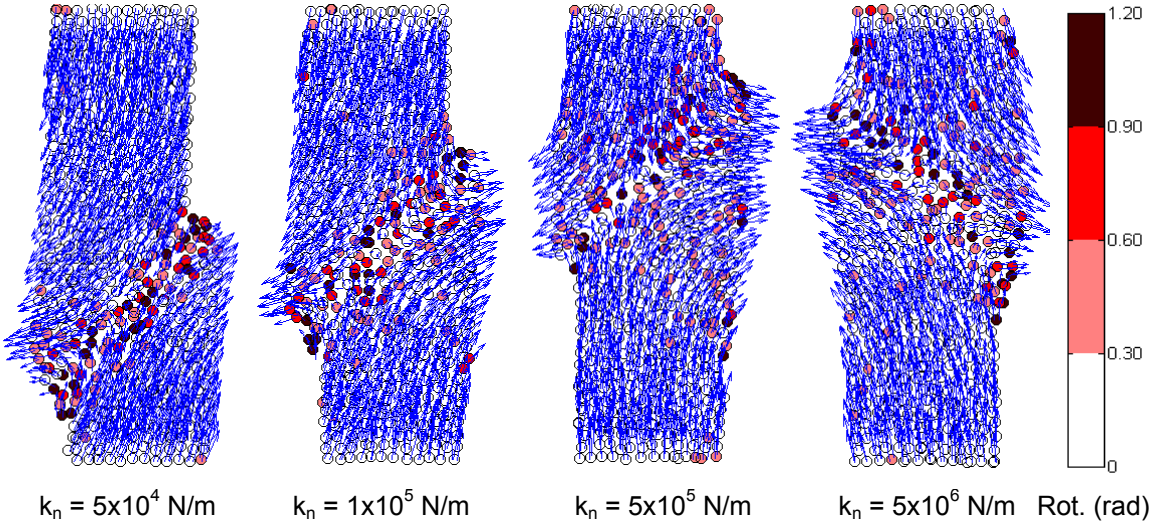

Figure 6.9 Particle rotations and displacements in X-Z plane for different normal stiffness of specimen particles

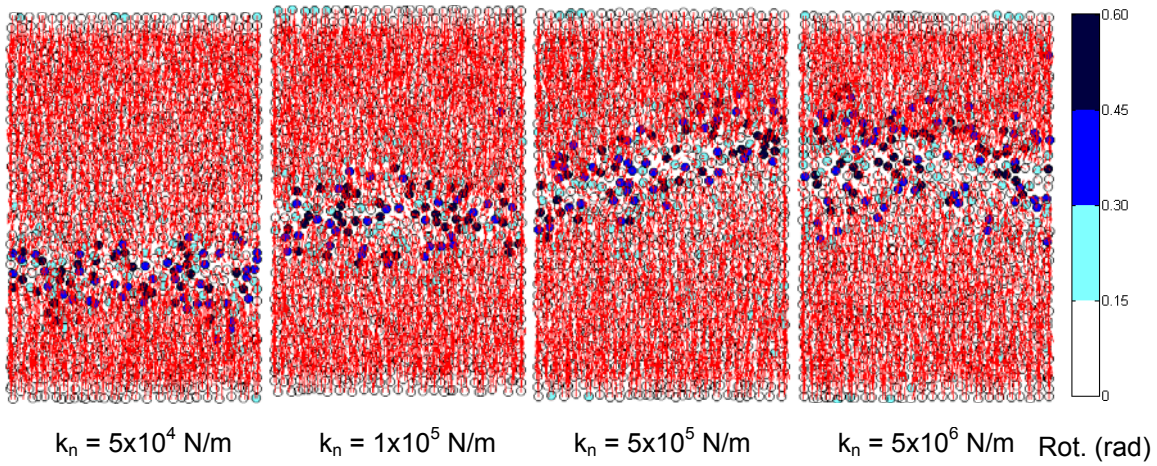

Figure 6.10 Particle rotations and displacements in Y-Z plane for different normal stiffness of specimen particles

6.3.2. Shear Stiffness of Specimen Particles

To look at the effect of the shear stiffness of the specimen particles, values of 5 x 10^3 N/m, 5 x 10^4 N/m, and 5 x 10^5 N/m were assigned to k_s while keeping k_n as 5 x 10^5 N/m. Consequently, the ratio of k_s/k_n was 1/100, 1/10 and 1 in this set of investigations.

The stress and volumetric strain of the modeling results are presented in Figure 6.11. When k_s changed from 5 x 10^4 N/m to 5 x 10^5 N/m, the initial modulus, peak stress, peak strain, and residual stress did not differ too much. However, if k_s was decreased to 5 x 10^3 N/m, the modeling results were substantially affected, especially the initial modulus and peak stress. In general, it shows that higher shear stiffness hardly stiffened the sample stress-strain behavior, whereas lower shear stiffness was capable of greatly softening the stress-strain behavior. If compared with normal stiffness, shear stiffness played a less significant role in the stress-strain behavior, especially the intermediate principal stress. For the volumetric strain, initial volumetric contraction was not affected by k_s but volumetric dilation was.

The particle rotations and displacements due to different shear stiffness at 11% global axial strain are shown in Figure 6.12 for the X-Z plane and in Figure 6.13 for the Y-Z plane. Unlike the normal stiffness, different shear stiffness always caused the

dominant shear band to occur in the upper portion of the specimen. Other than the particles inside the shear band, some particles outside the shear band also experienced substantial particle rotations, which implies that a secondary dominant band might occur. No matter what shear stiffness was used, the shear band tilted in the Y-Z plane. It is possible that the normal stiffness and the specimen fabric play more important roles in the shear band inclination in the Y-Z plane than the shear stiffness.

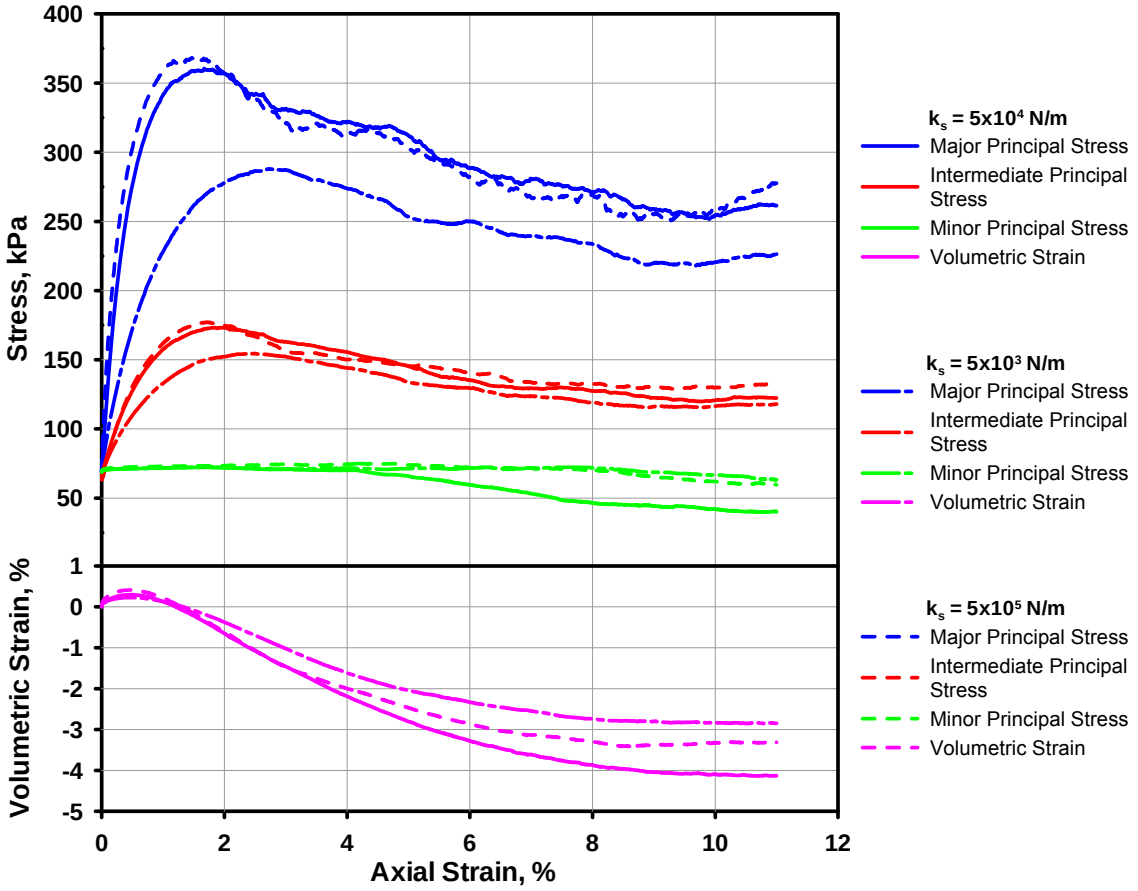

Figure 6.11 Stress-strain response and volumetric strain for different shear stiffness of specimen particles

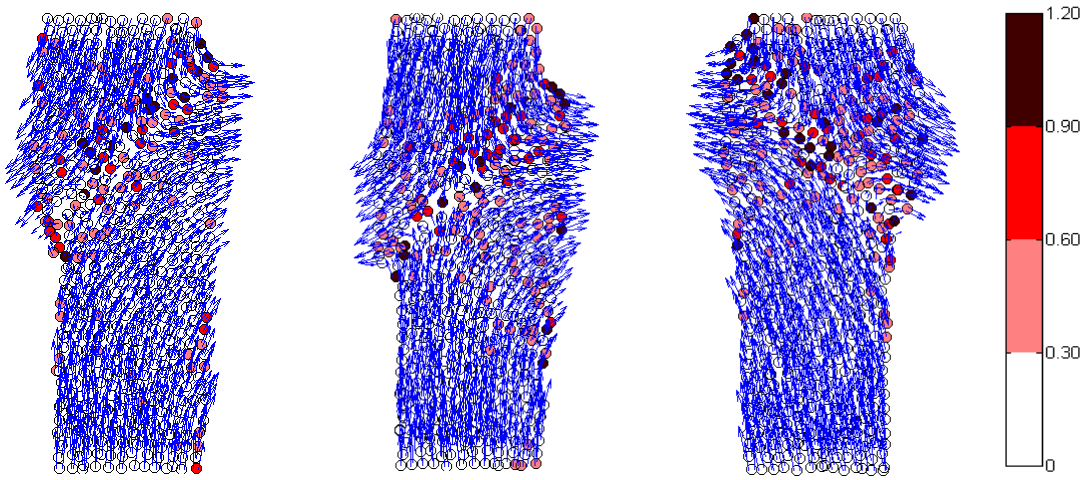

Figure 6.12 Particle rotations and displacements in X-Z plane for different shear stiffness of specimen particles

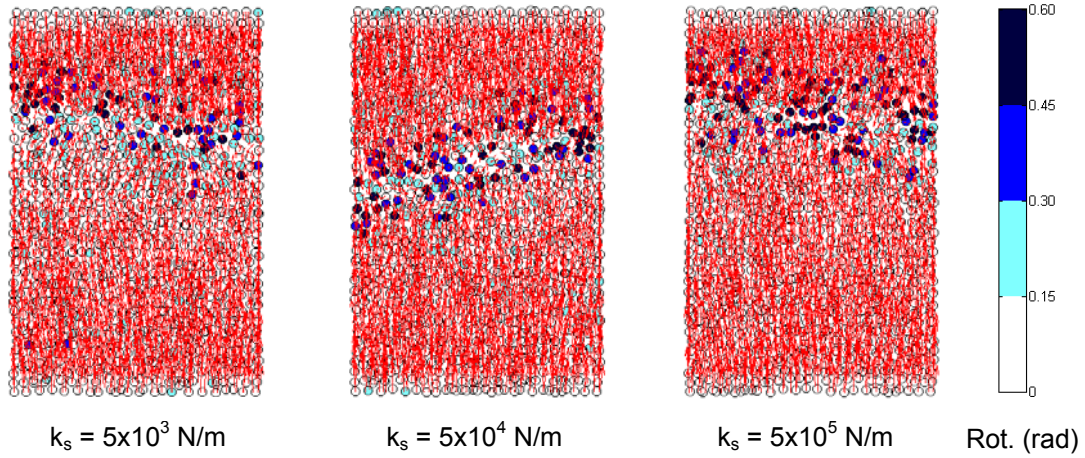

Figure 6.13 Particle rotations and displacements in Y-Z plane for different shear stiffness of specimen particles

6.3.3. Friction Coefficient of Specimen Particles

The friction coefficient was assigned with values of 0.23, 0.25 and 0.27 to see its effect. Figure 6.14 presents the stress-strain and volumetric strain curves for different friction coefficients. Most of the index strength parameters were not affected by the friction coefficient except for the peak and residual major principal stresses. Larger μ

resulted in not only larger major principal stress but also larger volumetric dilation as expected.

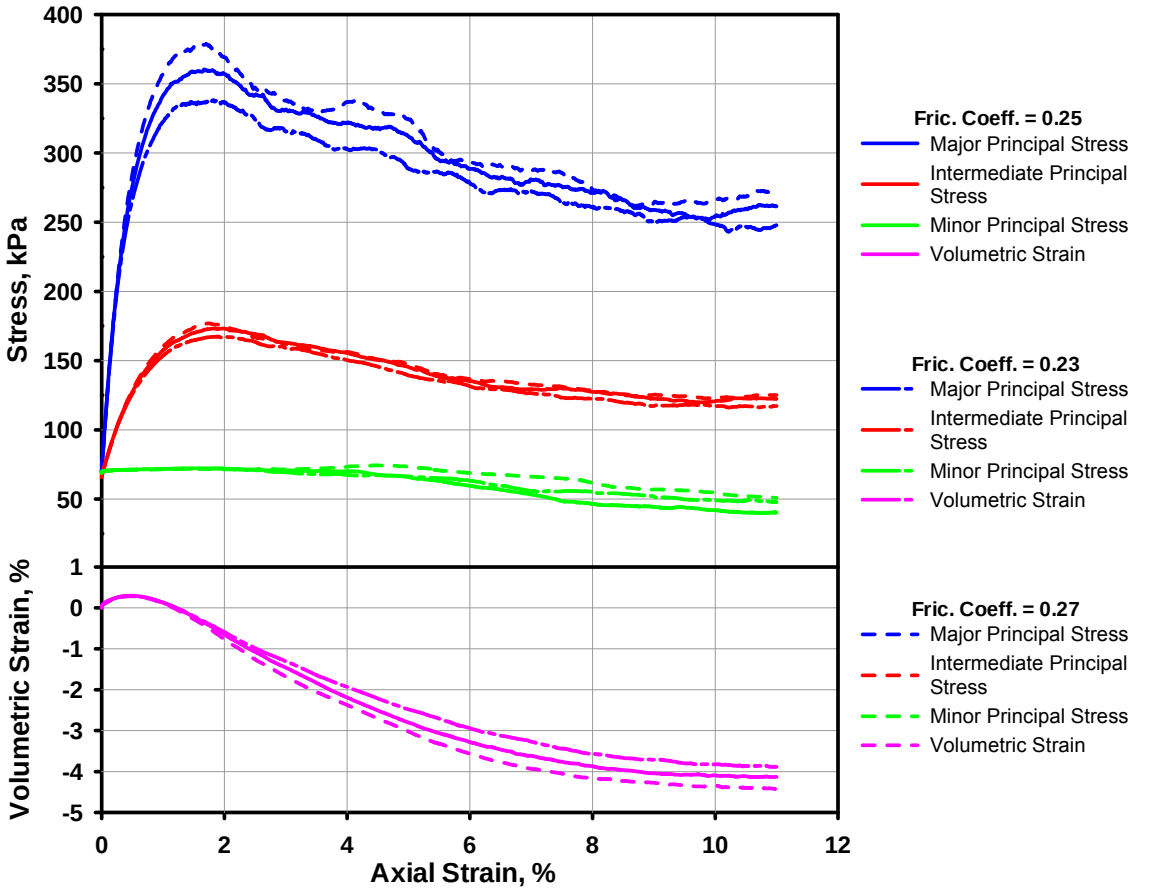

Figure 6.14 Stress-strain response and volumetric strain for different friction coefficients of specimen particles

The particle rotations and displacements in X-Z plane and Y-Z plane at 11% global axial strain are plotted in Figures 6.15 and 6.16. One interesting thing to note is that at least two dominant shear bands orthogonal to each other can be clearly discerned for these three numerical specimens, but the dual shear bands tended to be more symmetrical when the friction coefficient increased. The shear band tilted in the Y-Z plane for the three friction coefficients used.

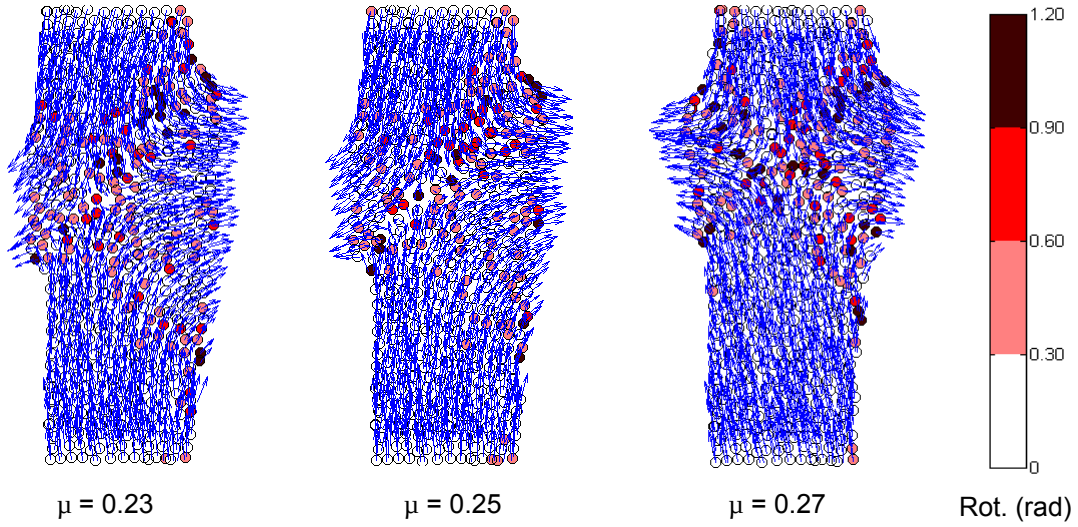

Figure 6.15 Particle rotations and displacements in X-Z plane for different friction coefficients of specimen particles

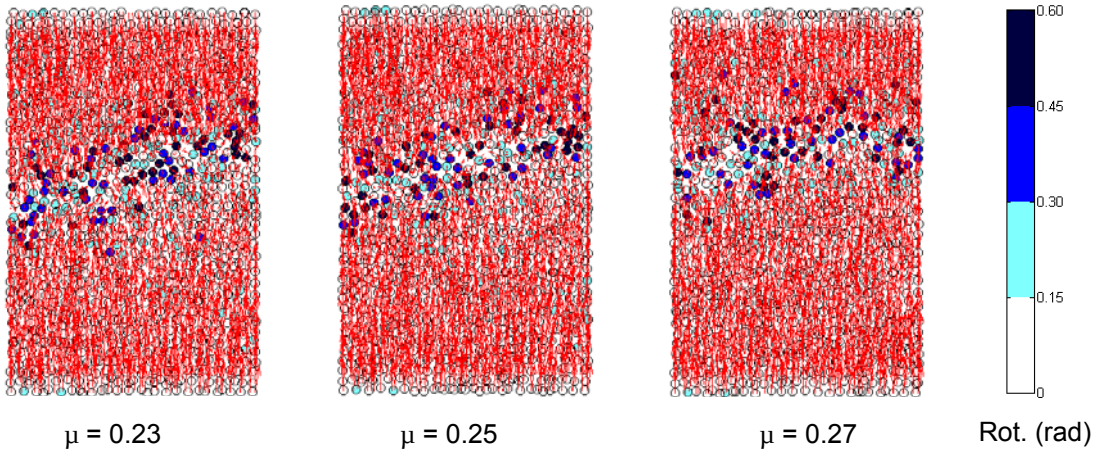

Figure 6.16 Particle rotations and displacements in Y-Z plane for different friction coefficients of specimen particles

6.3.4. Normal Stiffness of Membrane Particles

The effect of the normal stiffness of the membrane particles was studied using k_n of 1 x 10^4 N/m, 1 x 10^5 N/m, and 1 x 10^6 N/m, which yields values of the ratio between the normal stiffness of membrane particles to the shear stiffness of specimen particles of 1/50, 1/5, and 2.

Prior to this parametric study, it was expected that the specimen would exhibit stiffer behavior if it was bounded by a stiffer membrane. The stress-strain response in Figure 6.17 confirmed this expectation. Overall, the membrane stiffness did not affect specimen strength in the stress-hardening stage, but it greatly affected the stress-softening stage, especially at large strains. The parametric study on the membrane stiffness implies that a large percentage of the residual strength in biaxial shear tests might be provided by the membrane.

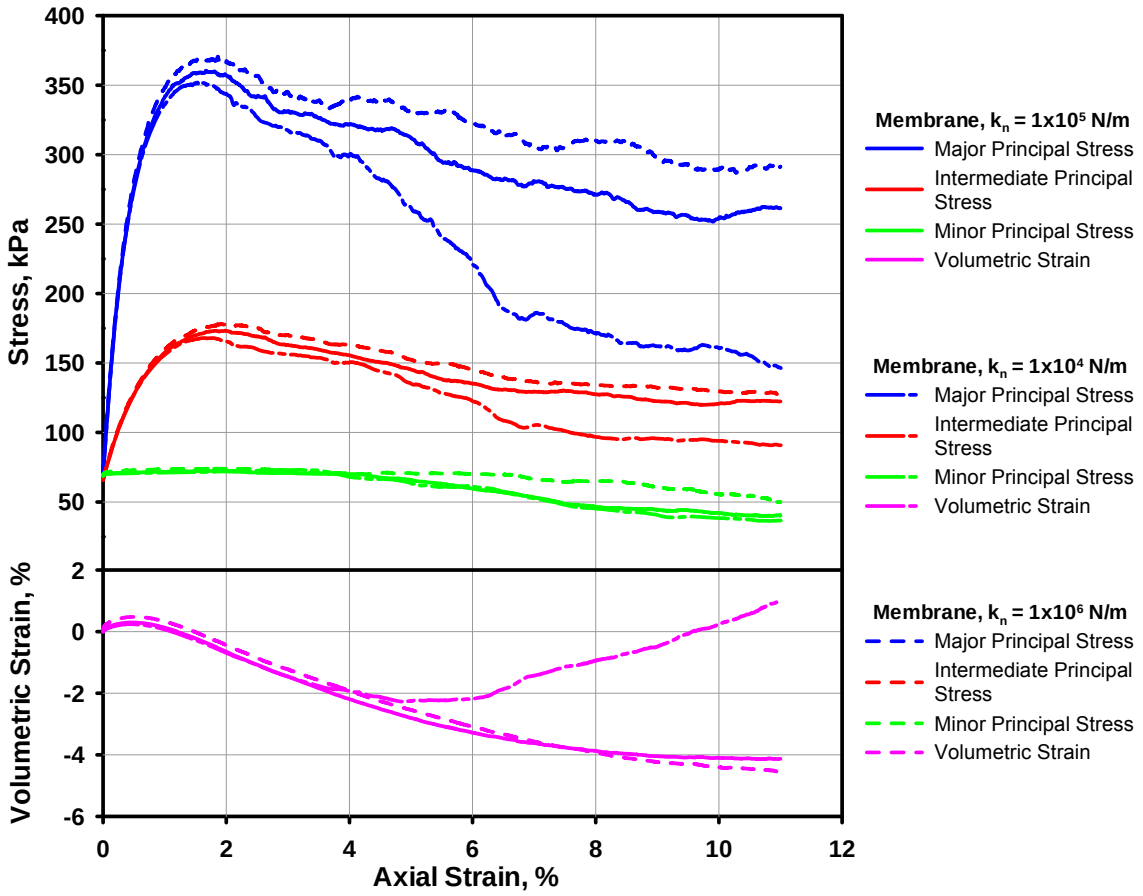

Figure 6.17 Axial stress and volumetric strain for different normal stiffness of membrane particles

The particle rotations and displacements at 11% global axial strain are presented in Figures 6.18 and 6.19. Comparing the rotation and displacement maps for different

membrane stiffness, it is found that the most flexible membrane did a better job than other two in allowing the shear band to develop. When the very flexible membranes with k_n = 1 x 10^4 N/m were used, the particles within each shear block moved consistently towards one direction and the relative translational movements between the two shear blocks could be clearly defined. This shearing pattern is very close to what is observed in the experimental biaxial tests, although the bottom platen was not sliding in the numerical tests to facilitate the development of the shear band. For the other two cases, although the shear blocks still formed, their ends were confined by the membranes and the relative movements between the shear blocks could hardly be distinguished. When the very stiff membrane with k_n = 1 x 10^6 N/m was used, two primary shear bands and three shear blocks formed, which represents a more rigid failure behavior.

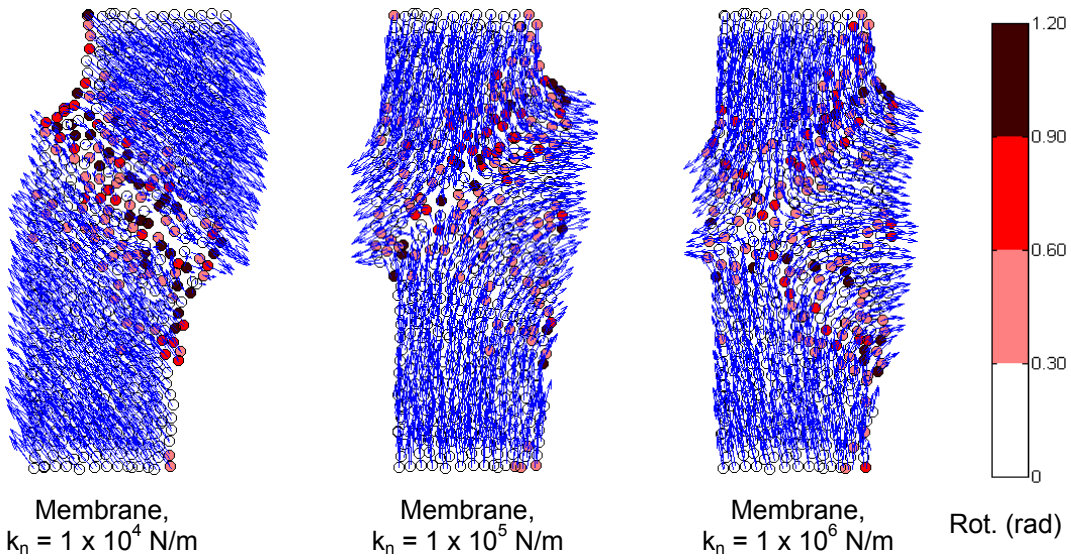

Figure 6.18 Particle rotations and displacements in X-Z plane for different normal stiffness of membrane particles

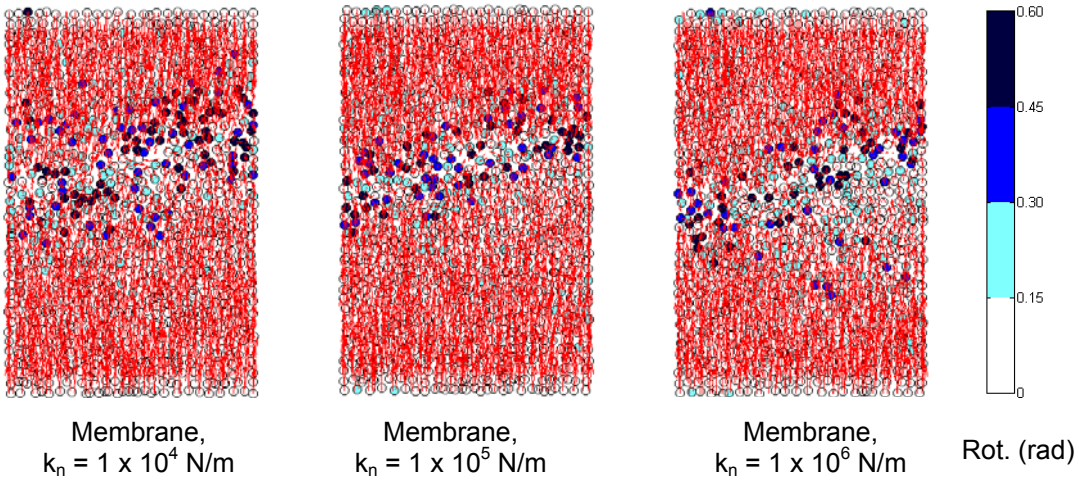

Figure 6.19 Particle rotations and displacements in Y-Z plane for different normal stiffness of membrane particles

6.3.5. Membrane Particle Size

As introduced in Section 6.2.1, the membrane was composed of simply-packed single spheres. To prevent any specimen particles from going through the membrane, the size of membrane particles cannot exceed 2.4 times the minimum specimen particle size in short axis. Other than holding specimen particles together, the membrane particles also acted as the media through which the confining pressure was applied to the specimen particles. As spheres transferred forces via point contacts, the smaller the membrane particle size, the more uniform the confining force distributes on the specimens. In this set of parametric investigations, two membrane particle sizes were used, which were 2.0 mm and 3.0 mm. Both sizes met the basic requirements for membrane particle size.

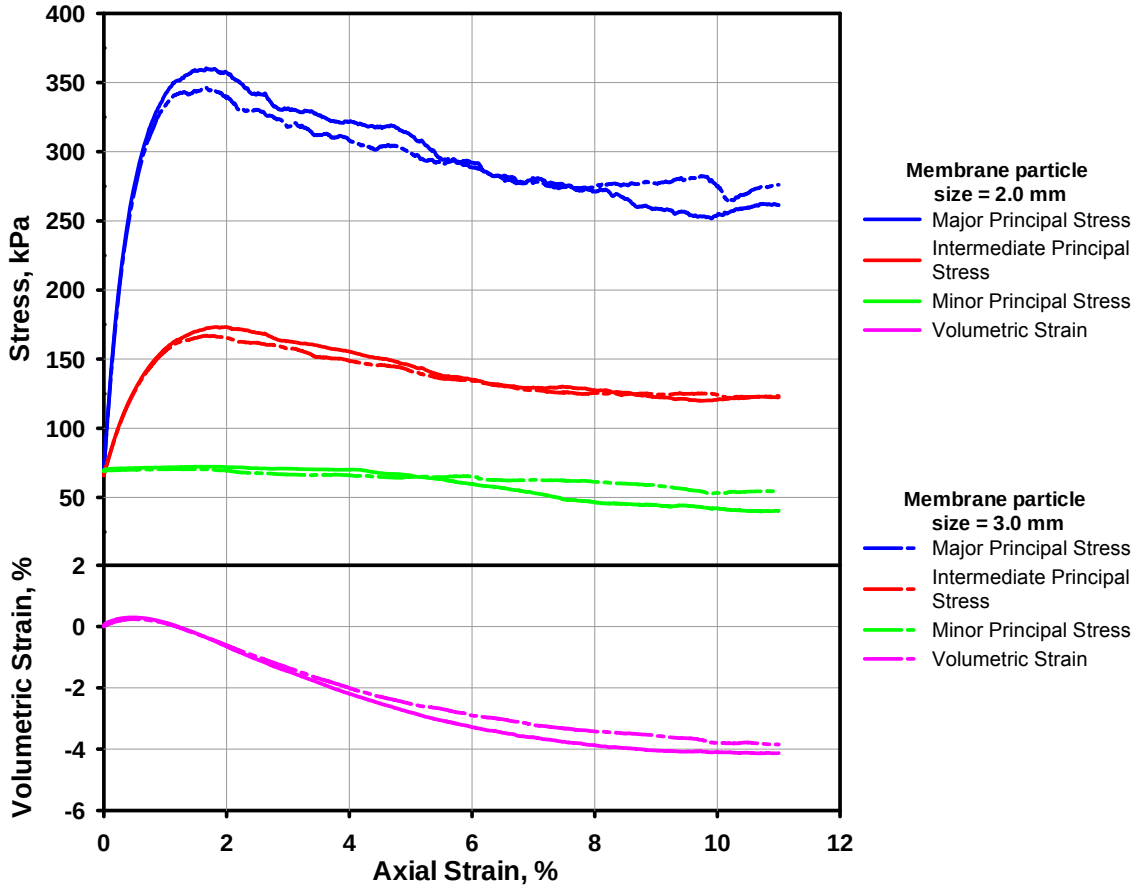

Figure 6.20 Stress-strain response and volumetric strain for different membrane particle sizes

Figure 6.20 presents the stress-strain response for different membrane particle sizes. The smaller size resulted in higher strength around peak and post-peak, nevertheless, the situation was reversed for the residual strength. The membrane particle size did not impose significant effect on the volumetric strain. The specimen bounded with larger membrane particles dilated slightly more than the specimen bounded with smaller particles. From the particle rotations and displacements shown in Figures 6.21 and 6.22, it can be noticed that smaller membrane particle size applied a comparatively stiffer confinement to the specimen.

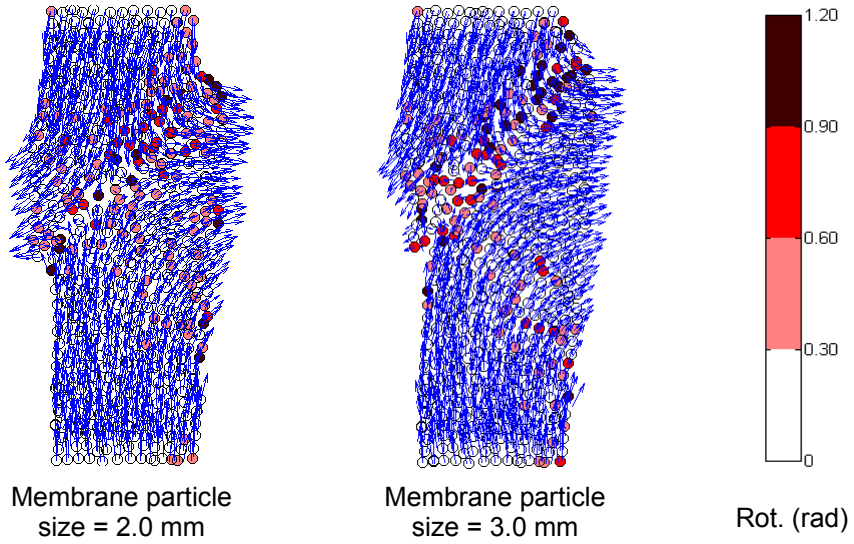

Figure 6.21 Particle rotations and displacements in X-Z plane for different membrane particle sizes

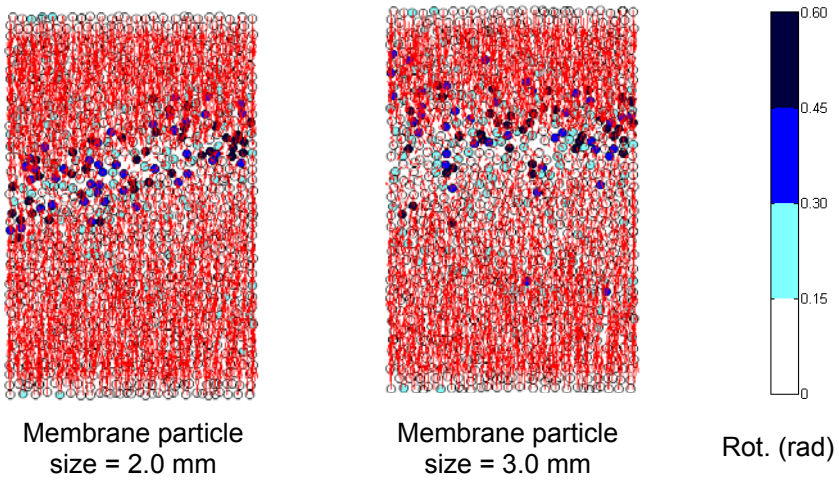

Figure 6.22 Particle rotations and displacements in Y-Z plane for different membrane particle sizes

6.4. DEM Simulation Results

Four numerical biaxial tests were performed to match the experimental biaxial tests. According to the initial void ratio, confining pressure, and the way the specimens were prepared, those numerical tests were designated as DEM_APSD, DEM_MTSD, DEM_APHD, and DEM_MTHD, representing air-pluviated slightly dilatant, moist-

tamped slightly dilatant, air-pluviated highly dilatant, and moist-tamped highly dilatant respectively. Model parameters of the numerical tests have been listed in Tables 6.1 to 6.3.

6.4.1. Stress-Strain Response

The modeling results for the slightly dilatant specimens along with experimental results are presented in Figure 6.23. The numerical preparation methods in this study created either a perfectly uniform specimen (air pluviation) or a strongly heterogeneous specimen (moist tamping). Although the physical specimen was prepared by a hand pluviator, its heterogeneity was likely somewhere between the air-pluviated and moist-tamped numerical specimens. Therefore, both DEM_APSD and DEM_MTSD were compared with the measured data. In general, the moist-tamped specimen displayed higher peak stress than the air-pluviated specimen, but their residual stresses converged at around 8% global axial strain. For the major principal stress, the DEM simulations did not show a good match with the experimental data. This is due to the way the physical specimens were prepared, consolidated and sheared during the experimental biaxial test. In the lab, the prismatic specimen was bounded by a latex rubber membrane and placed on the biaxial apparatus. Before it was sheared, the specimen was consolidated by the confining pressure which caused it to decrease in volume slightly and hence lose contact with the confining platens (parallel to X-Z plane). The gap between the specimen and the confining platens did not disappear until the specimen dilated in that direction during the shearing stage. This is proven by the fact that the measured intermediate principal stress remained the same as the confining stress until the axial strain exceeded 0.4% and the measured major principal stress showed different slopes during the stress-hardening stage. The DEM simulations yielded slightly higher peak stresses, 609 kPa for DEM_APSD and 642 kPa for DEM_MTSD, than the experimental data of 599 kPa, but the residual stresses showed a good match. For the intermediate principal stress, the

simulation results yielded higher stress prediction probably due to the same reason mentioned above. As to the minor principal stress, it was calculated based on the contact forces between the membrane particles and specimen particles. It equaled to the applied confining pressure when the membrane did not undergo large deformations. However, when the shear band initialized and two shear blocks sheared against each other, large membrane deformations occurred and some percentage of the applied stress was transferred to the boundary walls. Hence, the minor principal stress decreased at the end.

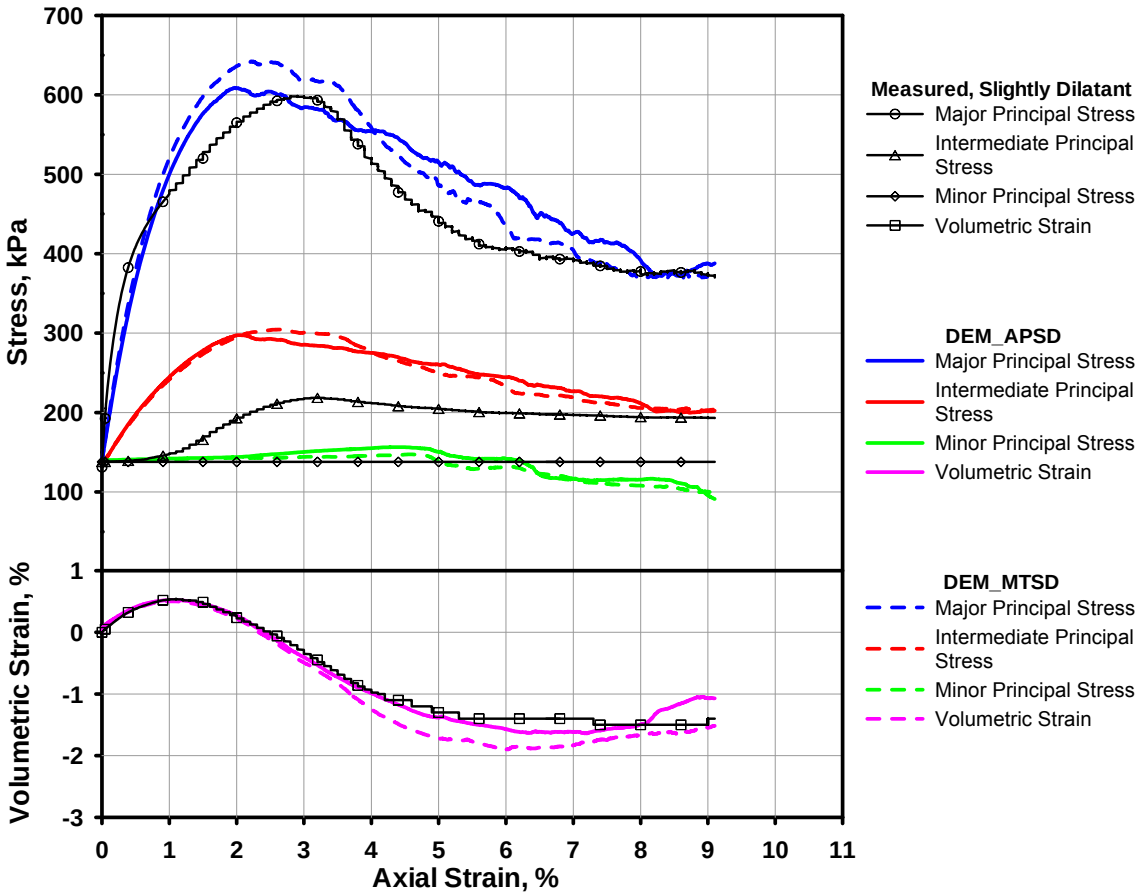

Figure 6.23 Axial stress and volumetric strain for slightly dilatant specimens

The stress-strain response for the highly dilatant specimens is presented in Figure 6.24. Again, both DEM_APHD and DEM_MTHD were plotted against the measured data. The peak stress of 335 kPa occurred at 2.4% strain for DEM_APHD, 353 kPa at

2.3% for DEM_MTHD, and 345 kPa at 3.0% strain for the experimental data. The apparently larger peak strain for the experimental data was due to the characteristics of the experimental biaxial tests aforementioned. The residual stresses of the simulated data were about 20 kPa less than the experimental data. In general, the simulations of the highly dilatant yielded a better match with the experimental data than those of the slightly dilatant, especially during the stress-softening stage.

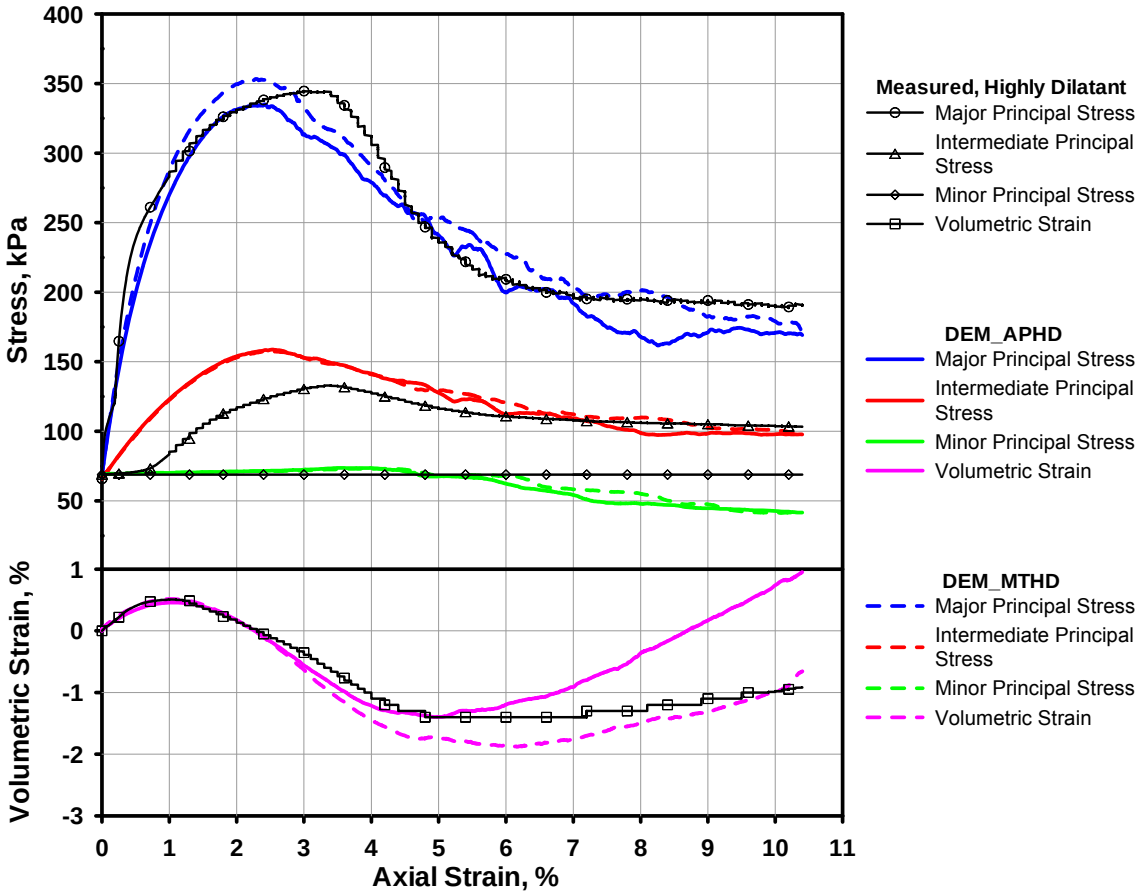

Figure 6.24 Axial stress and volumetric strain for highly dilatant specimens

The stress-strain responses for all the numerical tests are summarized and compared with the experimental tests in Table 6.4. In general, the numerical tests yielded good predictions of the peak and residual stresses, while the predicted peak strains were less than the measured values. As explained before, the large peak strain measured by the

experimental biaxial tests was due to lack of contact between the specimen and the confining platens. The moist-tamped numerical specimens always showed larger peak stress than the air-pluviated numerical specimens, however, the difference tended to diminish or even be reversed by the end of shearing.

Table 6.4 Summary of the stress-strain response

Tests	Peak Stress[1] (kPa)	Peak Strain (%)	Residual Stress[1] (kPa)
BT-2030-13 (SD)	598.5	2.90	370.0
DEM_APSD	609.0	1.97	387.9
DEM_MTSD	642.1	2.24	370.8
BT-2030-16 (HD)	344.8	3.00	190.2
DEM_APHD	335.1	2.41	169.2
DEM_MTHD	353.3	2.28	172.6

Note: [1] Major principal stress

6.4.2. Volumetric Strain

The volumetric strain was calculated by measuring the axial displacement and lateral displacement of the specimen. The axial displacement was usually measured through the vertical movement of loading platens. However, the measurements of lateral displacement were different for the experimental and numerical tests. In the experimental tests, the lateral displacements were measured by four LVDT. Detailed introductions on these LVDT can be found in Evans (2005). In the numerical tests, the lateral displacements were measured by tracking the movement of every membrane particle that was in contact with the specimen particles. Therefore, the displacements obtained from the experimental tests were only four point-measurements while in the numerical tests were based on thousands of point-measurements. From this point of view, the comparisons of volumetric strains between the experimental and numerical tests should be treated with some caution. One more thing needs to be noted here is that once the

shear band initializes and the shear blocks start to shear against each other, constitutive equations are not valid for the biaxial specimens anymore, which invalidates the volumetric strain calculated from axial displacements and lateral displacements. However, to make the data presentation complete, the volumetric strains are still plotted at large axial strains.

The volumetric strains for the slightly dilatant specimens are plotted in Figure 6.23. The simulation data matched well with the experimental data during the stress-hardening stage. Both of them experienced the maximum volumetric contraction of 0.5% at about 1.2% axial strain. After that, the experimental specimen underwent continuous volumetric dilation. Once the axial strain exceeded 5.3%, the measured volumetric dilation stabilized around 1.4 to 1.5% until the end of shearing. The numerical specimens also experienced continuous volumetric dilation after initial contraction. However, the volumetric dilation reached a maximum of 1.6% at 7.2% axial strain for DEM_APSD and 1.9% at 6.0% axial strain for DEM_MTSD. After the maximum volumetric dilation, both DEM_APSD and DEM_MTSD started to contract again. Comparing the air-pluviated and moist-tamped numerical specimens, it shows that different preparation methods did not result in different contracting behaviors, but caused the moist-tamped specimen to dilate more in the stress-softening stage.

The volumetric strains for the highly dilatant specimens are plotted in Figure 6.24. Again, the simulation results matched well with the experimental results during the initial volumetric contraction. After that, the volumetric dilation of the experimental specimen reached a maximum of 1.4% at 4.8% global axial strain. Unlike the slightly dilatant specimen, the highly dilatant experimental specimen started to contract after 7.2% axial strain. For the simulation results, the maximum volumetric dilation reached 1.4% at 5% global axial strain for DEM_APHD and 1.9% at 6.2% axial strain for DEM_MTHD. Then, both specimens started to contract. The DEM_APHD exhibited very large volumetric contraction at the end of shearing.

6.4.3. Void Ratio

Like the numerical triaxial tests, several measurement spheres were placed inside the numerical specimens to monitor the development of local void ratio and coordination number. The measurement logic has been introduced in Section 4.1.2. Due to the configuration of biaxial specimens, a total of nine measurement spheres with radius of 10 mm were used and each of them contained more than 100 clumps. Some criteria were applied when designing the locations of the measurement spheres: (1) three of them should measure the void ratio inside the shear band and are designated as middle level; (2) three of them would capture the void ratio in the upper shear block and are designated as upper level; (3) the rest three would capture the void ratio in the lower shear block and are designated as lower level; and (4) no overlap should be allowed between any of the spheres. As the location of the shear band differed for each numerical test, the location of the measurement spheres varied as approximate.

The void ratio measurement of DEM_APSD is presented in Figure 6.25. Prior to shearing, the void ratio throughout the specimen was within the range of 0.404 to 0.429. Once the shearing started, local void ratio showed some fluctuations but the range still remained within 0.404 to 0.429 until the principal stresses reached the peak value at 2.0% global axial strain. From this point on, the void ratio measured by the middle-level spheres differentiated themselves from that measured by the lower-level and upper-level spheres. The measured void ratio inside the shear band reached as high as 0.586 close to the end of shearing. The measured void ratio in the upper shear block and lower shear block showed no difference and remained around 0.414 to 0.454 after the peak strain. Overall, the development of void ratio inside the numerical specimen clearly indicates the onset of localization.

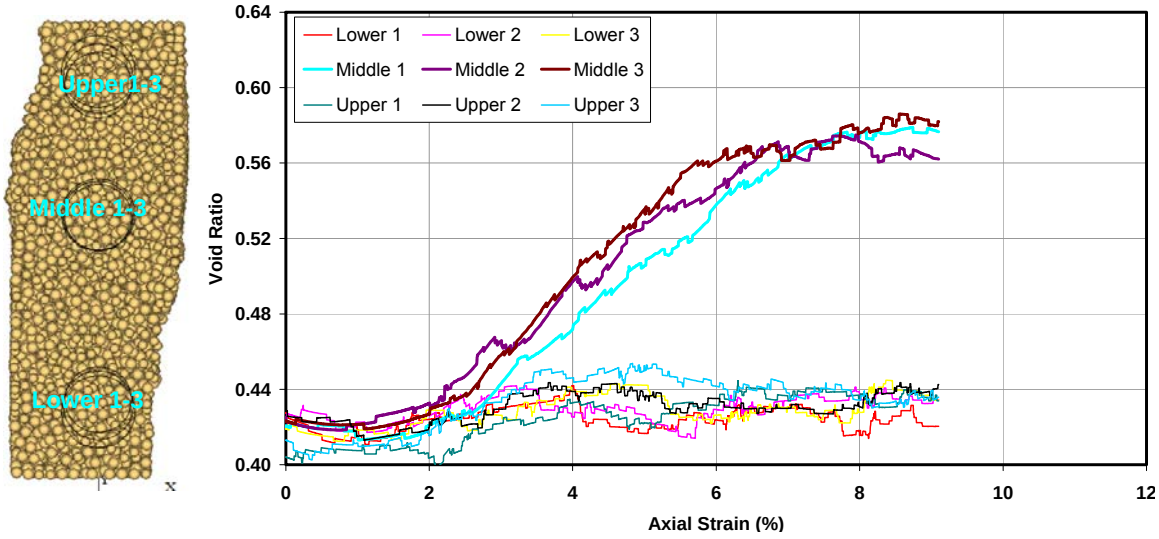

Figure 6.25 Void ratio measurement for DEM_APSD

The void ratio measured for DEM_MTSD is shown in Figure 6.26. The developing trend of void ratio for this case is very similar to DEM_APSD, but the magnitudes detected were generally larger. The void ratio range prior to shearing was 0.421 to 0.434. After the peak strain which was 2.2% for this case, the void ratio inside the shear band increased sharply while the void ratio in the two shear blocks increased slightly and then remained around 0.424 to 0.468. The maximum void ratio detected inside the shear band was 0.593.

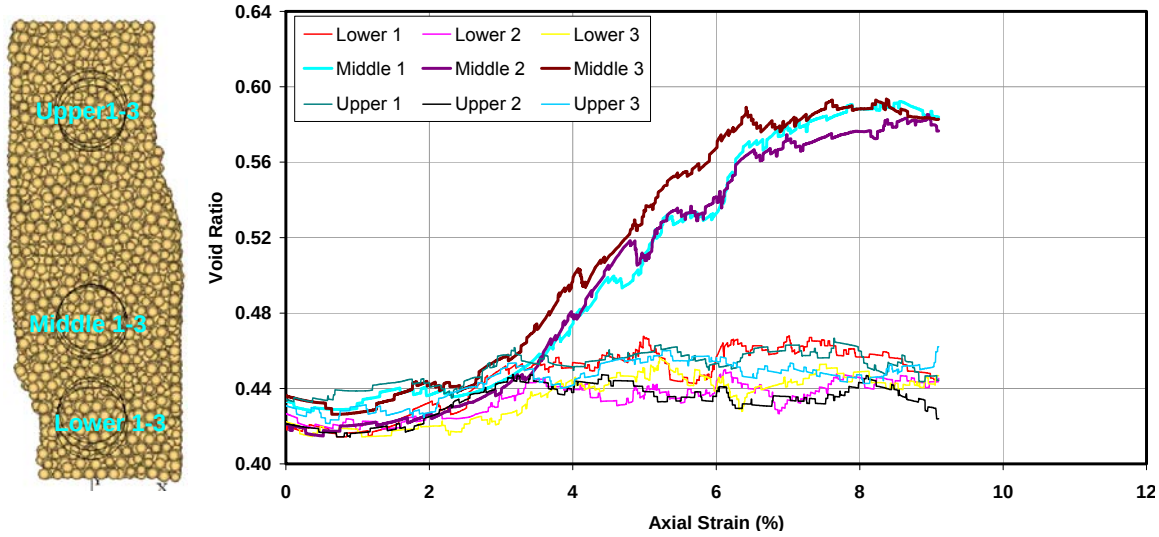

Figure 6.26 Void ratio measurements for DEM_MTSD

The void ratio measurement for DEM_APHD is presented in Figure 6.27. The void ratio prior to shearing was in the range of 0.417~0.436, which was higher than that of the air-pluviated slightly dilatant specimen. The higher void ratio was caused by the lower confining pressure (68.9 kPa). After the peak strain, which was 2.4% in this case, the void ratio inside the shear band experienced drastic increase and reached as high as 0.629. For the shear blocks, except for Lower 3, all the measurement spheres detected the void ratio between 0.403 to 0.456. The higher void ratio detected by Lower 3 of almost 0.46 might reflect the influence from the shear zone. When comparing DEM_APHD with DEM_APSD, it is found that higher confining pressure might suppress the void ratio development inside the shear band while it had almost no effect on the void ratio outside the shear band.

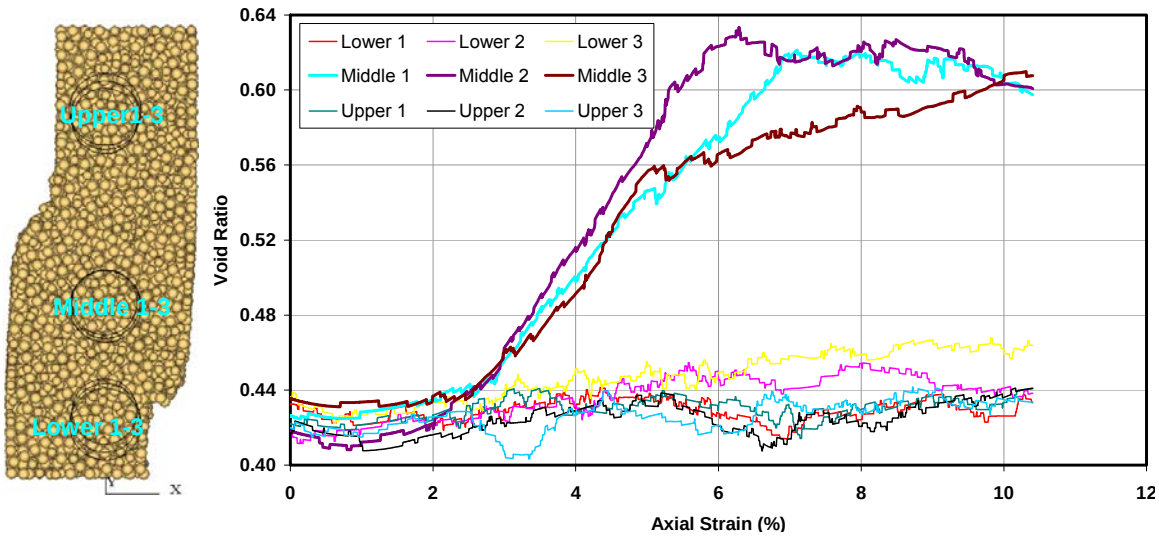

Figure 6.27 Void ratio measurements for DEM_APHD

The void ratio measurement for DEM_MTHD is presented in Figure 6.28. The void ratio prior to shearing was around 0.420 to 0.438 and comparable to DEM_APHD. After the peak strain of 2.3%, the void ratio within different portions of the specimen started to differentiate. In this particular case, as the shear band occurred at the bottom of the specimen, the measurement spheres at the lower level were inevitably affected by the

shear band and yielded larger void ratio measurements than those of upper-level spheres. The void ratio detected by the upper-level spheres was 0.421 to 0.458, which was similar to the void ratio detected inside the shear blocks for DEM_MTSD. The measured maximum void ratio inside the shear band was 0.644.

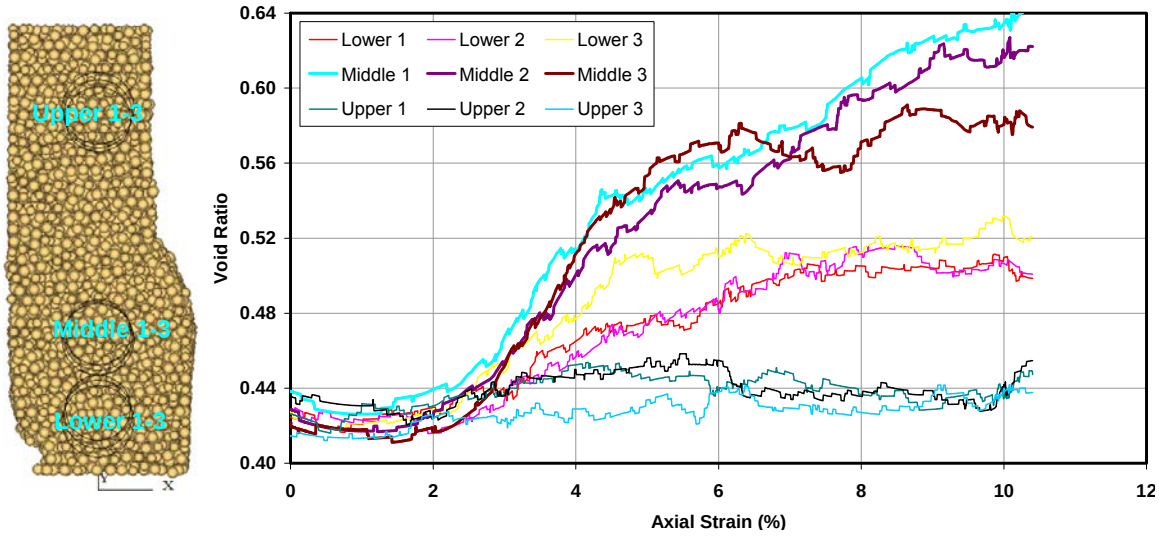

Figure 6.28 Void ratio measurements for DEM_MTHD

The following conclusions can be reached from the comparison of the four numerical tests:

- Prior to shearing, different void ratios result from different particulate behaviors during the consolidation stage. The factors that substantially affect the particulate behaviors during consolidation are the confining pressure and particle friction coefficient.
- Moist tamping leads to larger void ratio values than air pluviation during shearing. It seems that a heterogeneous specimen would lead to larger volumetric dilation.
- Higher confining pressure tends to suppress the increase of void ratio inside the shear band. However, it imposes no effect on the void ratio outside the shear band.

6.4.4. Contact Normals

The polar histograms of contact normals prior to shearing, at 1% axial strain, at peak strain, and at the end of shearing are plotted for the four numerical tests in Figures 6.29 to 6.32. Comparing all of the tests, it is found that the shape of the polar histograms is mostly affected by the preparation methods. Prior to shearing, the polar histograms for the air-pluviated specimens look like ellipsoids with a larger area in the projection in the X-Y plane than in the X-Z or Y-Z plane. Such polar histograms imply an isotropic loading condition and are comparable to the polar histogram of DEM_AP for the numerical triaxial test. However, the polar histograms for the moist-tamped specimens exhibit distinctive shapes and look more like “flying saucers”. A large percentage of the contact normals align parallel to the X-Y plane. Such polar histograms are also distinctive from the polar histogram of DEM_MT for the numerical triaxial test. One possible explanation is that rigid boundary is more capable of eliminating the heterogeneity caused by moist tamping under isotropic loading than the flexible boundary. As the shearing started, the number of contact normals in X-Y plane decreased quickly, while those along the diagonal planes almost remained constant. When the numerical tests approached the peak strains, the polar histograms became the most anisotropic due to formation of multiple particles chains and release of the load from those particles not belonging to the load-carrying chains. During post-peak shearing, the number of contact normals parallel to the diagonal planes decreased, indicating some of the particle chains collapsed.

Other than the polar histograms of contact normals, the numbers of contact normals at selected shearing stages are summarized in Table 6.5 and Figure 6.33. The decrease in the number of contact normals mainly took place prior to the peak state, and the number of contact normals tended to stabilize towards the end of shearing.

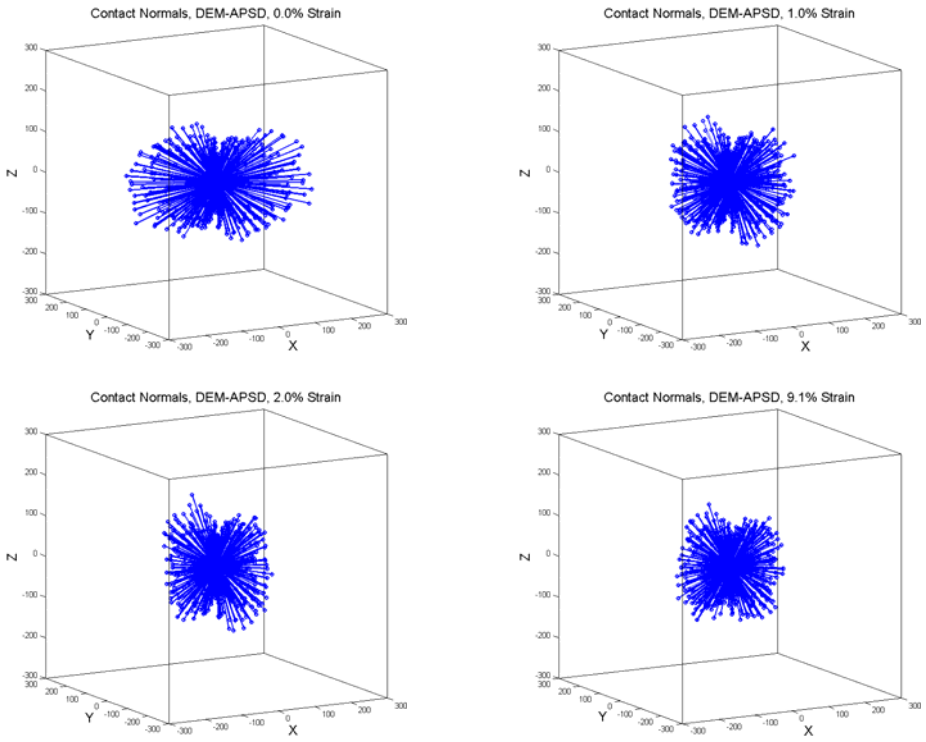

Figure 6.29 Polar histograms of contact normals for DEM_APSD

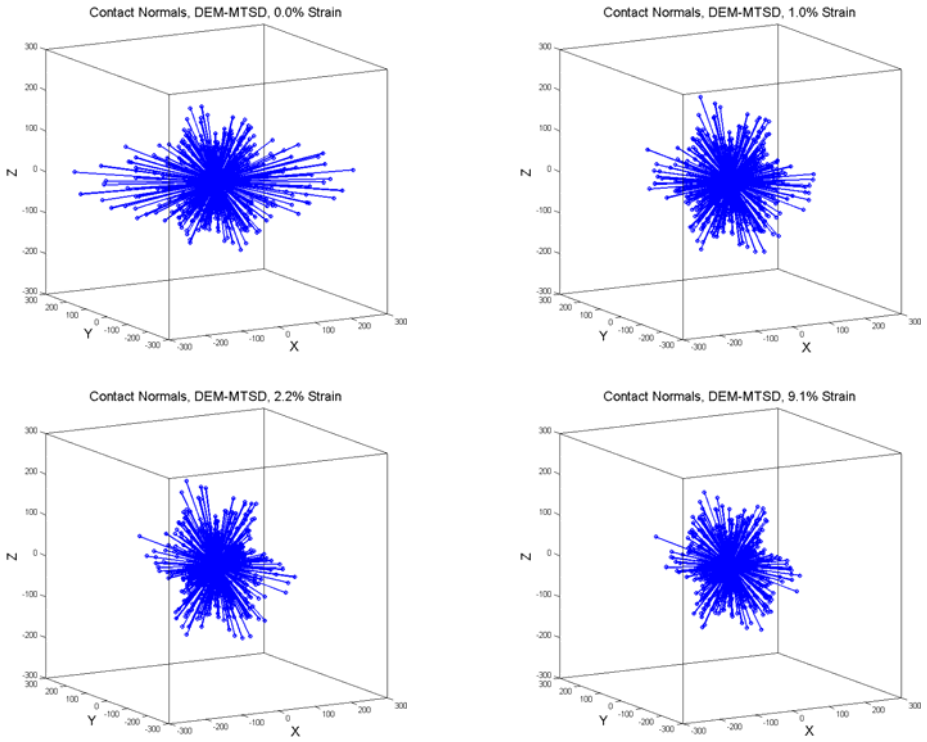

Figure 6.30 Polar histograms of contact normals for DEM_MTSD

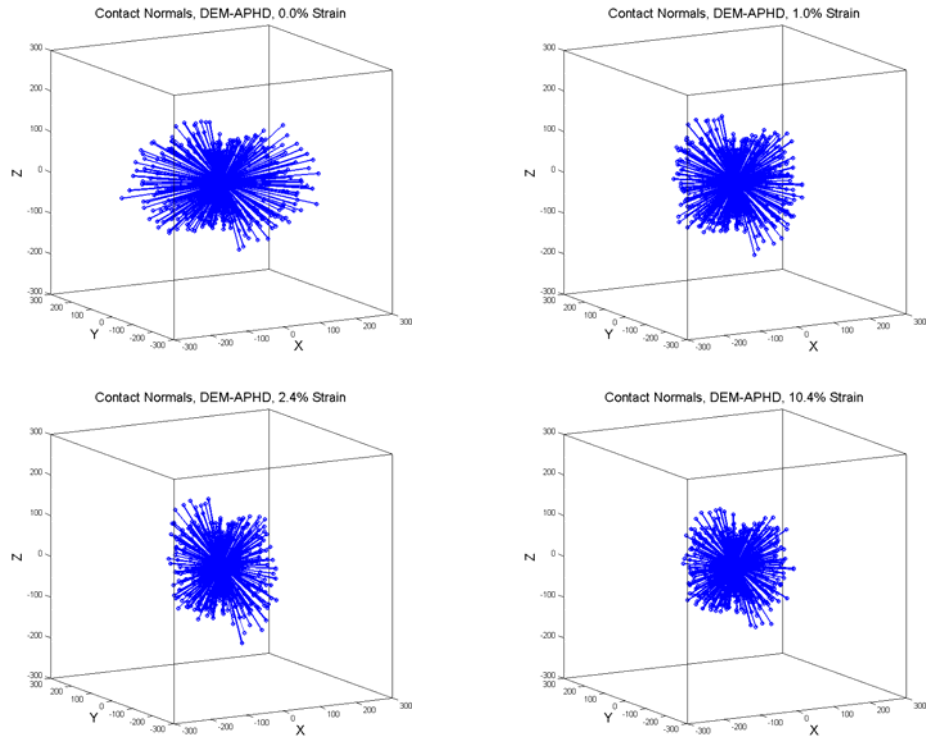

Figure 6.31 Polar histograms of contact normals for DEM_APHD

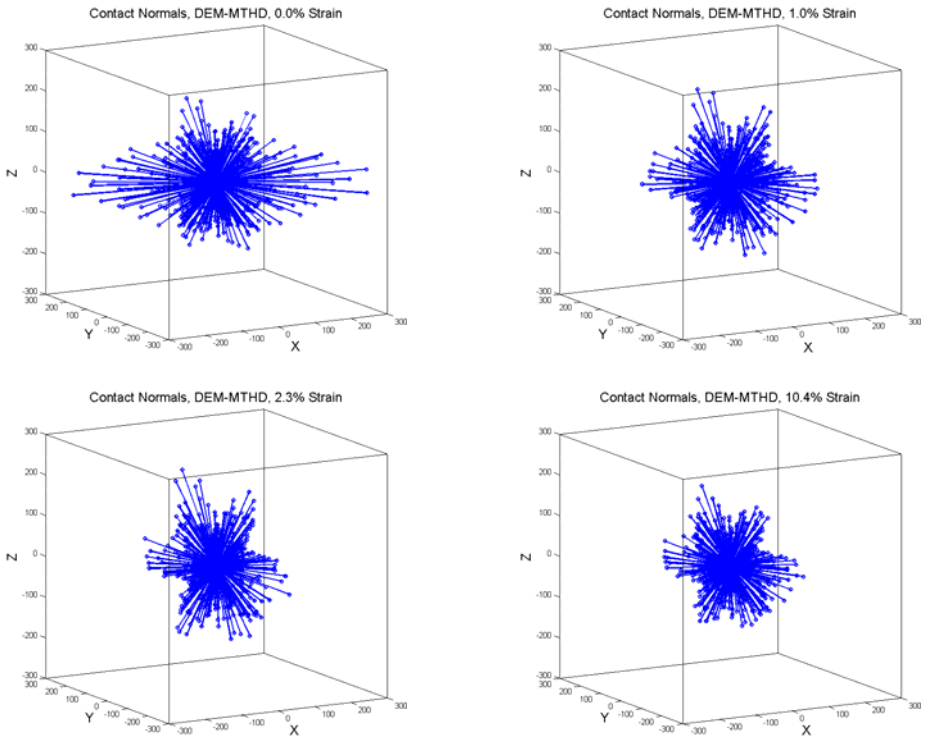

Figure 6.32 Polar histograms of contact normals for DEM_MTHD

Table 6.5 Number of contact normals and coordination numbers at different stages of shearing

Test	Number of Contact Normals					Coordination Number				
	0%[1]	1%[1]	Peak[2]	5%[1]	EOS[3]	0%[1]	1%[1]	Peak[2]	5%[1]	EOS[3]
DEM_APSD	51619	46569	43401	41565	41301	9.78	8.82	8.22	7.87	7.82
DEM_MTSD	51962	46328	42900	40940	40774	9.83	8.77	8.12	7.75	7.72
DEM_APHD	52915	47356	42869	41395	40829	9.77	8.75	7.92	7.65	7.54
DEM_MTHD	53248	47214	43140	41024	40573	9.83	8.71	7.96	7.57	7.49

Note: [1] Axial strain; [2] Peak axial strain; [3] End of shearing.

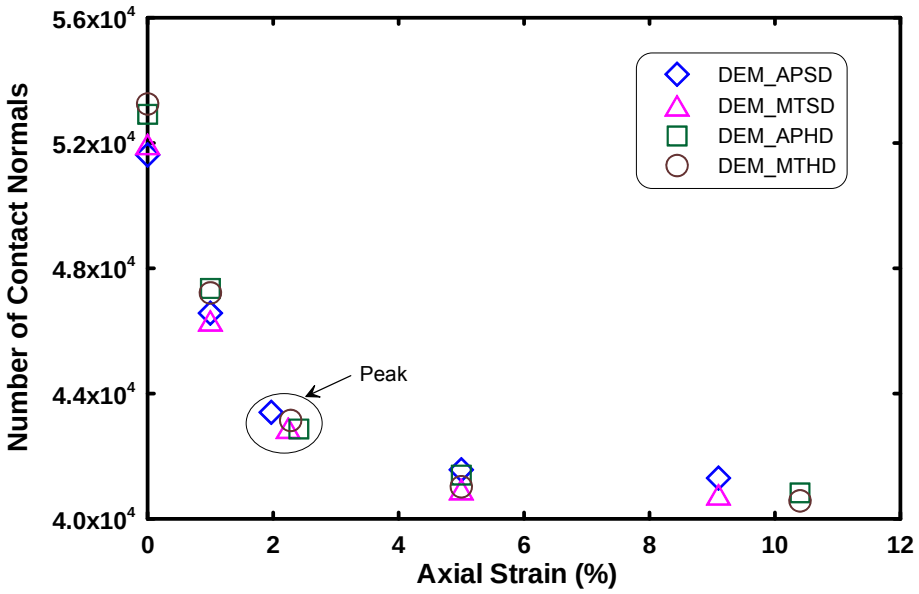

Figure 6.33 Number of contact normals at different stages of shearing

6.4.5. Coordination Number

The coordination number, *cn*, can be estimated from the number of contact normals, and is also summarized for selected loading stages in Table 6.5 and Figure 6.34. Prior to shearing, the coordination numbers of all the specimens were close to 10. The moist-tamped specimens had slightly higher coordination numbers than the air-pluviated specimens. Once the shearing started, the coordination numbers of highly dilatant specimens decreased more than the slightly dilatant specimens, which indicates that higher confining pressure managed to maintain a denser packing. At the end of shearing,

the coordination numbers of the moist-tamped specimens became smaller than the air-pluviated specimens. Such phenomenon proves that the moist-tamped specimens experienced greater volumetric dilation during shearing.

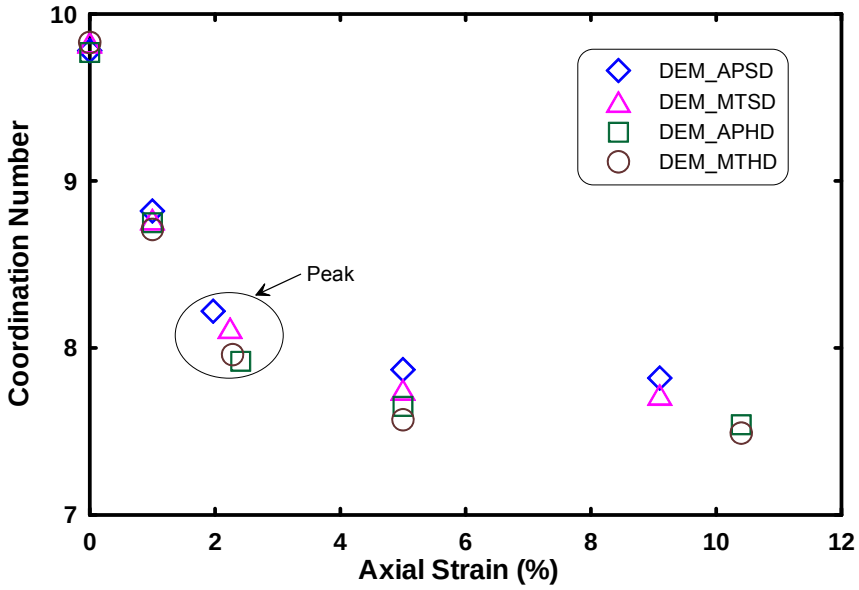

Figure 6.34 Coordination numbers at different stages of shearing

The development of local coordination numbers was recorded by the same measurement spheres used in Section 6.4.3, and they are plotted in Figures 6.35 to 6.38. For all of the specimens, the local coordination numbers were around 10.5 to 11.0 under isotropic loading conditions. Once the loading changed from isotropic to anisotropic, the coordination numbers decreased quickly during the stress-hardening stage and tended to stabilize during the stress-softening stage. After the shear band initialized, *cn* inside the shear band differentiated from *cn* outside the shear blocks. The *cn* curves of the shear band locate distinctly below those of the shear blocks and showed larger fluctuations. Considering that the void space inside the shear band was significantly larger than that inside the shear blocks, particles had more freedom to move inside the shear band and thus caused the *cn* curves to fluctuate substantially. Comparing all of the four specimens, the following findings can be noted: (1) *cn* of the slightly dilatant specimens was greater

than the highly dilatant specimens at the stress-softening stage; (2) *cn* inside the shear band was smaller in the air-pluviated specimens than in the moist-tamped specimens.

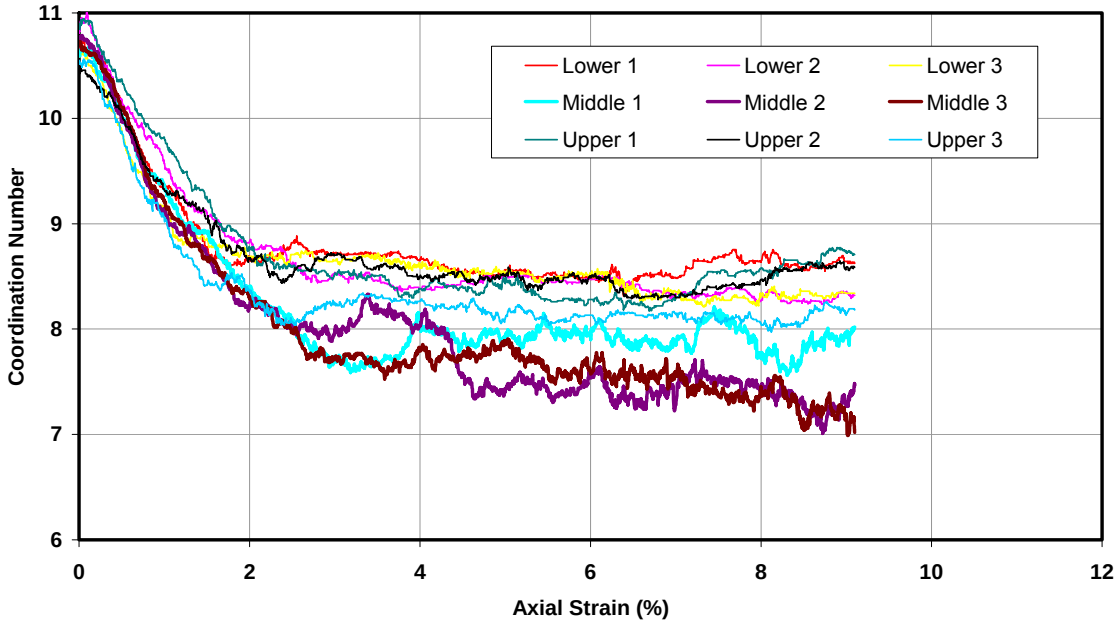

Figure 6.35 Coordination number of DEM_APSD

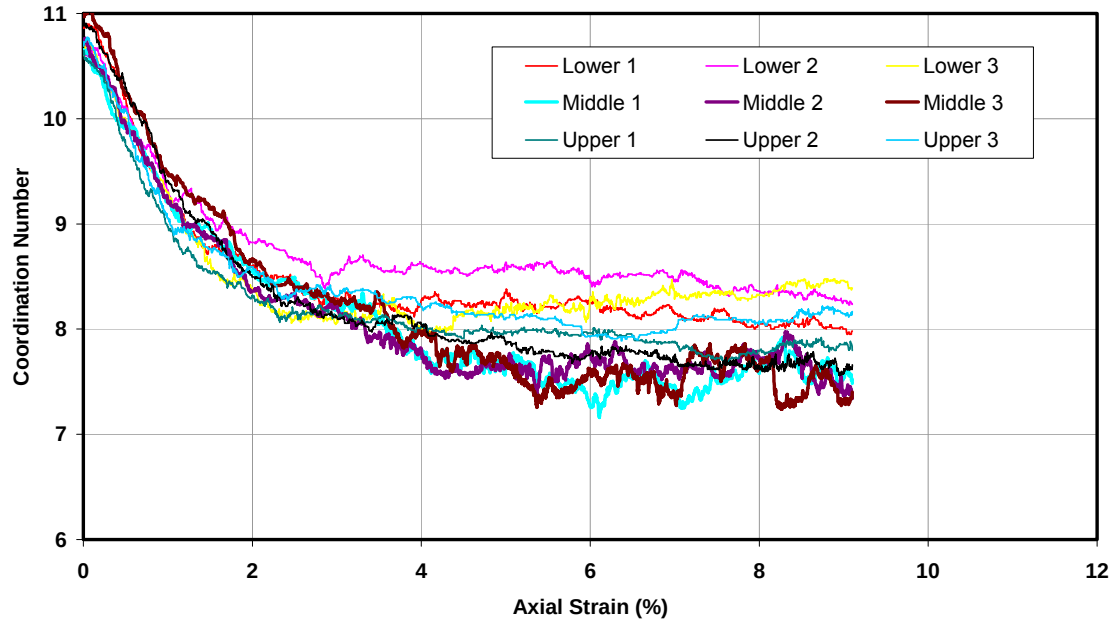

Figure 6.36 Coordination number of DEM_MTSD

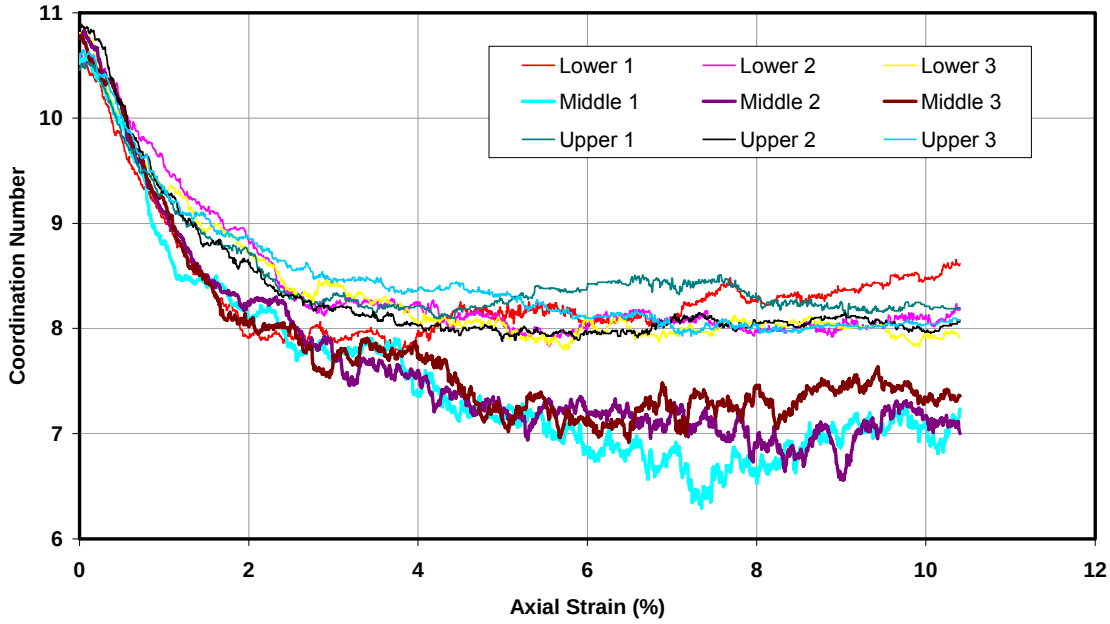

Figure 6.37 Coordination number of DEM_APHD

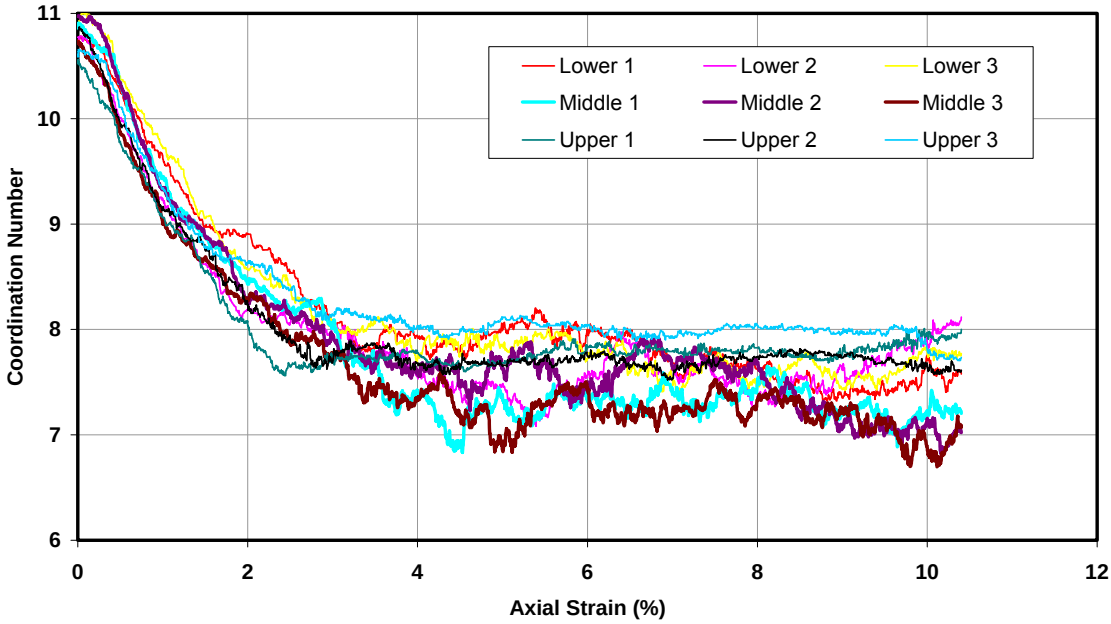

Figure 6.38 Coordination number of DEM_MTHD

6.4.6. Particle Orientation

For each of the numerical biaxial tests, the polar histograms of particle orientation prior to shearing, at peak, post peak, and at the end of shearing are plotted and presented

in Figures 6.39~6.42. Similar to the polar histograms of contact normals, the polar histograms of particle orientation are more affected by the preparation method than any other factors. Prior to shearing, the particles inside the air-pluviated specimens almost showed no preferred orientation, while the particles inside the moist-tamped specimens tended to align horizontally or vertically. It is believed that how the particles were deposited accounts for such distinctive shapes of polar histograms. Once the shearing started, more and more particles aligned horizontally, because the horizontal alignment is the most stable position for a two-sphere clump subject to vertical loading. Most of the re-aligning of particles occurred post peak, when collapse of multiple particle chains also took place.

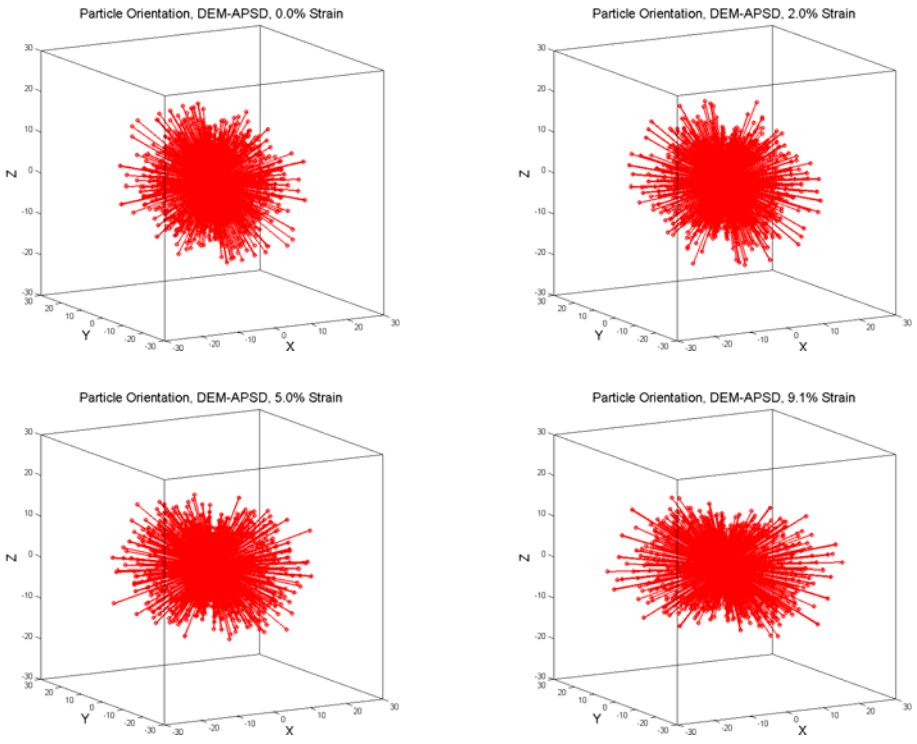

Figure 6.39 Polar histograms of particle orientation for DEM_APSD

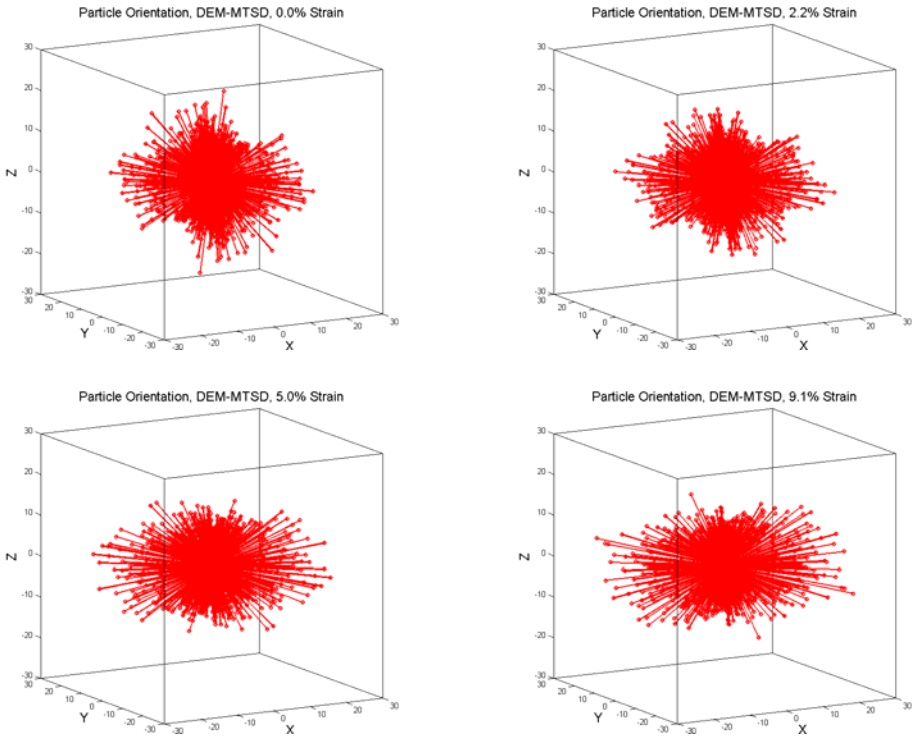

Figure 6.40 Polar histograms of particle orientation for DEM_MTSD

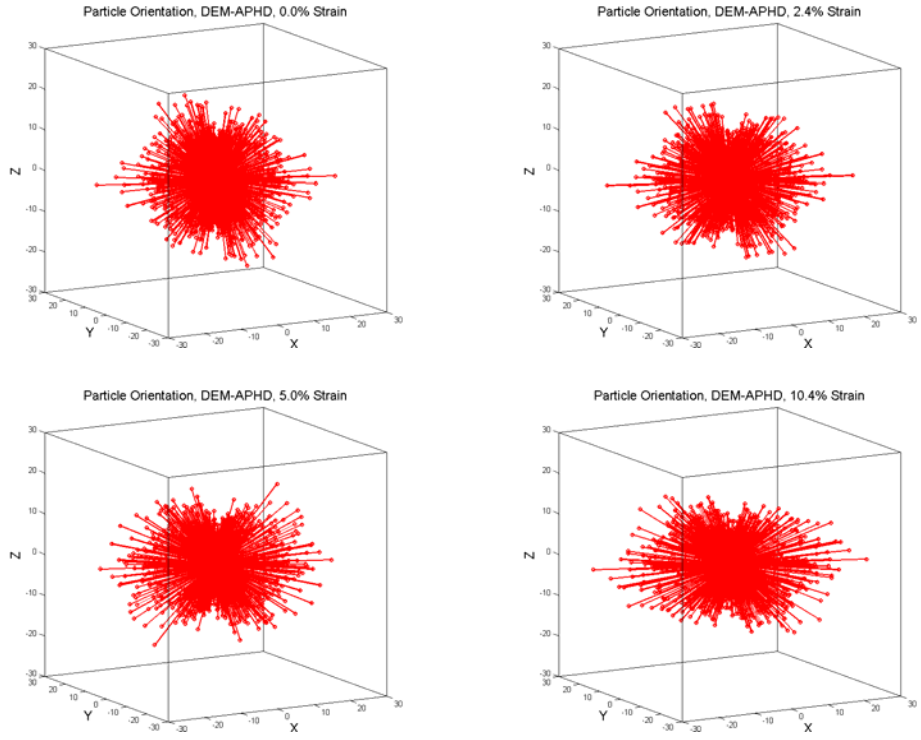

Figure 6.41 Polar histograms of particle orientation for DEM_APHD

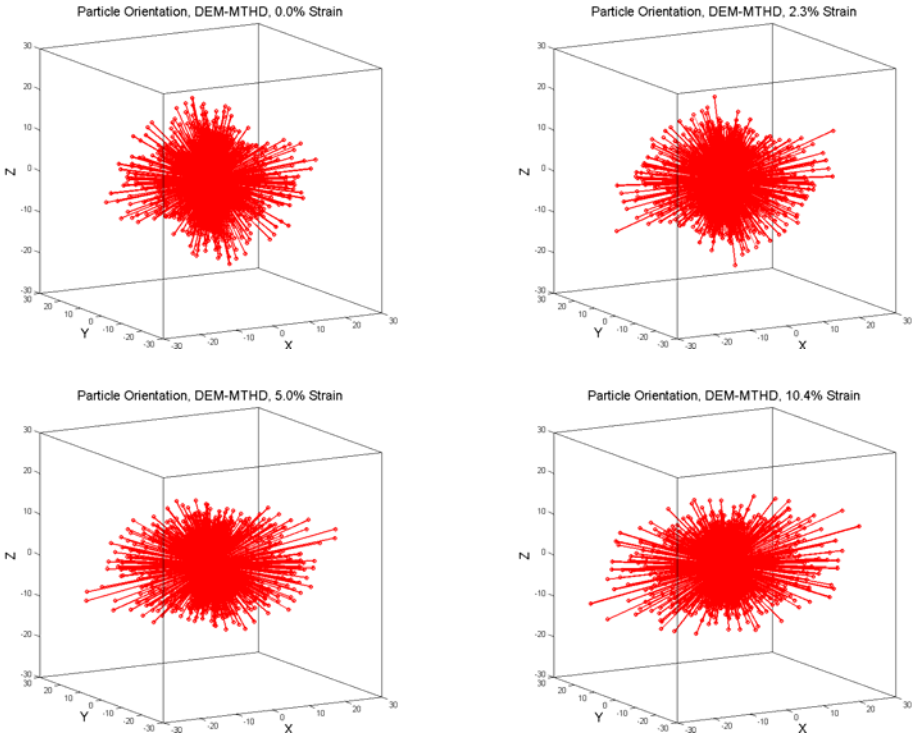

Figure 6.42 Polar histograms of particle orientation for DEM_MTHD

6.4.7. Particle Rotation and Displacement

To help illustrate how the shear bands evolved, particle rotation and displacement maps based on the particles in the middle planes are plotted in Figures 6.43 to 6.50 for the four specimens. For the numerical biaxial tests, different boundaries in the X-Z plane and the Y-Z plane lead to different shearing patterns, and thus the maps are plotted in both planes.

The particles rotations and displacements of DEM_APSD at selected strains, representing pre-shearing, pre-peak, peak, post-peak, and end of shearing, are plotted in Figure 6.43 for the X-Z plane and Figure 6.44 for the Y-Z plane. The particle rotations and displacements were zeroed before shearing started to exclude the influence from the consolidation stage. Prior to peak, no particle rotated more than 0.3 radians in the X-Z plane and 0.15 radians in the Y-Z plane. Particle displacements were generally small in

magnitude, but the particles at both ends experienced larger vertical displacements than those in the middle. Small-scale shear blocks had formed close to the end loading platens during this stage. When the specimen reached its peak stress, most of the particle rotations were still less than 0.3 radians in the X-Z plane and 0.15 radians in the Y-Z plane. The shear blocks included more particles and extended to the middle of the specimen as loading proceeded. After the peak, two shear blocks contacted and sheared against each other along the shear band over time. The particles inside the shear blocks basically underwent displacements while the particles inside the shear band mainly experienced rotations. It is interesting to notice that as the lateral boundaries were different for the X-Z and the Y-Z planes, different shearing patterns can be distinguished. For the X-Z plane, the lateral boundaries were flexible, and thus the particles were able to move horizontally. However, since the lateral boundaries for the Y-Z plane were rigid, which meant the particles were restrained from moving in the horizontal direction, none of the displacement vectors pointed out of the specimen. At the end of shearing, lateral relative displacement between the two shear blocks occurred, which was similar to what happened in the laboratory biaxial tests. The particles within the shear blocks moved consistently along the direction of shear band, and the particle rotations within the shear band increased as shearing progressed. The shear-induced failure in the X-Z plane proves that the flexible membrane algorithm implemented in this research succeeded in facilitating the initialization of the shear band. In the Y-Z plane, due to the constraint from the rigid boundary, the two shear blocks could only move vertically towards each other. However, the location and extent of the shear band could be clearly recognized.

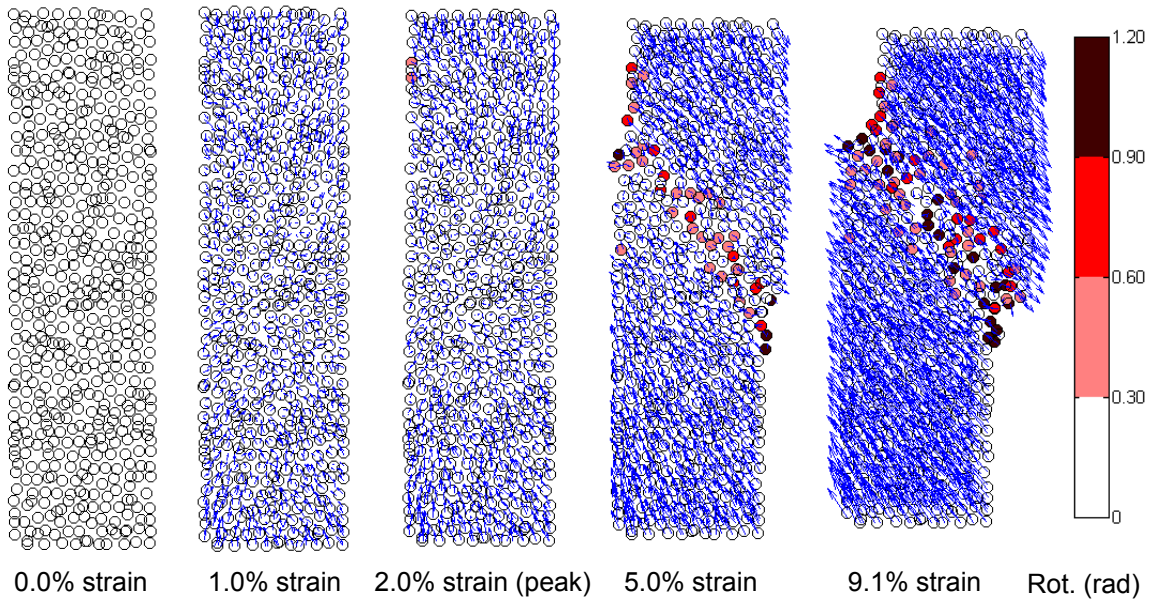

Figure 6.43 Particle rotations and displacements in X-Z plane for DEM_APSD

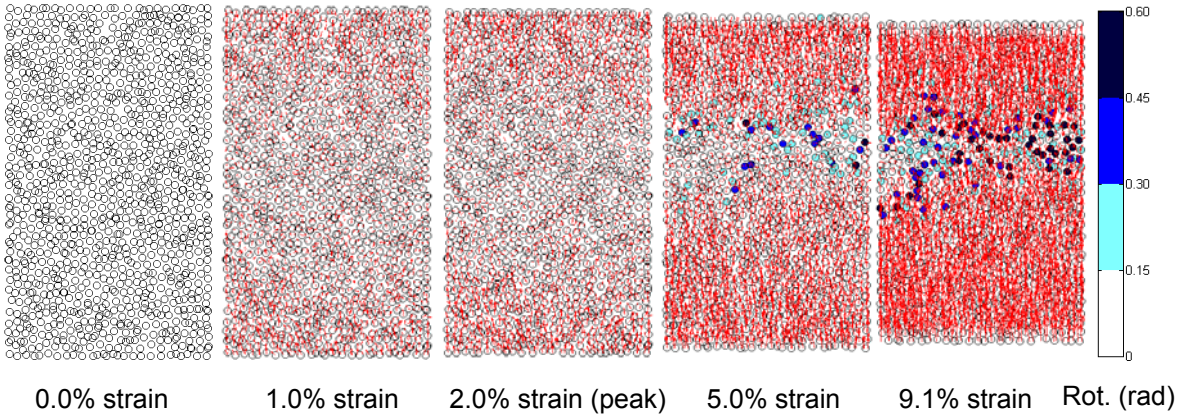

Figure 6.44 Particle rotations and displacements in Y-Z plane for DEM_APSD

How the particle rotations and displacements evolved inside the DEM_MTSD, DEM_APHD and DEM_MTHD numerical specimens is similar to what happened inside DEM_APSD, and hence won't be detailed here. Comparing all of the numerical tests, it is found that the location and inclination of shear bands was affected by confining pressure and preparation method as well as the particle properties. A direct measurement was performed on the particle rotation and displacement maps in the X-Z plane to check the inclination angle and width of the shear bands at the end of shearing. The results

along with the visual inspection on the experimental biaxial specimens (Evans, 2005) are summarized in Table 6.6. The inclination angles measured from the numerical tests are about 10° less than the experimental tests. The shear band widths of the numerical specimens are 3.4 ~ 4.2 D_{avg} in short axis while the shear band widths of the experimental specimens are 11.2 ~ 12.2 D_{50}. Such large discrepancies can be explained by that: (1) the particle size in the numerical modeling was scaled 5 times to reduce the number of particles in the numerical models; and (2) the direct measurement was based on personal judgment which easily resulted in errors. A more refined measurement of the shear band width will be presented in Chapter 7.

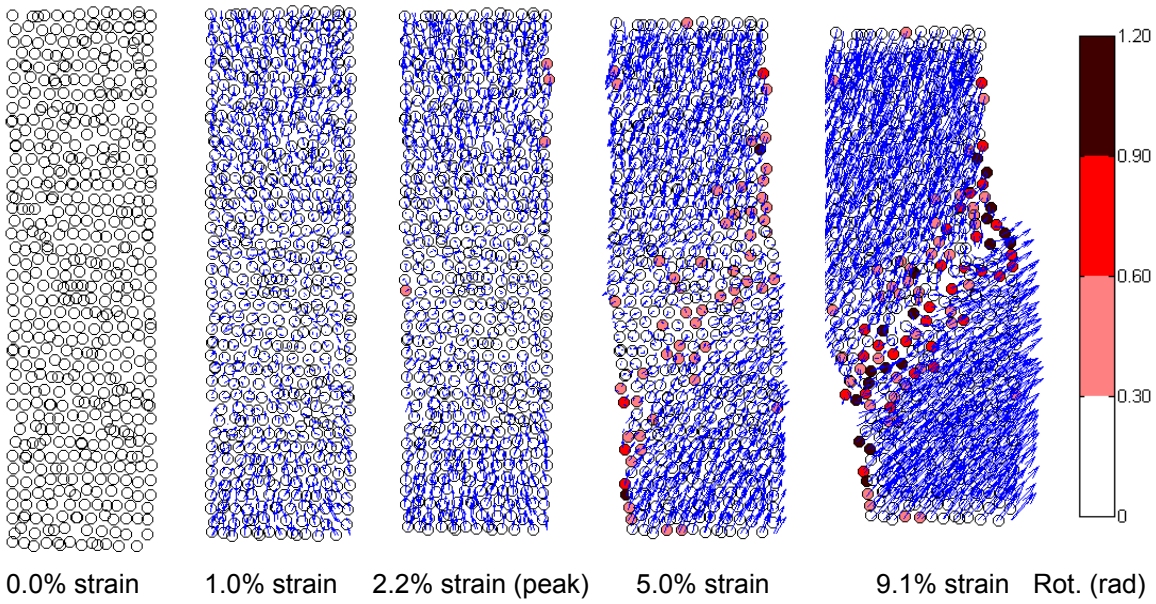

Figure 6.45 Particle rotations and displacements in X-Z plane for DEM_MTSD

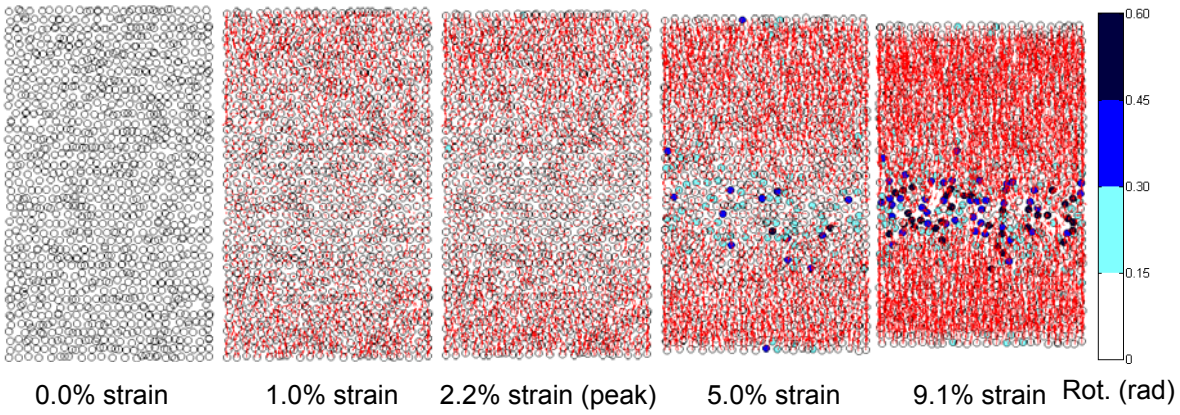

Figure 6.46 Particle rotations and displacements in Y-Z plane for DEM_MTSD

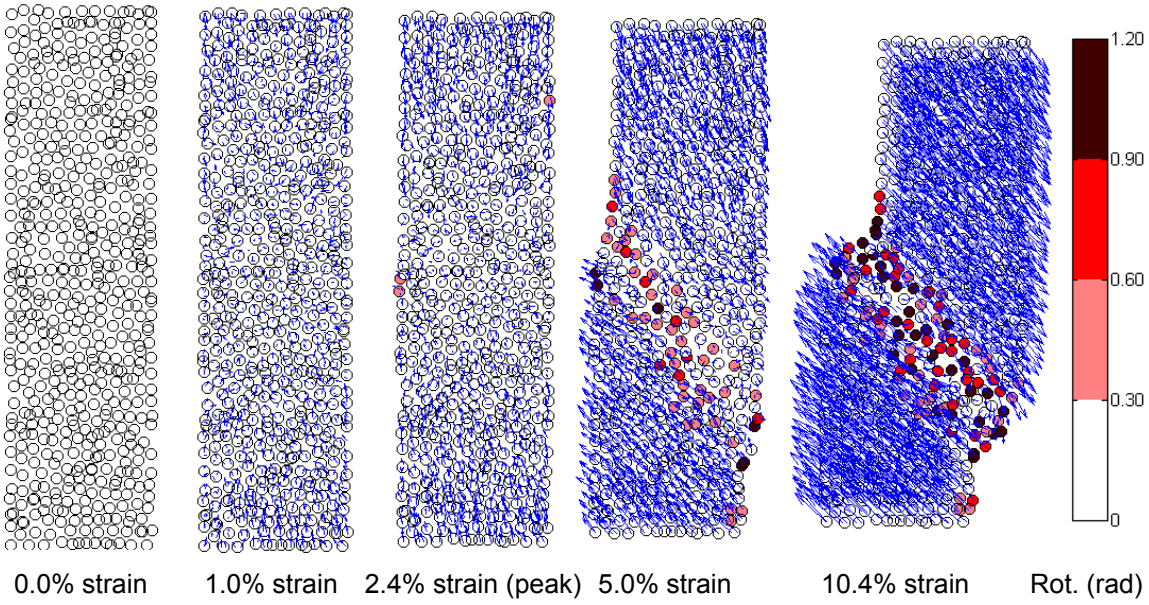

Figure 6.47 Particle rotations and displacements in X-Z plane for DEM_APHD

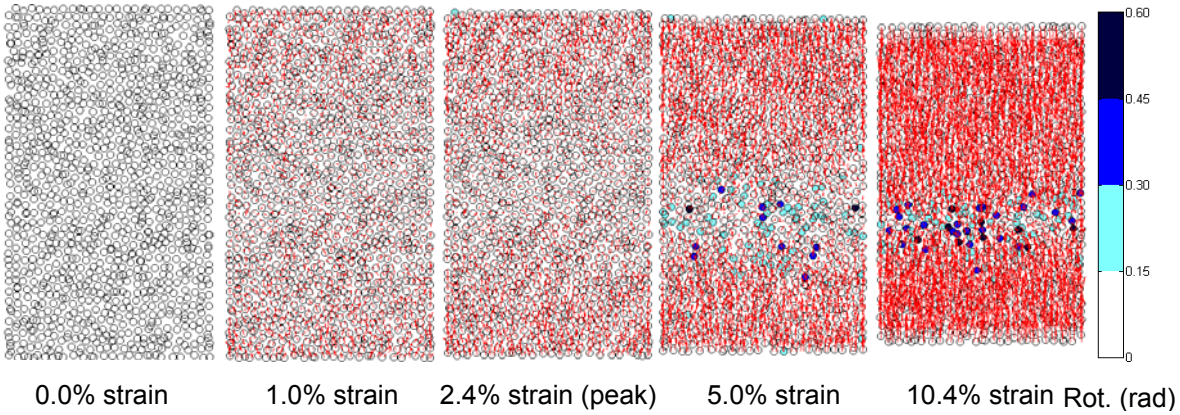

Figure 6.48 Particle rotations and displacements in Y-Z plane for DEM_APHD

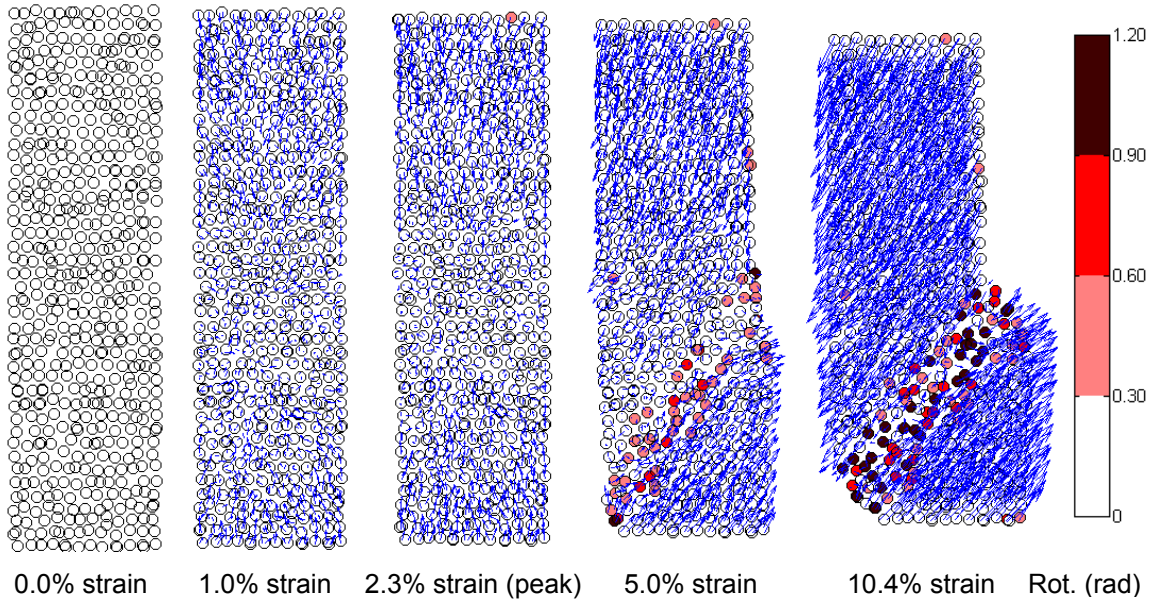

Figure 6.49 Particle rotations and displacements in X-Z plane for DEM_MTHD

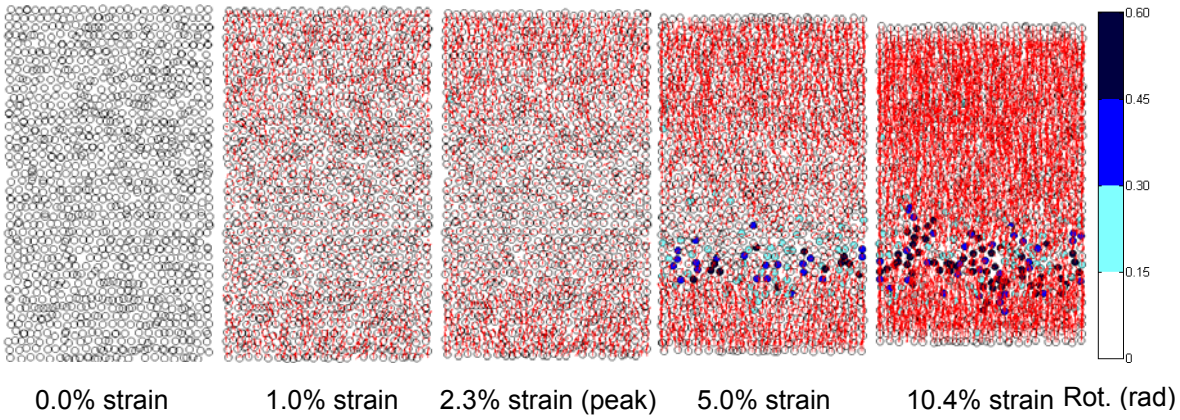

Figure 6.50 Particle rotations and displacements in Y-Z plane for DEM_MTHD

Table 6.6 Shear band inclination and width measured from the particle rotation and displacement maps (experimental data from Evans, 2005)

Test	Shear Band		
	Inclination (°)	Width (mm)	Width (D)[1]
BT-2030-13 (SD)	59.0	8.3	11.2
DEM_APSD	49.9	10.6	3.4
DEM_MTSD	49.3	11.2	3.6
BT-2030-16 (HD)	61.0	9.0	12.2
DEM_APHD	52.0	12.6	4.1
DEM_MTHD	50.7	12.9	4.2

Note: [1]Mean particles size: D_{50} of Ottawa 20-30 sand and D_{avg} in short axis for numerical specimens

6.4.8. Normal Contact Forces

To take a look at the evolution of force chains inside the specimens, normal contact forces are plotted at selected strain levels for the X-Z plane and the Y-Z plane. For the ease of observation, only the normal contact forces within ±10 mm from the central plane are presented for each numerical specimen in Figures 6.51 to 6.58. In those figures, compression is represented by black color and tension by red color.

Figures 6.51 and 6.52 show the normal contact forces in the X-Z and the Y-Z planes for DEM_APSD. During the isotropic loading prior to shearing, arrays of normal contact forces inside the specimen were loose but uniform. Once the shearing started, the specimen developed vertical force chains to sustain the loading. Such force chains increased both in number and magnitude until the deviatoric stress reached the maximum value. After the peak, some of the forces chains started to bend or collapse due to the initialization of some localization zones. When a dominant shear band formed, it cut off some of the major force chains. The density of normal contact forces also decreased substantially inside the shear band as this was where the major shearing behavior took place. Such phenomenon was particularly evident in the Y-Z plane and it helped in locating the shear band. In contrast to the specimen, the membranes basically underwent

tension instead of compression, and the magnitude of tension varied according to the deformation of the specimen. During the stress-hardening stage, the specimen contracted, and thus the tension forces decreased from the initial state. During the stress-softening stage, with the initialization of shear band, the specimen both dilated and sheared. In order to hold the specimen intact, the membranes developed large tension forces.

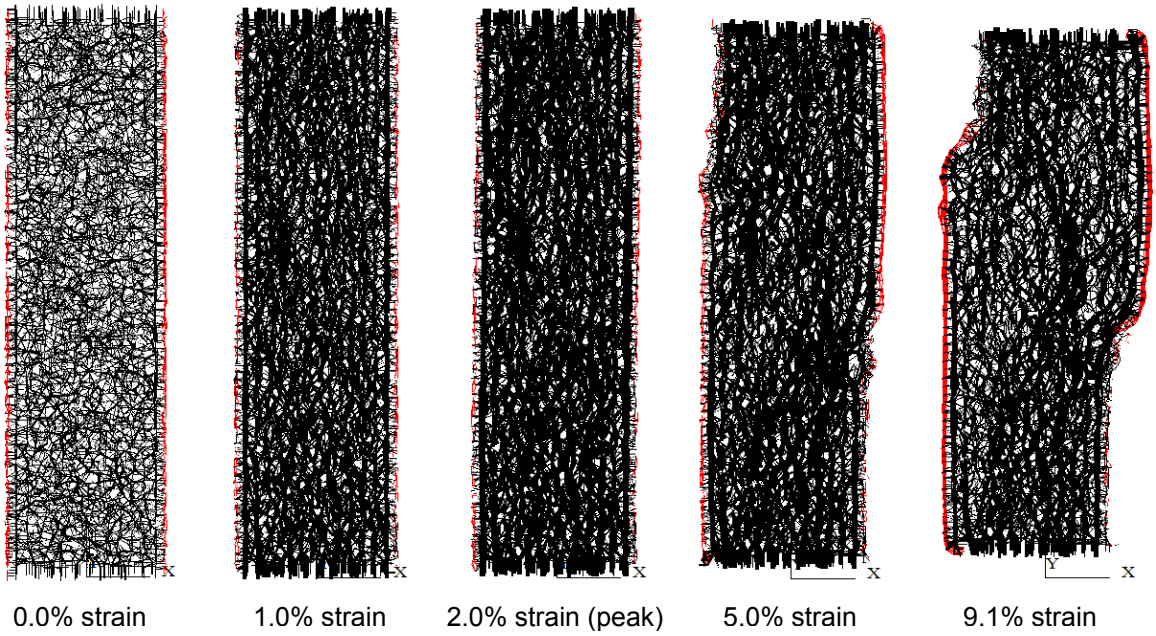

Figure 6.51 Normal contact forces in X-Z plane for DEM_APSD

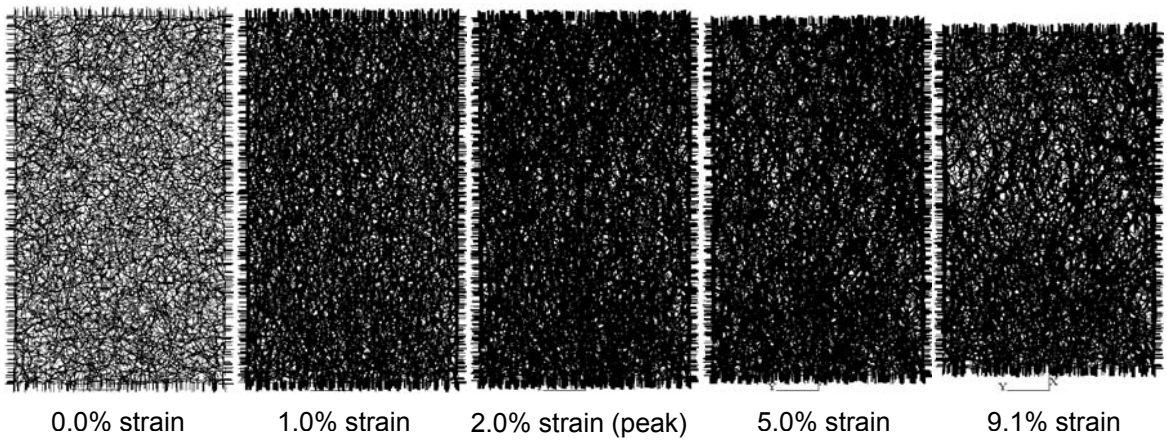

Figure 6.52 Normal contact forces in Y-Z plane for DEM_APSD

Evolution of normal contact forces for DEM_MTSD, DEM_APHD, and DEM_MTHD were generally similar to DEM_APSD. However, the lower confining pressure in DEM_APHD and DEM_MTHD resulted in less dense arrays of normal contact forces with smaller magnitudes.

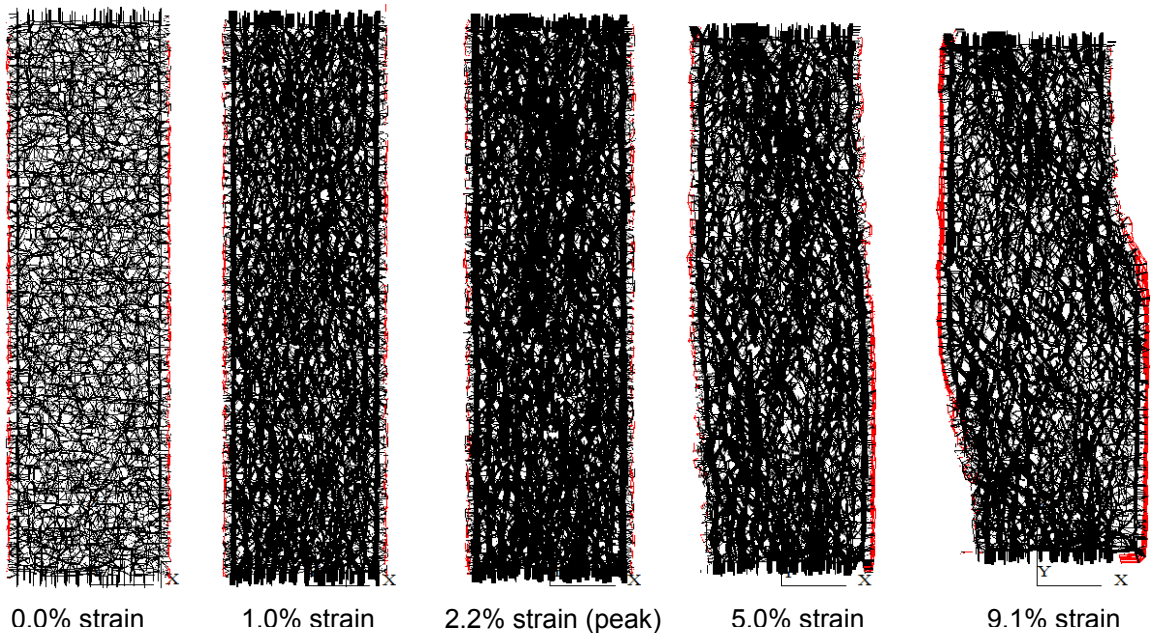

Figure 6.53 Normal contact forces in X-Z plane for DEM_MTSD

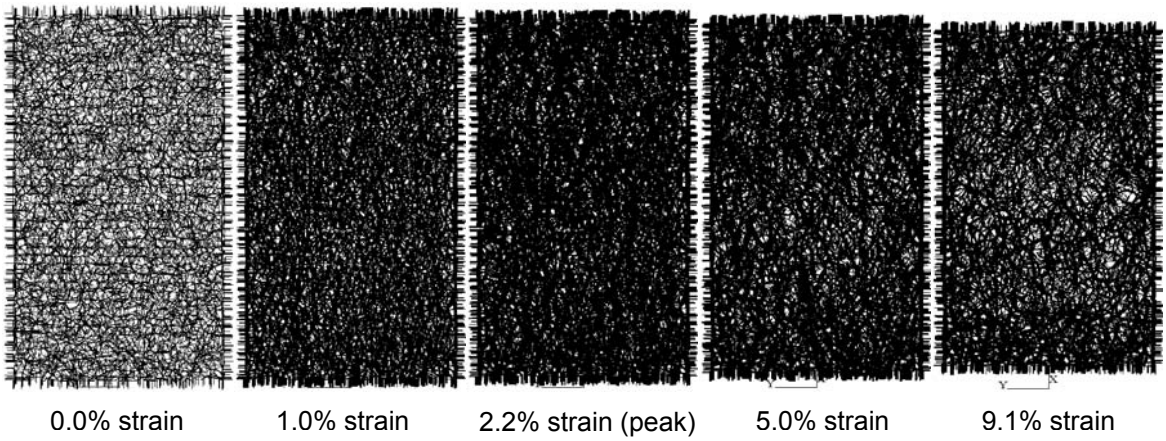

Figure 6.54 Normal contact forces in Y-Z plane for DEM_MTSD

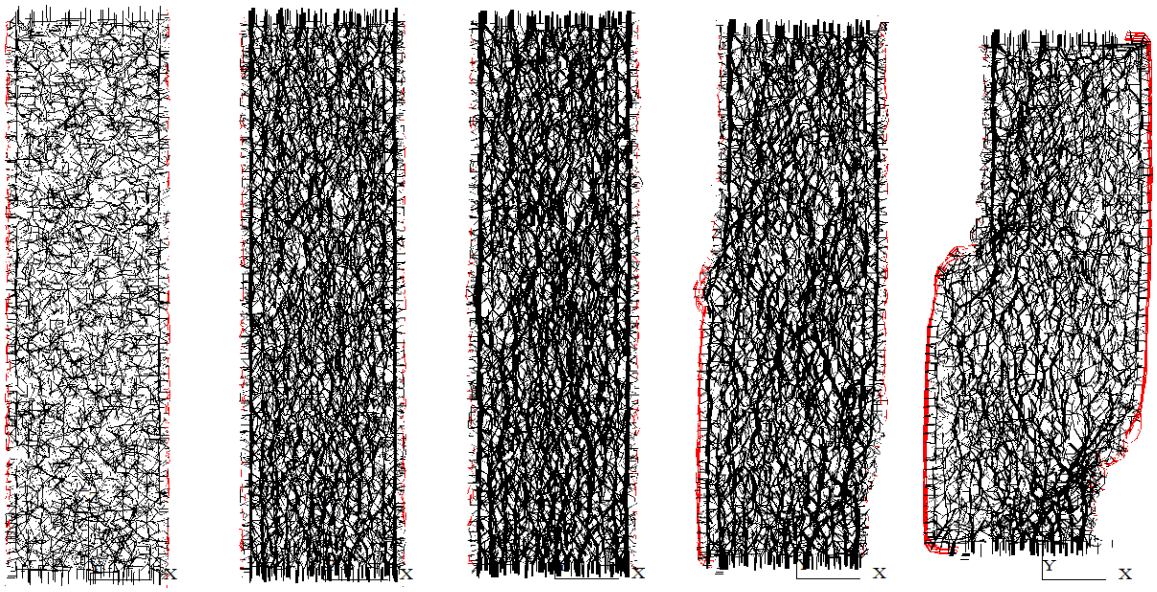

Figure 6.55 Normal contact forces in X-Z plane for DEM_APHD

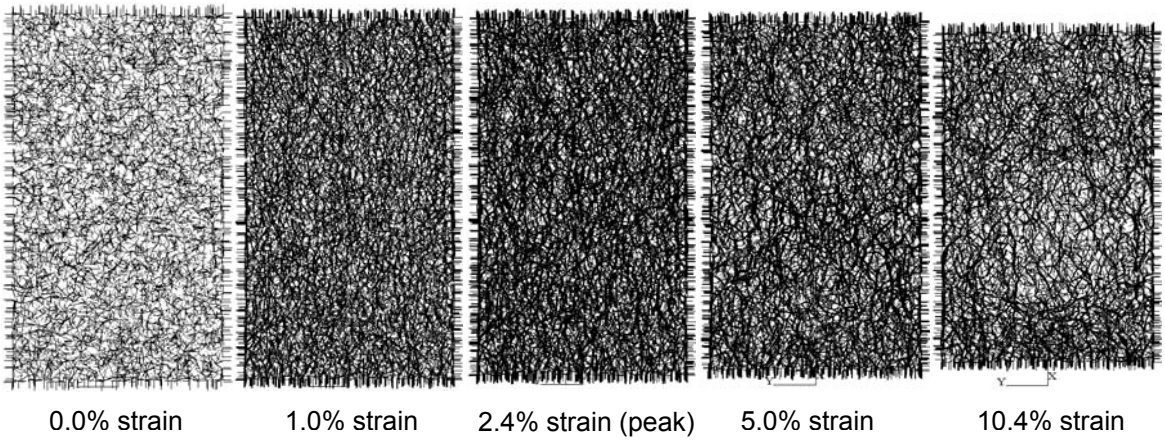

Figure 6.56 Normal contact forces in Y-Z plane for DEM_APHD

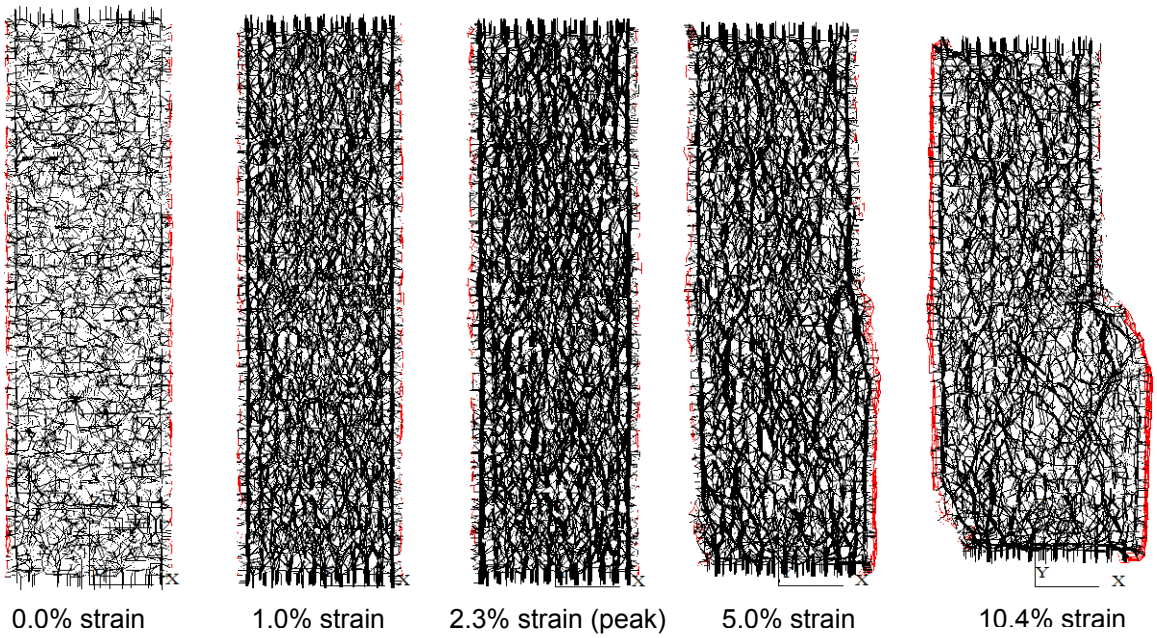

Figure 6.57 Normal contact forces in X-Z plane for DEM_MTHD

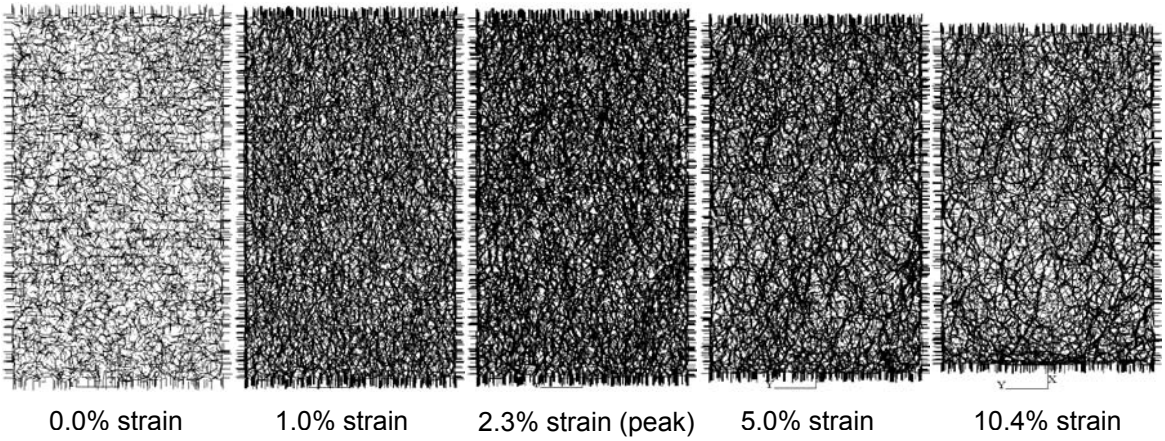

Figure 6.58 Normal contact forces in Y-Z plane for DEM_MTHD

6.4.9. Shear Stress on the Bottom Platen

It is believed that when the specimen is subject to shearing, the shear stress on the end platens will increase due to the accumulation of shear stress inside the specimen. In the experimental tests, such increase of shear stress will mobilize the frictionless bottom sled as noted in Section 3.3.1 and consequently facilitate the shear band development. However, the bottom platen was fixed for the numerical tests, and thus the shear stress on

the bottom platen was plotted to see its evolution at different loading stages. Figure 6.59 illustrates the shear stress on the bottom platen for DEM_APSD. From the beginning, the shear stress showed a gradual increase until the axial strain passed the peak strain. When the strain reached 2.15%, shortly after the peak strain, the shear stress suddenly decreased to zero and then increased in the reverse direction. After the platen shear stress accumulated to a certain level, 2 kPa in this case, it decreased gradually and then fluctuated between ±1 kPa. The platen shear stress of DEM_APHD showed similar developing trend in Figure 6.61. The development of platen shear stress of moist-tamped specimens, DEM_MTSD and DEM_MTHD (Figures 6.60 and 6.62), were different from the air-pluviated specimens. The shear stress remained around zero before it exhibited sudden post-peak increase. After the shear stress accumulated to a certain level, it decreased and fluctuated around 0 kPa. One postulation here is that such drastic change of shear stress in all of the specimens was caused by the collapse of some major force chains and consequent initialization of the shear band. The signs of the drastic shear stress increase for the air-pluviated and moist-tamped specimens were reversed, which indicates the inclination angles of the shear band were in different quadrants. Comparisons of the four tests indicate the following findings: (1) the shear stresses of the slightly dilatant specimens were almost twice the shear stresses of the highly dilatant specimens; and (2) the rapid accumulation of shear stress on the bottom platen took place much later than the peak strains for the moist-tamped specimens. If using the rapid accumulation of shear stress as a sign for shear band initialization, then localization occurred at 0.18 to 0.25% strains later than the peak strain for the air-pluviated specimens, while it occurred 0.61 to 0.76% later than the peak for the moist-tamped specimens.

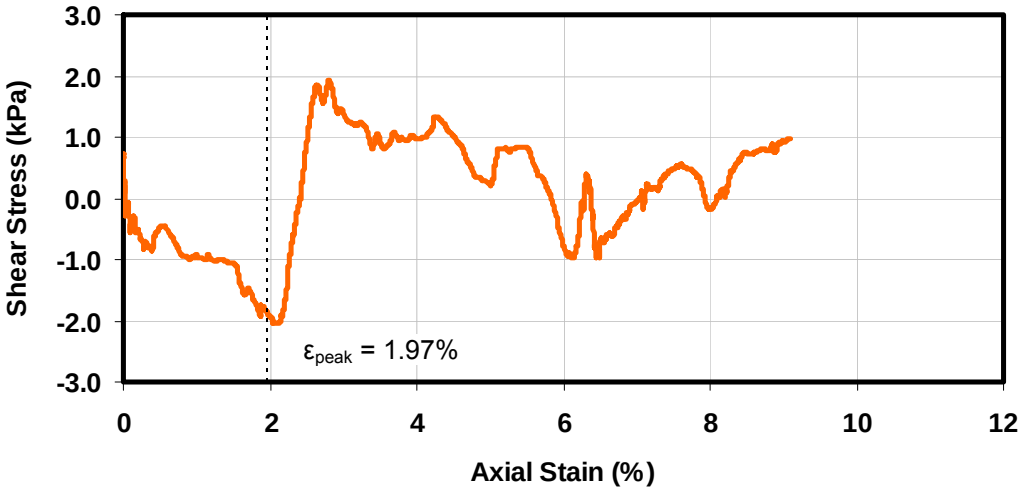

Figure. 6.59 Shear stress on the bottom platen for DEM_APSD

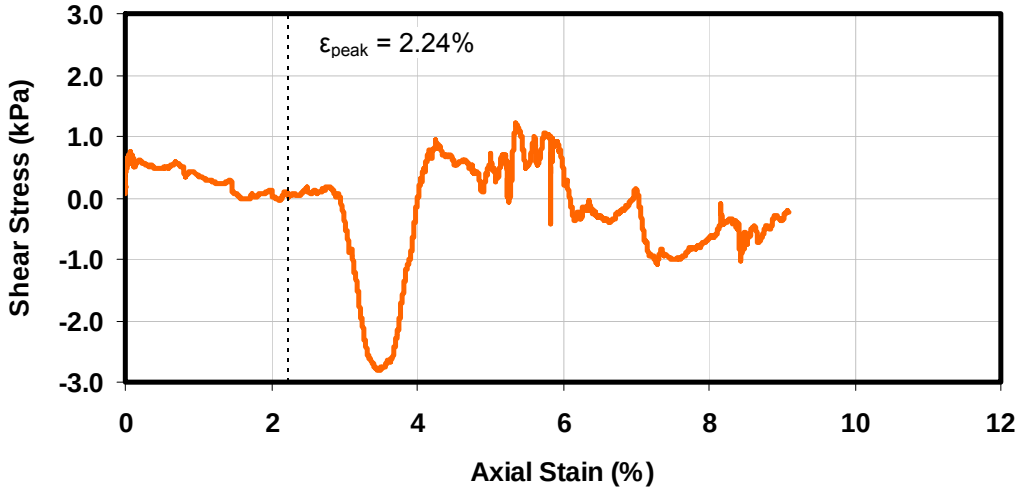

Figure. 6.60 Shear stress on the bottom platen for DEM_MTSD

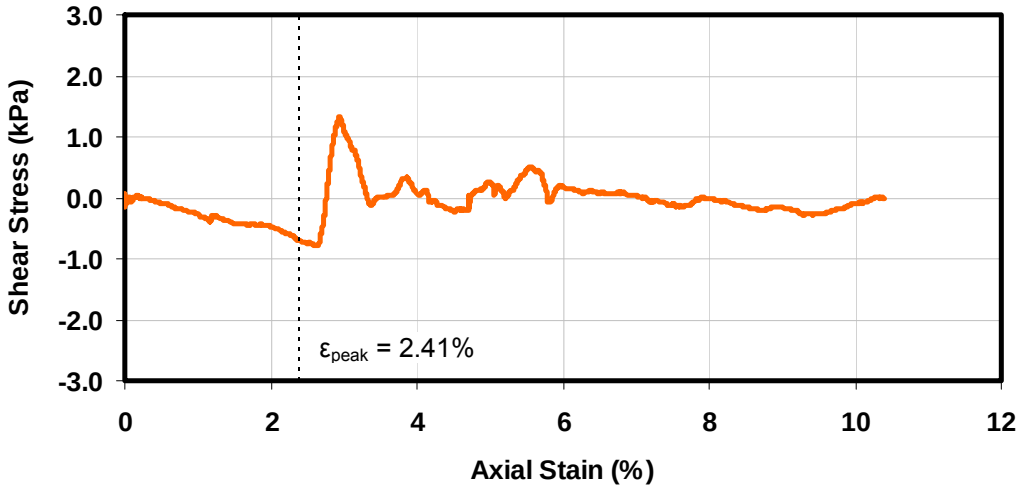

Figure. 6.61 Shear stress on the bottom platen for DEM_APHD

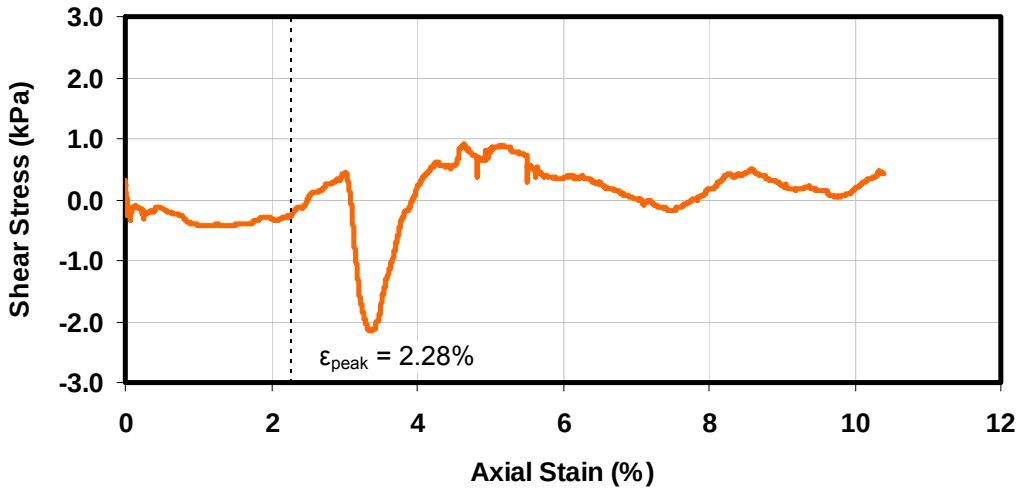

Figure. 6.62 Shear stress on the bottom platen for DEM_MTHD

6.5. Summary and Conclusions

A flexible membrane algorithm was designed and implemented for the numerical biaxial tests. The flexible membrane was modeled using a sheet of simply-packed bonded spheres. The flexible membrane was able to be stretched or contracted as the specimen experienced deformation. To maintain a constant confining pressure on the membrane, a force-controlled servo-mechanism was applied and retrieved the force information on the membrane particles within each calculation circle. For each numerical test, about the same number of particles was used for the membranes as for the specimen. Given the volume of computation related to the membrane particles, it highlights that correct modeling the membrane particles is as equally important as modeling of the specimen particles.

A series of parametric studies were conducted to investigate the effects of different parameters. The investigated parameters were grouped into two categories: (1) the normal stiffness, shear stiffness and friction coefficient of the specimen particles; and (2) the normal stiffness and particle size of the membrane particles. The parametric studies indicated that the normal stiffness of the specimen particles showed more significant effect on the strength behaviors of the specimen than the shear stiffness and

friction coefficient of the specimen particles. The normal stiffness of the membrane particles greatly affected the residual stress, which correlated well with the findings in Frost and Evans (2009) that a non-negligible percentage of the specimen strength measured at the end of shearing was provided by the membranes.

Two groups of numerical biaxial tests, highly dilatant and slightly dilatant, were performed to compare with the experimental biaxial test results. In general, the stress-strain response and the volumetric strain of the simulated tests matched well with the experimental tests. The micro-scale and meso-scale behaviors of the simulated specimens were also characterized to investigate the influence of shear banding. It showed that the localized zone usually featured larger local void ratios, smaller local coordination numbers, larger particle rotations with minor particle displacements and less dense arrays of normal contact forces than the zones outside the shear band. Although the physical biaxial specimens were prepared by a hand pluviator, it is possible that the initial soil fabrics reflected conditions between the air-pluviated state and the moist-tamped state. Therefore, the numerical biaxial tests were performed using the same two preparation methods used in Chapter 4 and compared with the experimental tests. The simulation results showed that the specimen fabrics resulted in different internal microstructural behaviors.

As inclined shear bands initialized and developed in the simulated specimens, the microstructures of the simulated biaxial specimens were characterized and compared with the real specimens in Chapter 7.

CHAPTER 7

CHARACTERIZATION AND VISUALIZATION OF DIGITAL RECONSTRUCTED REAL AND SIMULATED MICROSTRUCTURES

7.1. Introduction

In the current study, two types of digital microstructures were analyzed and characterized – one type was reconstructed from real specimens and the other type was simulated using a discrete element method code. Images for the reconstructed real microstructures were captured from two impregnated biaxial specimens using an optical microcopy serial sectioning technique. Information of the biaxial specimens can be found in Chapter 3 and detailed introduction on the serial sectioning method can be found in Chapter 5. The two reconstructed biaxial specimens were designated as unsheared (UN) and highly dilatant (HD) in the subsequent sections of this chapter. About 430 serial slices were generated for the UN specimen and 600 for the HD specimen. Each of the slices was 1300 x 800 pixels in size and had a 13.96 μm/pixel resolution. The simulated microstructures refer to the biaxial specimens assembled and subsequently sheared in the DEM code PFC3D. The particle information was retrieved from four numerical modeling setups to reconstruct their microstructures, and they were APHDU, APHDS, MTHDU and MTHDS. To make the simulated structures comparable to the reconstructed structures, about 600 serial slices were produced using a dissection algorithm in MATLAB for each specimen. Detailed information regarding the slices of the simulated structures for all specimens will be introduced in Section 7.4.

7.2. Packing Signature Effect

As a particulate material, the behavior of sand is not only affected by the material properties of the particles but also the geometric relationships (fabric) of the particles. These geometric relationships have a significant, but all too frequently ignored, effect on the behavior of particulate materials. To help identify the extent of this effect as well as a framework of understanding, the microstructural characterization and analysis studies that were performed on the reconstructed real and simulated specimens were also implemented for five idealized packings with monosized spheres: Simple Cubic (SCP), Cubic-Tetrahedral (CTP), Tetragonal-Sphenoidal (TSP), Face-Centered Cubic (FCP) and Tetrahedral (TP). These packings have been extensively studied by previous researchers and their void ratios and coordination numbers were reported by Deresiewicz (1958). The monosized spheres used in the packings in this study were 50 pixels in diameter and packed into a cube of 250 x 250 x 250 voxels. For each idealized packing, a serial dissectioning generated 250 slices, each 250 x 250 pixels in size, on 1 pixel spacing in each orthogonal directions (A, B and C). The 2-D void ratio was calculated for each slice by pixel counting, and the results along with the packing information (coordination number, *cn*, and 3-D void ratio) are presented in Figures 7.1 to 7.5. For all the idealized packings, the void ratio per slice along the cumulative removed thickness reveals a wave like signal with certain periods and amplitudes that are directly related to the shape and arrangement of the particles. The presence of a wave-shaped relationship for the void ratio profile is termed as the packing signature effect in the current study. For SCP, for which the coordination number is 6 and the 3-D void ratio is 0.908, the void ratio profiles are the same in the three orthogonal directions. The void ratio profiles of SCP exhibit two features: (1) only one period, equal to the diameter of the monosized spheres which dominates the profiles; and (2) the magnitudes of the void ratios range between 0.28 and infinity. A review of the profiles for all the packings shows that when the coordination number increases, both the periods and magnitudes of the void ratio profiles decrease and

more than one period appears (e.g., FCP and direction C of TSP). Among the five ideal packings, two of them (SCP and FCP) have the same void ratio profiles in three orthogonal directions while the other three (CTP, TSP and TP) do not. It appears that the void ratio profiles contain specific information related to the packing, and it is likely that some microstructural information can be extracted from the profiles. Wile the packing signature effect is readily discernable in the idealized packings, the degree to which the packing signature effect will exist in the characterization results of the reconstructed real and simulated specimens remains unknown, as the specimens are randomly packed (contrary to the ideal packings) and the particles are not ideally spherical and monsized (the grains of Ottawa sands are sub-rounded and the particles of the numerical specimens are 2-ball clumps).

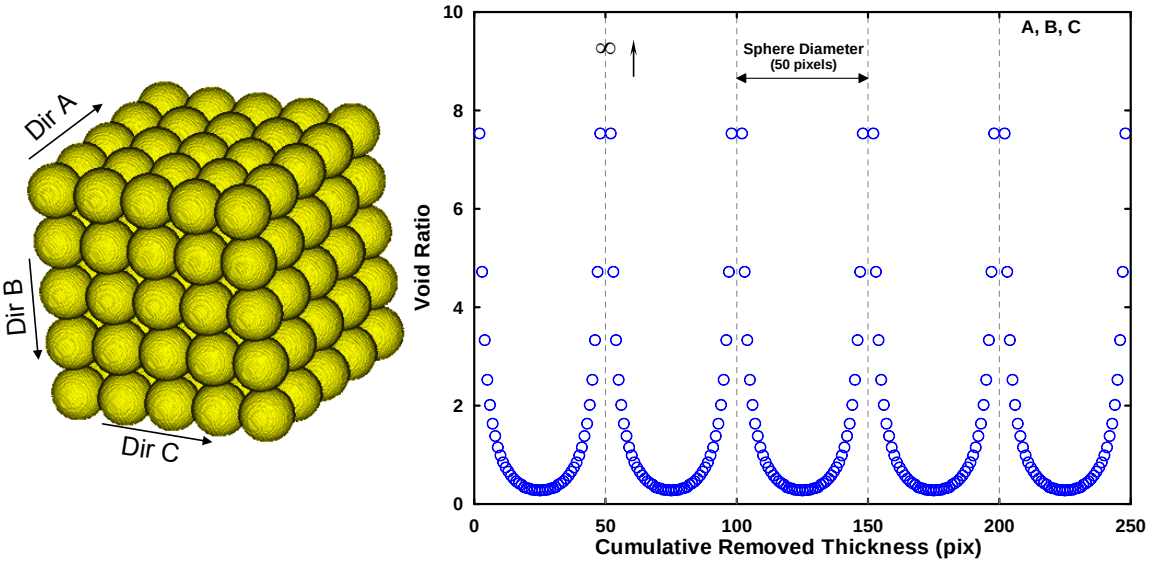

Figure 7.1 2-D void ratio for Simple Cubic Packing

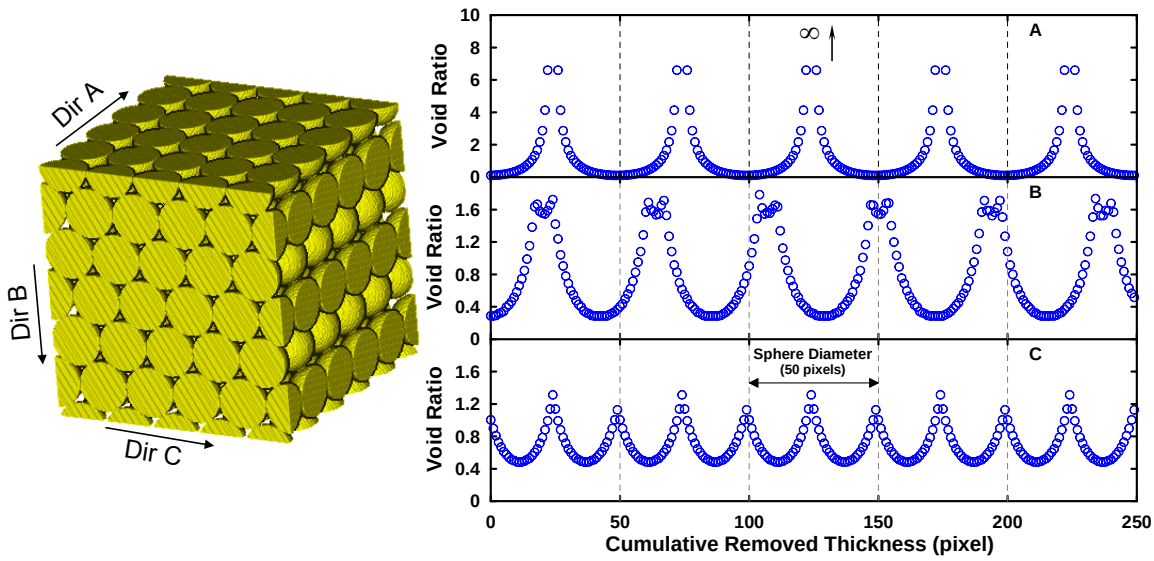

Cubic-Tetrahedral Packing (CTP), cn = 8, 3D void ratio = 0.652

Figure 7.2 2-D void ratio for Cubic-Tetrahedral Packing

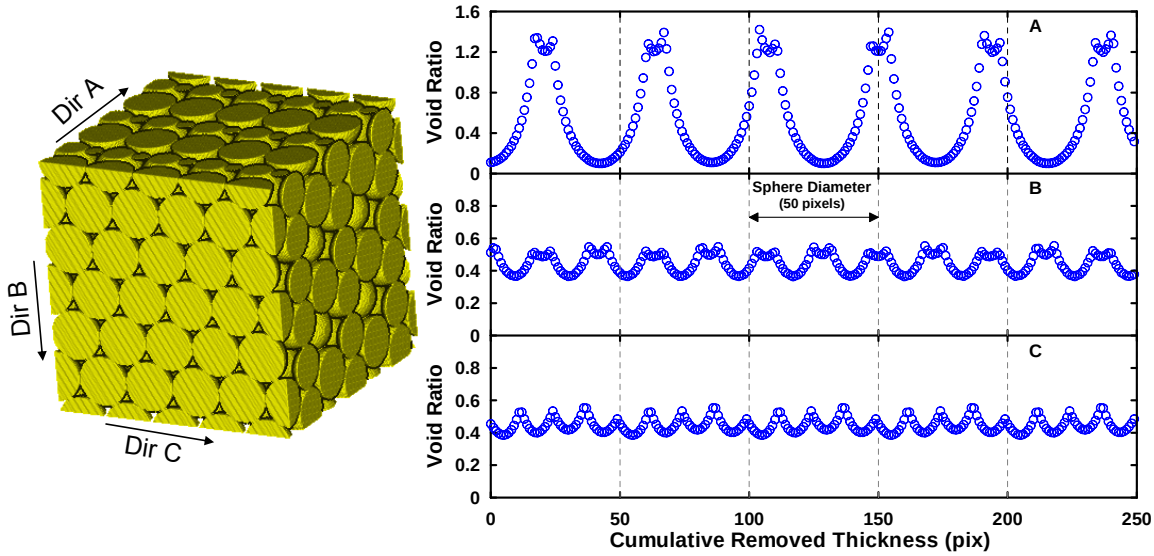

Tetragonal-Sphenoidal Packing (TSP), cn = 10, 3D void ratio = 0.432

Figure 7.3 2-D void ratio for Tetragonal-Sphenoidal Packing

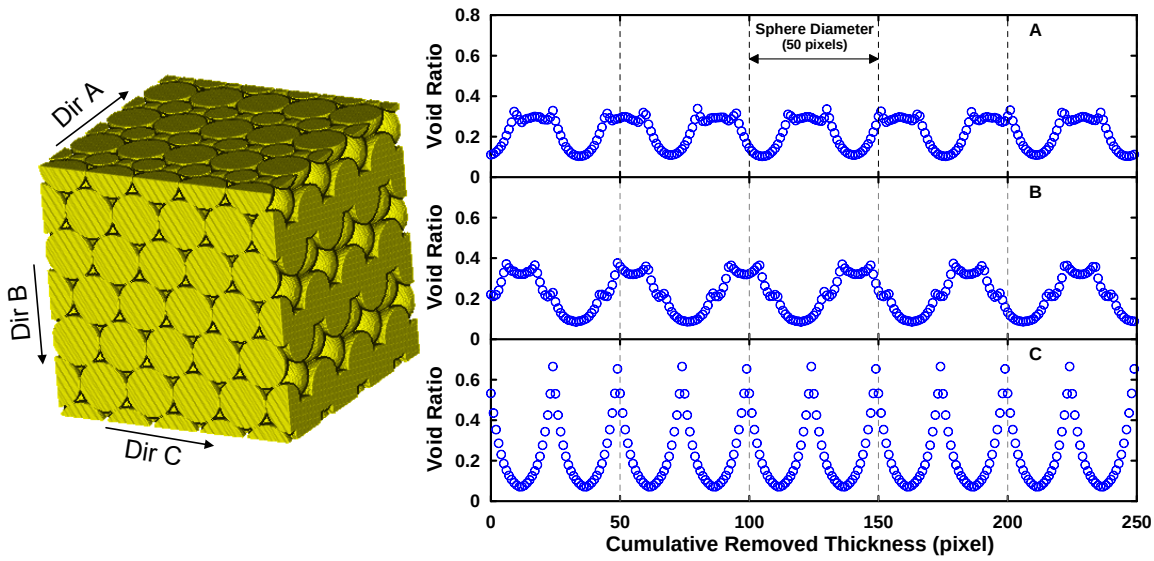

Tetrahedral Packing (TP), cn = 12, 3D void ratio = 0.351

Figure 7.4 2-D void ratio for Tetrahedral Packing

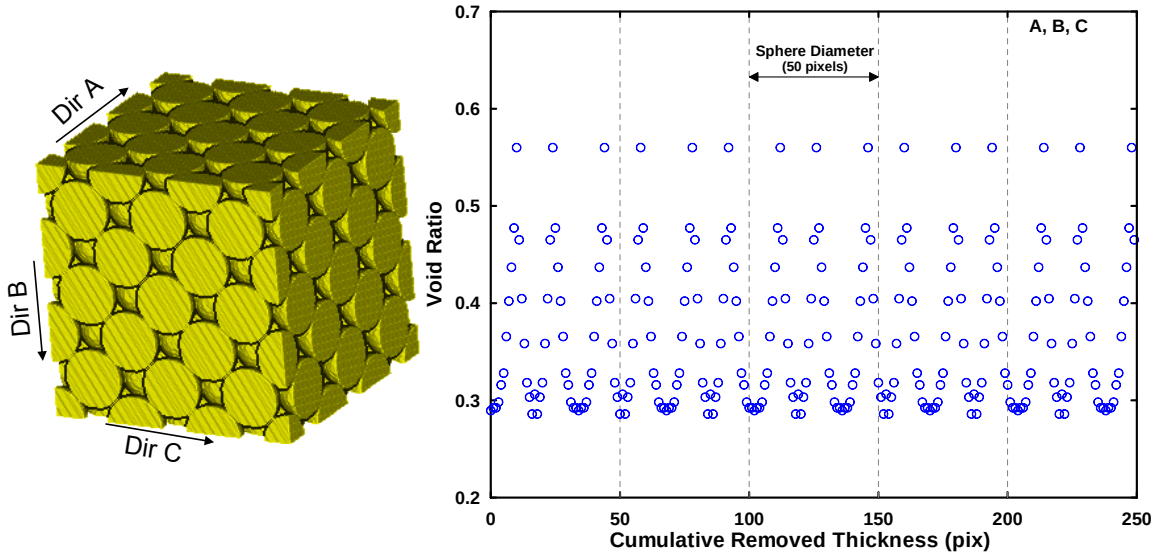

Face-Centered Cubic Packing (FCP), cn = 12, 3D void ratio = 0.351

Figure 7.5 2-D void ratio for Face-Centered Cubic Packing

7.3. Reconstructed Digital Microstructures

In this section, a series of 2-D and 3-D analyses and characterizations were performed on the 2-D serial slices of the reconstructed real specimens.

7.3.1. Void Ratio Per Slice

A straightforward calculation of void ratio was made for each 2-D slice by counting the total number of void pixels and the total number of solid pixels. Although such void ratio is a general value for one slice, it is different from the global void ratio of the entire specimen. Therefore, it is designated as void ratio per slice.

7.3.1.1. 2-D Analysis

The void ratio per slice is plotted versus the cumulative removed thickness in Figure 7.6 for UN. Although scattered by some "noise", the void ratio profile clearly indicates the presence of packing signature effect. This phenomenon was not originally expected for the reconstructed real specimens. It is more reasonable to expect that when a specimen is composed by tens or hundreds of thousands of non-spherical multi-sized particles, the void ratio of each slice that sections through it should be constant, as the number of particles that appears on any slice roughly balances the number of particles that disappears from the slice. However, Figure 7.6 proves the existence of a packing signature effect inside the reconstructed Ottawa sand specimens. The periods of the void ratio profiles are somewhat related with the particle size (D_{50}) and the maximum amplitude of void ratio is 0.120. Here the amplitude of the void ratio profile is defined as the difference between a data point and the average line. Figure 7.7 presents the variation of void ratio with cumulative removed thickness for the HD specimen. As the specimen contains the shear band, the average void ratio is higher than that of UN. Similar to UN, the periods of the void ratio profile are D_{50}-related, and the maximum amplitude is 0.077 which is about 14% of the average void ratio (0.567). To make sure that the packing

signature effect was not caused by some external factors like operational errors during serial sectioning, loading conditions and boundary conditions, the serial slices produced in the previous 3-D reconstruction study were examined. These slices were captured from four triaxial specimens by Yang (2005) using a similar serial sectioning technique. The triaxial specimens were AP0, AP14, MT0 and MT14, with the designation 'AP' for air-pluviated, 'MT' for moist-tamped, '0' for 0% global axial strain, and '14' for 14% global axial strain. About 600 slices were generated for each specimen, and each slice was 1800 x 1100 pixels in size and 7.83 μm/pixel in resolution. The void ratio per slice was calculated and the results are presented in Figures 7.8 to 7.11. Although there is more noise scattered in the profile, the packing signature effect still can be recognized for the four triaxial specimens.

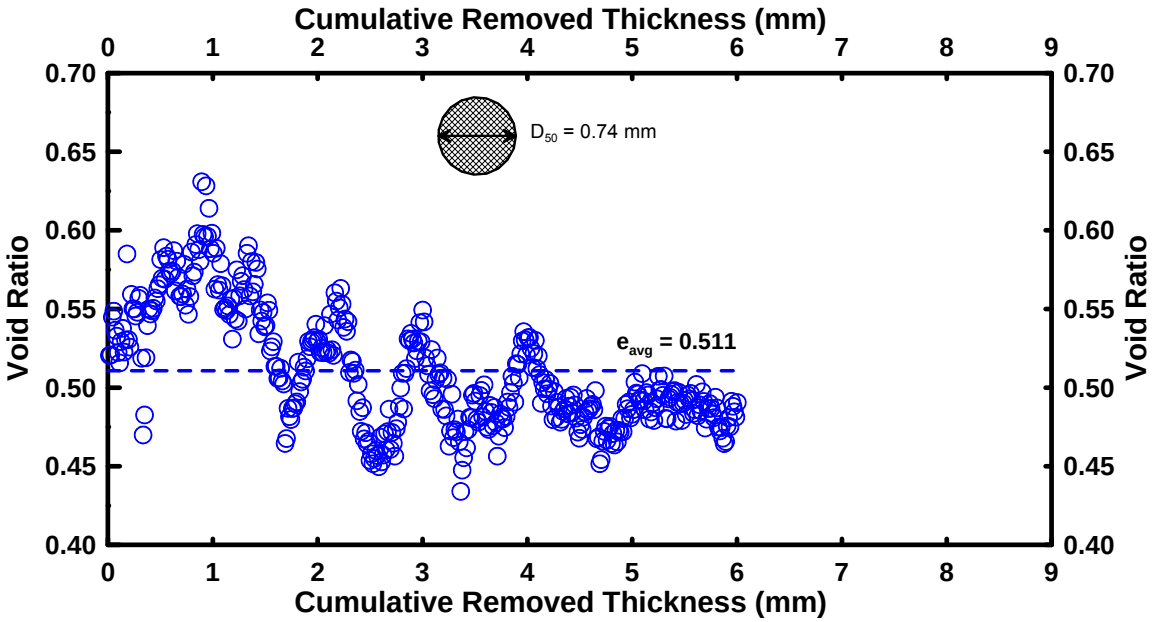

Figure 7.6 Variation of void ratio with removed thickness for UN

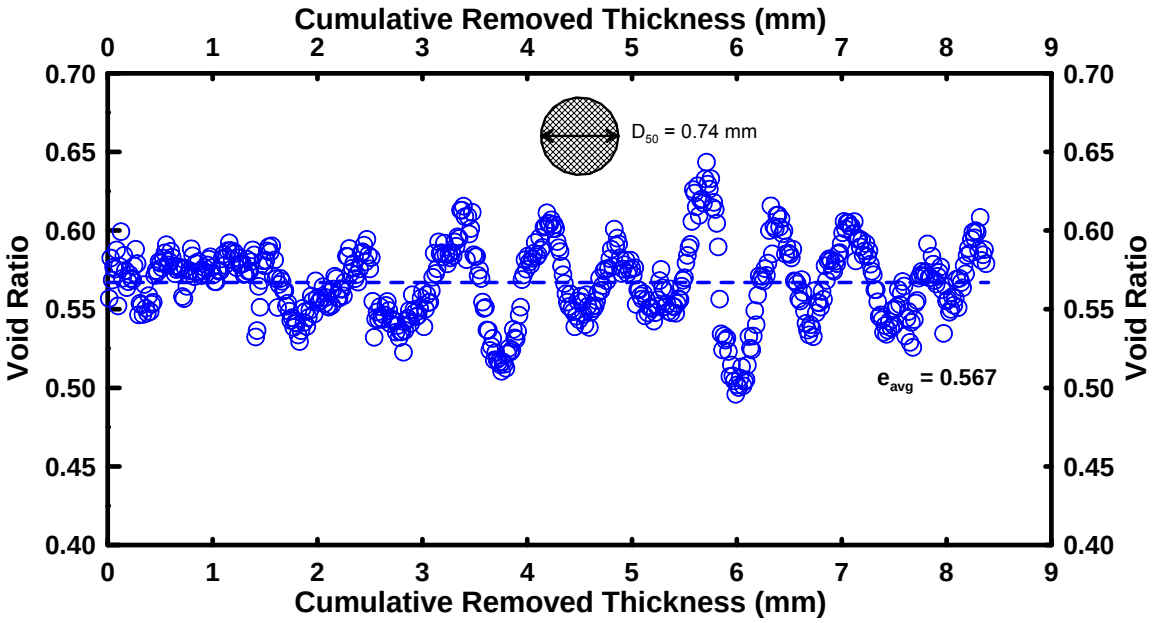

Figure 7.7 Variation of void ratio with removed thickness for HD

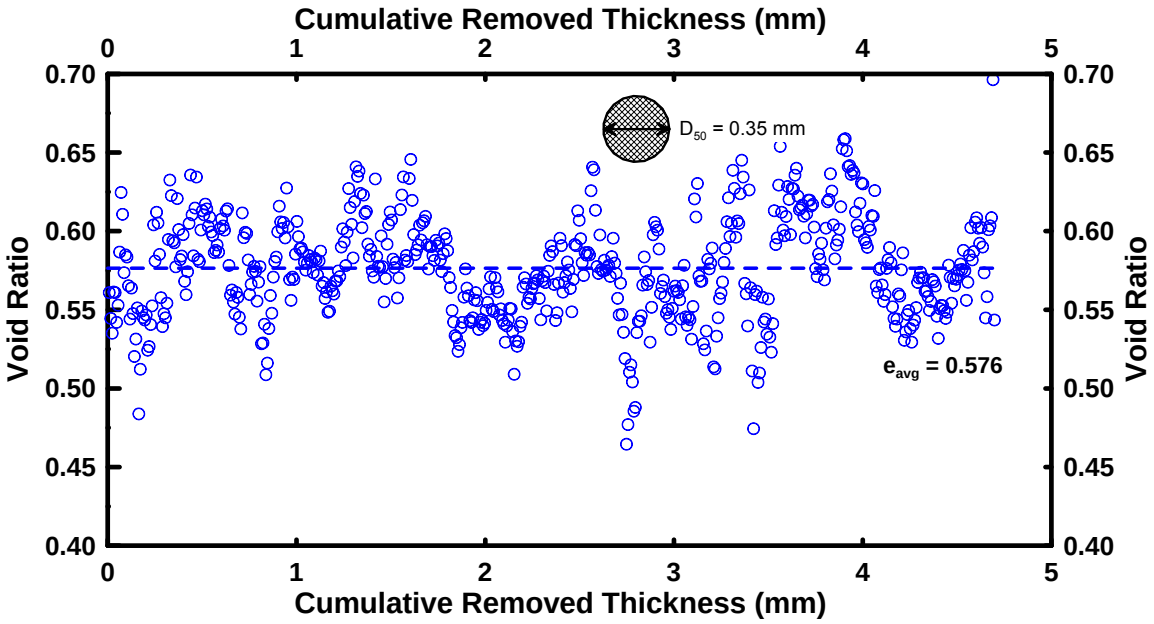

Figure 7.8 Variation of void ratio with removed thickness for AP0 (triaxial)

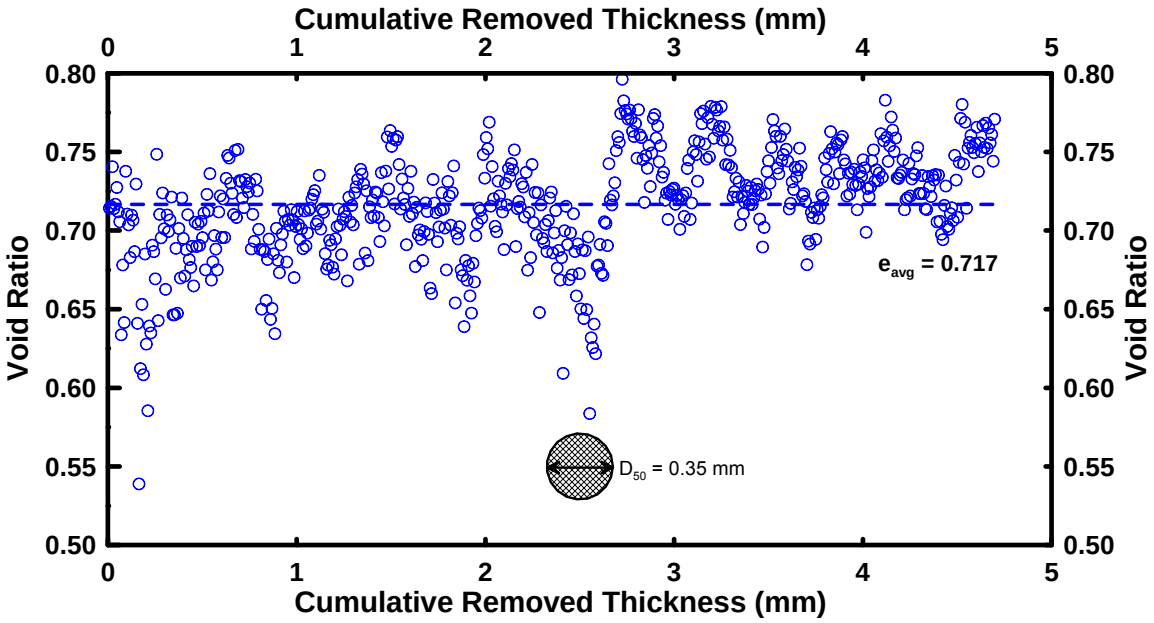

Figure 7.9 Variation of void ratio with removed thickness for AP14 (triaxial)

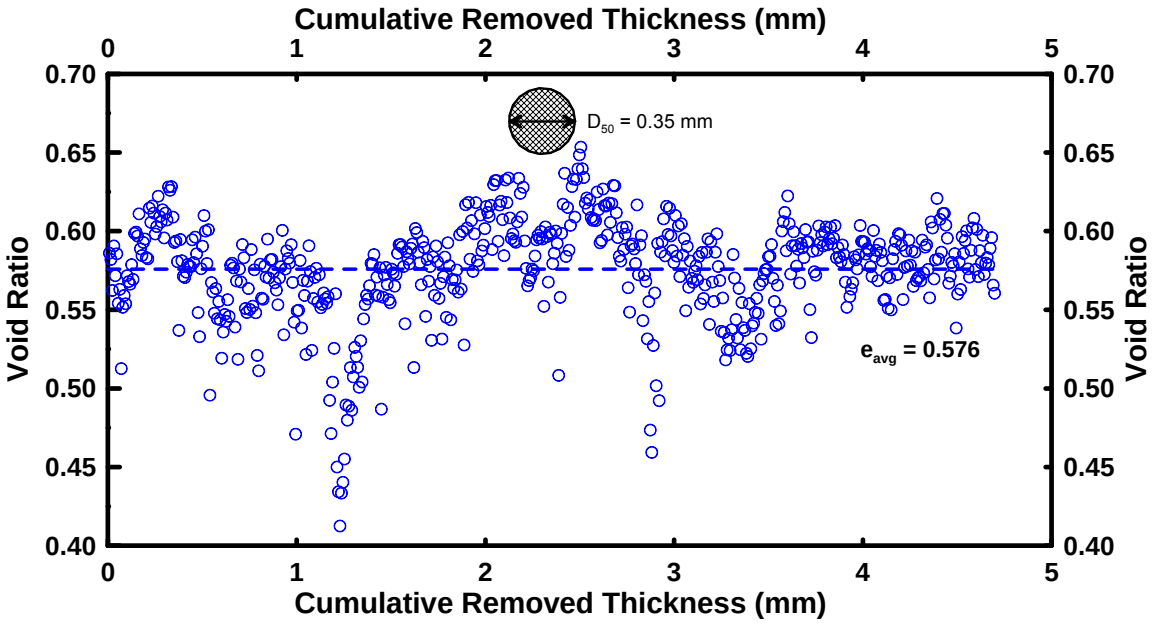

Figure 7.10 Variation of void ratio with removed thickness for MT0 (triaxial)

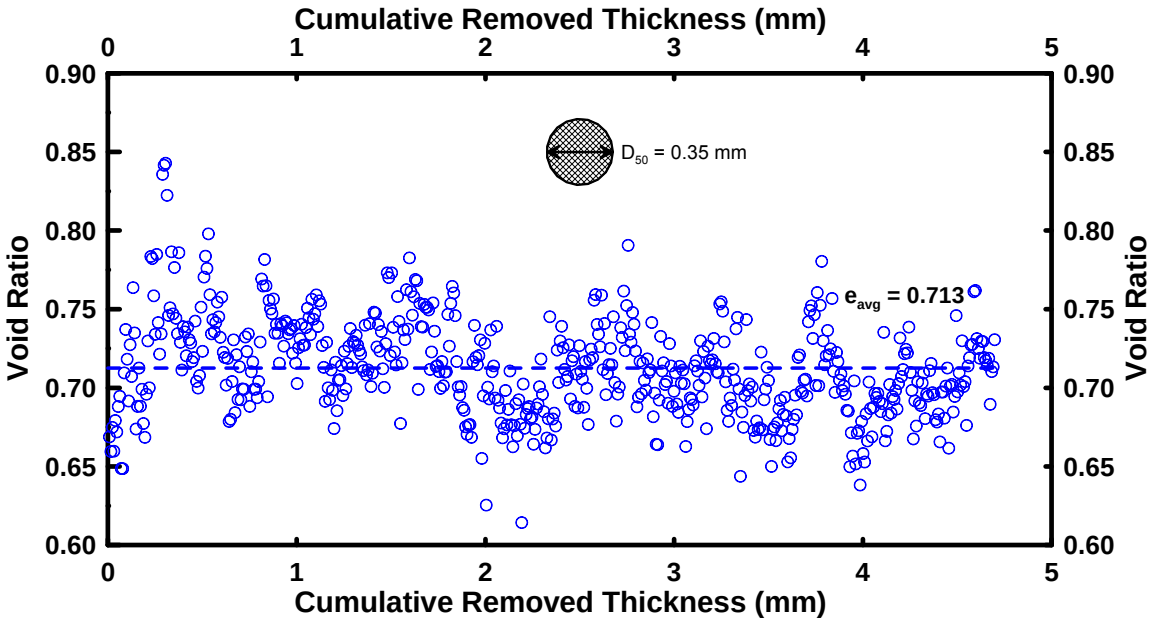

Figure 7.11 Variation of void ratio with removed thickness for MT14 (triaxial)

7.3.1.2. 3-D Analysis

When performing the serial sectioning of the real specimens in the present study, each slice was imaged after every 14 μm of materials were removed. That means the slices were spaced at 14-μm interval, the same as their image resolution. Therefore, it is feasible to generate new slices in other orthogonal directions just by converting the 2-D slices. Figure 7.12 illustrates a 3-D view of UN specimen. The slices captured from the serial sectioning were orthogonal to the intermediate principal stress and designated as primary slices A. Two sets of secondary slices were produced from the primary slices using MATLAB, one of which was orthogonal to the major principal stress and designated as slices B, and the other one was orthogonal to the minor principal stress and named slices C. The secondary slices are shown in 2-D view in Figure 7.13. Dimensions of the slices were 1300 x 800 pixels for A, 1300 x 430 pixels for B, and 800 x 430 pixels for C. The approximate number of particles contained in the slices was 312 in A, 169 in B, and 104 in C. The void ratios were calculated for those slices and plotted against the cumulative removed thickness in Figure 7.14. Similar to slices A, the void ratios

calculated from slices B and C were also affected by the packing signature effect and varied between 0.45 and 0.60. In contrast to slices A, the void ratio profiles for slices B and C were absent of noise, and hence the effect of beat function (the phenomenon of wave amplitude canceling or magnifying each other when two different waves are superimposed) could be readily observed. The cause of the noise in the primary slices may be minor operational errors during the serial sectioning. When performing the serial sectioning to produce slices A in the laboratory, the removed thickness was controlled within 14 ± 2 μm and the sectioned surfaces were not perfectly level due to the limitations of the experimental apparatuses. However, when generating the secondary slices using MATLAB, the slice spacing was controlled exactly at 14 μm and the sectioned surfaces were perfectly level.

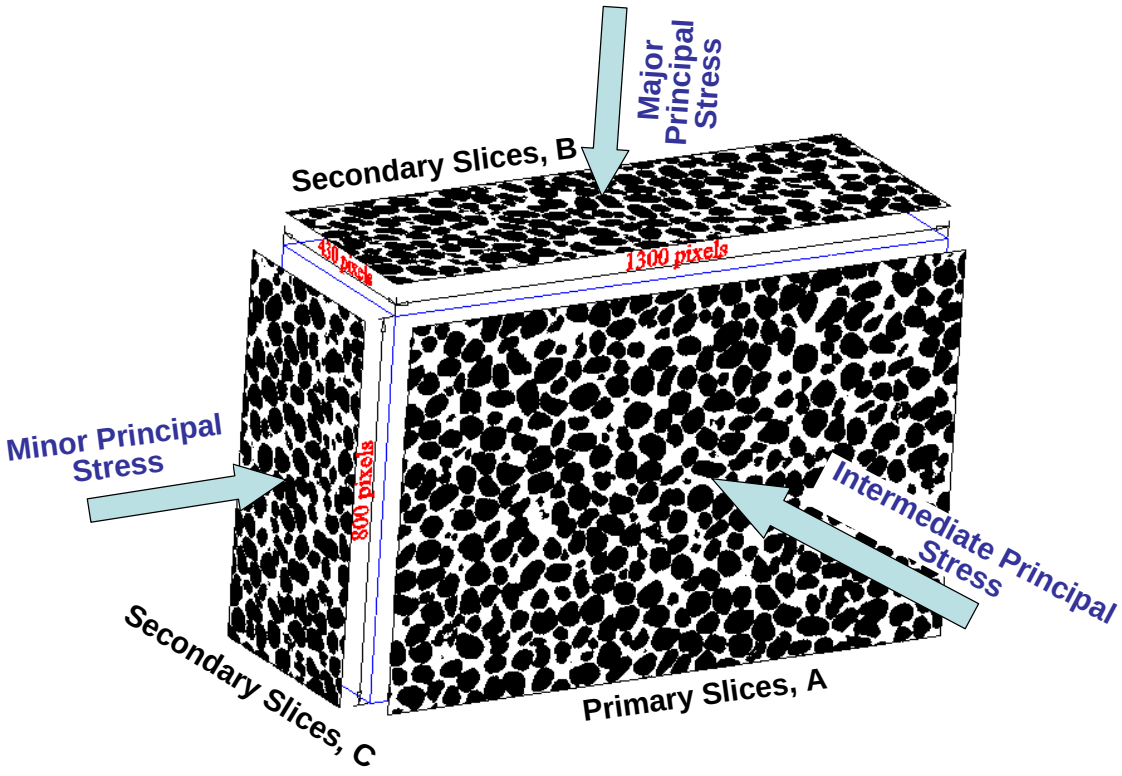

Figure 7.12 3-D schematic view of the primary and secondary slices for UN

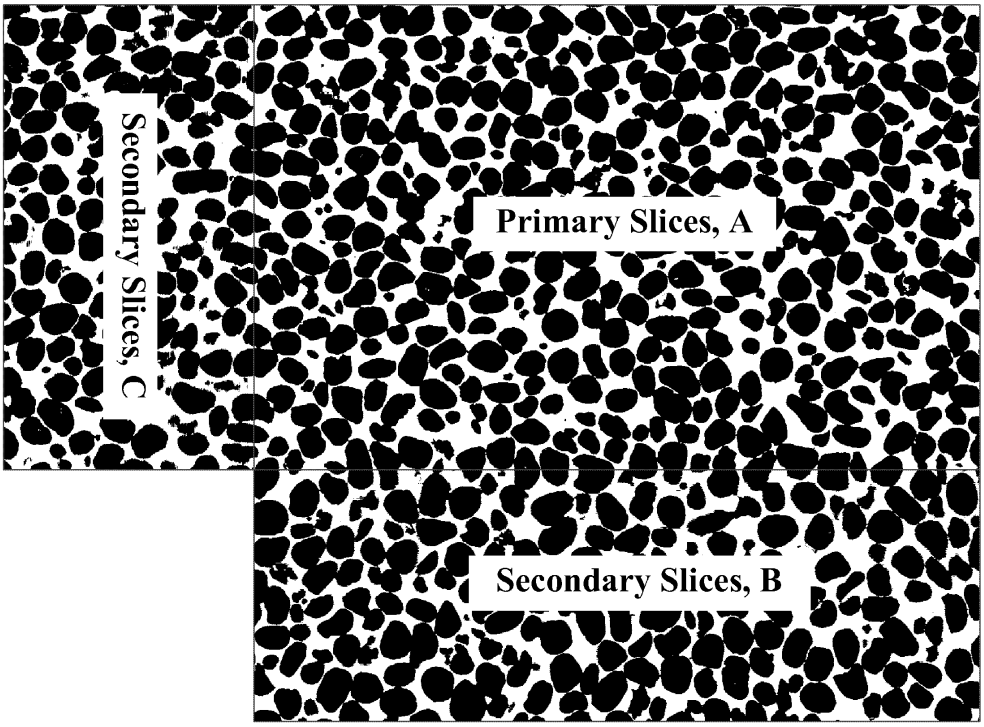

Figure 7.13 2-D schematic view of the primary and secondary slices for UN

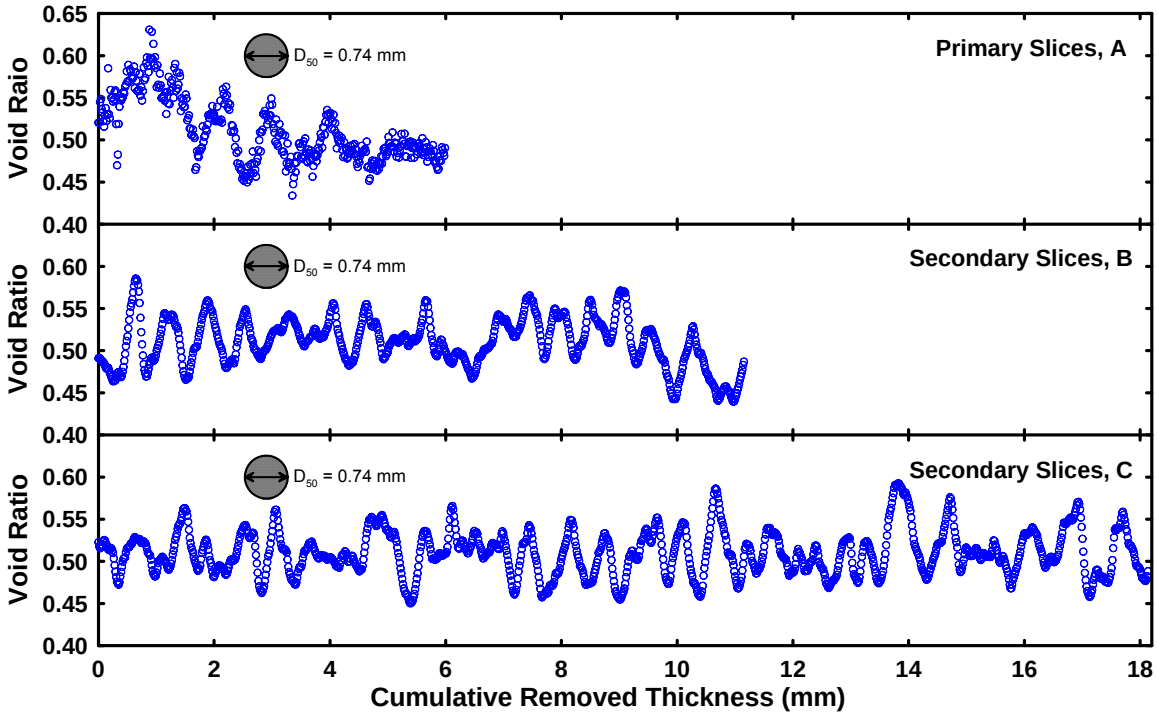

Figure 7.14 Variation of void ratio in three orthogonal directions for UN

The same secondary slices were generated for the HD specimen, and they are illustrated in Figure 7.15 for 3-D view and Figure 7.16 for 2-D view. Dimensions of the slices were 1300 x 800 pixels for A, 1300 x 600 pixels for B, and 800 x 600 pixels for C. The approximate number of particles contained in the slices was 301 in A, 227 in B, and 139 in C. Figure 7.17 shows the void ratio per slice versus the cumulative removed thickness in three orthogonal directions for HD. Except for the packing signature effect, the void ratio profile of slices C exhibits a plateau in the middle. Such a plateau actually indicates the location and extent of the shear band. The manner in which additional information about the shear band can be extracted from the void ratio profile will be discussed in Section 7.3.4.

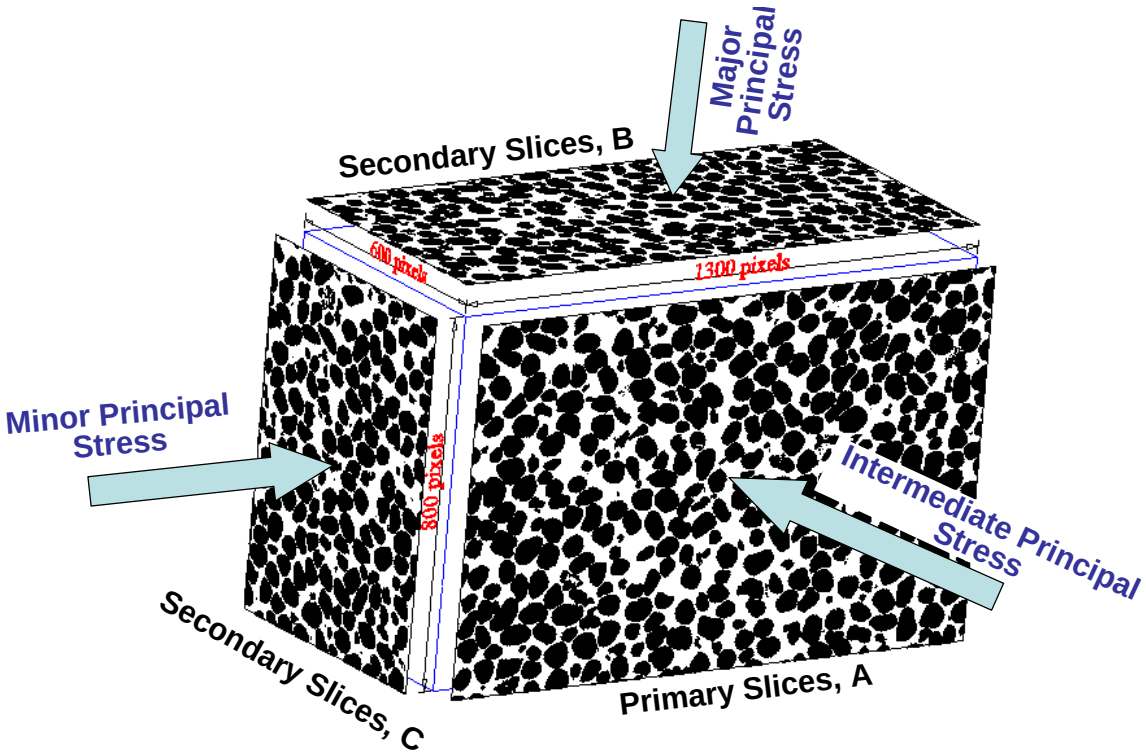

Figure 7.15 3-D schematic view of primary and secondary slices for HD

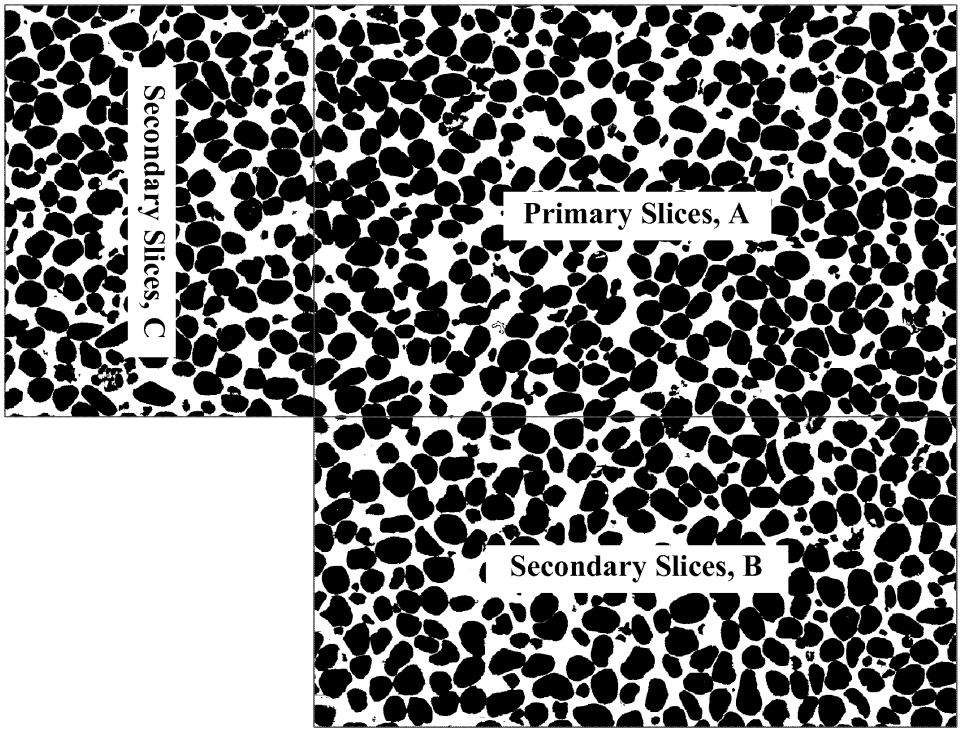

Figure 7.16 2-D schematic view of primary and secondary slices for HD

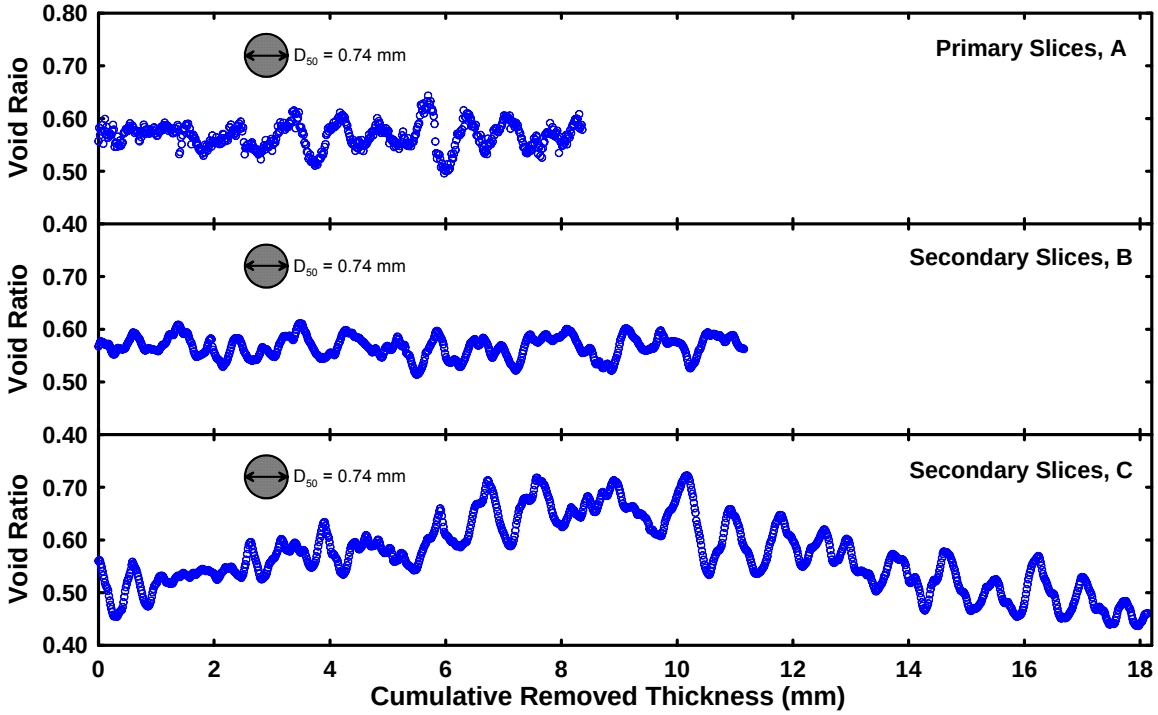

Figure 7.17 Variation of void ratio in three orthogonal directions for HD

7.3.1.3. Effects of Image Size on Packing Signature

To examine how the image size will affect the packing signature effect, void ratio per slice was calculated within a series of counting frames. The sizes of the counting frames were in a descending order and their centers were fixed to the center of the specimen for UN and the center of the shear zone for HD. The definition of the shear zone is different from the shear band, and a detailed description can be found in Section 7.3.2.2. Three such counting frames are presented in Figure 7.18 for UN and in Figure 7.19 for HD. The void ratios quantified within the different counting frames are plotted against the cumulative removed thickness in Figures 7.20 and 7.21 for UN and HD, respectively. As the counting frames decreased in size, the following observations were noted: (1) the average line was raised; and (2) the amplitudes increased slightly. If defining the average void ratio as the baseline, a roughness parameter, root mean square roughness, can be used to characterize the relationships between the image size and the packing signature effect. The root mean square roughness, R_{RMS}, is expressed by the following equation:

$$R_{RMS} = \sqrt{\frac{1}{L} \cdot \sum_{i=0}^{j} \left(e_i - e_{avg}\right)^2} \tag{7.1}$$

where L is the total removed thickness, e_i is the void ratio per slice, and e_{avg} is the average over all of the void ratios. R_{RMS} is plotted versus the area of counting frames in Figure 7.22, and the approximate number of particles contained in each counting frame is also listed. In general, two slopes can be defined for the R_{RMS} curve. When the number of particles contained in the counting frame was less than 110~120, R_{RMS} decreased quickly as the counting area increased. When the number of particles contained in the counting frame increased to more than 110~120, R_{RMS} showed minor decrease with the increase of counting areas. This means when the number of sampled particles was less than 110, the amplitudes of the void ratio profile would increase drastically and the packing signature effect became prominent. The root mean square roughness was also calculated for the

triaxial specimens from Yang (2005) in Figure 7.23. Due to the similarity of data, R_{RMS} curves of MT0 and MT14 are not emphasized and the number of particles included in each counting frame is not listed. For the triaxial specimens, the slope of R_{RMS} curves significantly decreased when the number of particles exceeded 180 to 200 and tended to stabilize when the number of particles approached 300. Based on the analyses of the biaxial specimens (Ottawa 20-30 sands) and the triaxial specimens (Ottawa 30-50 sands), the packing signature effect tended to stabilize when more than 300 particles were included in one slice.

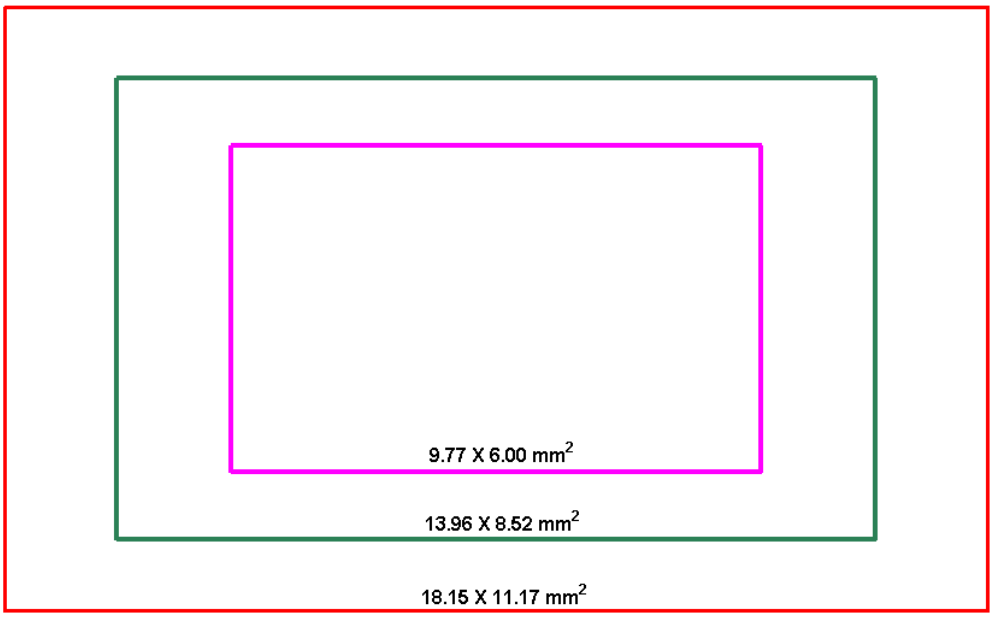

Figure 7.18 Sizes and positions of the counting frames for UN

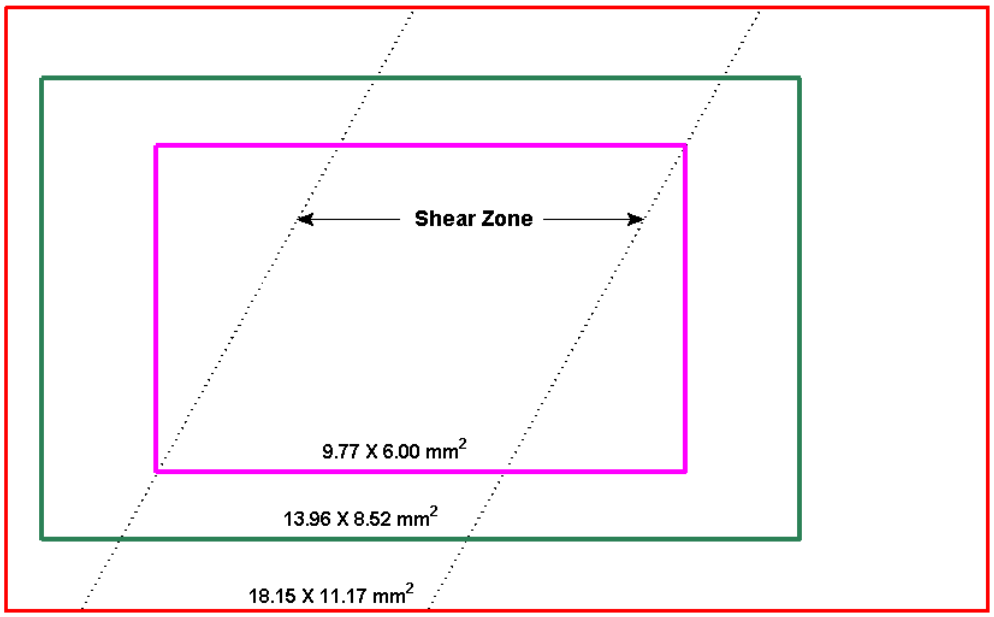

Figure 7.19 Sizes and positions of the counting frames for HD

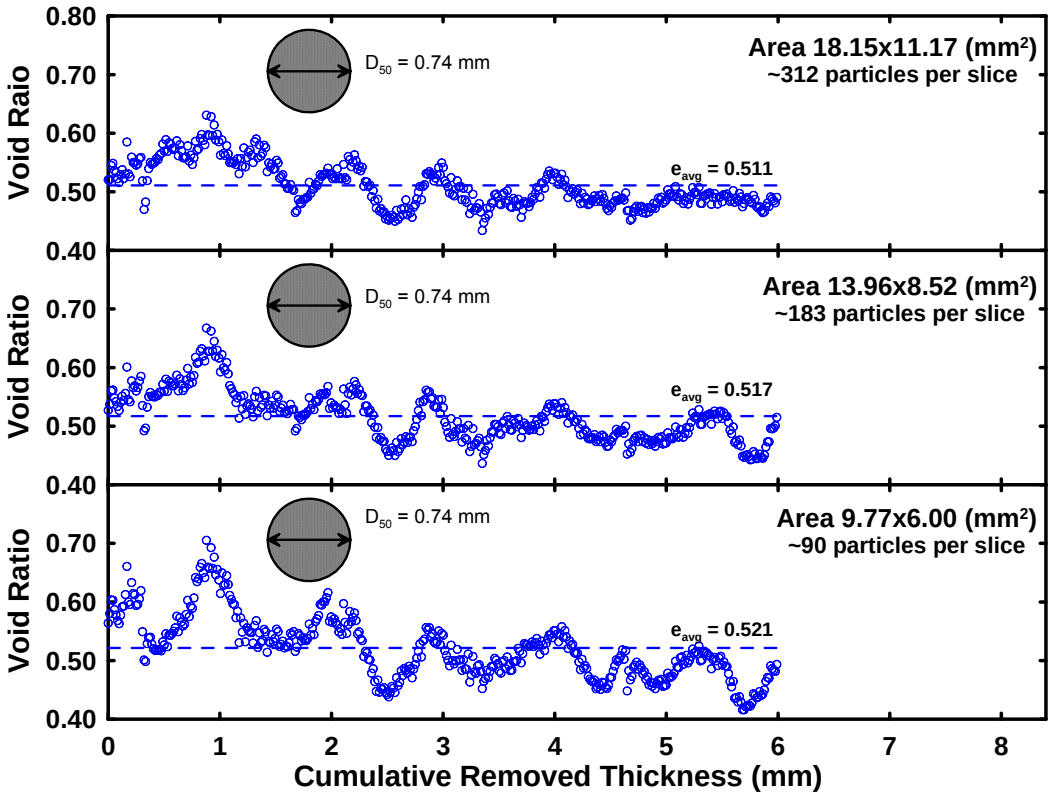

Figure 7.20 Void ratios calculated within different counting frames for UN

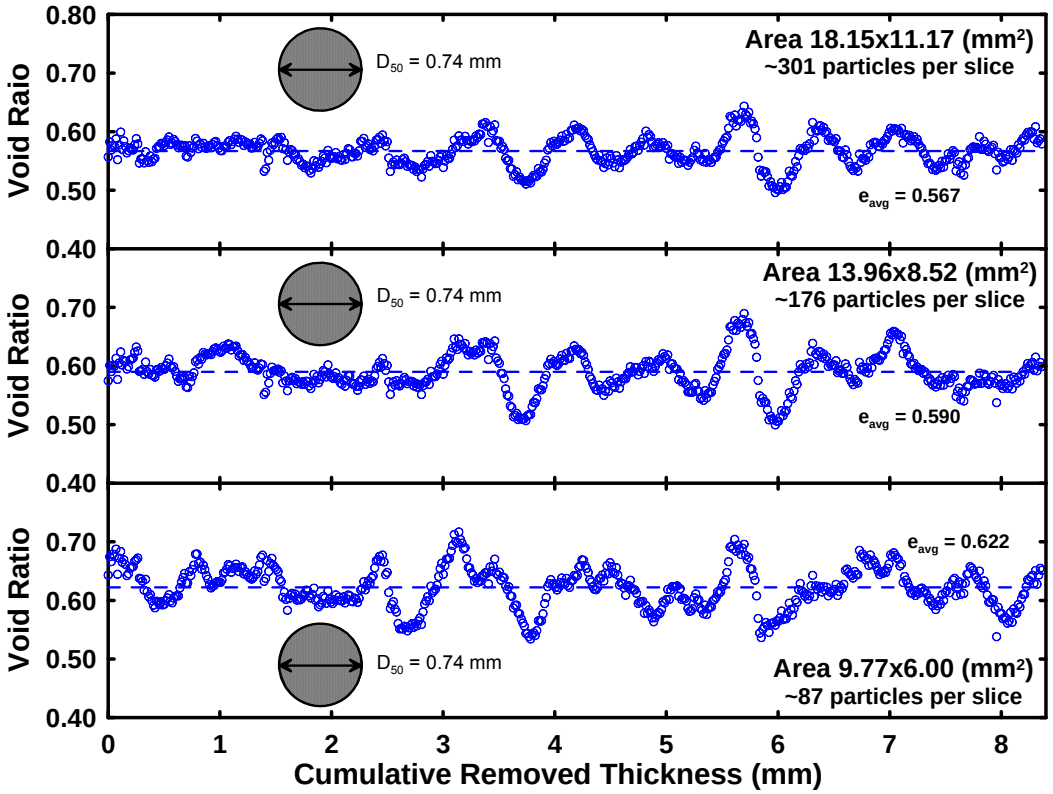

Figure 7.21 Void ratios calculated within different counting frames for HD

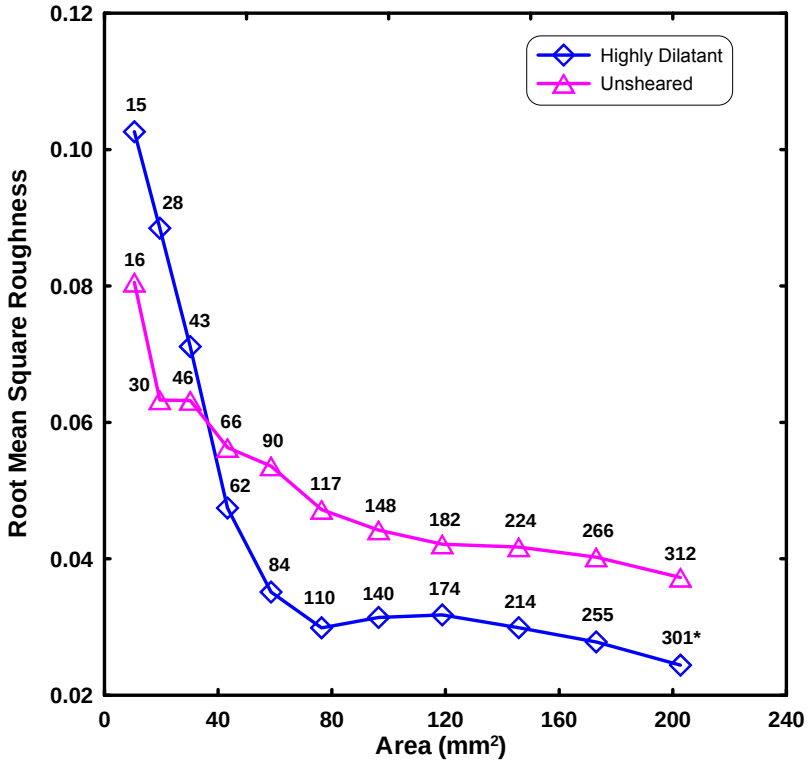

Note: *Approximate number of particles contained in the designated counting frame.

Figure 7.22 Root mean square roughness for void ratio variation of biaxial specimens

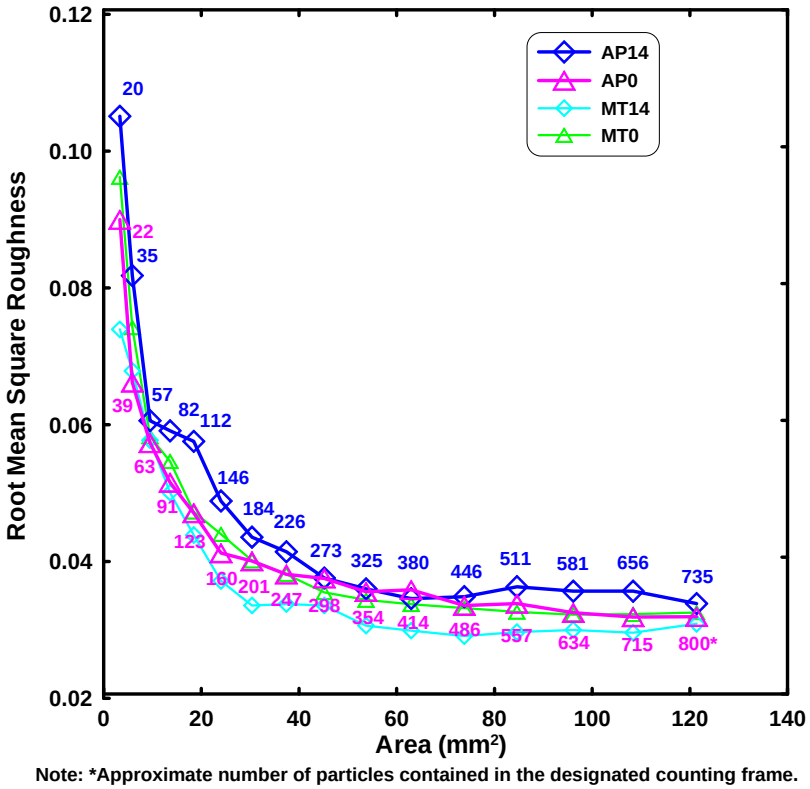

Figure 7.23 Root mean square roughness for void ratio variation of triaxial specimens

7.3.2. Spatial Averaging Along Pre-Determined Inclined Strips

The spatial averaging analysis along pre-determined inclined strips performed at part of this study followed the same procedures proposed by Evans (2005). In the current study, the slices were divided into 50-pixel (0.70 mm, approximately D_{50}) wide strips parallel to the shear band, as illustrated in Figure 7.24. Inclination angle of the shear band was 61° based on the measurement for highly dilatant (HD) specimen from Evans (2005). The void ratio was calculated within each strip by counting the pixels belonging to the grains and the pixels belonging to the voids. The calculated results were plotted as the function of distance along a transect normal to the shear band. The transect traversed the slice from the corner above the shear band (U) to the corner below the shear band (L). Such analysis was done in both 2-D and 3-D and will be called 'strip' analysis in the following sections.

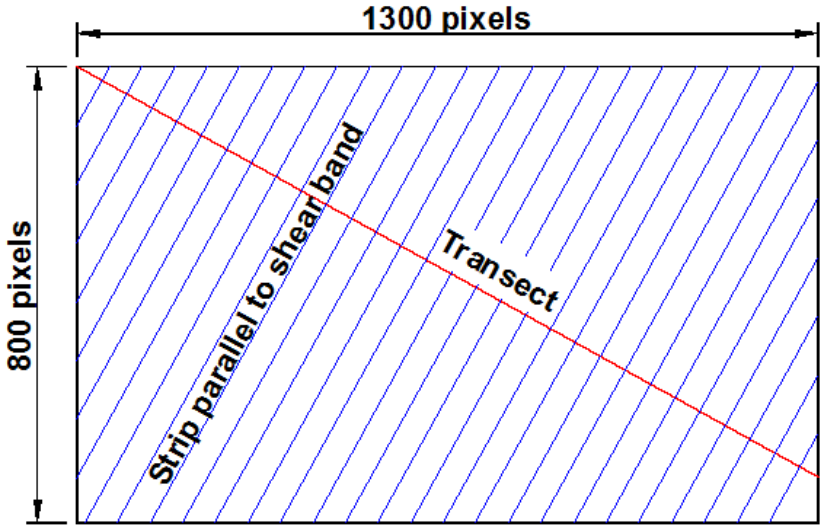

Figure 7.24 Schematic view of the pre-determined strips

7.3.2.1. 2-D Analysis

2-D strip analysis was performed on each serial slice and the results are shown in Figure 7.25 for UN. To make the plot discernable, void ratio curves are presented for selected slices, i.e., slice #001, #021, #041, #061, etc. Although the averaged curve was fairly constant, the void ratio curves differed substantially from slice to slice because of the regularly spaced sampling along the void ratio profile. Larger variation between slices occurred at both ends of the transect than in the middle portion. This resulted from the fact that the strips at the ends were the smallest in area. As discussed in Section 7.3.1.3, the packing signature effect will become very substantial when the number of particles included in the slice decreases. The maximum void ratio difference between slices at the end of the transect was 0.820 at 0.70 mm between slice #061 and slice #301, and the maximum void ratio difference in the middle portion was 0.428 at 13.98 mm between slice #061 and slice #421. In order to reduce the slice to slice difference, larger strips, 100-pixel (1.40 mm, approximately 2 x D_{50}) wide strips and 150-pixel (2.09 mm, approximately 3 x D_{50}) wide strips, were used to characterize the slices. The results are

shown in Figures 7.26 and 7.27. As expected, the calculated void ratios were less deviated from slice to slice as the areas of the strips increased.

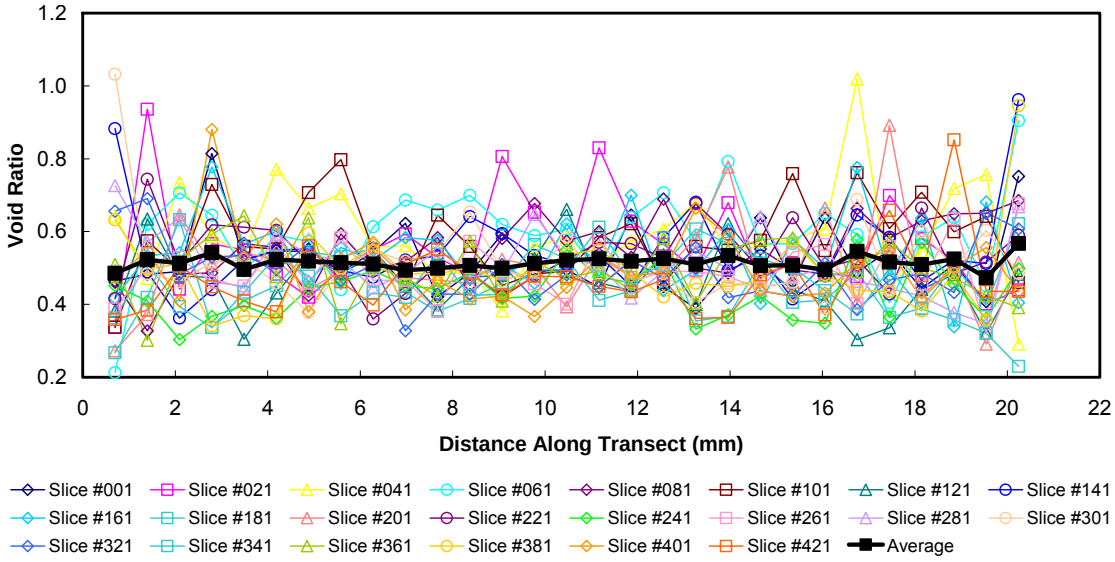

Figure 7.25 Void ratios along the pre-determined strips (50-pixel wide) for UN

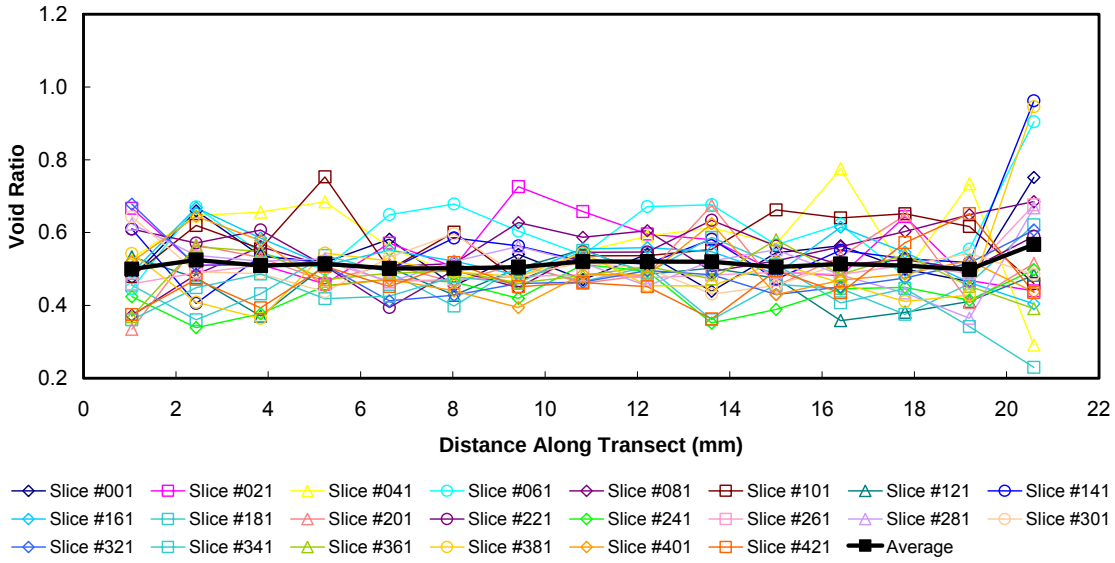

Figure 7.26 Void ratios along the pre-determined strips (100-pixel wide) for UN

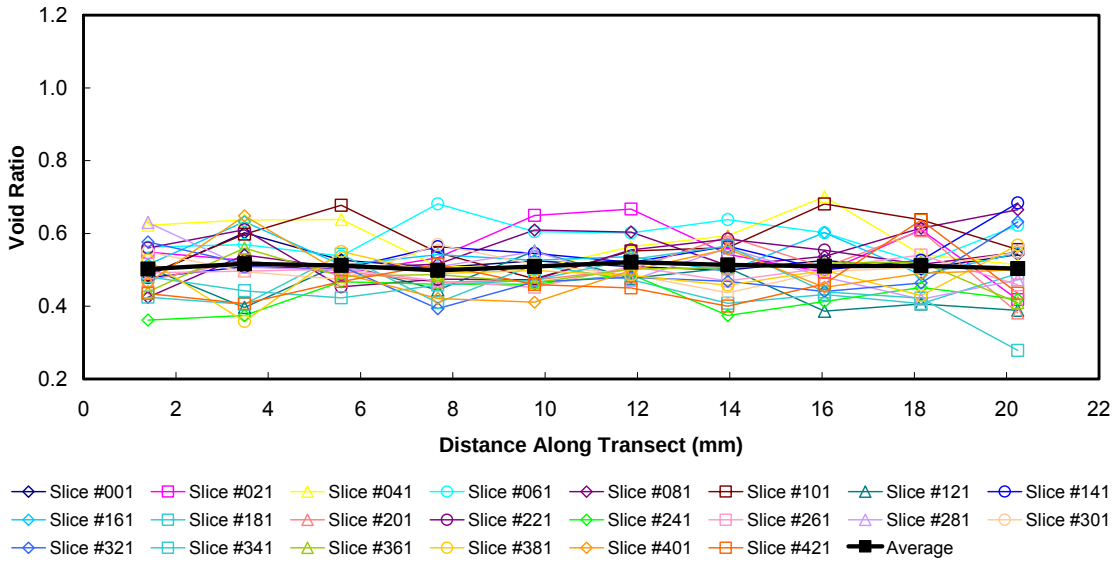

Figure 7.27 Void ratios along the pre-determined strips (150-pixel wide) for UN

The same 2-D strip analysis was performed on the highly dilatant (HD) biaxial specimen and plotted in Figures 7.28 to 7.30 for 50-pixel, 100-pixel, and 150-pixel wide strips, respectively. Due to the existence of the shear band, the void ratios along the transect increased in the middle. However, the boundaries of the shear band are difficult to define because of the packing signature effect. If using large strips, although the packing effect was less prominent, the subtle transitions between outside shear band and inside shear band were also blurred. As the result, definition of the shear band width will be less accurate if using 100-pixel and 150-pixel wide strips. One possible solution to the dilemma here is using the averaged void ratio curve based on a large quantity of 2-D slices that are characterized by 50-pixel wide strips.

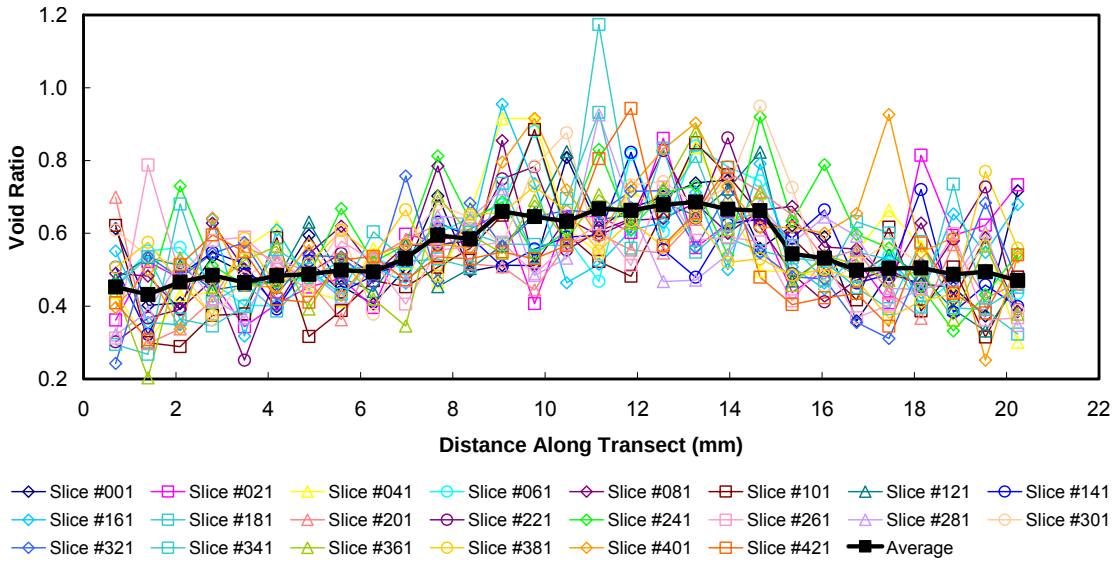

Figure 7.28 Void ratio along the pre-determined strips (50-pixel wide) for HD

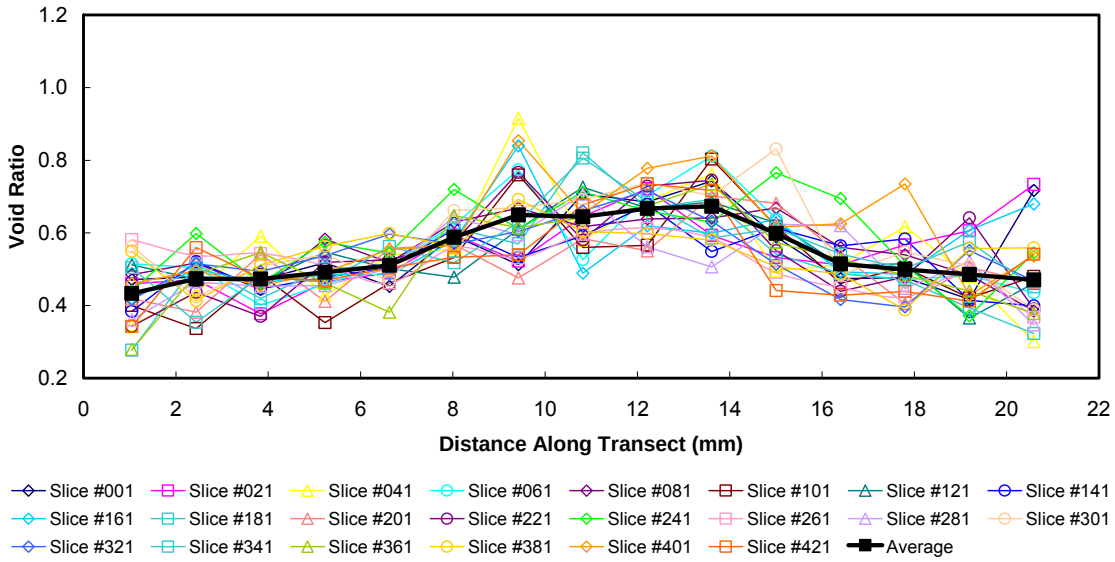

Figure 7.29 Void ratio along the pre-determined strips (100-pixel wide) for HD

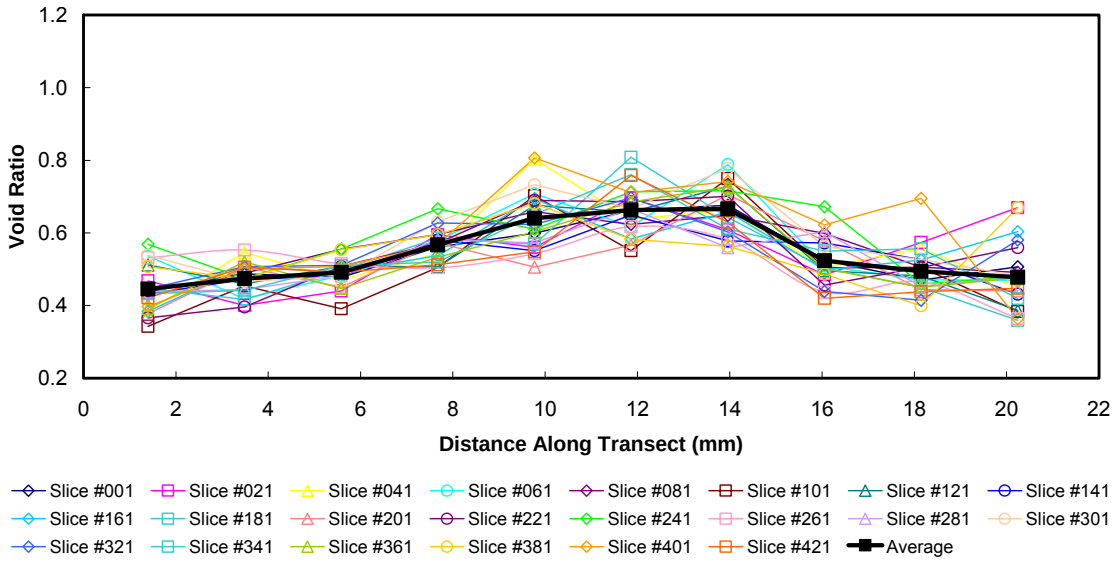

Figure 7.30 Void ratio along the pre-determined strips (150-pixel wide) for HD

7.3.2.2. 3-D Analysis

The previous analysis indicates that 2-D strip analysis on single or a few 2-D slices are less accurate. Therefore, an improved 3-D strip analysis was performed on the specimens. In the analysis, the specimens were visualized as 3D entities and divided into 50-pixel wide strips. The strips were prismatic in shape, and their thicknesses were the same as the correlated specimens, i.e., 430 pixels for UN and 600 pixels for HD. Incremental void ratio was calculated within each strip using the following equation:

$$e_i = \frac{(V_v)_i}{(V_s)_i} \tag{7.2}$$

where e_i is the incremental void ratio in the i^{th} prismatic strip (incremental from above the shear band to below the shear band), $(V_v)_i$ is the volume of voids in the i^{th} prismatic strip and $(V_s)_i$ is the volume of solids in the i^{th} prismatic strip. Other than the incremental void ratio, cumulative void ratio was also calculated using the following equation:

$$e_j = \frac{\sum_{i=0}^{j} (V_v)_i}{\sum_{i=0}^{j} (V_s)_i} \tag{7.3}$$

where e_j is the j^{th} cumulative void ratio (incremental from U to L or L to U). It should be noted that the volumes of voids and solids were estimated from voxel counting. Both the incremental and cumulative void ratios were plotted against the distances along the same transects used in 2-D analyses. Figure 7.31 presents the calculation results for UN. In general, as one prismatic strip in the 3-D analysis contained more particles than a strip in the 2-D analysis, the packing effect imposed minor influence and the incremental void ratios did not vary a lot from strip to strip. The two cumulative curves almost overlapped each other, indicating the void ratios inside UN were fairly homogeneous. Figure 7.32 presents the strip analysis results for HD. The incremental void ratio along the transect clearly defined three types of zones: non-dilatant zone, transition zone, and shear zone. The non-dilatant zone was eventually unaffected by the shear band, and its measured void ratios were comparable to those measured in UN. The shear zone was basically where two shear blocks sheared against each other, and thus shear-induced volumetric dilation occurred and its void ratios were constantly higher than the void ratios of the non-dilatant zone. The transition zone was the region close to and substantially affected by the shear zone, and gradual transition from low void ratios (as those in the non-dilatant zone) to high void ratios (as those in the shear zone) could be recognized in this zone. The shear band defined by Evans and Frost (2010) to include the shear zone and two transition zones is confirmed in the current study. Based on the incremental void ratio, the extent of the shear zone was 5.6 mm and the transition zones 2.1 to 2.8 mm for a total shear band thickness of 10.5 mm. The demarcation between the shear zone and transition zone was defined by the cumulative void ratio. The U-to-L cumulative curve increased when it entered the left transition zone and then the shear zone, and started to decrease when

entering the right transition zone. Therefore, the peak of the U-to-L cumulative curve approximately marked the right boundary of the shear zone. Similarly, the peak of the L-to-U cumulative curve marked the left boundary of the shear zone. Figure 7.33 shows an additional analysis using 100-pixel wide strips performed on HD. Although three types of zones still could be distinguished from the incremental void ratio, the extent of the shear zone decreased to 4.2 mm. This verifies the finding in the 2-D strip analysis that larger strips tend to miss the boundaries of the transitions and yield less accurate predictions.

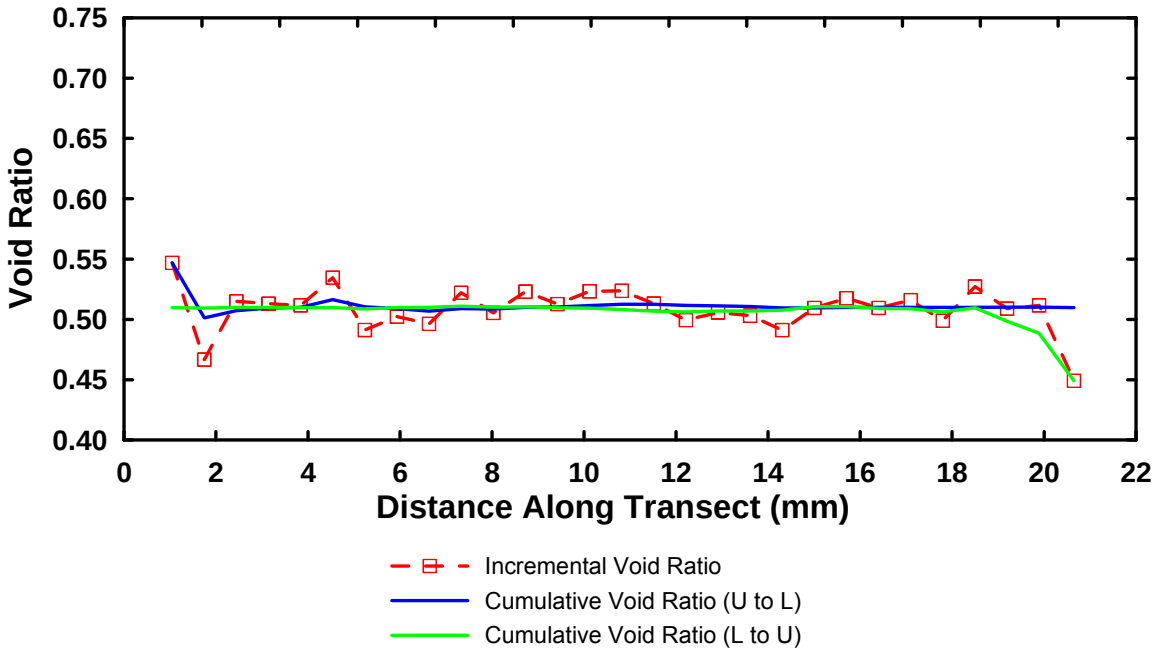

Figure 7.31 Incremental and cumulative void ratios characterized by 50-pixel wide 3-D strips for UN

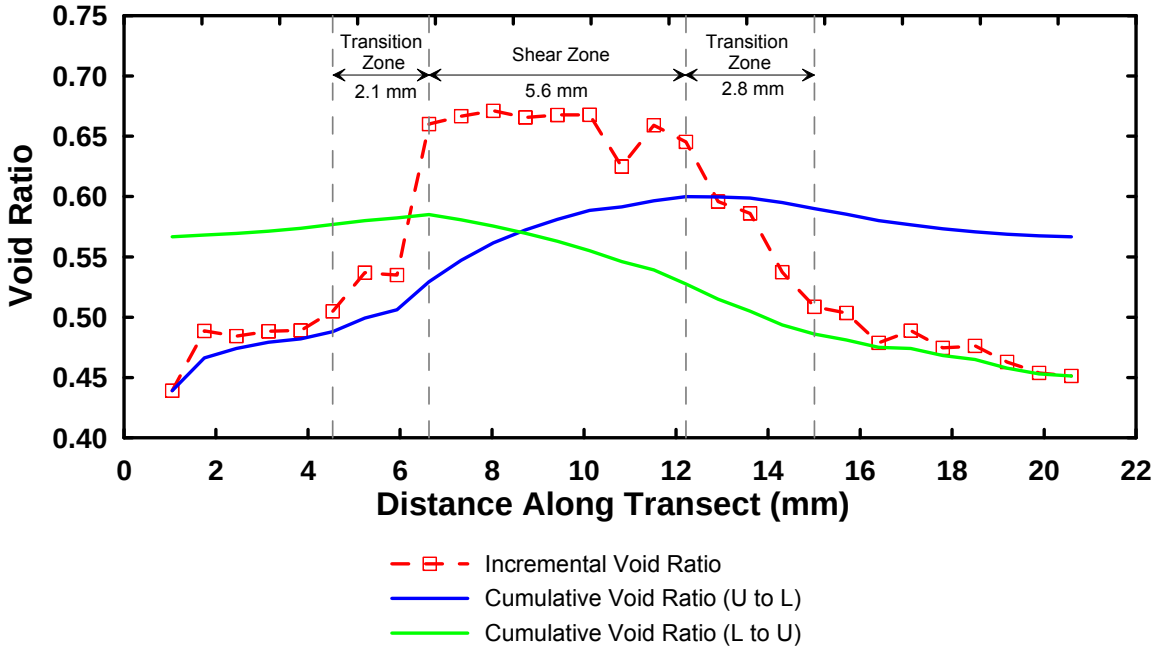

Figure 7.32 Incremental and cumulative void ratio characterized by 50-pixel wide 3-D strips for HD

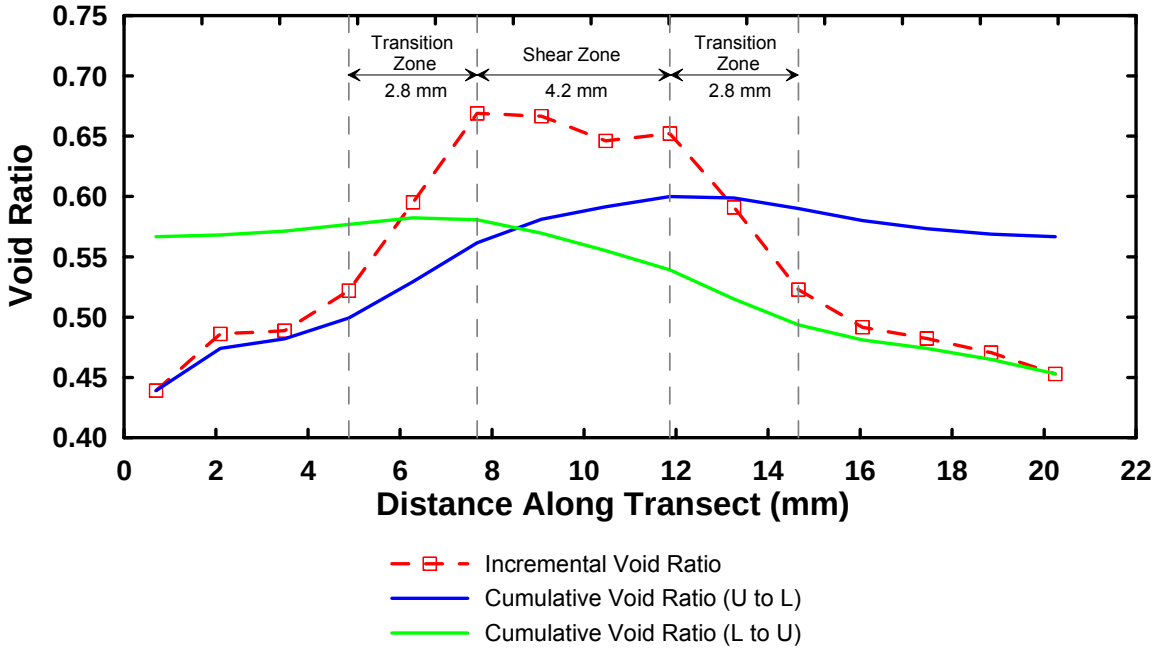

Figure 7.33 Incremental and cumulative void ratio characterized by 100-pixel wide 3-D strips for HD

7.3.3. Local Void Ratio Distribution

For granular materials, their mechanical behavior is not only affected by global void ratio, but also by local void ratio. Oda (1976) defined local void ratio as the void ratio within a polygon which is formed by connecting the centers of gravity of particles. Some researchers have proposed several procedures to calculate the distribution of local void ratios from 2-D slices using Oda's (1976) definition. One of the procedures was proposed by Frost and Kuo (1996), which involved multiple morphological operations. It was automated using Cambridge Instruments Quantimet Q570 by Kuo and Frost (1995), and later updated to Leica Qwin 3.0. This procedure was used for the current study.

When plotting the histogram of local void ratio distribution (LVRD), the solid area weighted histogram was used instead of the standard histogram. The solid area weighted local void ratio is the local void ratio weighed by the local solid area within each polygon. Background and equations about the solid area weighted local void ratio can be found in Frost and Kuo (1996). LVRD for UN was calculated from 430 slices and HD from 600 slices, and is presented in Figure 7.34. The statistical mean for UN was 0.511, the same as e_{avg} estimated from void ratio per slice. The statistical mean for HD was 0.569, slightly higher than e_{avg} of 0.567. In general, LVRD of HD showed a shift to the right of UN and a flatter shape. This can be justified by the fact that shearing resulted in the increase of the local void ratios and the degree of heterogeneity. As the location and extent of the shear zone has been defined by the 3-D strip analysis in the previous section, LVRD inside the shear zone and outside the shear zone was able to be estimated and is presented in Figure 7.35 for UN and Figure 7.36 for HD. For UN specimen, the two histograms almost overlapped and the statistical parameters did not differ much for inside and outside the shear zone. This indicates no shear band existed in the specimen. For HD specimen, dilation inside the shear zone could be easily discerned by a larger statistical mean and a larger standard deviation than outside the shear zone.

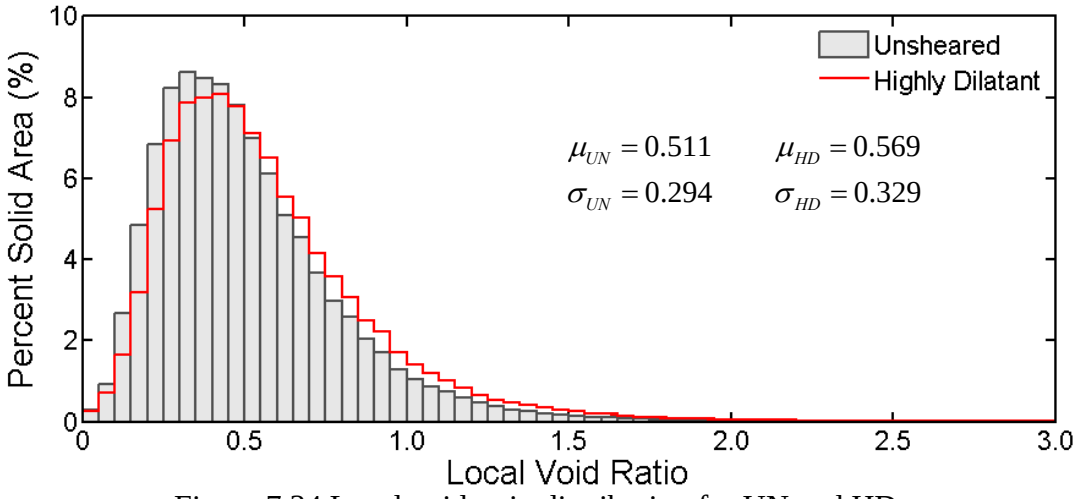

Figure 7.34 Local void ratio distribution for UN and HD

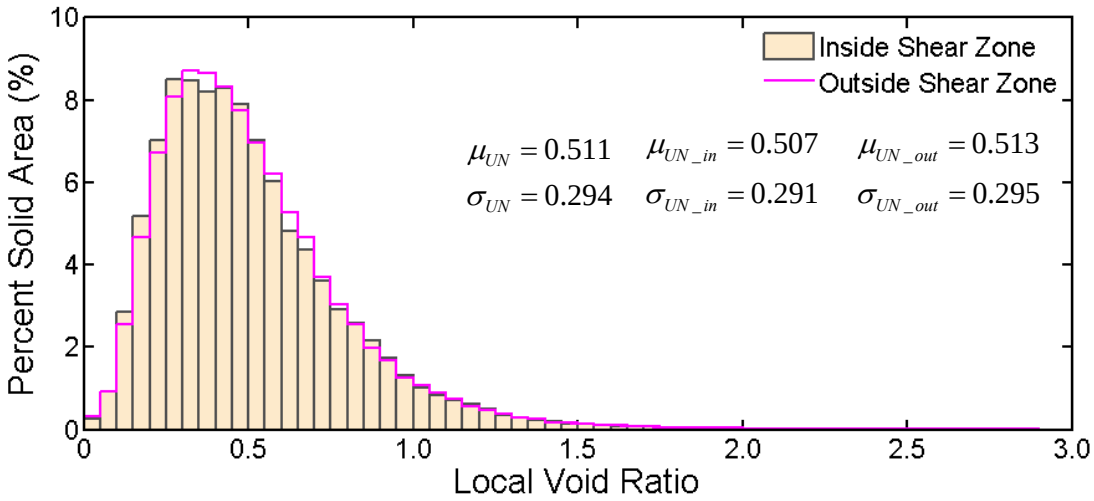

Figure 7.35 Local void ratio distribution inside and outside shear zone for UN

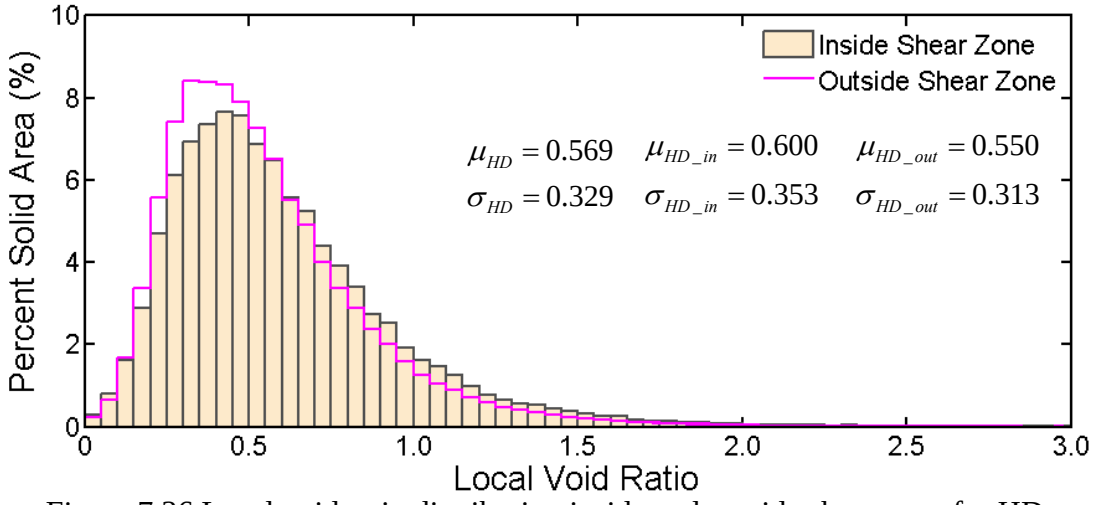

Figure 7.36 Local void ratio distribution inside and outside shear zone for HD

7.3.4. Shear Band Width

The shear band width of the reconstructed specimen can be estimated from the 3-D strip analysis and the void ratio per slice. Based on the 3-D strip analysis, the extent of the shear zone was 5.6 mm and the transition zones were 2.1 to 2.8 mm for HD. As the shear band is defined to include the shear zone and two transition zones, its width would be 10.5 mm, approximately 14.2 x D_{50}. When analyzing the void ratio per slice over the removed thickness in three directions, it was found that if the local variations due to the packing signature effect were ignored, the void ratios in slices A and B remained rather constant while the void ratios in slices C did not. This is attributed to the fact that all the slices A and B and only some slices C intersected with the shear band due to their orientations and positions. Then, it is proposed herein that the void ratio profile from slices C can be used to characterize the shear band width. Figure 7.37 illustrates a prototype specimen with constant void ratios inside and outside the shear band. The secondary slices C are orthogonal to W and sectioning the specimen along L. The first and last few slices C do not intersect with the shear band, and their void ratios should remain low values. Once the sectioning passes point I, void ratio gradually increases as the shear band accounts for more percentage of the slice area. The void ratio per slice becomes constant again when the sectioning proceeds between point II and point III, and then decreases after point III until it becomes constant again at point IV. Overall, the void ratios estimated from slices C follow a stepping profile illustrated in Figure 7.38. From Figure 7.17, the length between point II and point III, l, is estimated to be 4.86 mm. Inclination angle of shear band, α, is 61° measured by Evans (2005), and W equals to 11.17 mm. Based on those numbers, the calculated shear band width, d, is estimated to be 9.66 mm, approximately 13.1 x D_{50}. This estimation is comparable to the prediction of 10.5 mm from the 3-D strip analysis presented in section 7.3.2.2.

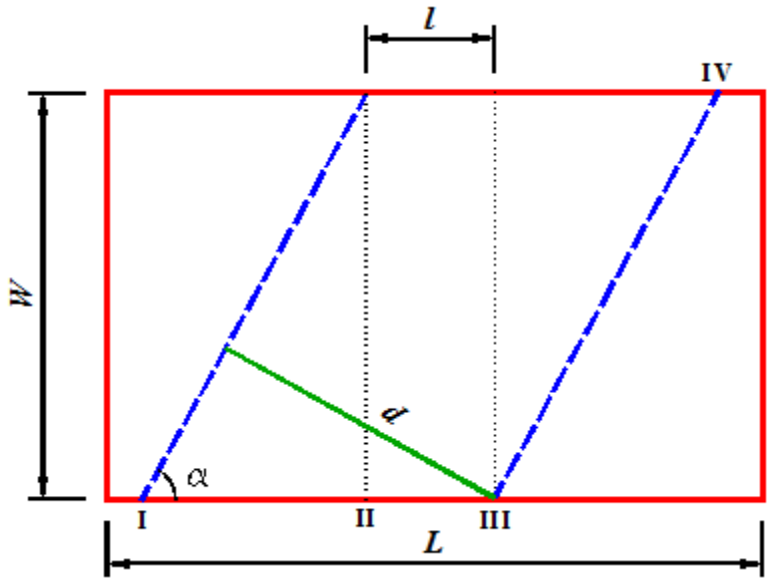

Figure 7.37 Prototype model for characterization of shear band thickness

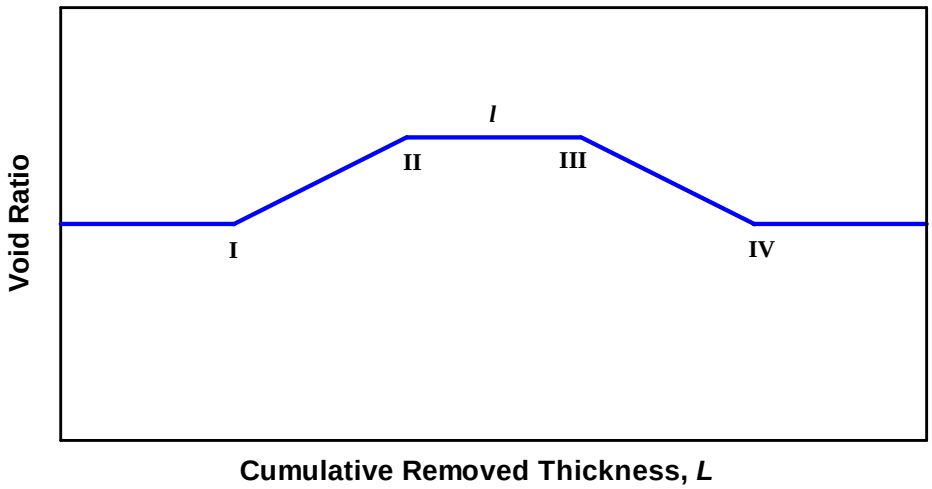

Figure 7.38 Idealized void ratio profile along *L*

7.3.5. 3-D Pore Size Distribution

3-D pore size was characterized using the research software package, 3DMA (Lindquist, 1999). The characterization was performed on two cubes of 600 x 600 x 430 voxels that were extracted from the UN specimen and the localization zone of the HD specimen. Before the images were imported into 3DMA, they were processed by image dilation to create more touching points between particles. 3DMA partitioned 1130 and

559 internal nodal pores for UN and HD, and the 3-D pore size distributions are presented in Figure 7.39. Contrary to expectation, the histogram of the sheared specimen was shifted to the left of the unsheared specimen. Considering the fact that the sheared specimen features higher void ratios in the shear band than the unsheared specimen, the 3-D pores inside HD should be fewer but larger than those inside UN. However, although fewer pores were partitioned from the HD specimen, its pore size was smaller than the UN specimen. The same phenomenon was observed from the 3-D pore size distributions of the moist-tamped triaxial specimens in Yang (2005). Yang (2005) explained that the possible causes are the algorithm used in the software (3DMA) to partition the pore space and the 3-D morphological operations performed on the non-uniform structure. Compared with the 3-D pore sizes of the triaxial specimen (Ottawa 30-50 sands) in Figure 3.5, the 3-D pore sizes of the biaxial specimen (Ottawa 20-30 sands) in the current study are almost doubled. This indicates that larger grain size results in larger pore size. Further analysis of these surprising results in wanted, however, the 3DMA software is in transition from the original develop to a commercial code and thus its future availability is unknown at this time.

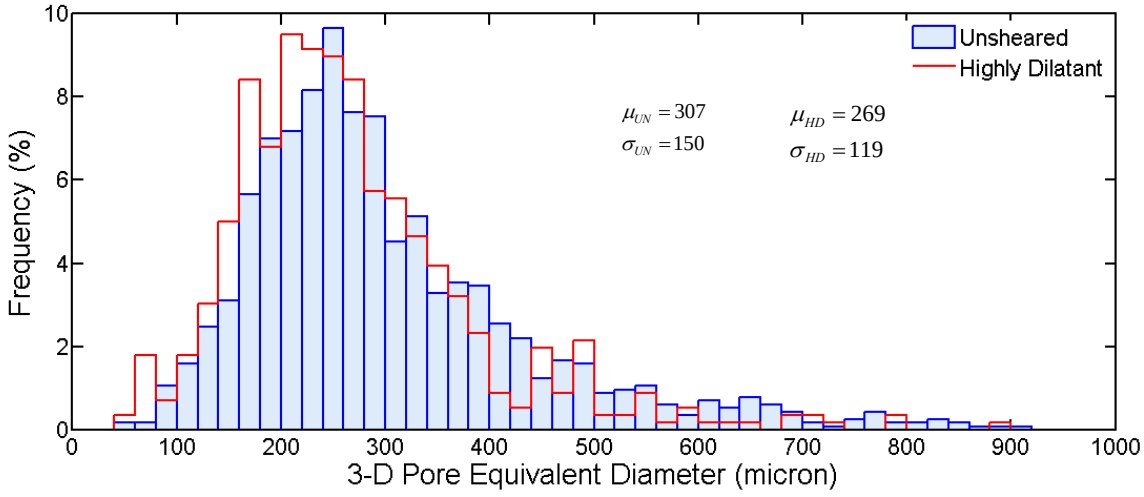

Figure 7.39 3-D pore size distributions for the biaxial specimens

7.3.6. 3-D Visualization of Reconstructed Microstructures

To visualize the particulate structures, especially the shear zone, 3-D volumes were rendered from the serial slices using VoxBlast from VayTek Inc. VoxBlast is a volume rendering program and features creating 3-D projections using an alpha blending or surface rendering algorithm from stacks of registered 2-D images. The reconstructed specimens, UN and HD, were rendered in 3D volumes using 430 and 600 registered serial slices respectively. The slices were 1300 x 800 pixels in dimension and 14 μm/pixel in resolution. The spacing between every two slices was 14 μm.

7.3.6.1. 3-D Microstructures

Figure 7.40 presents the rendered 3-D microstructure for the UN specimen. The microstructure is 18.2 mm x 11.2 mm x 6.0 mm and contains approximately 3800 particles. The two phases are illustrated in two colors – yellow for sand grains and purple for voids. It can be noticed from the 3-D image that the particles are sub-rounded and the particle size range is very narrow. In general, the particles distributed fairly uniformly inside the specimen. Figure 7.41 shows the rendered 3-D image for the HD specimen. This microstructure is 18.2 mm x 11.2 mm x 8.4 mm and contains approximately 5100 particles. The shear-induced dilatant zone can be visually distinguished from the non-dilatant zones by larger local voids. Other than the voids, the particles inside the shear zone have fewer contacts with the neighboring particles than those outside the shear zone. The approximate shear zone location is marked by a pair of red dashed lines in the figure for ease of observation. To check the internal structures, the HD specimen was hollowed out by 1/3 and 2/3 thickness in Figures 7.42 and 7.43. It shows that due to the characteristics of particle packing, defining the shear zone was not easy and might be inaccurate at different depths if only accounting on visual inspection.

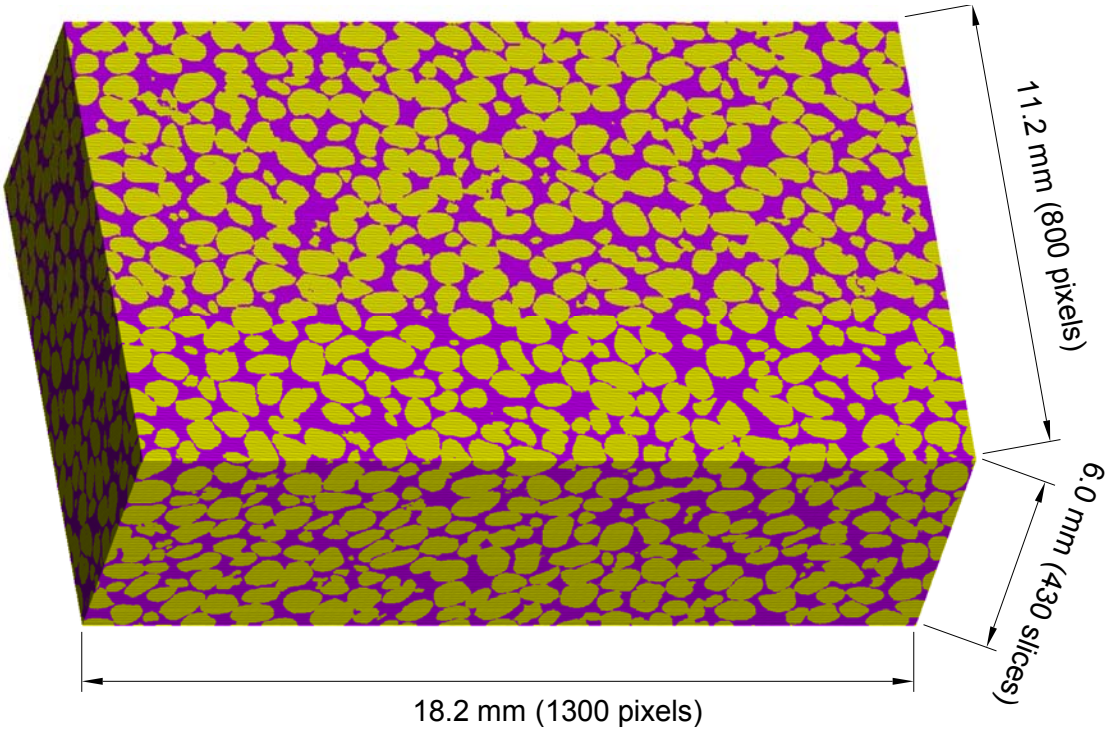

Figure 7.40 3-D reconstructed structure of UN (yellow: sand grains; purple: voids)

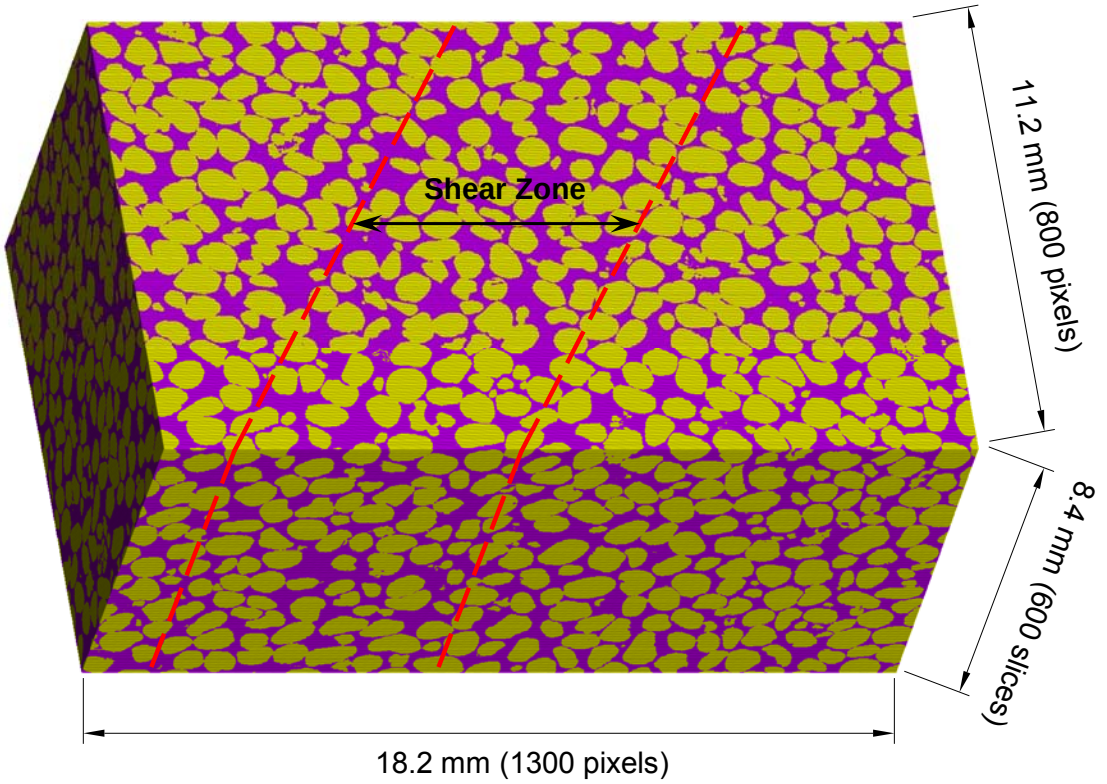

Figure 7.41 3-D reconstructed structure of HD (yellow: sand grains; purple: voids)

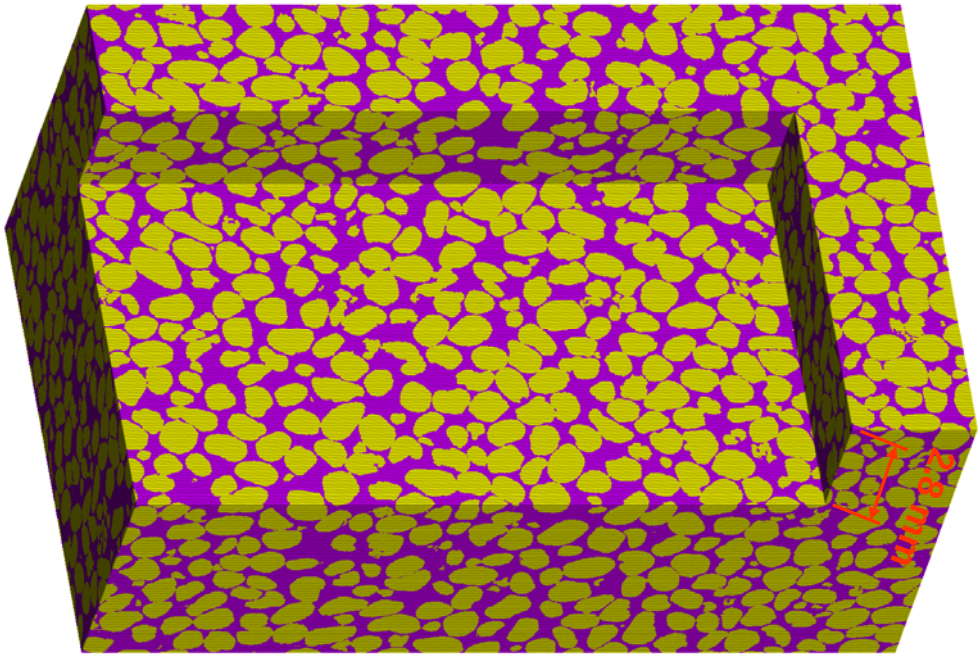

Figure 7.42 An inside view of HD with hollowed depth of 2.8 mm

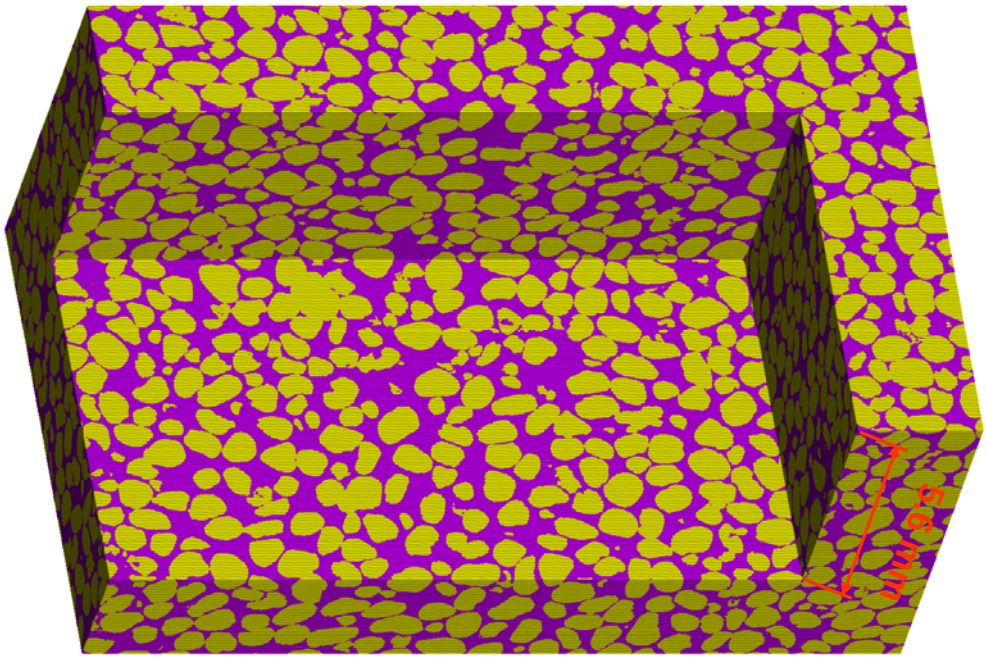

Figure 7.43 An inside view of HD with hollowed depth of 5.6 mm

7.3.6.2. Influence of Shear Zone

For the sheared specimen, the presence of the shear zone resulted in distinctive particle-pore structures compared to the unsheared specimen. To visualize the influence of the shear zone, two cubic sub-volumes were extracted from different locations inside the HD specimen. One sub-volume was extracted from the center of the shear zone, and another one was extracted to the right of the shear zone. The sub-volumes are 5.6 mm x 5.6 mm x 5.6 mm (400 x 400 x 400 voxels) and presented in the form of continuum, particles and pores in Figure 7.44. For the cube inside the shear zone, it shows an obviously looser packing and larger pore structures than the cube extracted from outside the shear zone. The evidence of shear-induced dilation can be clearly visualized.

7.4. Simulated Digital Microstructures

To be consistent with the reconstructed real microstructures, four highly dilatant simulated microstructures were selected from Chapter 6 for this part of analysis. These four microstructures were DEM_APHD (unsheared and sheared) and DEM_MTHD (unsheared and sheared). They were renamed as APHDU, APHDS, MTHDU, and MTHDS, where ‘U’ represents unsheared, and ‘S’ represents sheared. In order to perform the same image analyses as for the reconstructed real microstructures, stacks of serial slices were created for the simulated microstructures. First, information of the particle coordinates and radii were retrieved from PFC3D. Then 2-D serial slices orthogonal to the intermediate principle stress were generated based on the particle information. Considering the specimen size and particle size, resolution of the slices was set to be 0.1 mm/pixel and the removed thickness per slice was 0.1 mm. Because of the large deformation that took place at the end of shearing, the slices were cropped into 1100 x 200 pixels to exclude the deformed part and the boundary part.

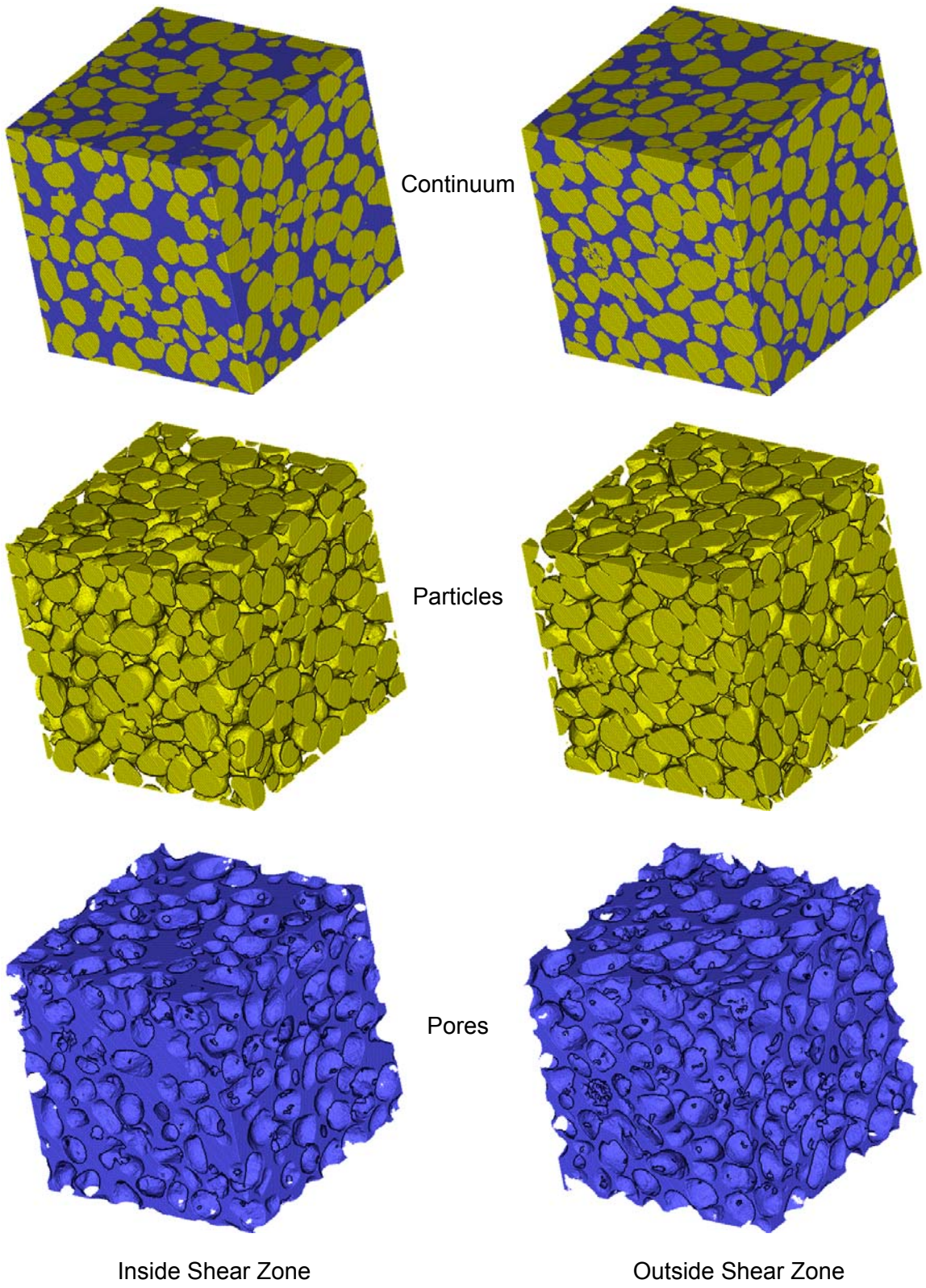

Figure 7.44 Extracted sub-volumes from inside and outside the shear zone

7.4.1. Void Ratio Per Slice

In order to calculate the void ratio per slice in three orthogonal directions, two secondary sets of slices were produced based on the primary slices generated from particle coordinates and radii. The two sets of secondary slices were produced using the approach noted in Section 7.3.1.2. As with the reconstructed real microstructures, the original slices were orthogonal to the intermediate principal stress and called slices A. One set of secondary slices was orthogonal to the major principal stress and designated as B. The other set was orthogonal to the minor principal stress and designated as C. Dimensions of the slices were 1100 x 200 pixels for A, 600 x 200 pixels for B, and 1100 x 600 pixels for C. The void ratio per slice is plotted against the cumulative removed thickness in three orthogonal directions for APHDU in Figure 7.45. The packing signature effect can be clearly observed in all of the three directions, and it resulted in the void ratios range between 0.35 to 0.50. Figure 7.46 shows the void ratio per slice for APHDS which is a sheared specimen. If ignoring the signature packing effect, the void ratios of slices A and C remain rather constant over the removed thickness. However, the void ratios of slices B increase around the middle. These two behaviors resulted from the relative positions between the slices and the shear band – slices A and C always intersected with the shear band while slices B intersected with different zones (shear zone, transition zone, and non-dilatant zone) of the specimen. Figure 7.47 presents the influence of the different structure of the MTHDU specimen. Although void ratio variations in slices A and C of MTHDU were comparable to those of APHDU, the void ratios in slices B exhibited rhythmic periodicity similar to those observed in the ideal packings. The cause of such phenomenon was the way the particles were placed in the specimen. For the moist-tamped numerical specimens, the particles were generated layer by layer with different relative densities. A total of 21 sub-layers, 6.7 mm in height, were separated using rigid platens. Because the particle size was 3.1 mm in short axis and 4.65 mm in long axis, less than 3 particles could be aligned along the height of one sub-layer.

Such an arrangement forced most of the particles to rotate or align horizontally, and this is supported by the polar histogram of particle orientation in Figure 6.40. The void ratios for the sheared specimen MTHDS are plotted in Figure 7.48. Ignoring the packing signature effect, the shear band caused a different profile of void ratio in slices B compared with slices A and C.

7.4.2. Spatial Averaging Along Pre-Determined Inclined Strips

3-D strip analysis was performed on the simulated microstructures using the same procedures in Section 7.3.2.2. The measured inclination angle of the shear band was 52° for APHD and 51° for MTHD. The slices were divided into 30-pixel (3 mm, approximately D_{avg} in short axis) wide strips. The void ratio was calculated using voxel counting within each strip and plotted against the distance along the transect. The analysis results are presented in Figures 7.49 to 7.52 for APHDU, APHDS, MTHDU and MTHDS, respectively. For the unsheared specimens, the void ratios varied slightly from strip to strip. Meanwhile, the shear zone, transition zone and non-dilatant zone can be clearly defined from the incremental void ratios of the sheared specimens. The extent of the shear zone was 18 mm and the transition zones were 9 to 12 mm for APHDS. For MTHDS, as the shear band interfered with the bottom platen, the development of the void ratios inside the shear band was likely affected. Therefore, estimation on the shear band width for MTHDS unreliable.

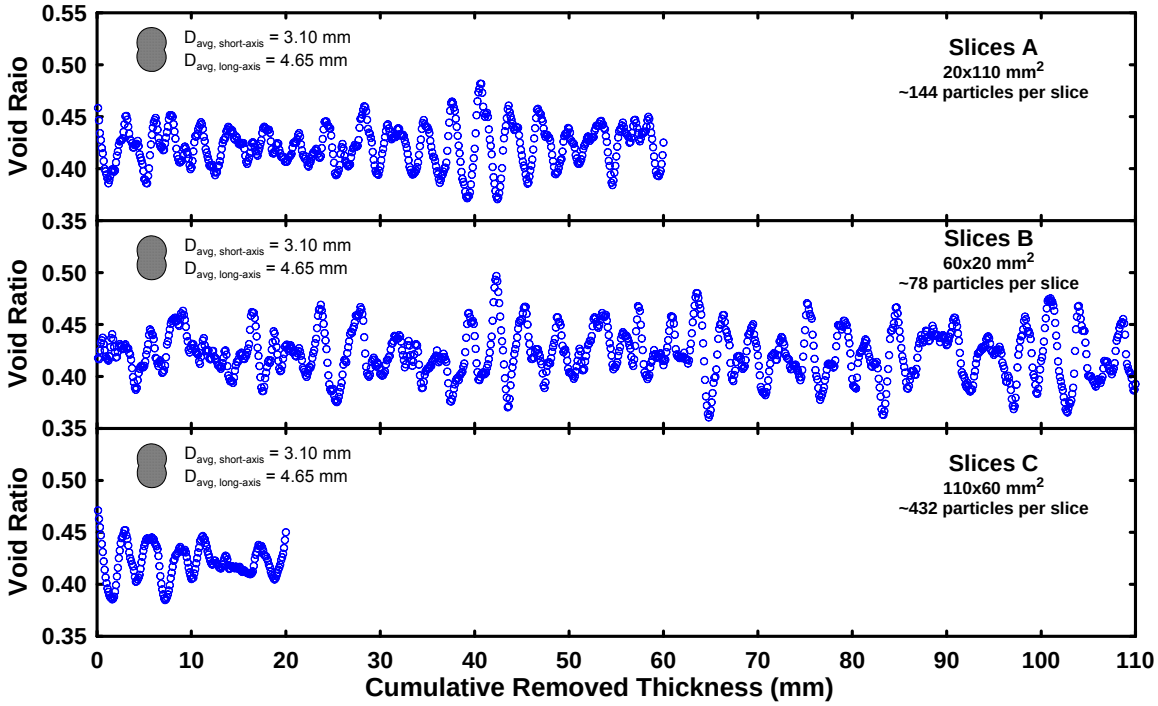

Figure 7.45 Variation of void ratio in three orthogonal directions for APHDU

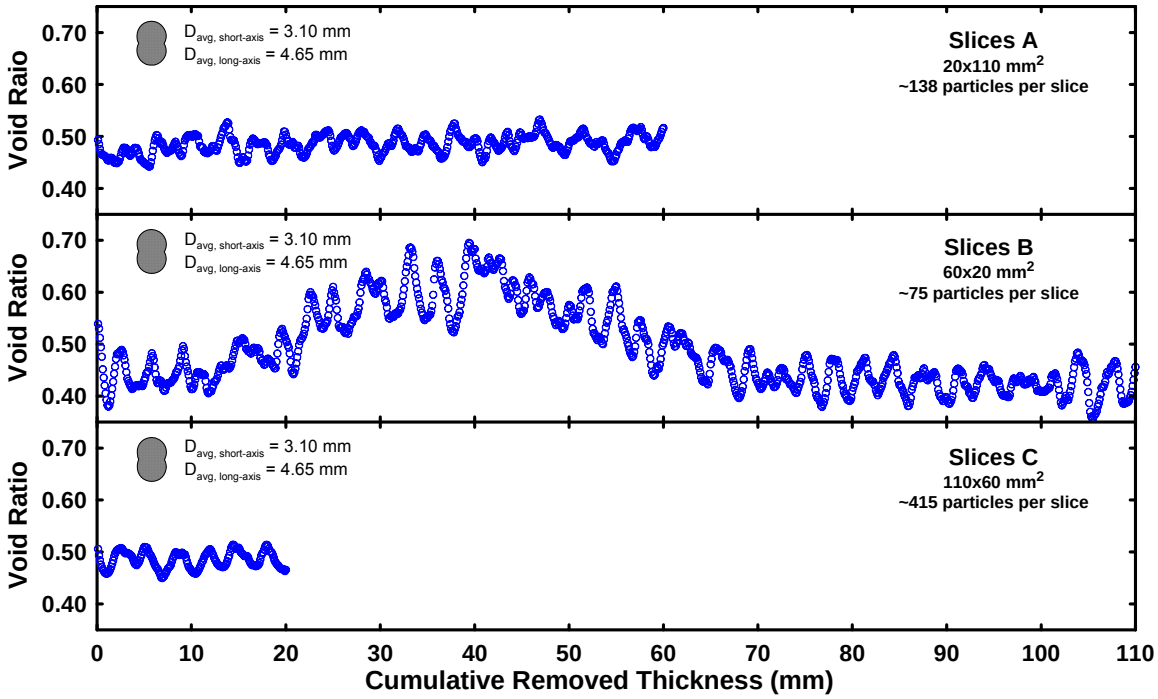

Figure 7.46 Variation of void ratio in three orthogonal directions for APHDS

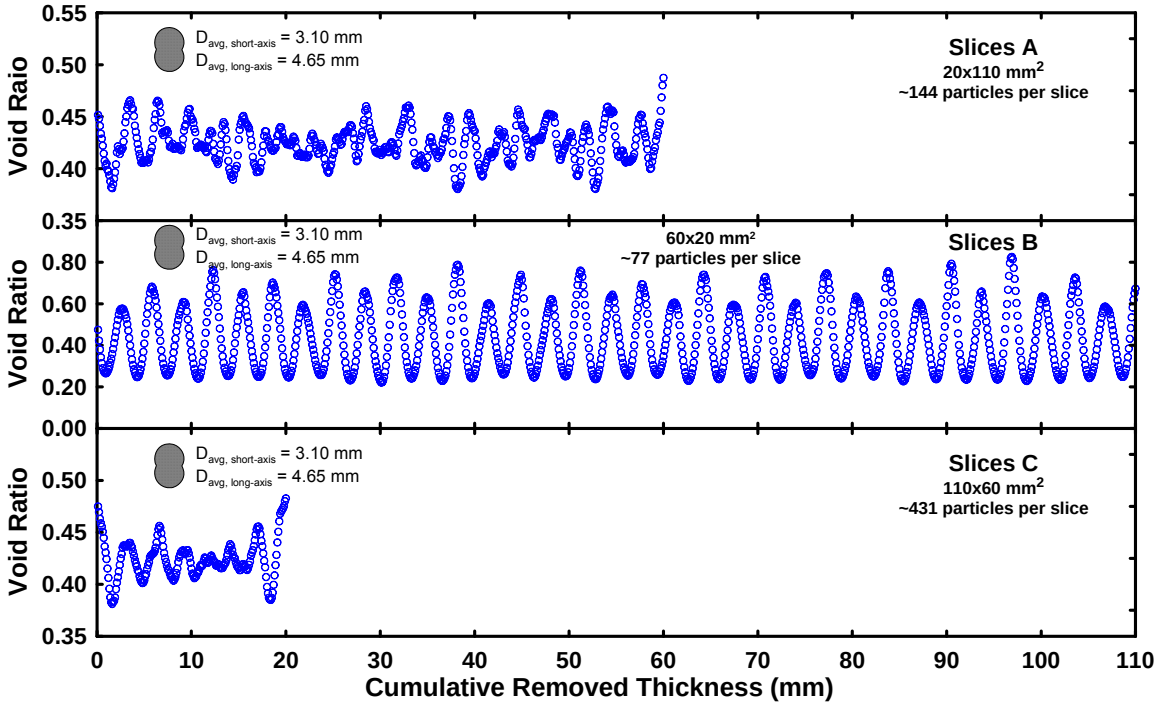

Figure 7.47 Variation of void ratio in three orthogonal directions for MTHDU

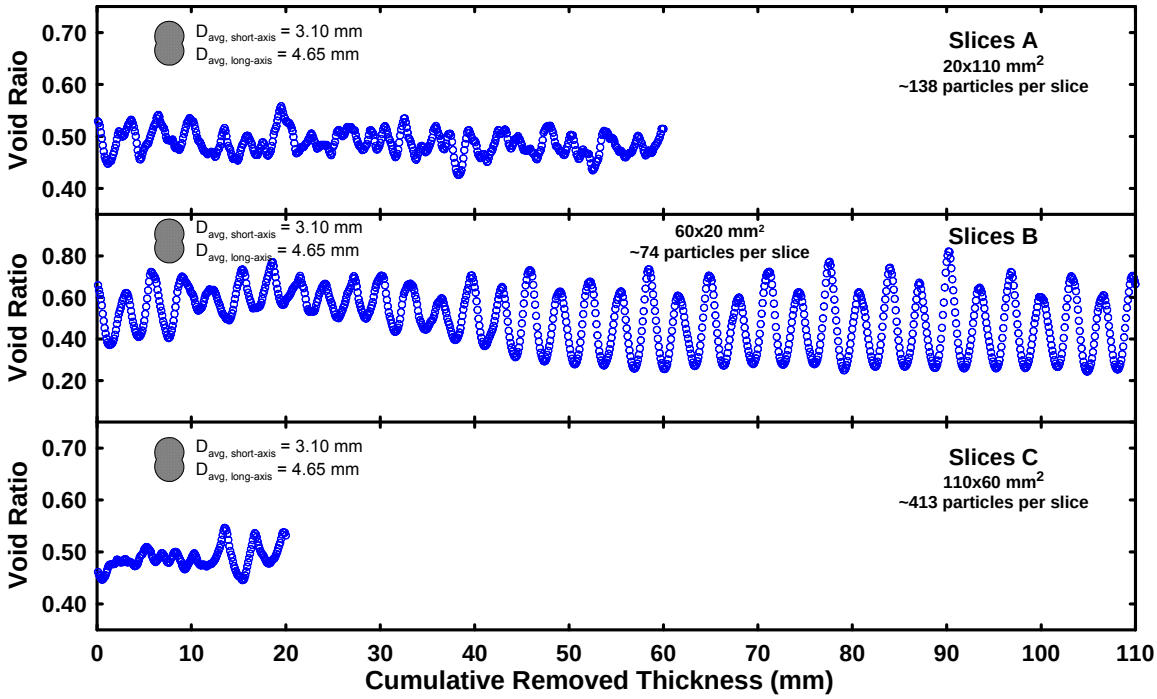

Figure 7.48 Variation of void ratio in three orthogonal directions for MTHDS

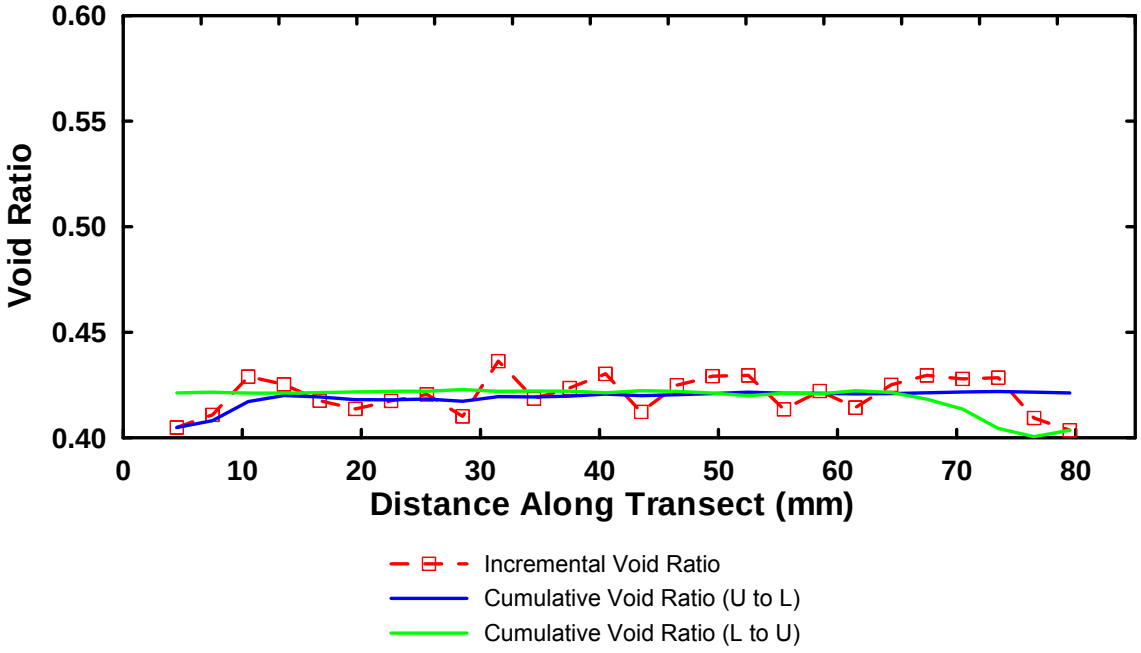

Figure 7.49 Incremental and cumulative void ratios using 30-pixel wide 3-D strips for APHDU

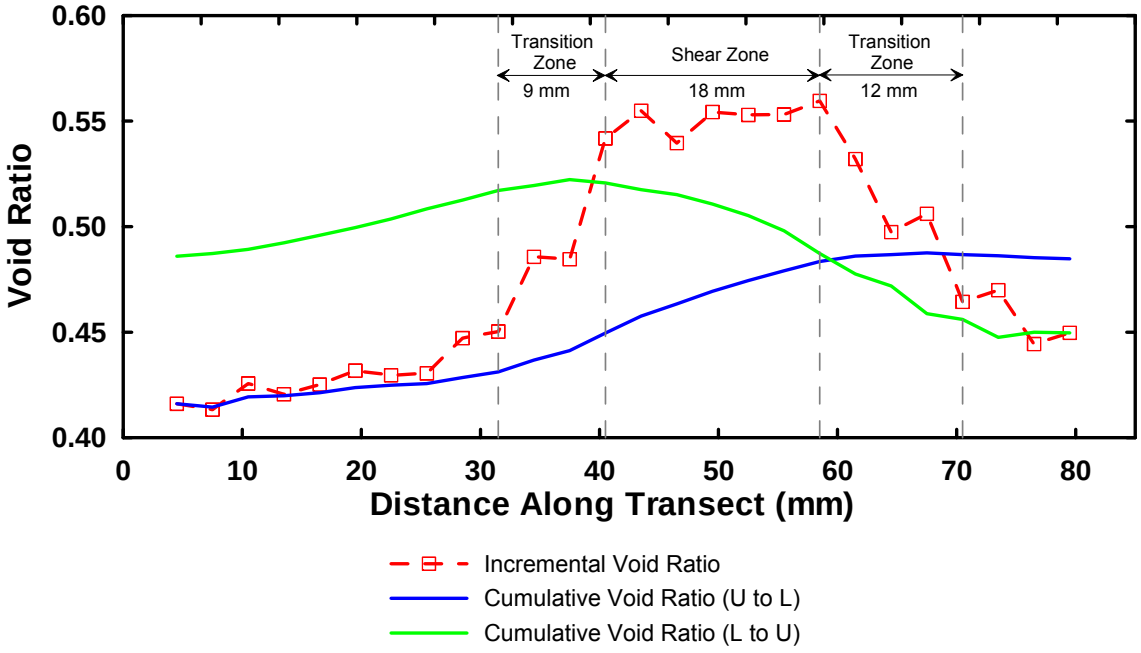

Figure 7.50 Incremental and cumulative void ratios using 30-pixel wide 3-D strips for APHDS

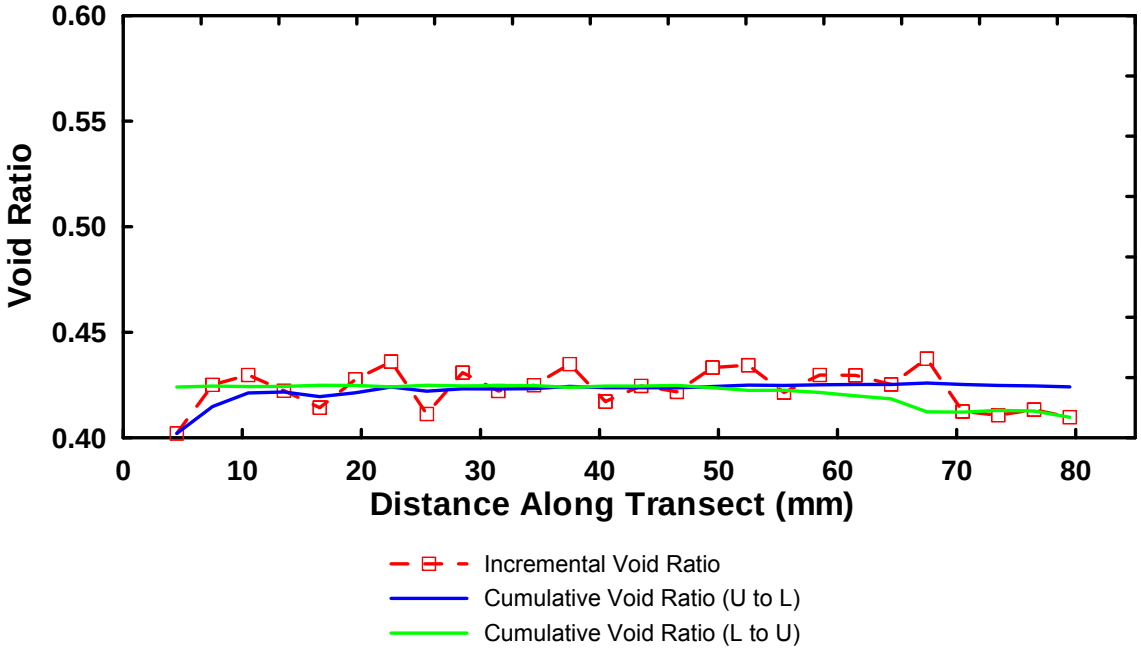

Figure 7.51 Incremental and cumulative void ratios using 30-pixel wide 3-D strips for MTHDU

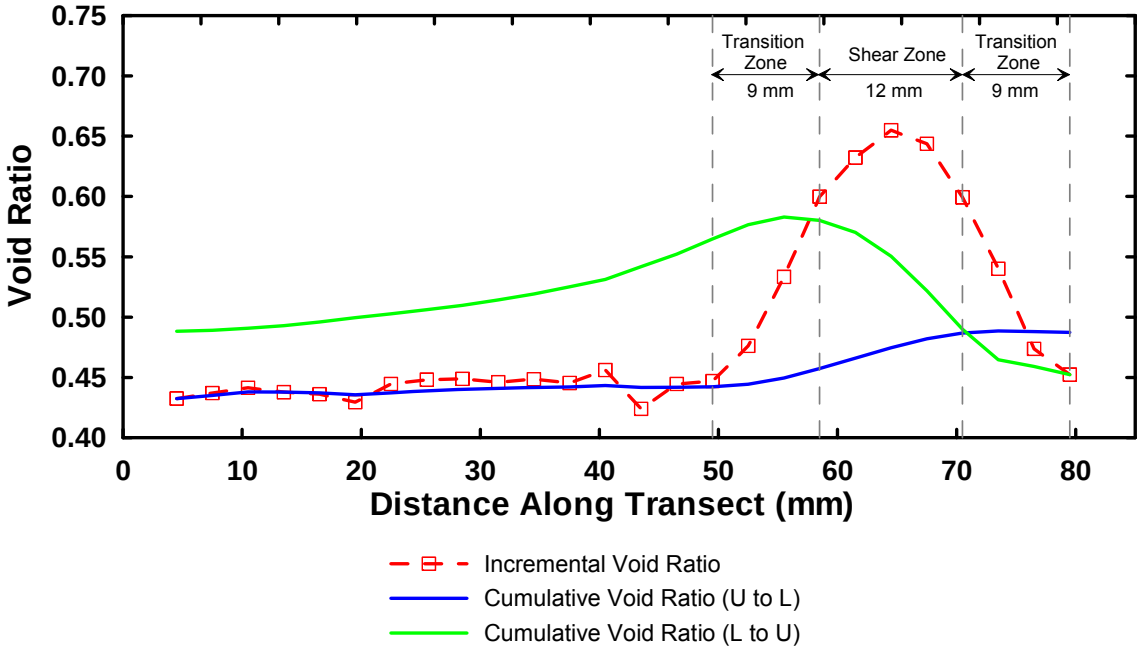

Figure 7.52 Incremental and cumulative void ratios using 30-pixel wide 3-D strips for MTHDS

7.4.3. Local Void Ratio Distribution

Local void ratios were characterized for the simulated microstructures using the procedure proposed by Frost and Kuo (1996) and weighted by the local solid areas. Figures 7.53 and 7.54 present the histograms for the simulated specimens. Similar to the reconstructed real structures, shearing caused LVRD of the simulated sheared structure to shift to the right of the unsheared structure and produce a flatter shape. Based on the extent of the shear zone defined in the previous section, LVRD was characterized inside and outside the shear zone for the sheared specimens in Figures 7.55 and 7.56. LVRD inside the shear zone clearly distinguished itself from LVRD outside the shear zone by higher statistical means and standard deviations.

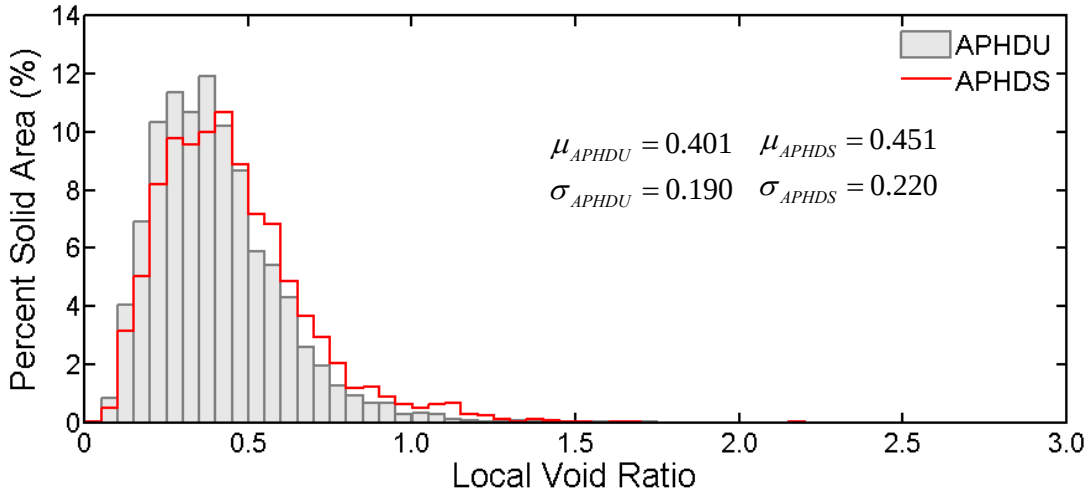

Figure 7.53 Local void ratio distribution for air-pluviated specimens

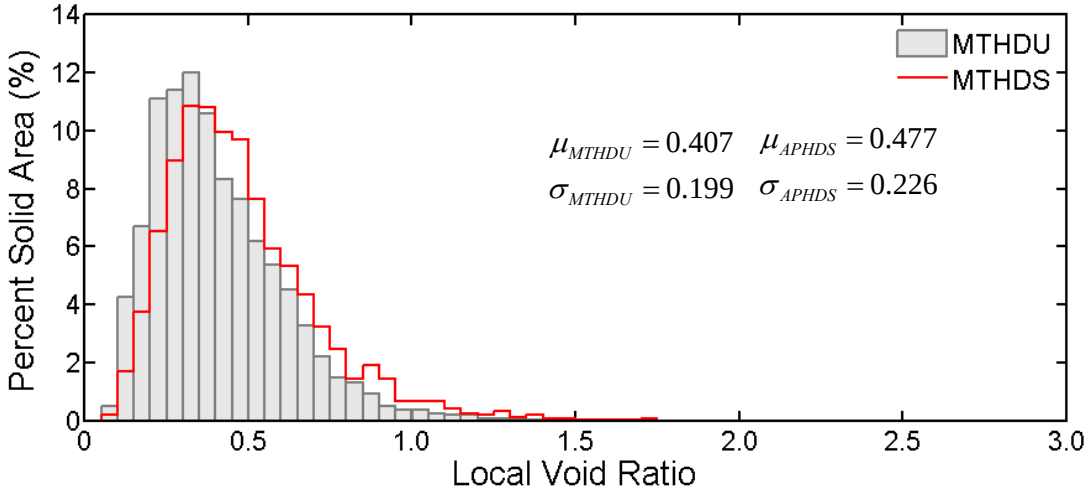

Figure 7.54 Local void ratio distribution for moist-tamped specimens

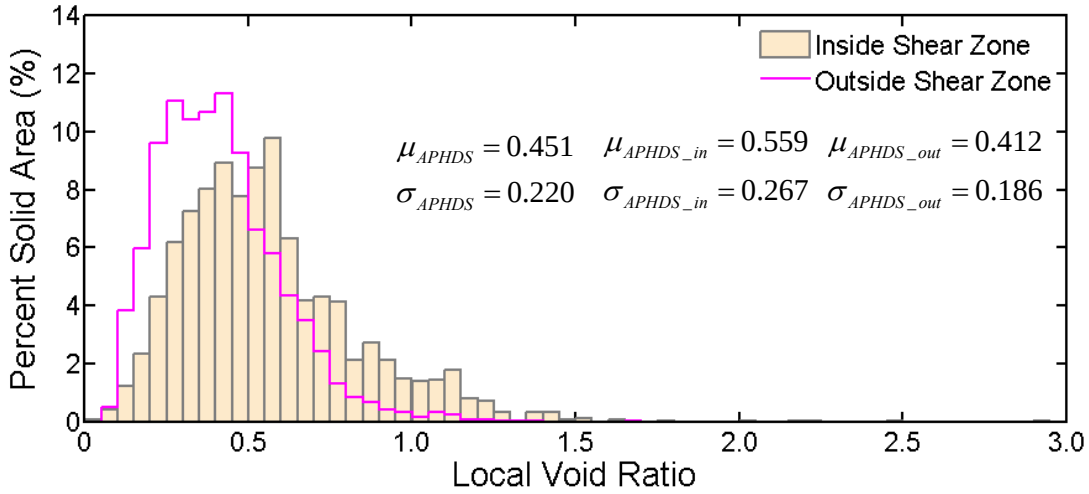

Figure 7.55 Local void ratio distribution inside and outside shear zone for APHDS

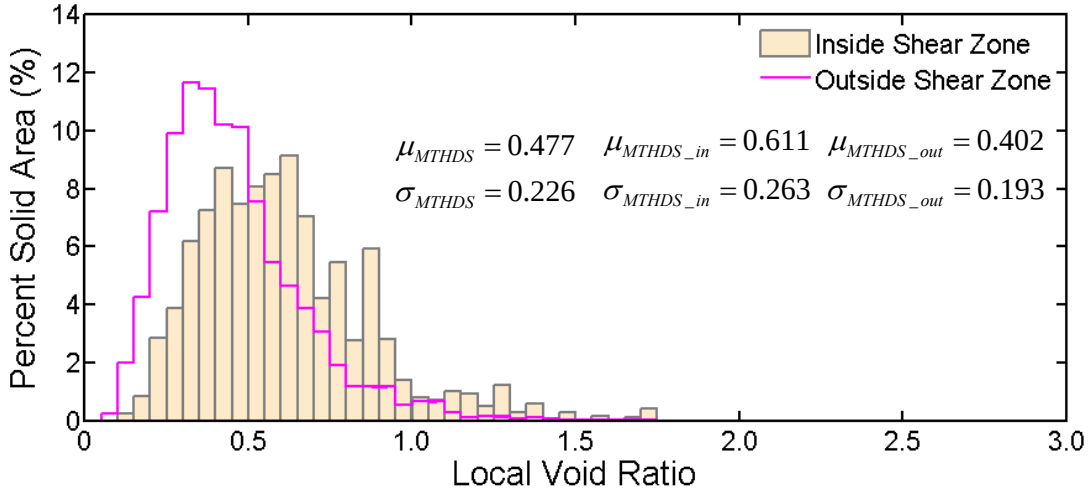

Figure 7.56 Local void ratio distribution inside and outside shear zone for MTHDS

7.4.4. Shear Band Width

The shear band width was estimated for the sheared simulated structures using the 3-D strip analysis and the void ratio per slice. From the 3-D strip analysis, the extent of the shear zone was 18 mm and the transition zones were 9 to 12 mm for APHDS. Thus, the shear band width equaled 39 mm or approximately 12.6 x D_{avg} in short axis. The estimation of the shear band width for APHDS was comparable to HD (14.2 x D_{50}). The extent of the shear zone was 12 mm and the transition zones 9 mm for MTHDS, and thus the shear band width equaled to 30 mm or approximately 9.7 x D_{avg} in short axis. As mentioned previously, the bottom platen interfered with the development of the shear band and resulted in an unreliable estimation of the shear band width for MTHDS. Similar to the reconstructed real microstructures, the shear band width can also be estimated for the simulated microstructures from the void ratio profile of slices B (Figures 7.46 and 7.48). For the simulated microstructures, the slices B are orthogonal to W and sectioning the specimen along H, as illustrated by the prototype model in Figure 7.57. The idealized void ratio profile is the same as the one shown in Figure 7.38, nevertheless the width of the plateau (between point II and point III) is much smaller for the simulated structures and easily missed out from the profile. Therefore, for the simulated structures, the shear band width was calculated by defining the height of the shear band, h, from void ratio variation. For APHDS, inclination angle of the shear band, β, was 52°, h was 56.2 mm, W was 20 mm, and consequently, the shear band width d was 18.8 mm, approximately 6.1 x D_{avg} in short axis. For MTHDS, β was 51°, h was 50.7 mm, W was 20 mm, and then d equaled to 16.6 mm, approximately 5.1 x D_{avg} in short axis. It should be noted here that estimation of the shear band width from the void ratio per slice was based on the assumption that the void ratios inside and outside the shear band are constant. However, as illustrated by the 3-D strip analysis, the shear band is actually composed of the shear zone (with constant void ratio) and two transition zones (with changing void ratio). That means when slices B section through the specimen, they

are intersecting a mingling of non-dilatant zone, transition zone and shear zone. Therefore, the void ratio profile should be rather complicated, especially with the presence of the packing signature effect which affected the judgment on *h* as well.

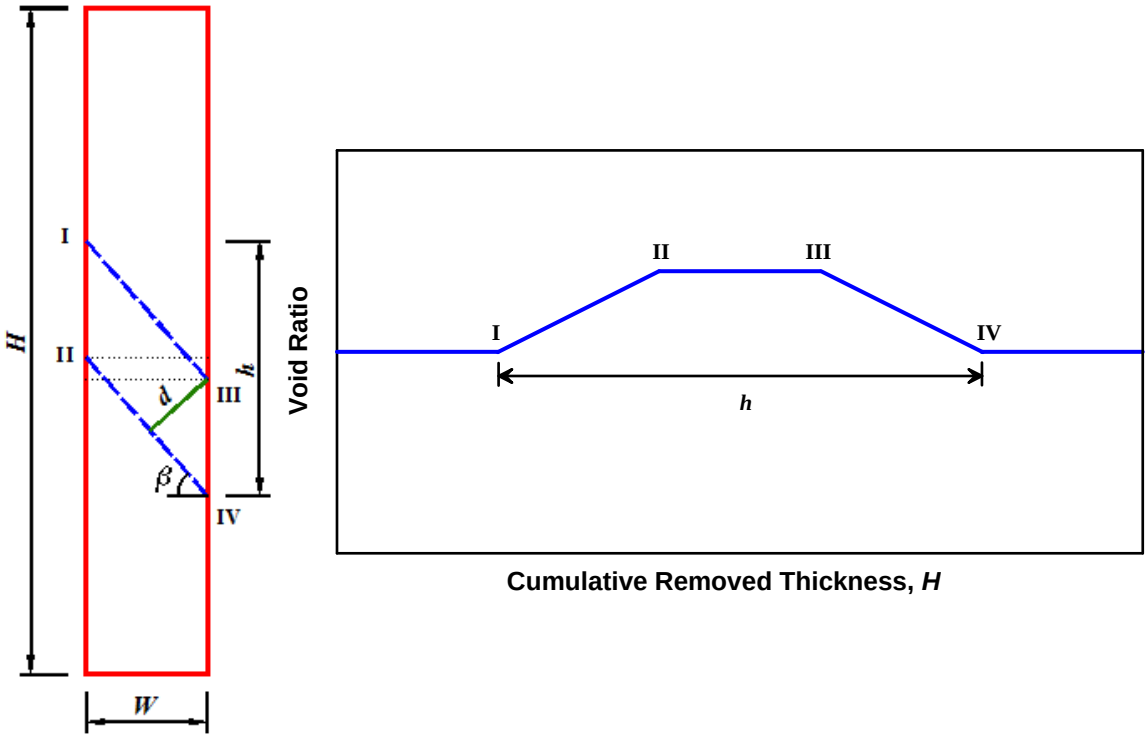

Figure 7.57 Prototype model for characterization of shear band width

7.4.5. 3-D Visualization of Simulated Microstructures

Four simulated microstructures were visualized in 3-D (APHDU, APHDS, MTHDU, and MTHDS). Each microstructure was rendered using 600 slices, and each slice was 1100 x 200 pixels in dimension and 0.1 mm/pixel in resolution. The slices were spaced at 0.1 mm, which yielded equivalent resolutions in three orthogonal directions.

7.4.5.1. 3-D Microstructures

Figure 7.58 presents a 3-D view of the rendered microstructures for the air-pluviated simulated specimens. Both the unsheared and sheared specimens are 110 mm x

60 mm x 20 mm. APHDU contains approximately 3500 particles (clumps), and APHDS contains approximately 3350 particles. Compared with the unsheared specimen, the sheared specimen looks very similar except for the existence of the dilatant zone marked by a pair of red dashed lines. This dilatant zone was caused by the shearing between the upper and lower blocks and is evident by larger local voids. Figure 7.59 presents the 3-D structures for the moist-tamped simulated specimens. They are the same in dimension as the air-pluviated specimens. The moist-tamped and air-pluviated numerical specimens were prepared with the same initial void ratio, and their global void ratios were very close both before and after being sheared. Therefore, MTHDU contains approximately 3500 particles, and MTHDS contains approximately 3350 particles. The two moist-tamped specimens look similar except for the shear-induced dilatant zone in MTHDS. The dilatant zone, marked by the red dashed lines, is located near the bottom of MTHDS. If comparing the 3-D microstructures of the air-pluviated and the moist-tamped specimens, the difference between their fabrics can be clearly visualized. For the air-pluviated specimens, as the particles were loaded randomly, they did not show any preference in the particle orientation. However, for the moist-tamped specimens, the layered structures can be observed and a large number of particles oriented either horizontally and vertically, especially at the horizontal boundaries of the layers. Such structure was caused by the way the particles were generated, which has been previously explained in Section 7.4.1.

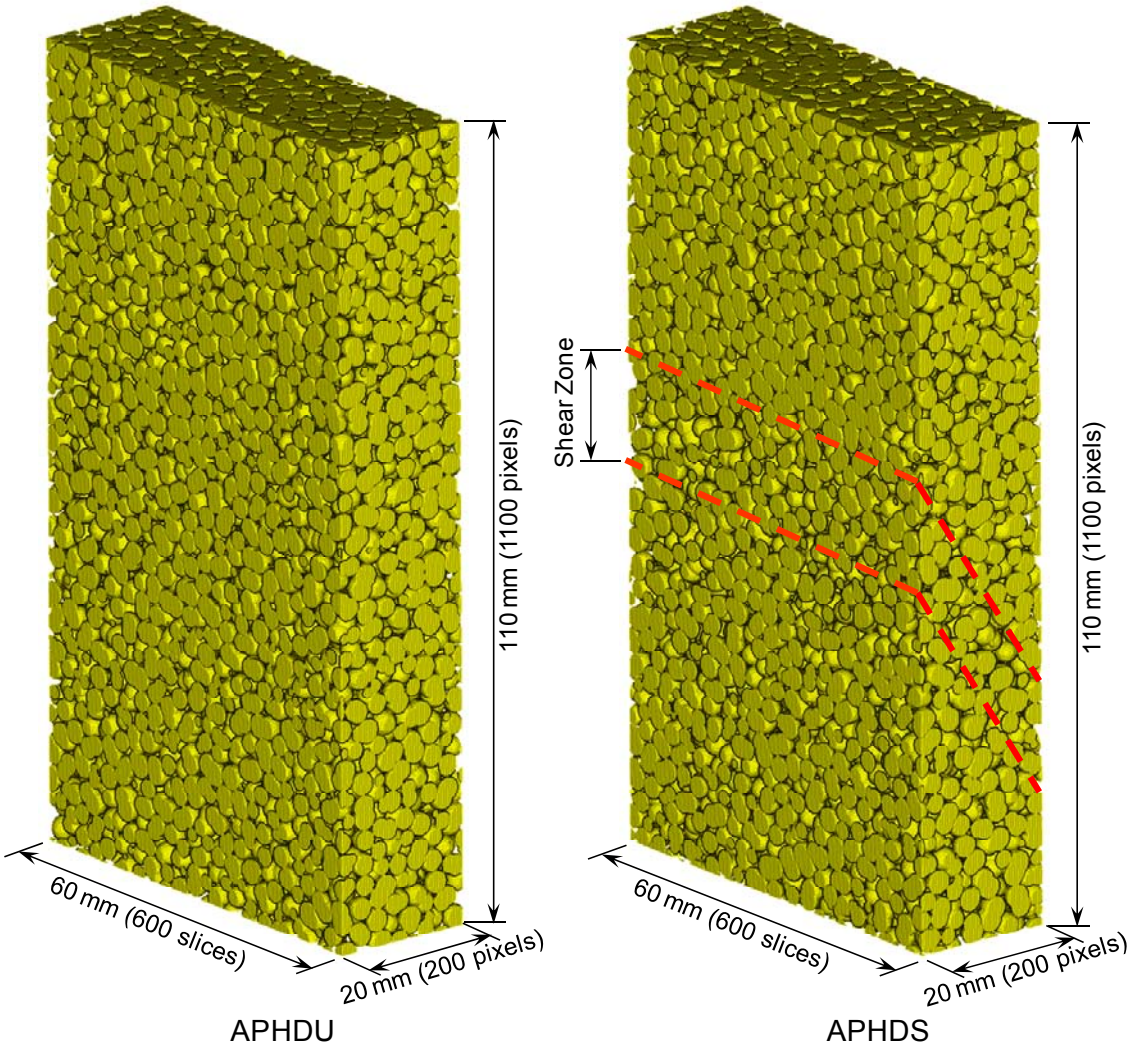

Figure 7.58 3-D structures of the simulated specimens (air-pluviated)

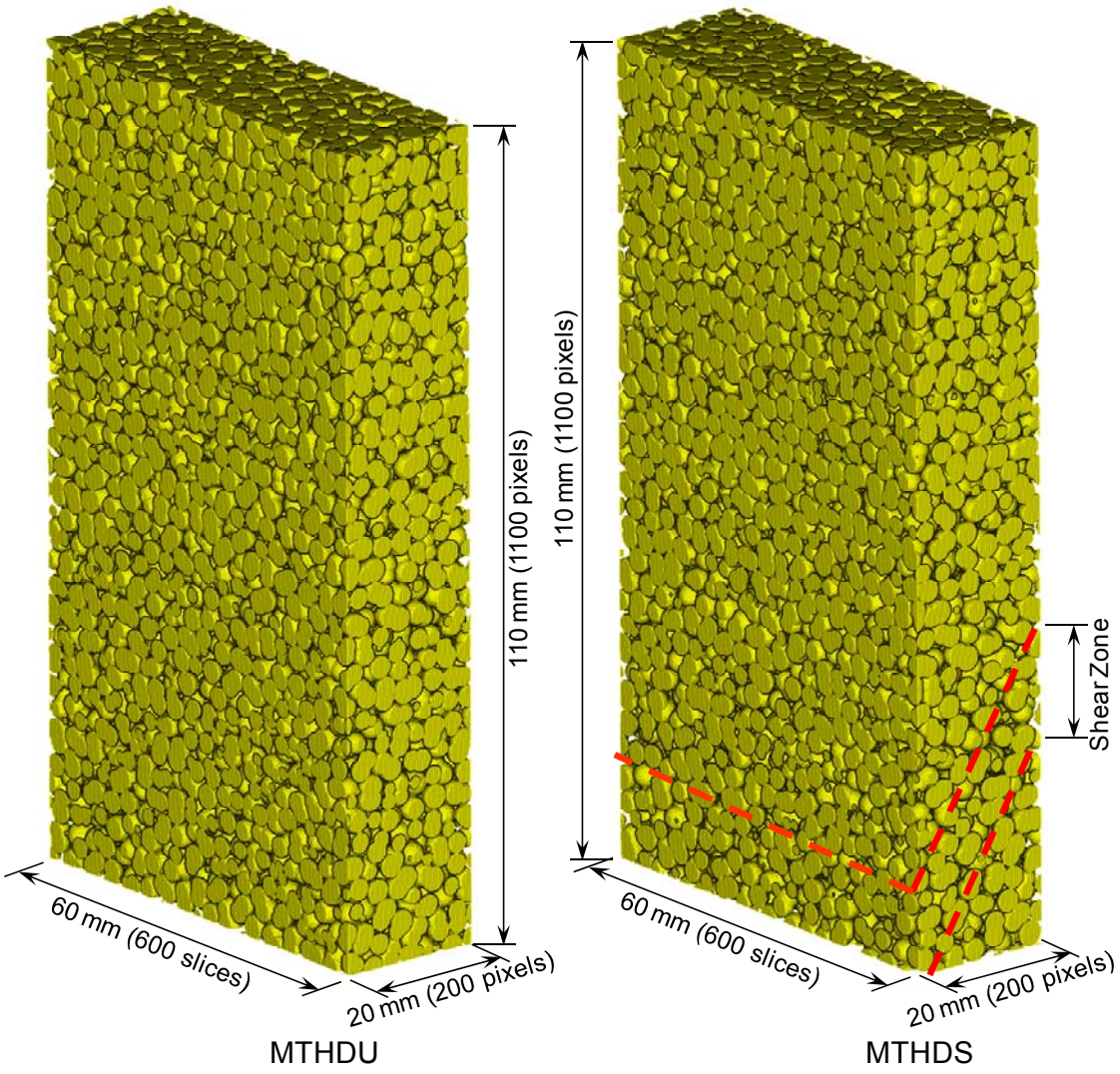

Figure 7.59 3-D structures of the simulated spcimens (moist-tamped)

7.4.5.2. Comparison of Reconstructed and Simulated Microstructures

Two cubic sub-volumes were extracted from UN (reconstructed) and APHDU (simulated) to compare their microstructures. The cubes were 5.6 mm in each side for the reconstructed specimen and 23 mm for the simulated specimen to keep the ratio between the cube size and the average particle size (D_{50} for reconstructed and D_{avg} in short axis for simulated) around 7.5. The cubes are shown in continuum, particle and void space in

Figure 7.60. In general, the simulated structure demonstrates a very good resemblance of the reconstructed structure.

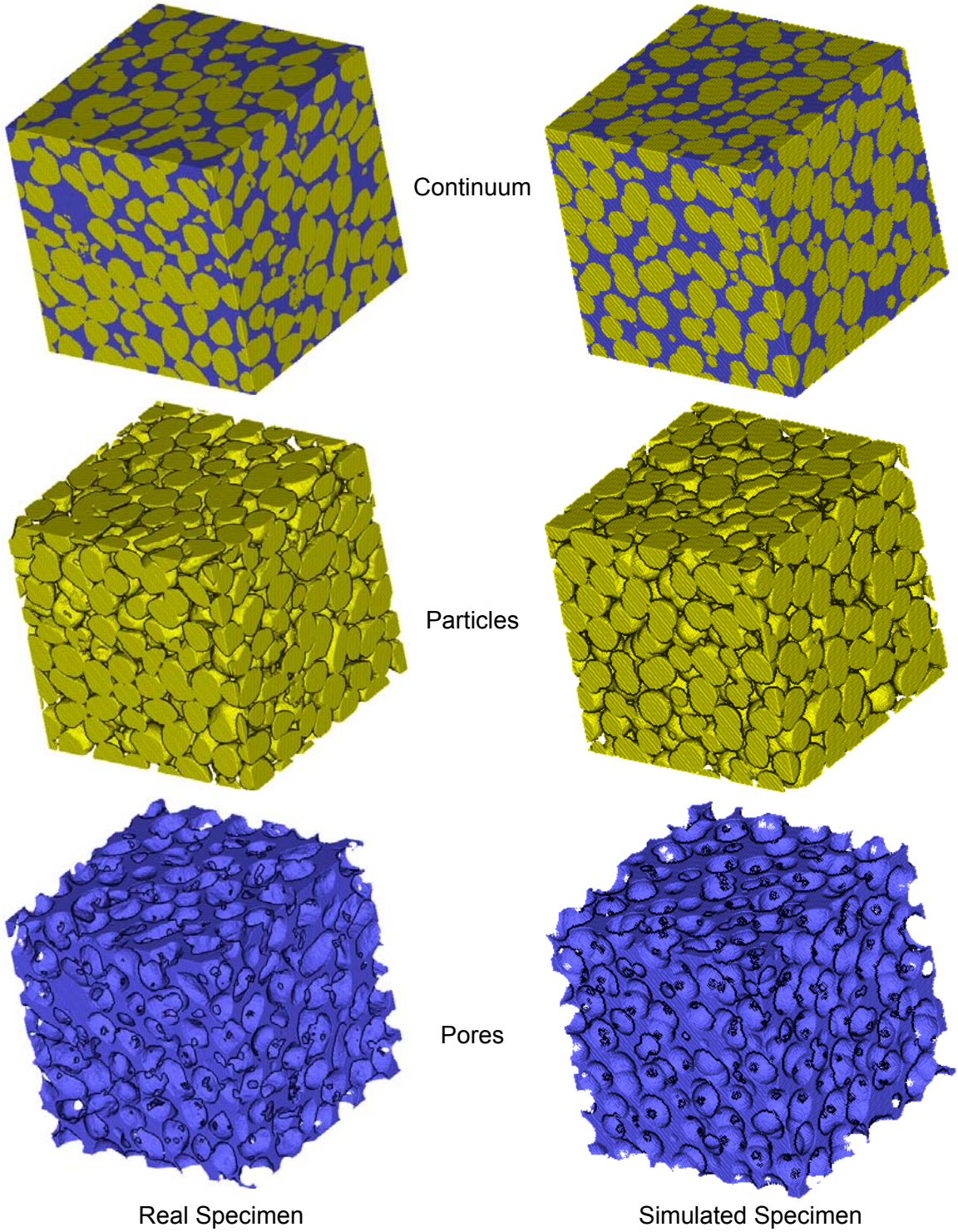

Figure 7.60 Comparison of reconstructed and simulated microstructures

7.5. Summary Observations Relating to Void Ratio Profile

In this chapter, three types of particle assemblies, ideal packing, reconstructed real specimens and simulated specimens, were dissected in three orthogonal directions. The 2-D void ratios were estimated from the dissected slices and plotted against the cumulative slice spacing distance. For all the void ratio profiles, the packing signature effect exhibits its influence, regardless of the particle size, particle shape, loading conditions and direction of dissections. The packing signature effect caused the estimated void ratios vary periodically from slice to slice, and the ranges of the void ratio variation of all the specimens are summarized in Table 7.1. Generally, more than one period can be recognized from the void ratio profiles except for SCP. The recognized periods are related to the particles size of the specimens. For the reconstructed real and simulated specimens, as their particles are multi-sized, the void ratio profiles even show the effect of a beat function (the phenomenon of the wave amplitude canceling or magnifying each other when two different waves are superimposed). It is possible that some packing information can be extracted from the void ratio profiles. Figure 7.61 presents the relationship between the 3-D void ratio and the coordination number for the ideal packings and the simulated structures. The figure illustrates that the relationship between the void ratio and the coordination number is not linear even for the ideal packings of monosized spherical particles. When the coordination number is less than 9, the void ratio of the ideal packing (composed of monosized spherical particles) is larger than the void ratio of the simulated specimens (composed of multi-sized 2-ball clumps). However, when the coordination number increases to more than 9, the void ratios of both types of assemblies get close. To check the uncertainties associated with the void ratios, the concept of entropy was applied to characterize the void ratio profiles of the ideal packings and the simulated specimens. The entropy is defined as:

$$H = -\sum_{i=1}^{N} p_i \cdot \ln p \tag{7.4}$$

where p_i is the frequency of a void ratio interval in the histogram; N is the number of void ratio interval. The entropies were estimated in all of the three orthogonal directions for the ideal packings and the simulated specimens. The calculated entropies are summarized in Table 7.2 and plotted against the coordination number in Figure 7.62. When the coordination numbers are close, the entropies of the simulated specimens are usually smaller than those of the ideal packings. For the simulated specimen, if its particles are randomly generated and oriented (air-pluviated), the entropies are very close in three orthogonal directions. However, if some kinds of heterogeneity exist (e.g., shear band or layer structures), the entropy of the specimen will be anisotropic and go up.

Table 7.1 Void ratio ranges for the dissections of the specimens

	Specimen Designation[1]	Void Ratio Range		
		Min.	Interm.	Max.
Ideal Packings	SCP	0.276 ~ Inf	0.276 ~ Inf	0.276 ~ Inf
	CTP	0.485 ~ 1.313	0.288 ~ 1.784	0.108 ~ Inf
	TSP	0.385 ~ 0.553	0.364 ~ 0.554	0.100 ~ 1.422
	TP	0.103 ~ 0.338	0.085 ~ 0.376	0.072 ~ 0.665
	FCP	0.286 ~ 0.560	0.286 ~ 0.560	0.286 ~ 0.560
Reconstructed Specimens	UN	0.450 ~ 0.593	0.439 ~ 0.586	0.434 ~ 0.631
	HD	0.514 ~ 0.611	0.496 ~ 0.644	0.437 ~ 0.722
Simulated Specimens	APHDU	0.385 ~ 0.471	0.371 ~ 0.482	0.361 ~ 0.497
	APHDS	0.450 ~ 0.514	0.442 ~ 0.533	0.357 ~ 0.695
	MTHDU	0.381 ~ 0.483	0.380 ~ 0.487	0.221 ~ 0.826
	MTHDS	0.446 ~ 0.547	0.426 ~ 0.558	0.243 ~ 0.821

Note: [1]Specimen designations represent:

Ideal Packing

SCP – simple cubic packing
CTP – cubic-tetrahedral packing
TSP – tetragonal-sphenoidal packing
TP – tetrahedral packing
FCP – face-centered cubic packing

Reconstructed Specimens

UN – unsheared
HD – highly dilatant

Simulated Specimens

APHDU – air-pluviated, highly dilatant, unsheared
APHDS – air-pluviated, highly dilatant, sheared
MTHDU – moist-tamped, highly dilatant, unsheared
MTHDS – moist-tamped, highly dilatant, sheared

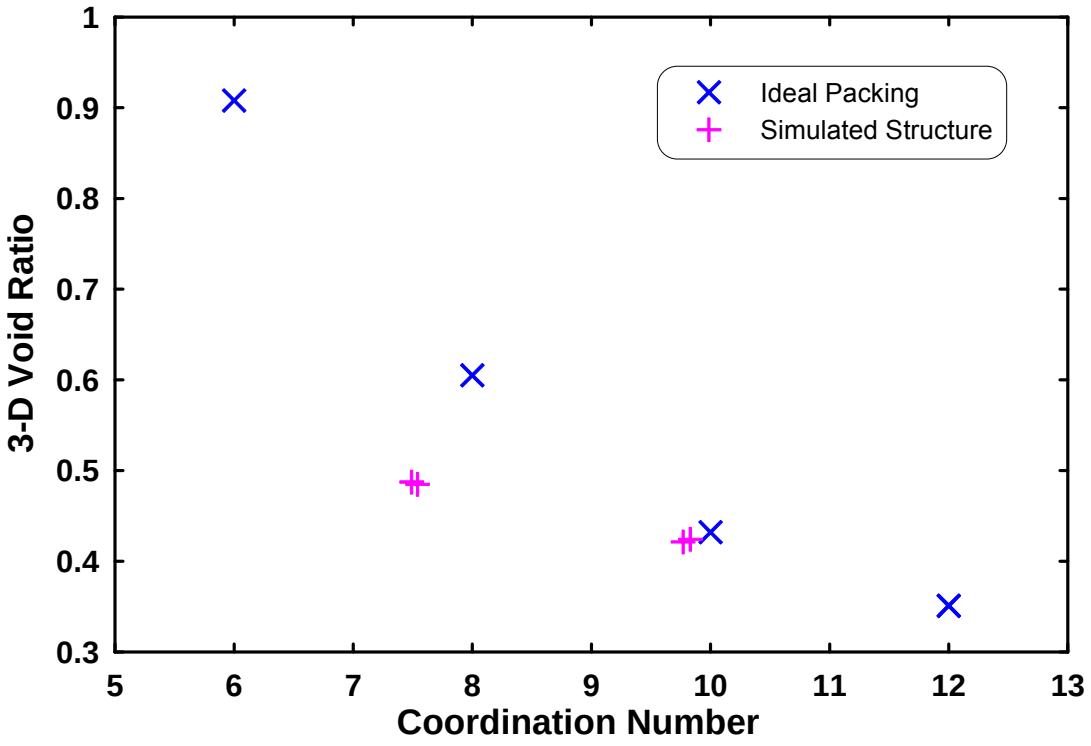

Figure 7.61 Relationship between 3-D void ratio and coordination number

Table 7.2 Summary of entropies for ideal packings and simulated specimens

	Specimen Designation	Entropy		
		Min.	Interm.	Max.
Ideal Packings	SCP	0.540	0.540	0.540
	CTP	0.551	0.577	0.774
	TSP	0.503	0.529	0.808
	TP	0.527	0.529	0.579
	FCP	0.454	0.454	0.454
Simulated Specimens	APHDU	0.359	0.393	0.425
	APHDS	0.348	0.375	0.619
	MTHDU	0.377	0.381	0.736
	MTHDS	0.385	0.419	0.737

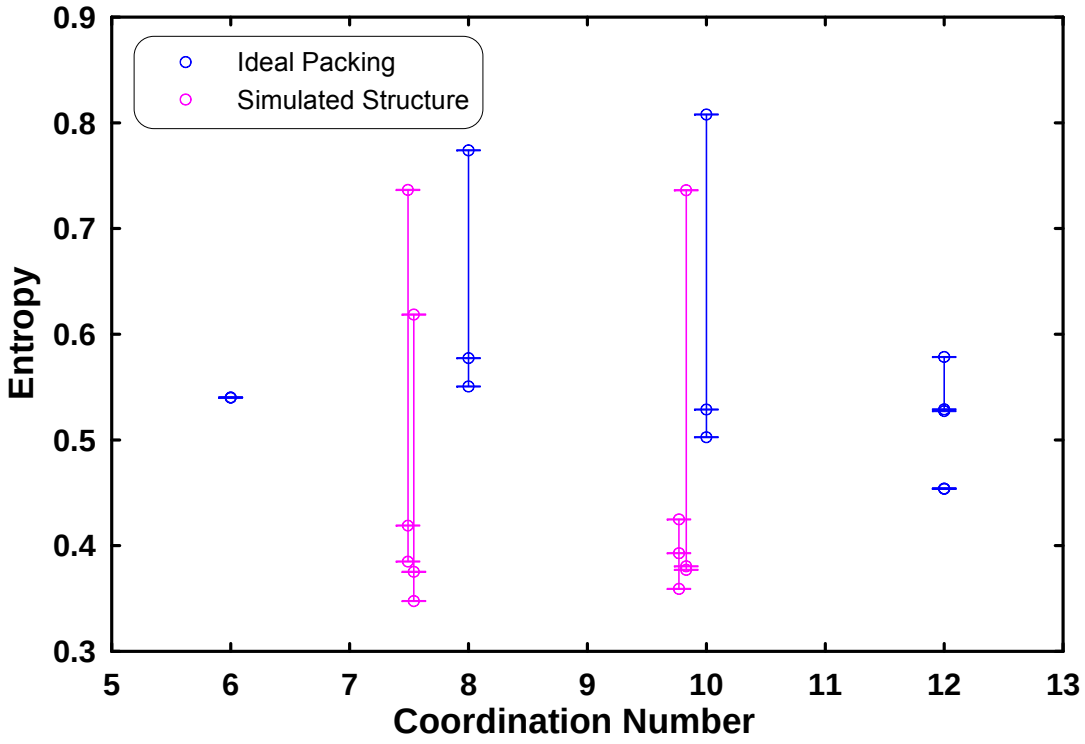

Figure 7.62 Relationship between void ratio entropy and coordination number

7.6. Summary and Conclusions

The reconstructed digital microstructures of two biaxial real specimens, a sheared highly dilatant specimen and an unsheared specimen, were characterized and analyzed in both 2-D and 3-D space. The spatial analysis along the pre-determined inclined strips defined three types of zones inside the highly dilatant specimen: the non-dilatant zones with consistently low void ratios, the shear zone with consistently high void ratios, and two transition zones with changing void ratios from low to high. The shear band width was estimated to be 14.2 x D_{50} from the strip analysis and 13.1 x D_{50} from the void ratio profile. The histograms of the local void ratio distribution of the highly dilatant specimen showed a higher statistical mean and standard deviation than that of the unsheared specimen, which indicated that shearing resulted in an increase of local void ratios and the degree of heterogeneity. For the sheared specimen, dilation inside the shear zone

could be easily discerned by a larger statistical mean and standard deviation than outside the shear zone.

The microstructures of the simulated air-pluviated and moist-tamped highly dilatant specimens were also analyzed and characterized in the same way as the reconstructed real specimens. The same three types of zones were evident in the simulated specimens by the spatial analysis along the pre-determined inclined strips. The shear band width of the air-pluviated simulated specimen was estimated to be 12.6 x D_{avg} in short axis by the strip analysis and only 6.1 x D_{avg} in short axis by the void ratio profile. Boundary, end platen and meso-structure effects contributed to this lower than expected value. Similar to the real specimens, the histograms of the local void ratio distribution of the simulated specimens consistently showed a higher statistical mean and standard deviation in the sheared specimen than in the unsheared specimen.

The packing signature effect was consistently identified in the reconstructed real specimens, the simulated specimens and the idealized packings. This phenomenon results from the shape and spatial arrangement of the particles. The amplitudes of the packing signature effect decreased as the number of sampled particles increased and tended to stabilize when certain number of particles were exceeded confirming it is a material structure property, not a measured artifact. The packing signature effect contains packing information both at the micro-scale and meso-scale, and further systematic statistical analyses should be developed and applied to quantifying its presence and influence.

CHAPTER 8

CONCLUSIONS AND RECOMMENDATIONS

8.1. Conclusions

The phenomenon of strain localization commonly manifests itself in the failures of both in-situ geo-structures and laboratory soil tests. In the last ten years, several extensive studies have been conducted at Georgia Tech to investigate the mechanism of strain localization and link the microstructural properties with the engineering behavior of Ottawa sands. As an effort to extend and complement the previous studies, the current study tried to reconstruct, characterize, numerically simulate and visualize the inherent and induced microstructures of Ottawa sand specimens subject to triaxial and biaxial loading. The current study is composed of three components: experimental work, numerical modeling and microstructural analysis. For the experimental work, some modifications were implemented to the available serial sectioning technique, which had been successfully applied to reconstruct 3-D volumes of the triaxial specimens, to make it useful for biaxial specimens also. Then, both the triaxial and biaxial specimens were simulated by the 3-D DEM code PFC3D, and their local void ratios, coordination numbers, particle rotations and displacements, contact normal distributions and normal contact forces as well as stress and strain responses were investigated. Both the reconstructed and simulated structures were characterized and analyzed in 2-D and 3-D to examine their local void ratio distributions, extent of shear bands, influence of soil fabrics and packing signature effect. Finally, the reconstructed and simulated structures were visualized in 3-D volume to provide a direct impression of the inherent and induced soil microstructures. Based on the current study, the following conclusions were reached:

- The optical microscopy based montage and serial sectioning technique is an efficient tool to reconstruct the 3-D microstructures of sand specimens. By stitching small images captured contiguously by a grid pattern into a big image, the montage technique can cover a much larger field of view while not losing needed resolution for small-scale features. The available surface preparation (grinding and polishing) apparatus is able to produce a large number of high-quality slices within a short time. Compared with other technologies that can produce 3-D images of similar quality like high-energy X-ray CT, the serial sectioning in the current study has the following advantages: (1) easy to operate; (2) much less expensive; and (3) easily accessible to most researchers in geotechnical engineering.
- Two types of surface preparation procedures have been developed for image analysis purpose and implemented in the previous and current studies. The short-duration grinding procedure prepares a slice within 2 to 3 minutes while the long-duration grinding procedure takes 30 to 60 minutes to complete a slice. Due to the different preparation time, apparatus and abrasive used, these two procedures create distinctive surface conditions which result in different images captured by the microscope. By conducting a comparison study on the two preparation procedures, it was found that the short-duration grinding can produce images of better quality than the long-duration grinding, and hence substantially reduce the subsequent image processing work required.
- The numerical modeling results indicate that the intermediate principal stress plays a non-negligible role in the mechanical behavior of triaxial and biaxial specimens. Therefore, 3-D DEM modeling provides a superior solution than 2-D DEM modeling.
- In order to investigate the influence of soil fabrics in the 3-D DEM simulation, two preparation approaches were designed and applied. One approach created

numerical specimens with uniformly distributed and oriented particles, and the other one produced layered structures with preferentially oriented particles. The two types of soil fabrics were used in the numerical modeling and their mechanical material behaviors were characterized.

- The basic element in 3-D DEM is a spherical particle, but more complex shapes can be formed by overlapping two or more spheres and such structures are called clumps. A comparison study between single sphere models and clump models indicate that the application of 2-sphere clumps reduces large-magnitude particle rotations and enhances the global strength of the specimens under shearing.
- In the numerical triaxial tests, evidence of the turbine-like internal failure structures proposed by Desrues et al. (1996) was mixed. While the cone structures were able to be clearly defined, the “blade” structures were not. Multiple factors, such as boundary conditions (velocity-controlled rigid cylindrical walls) and particle scaling, may be responsible for the absence of the “blade” structures.
- A flexible membrane algorithm was designed and successful implemented for the numerical biaxial tests. The flexible membranes were composed of simply-packed bonded single spheres. The membrane was force-controlled and able to contract and stretch when the specimen deformed. The modeling results prove the application of the flexible membranes enabled the shear band to initialize and develop in the biaxial numerical tests. A total of 10,800 spheres were used for the membranes, about half the number of spheres used for the specimen (approximately 11,000 2-sphere clumps), which means a large percentage of the computation was used to deal with the membrane particles. This fact indicates that the boundaries are as important as the specimen particles and more effort should be contributed to modeling the boundaries better in the DEM simulation.
- A parametric study was performed to investigate the effects of some model parameters on the numerical biaxial tests. The investigated parameters are: normal

stiffness, shear stiffness and friction coefficient of specimen particles, and normal stiffness and particle size of membrane particles. The parametric study shows the model parameters of specimen particles have substantial effects on the strength of the specimens (i.e., initial modulus, peak stress, peak strain, residual stress and volumetric strain), while the model parameters of membrane particles primarily affect the principal stresses in the stress-hardening stage.

- Through the numerical modeling, it was found that when strain localization initializes in the biaxial specimens, distinctive microstructural behaviors take place inside and outside the localized zones. The localized zone usually features larger void ratio, smaller coordination number, larger particle rotations with minor particle displacements and less dense arrays of normal contact forces than the zones outside the shear band.
- To obtain the microstructural information, a series of 2-D and 3-D characterizations and analyses were performed on the 2-D slices generated by serial sectioning from the biaxial specimens. Two methods, strip analysis and void ratio per slice, were used to define the extent of the shear band. The results from these two methods are close: 14.2 x D_{50} from strip analysis and 13.1 x D_{50} from void ratio per slice.
- In order to perform the same 2-D and 3-D characterizations and analyses, 2-D slices were created using a serial dissection approach for the simulated specimens. The extent of the shear band was defined to be 12.6 x D_{avg} in short axis by strip analysis and 6.1 x D_{avg} in short axis by void ratio per slice. The smaller shear band thickness estimated by void ratio per slice was due to the fact that the shear band height, h, was difficult to define from the void ratio profile.
- Three types of particle assemblies, ideal packing, reconstructed real specimen and simulated specimen, were dissected in three orthogonal directions. The 2-D void ratio was estimated for each dissected slice by pixel counting and plotted against

the cumulative slice spacing distance. All the void ratio profiles exhibited a wave-like shape with certain periods and amplitudes. Such phenomenon is termed as the packing signature effect. The packing signature effect results from the shape and spatial arrangement of the particles of granular materials, regardless of the particle size, loading conditions and direction of dissections. The amplitudes of the packing signature effect decreased as the number of sampled particles increased and tended to stabilize when the number of sampled particles exceeded 300 in the current study.

- The particulate structures of the reconstructed and simulated specimens were rendered in 3-D volumes to visualize the influence of strain localization. The localization zones exhibit loosely-packed particle structures and larger pore structures than the zones outside the shear band. By comparing the microstructures of the reconstructed and simulated structures, it is noted that the simulated structure composed of 2-ball clumps demonstrates a good resemblance of the reconstructed structure composed of sub-rounded Ottawa sands.

8.2. Recommendations

Although the current study shed some important new insights into the inherent and induced sand microstructures subject to triaxial and biaxial loading, some improvements and further work need to be done in the future to enhance the knowledge and understanding of strain localization:

- Only two 3-D digital structures were created and analyzed in the current study, and they were the highly dilatant specimen and its correlating unsheared specimen. Additional 3-D structures need to be created and analyzed for other initial states (e.g., contractive and slightly dilatant specimen and its correlating unsheared specimen). As a result, the influence of confining pressure can be better quantified.

- A flexible membrane is essential to the strain localization in both triaxial and biaxial specimens. However, the numerical triaxial specimens in the current study were bounded by the rigid cylindrical walls, which impeded the formation of the localized zones. A flexible confining membrane, like the one used in the numerical biaxial tests, should be designed and implemented in future numerical triaxial tests.
- Although the two preparation methods created two distinctive soil fabrics for the numerical modeling, they did not yield a direct match with the physical air-pluviation and moist-tamping methods due to the fact that the generated particles were not subject to any gravitational fields. Some new numerical algorithms and setups are needed to solve this problem.
- The estimated void ratio profiles for the reconstructed and simulated structures were affected by the packing signature effect. It seems some internal packing information can be extracted from the void ratio profiles, nevertheless, they were only qualified in the current study. Further systematic statistical analyses should be developed and applied to quantify the packing signature effect and help extract internal packing information.

REFERENCES

Abràmoff, M. (2004). "Bio-Medical Imaging in Java." http://bij.isi.uu.nl/.

Alshibli, K.A., and Hasan, A. (2008). "Spatial variation of void ratio and shear band thickness in sand using X-ray computed tomography." *Géotechnique*, 58(4): 249-257.

Alshibli, K.A., Sture, S., Costes, N.C., Frank, M.L., Lankton, M.R., Batiste, S.N., and Swanson, R.A. (2000). "Assessment of localized deformations in sand using X-Ray computed tomography." *Geotechnical Testing Journal*, 23(3): 274-299.

Arthur, J.R.F., Dunstan, T., Al-Ani, Q.A.J.L., and Assadi, A. (1977). "Plastic deformation and failure in granular media." *Géotechnique*, 27(1): 53-74.

Belheine, J.P., Plassiard, J.P., Donzé, F.V., Darve, F., and Seridi, A. (2009). "Numerical simulation of drained triaxial test using 3D discrete element modeling." *Computers and Geotechnics*, 36: 320-331.

Bertrand, D, Nicot, F., Gotteland, P., and Lambert, S. (2005). "Modelling a geo-composite cell using discrete analysis." *Computers and Geotechnics*, 32: 564-577.

Bhatia, S.K., and Soliman, A.F. (1990). "Frequency distribution of void ratio of granular material determined by an image analyzer." *Soils and Foundations*, 30(1): 1-16.

Bishop, A.W. (1961). "Discussion on soil properties and their measurement." *Proceedings of 4$^{th\ t}$ International Conference on Soil Mechanics and Foundation Engineering*, Vol. I, 16-20.

Bystrzycki, J., and Prezetakiewicz, W. (1992). "3-dimensional reconstruction of annealing twins shape in FCC metals by serial sectioning." *Scripta Materialia*, 27: 893-896.

Chen, C.C. (2000). "Shear induced evolution of structure in water-deposited sand specimens." Ph.D Thesis, Georgia Institute of Technology, Atlanta.

Cheng, Y.P., Peng, Q., and Hughes, L. (2008). “Shear band and strength of crushable agglomerates in direct shear box simulations of discrete element method.” *Proc. 4th International Symposium on Deformation Characteristics of Geomaterials*, Atlanta, GA, September 22-24: 357-364.

Cheung, G., and O’Sullivan, C. (2008). “Effective simulation of flexible lateral boundaries in two- and three-dimensional DEM simulations.” *Particuology*, 6: 483-500.

Claquin, C., Emeriault, F., and Nouguier-Lehon, C. (2003). “Influence of particles shape on the macroscopic behavior of granular material.” *Proceedings of the 3rd International Symposium on the Deformation Characteristics of Geomaterials*, Lyon, 1175-1182.

Clough, R.W. (1960). “The finite element method in plane stress analysis.” *Proceedings of the Second ASCE Conference on Electronic Computation*, Pittsburgh, PA.

Cundall, P.A. (1971). “A computer model for simulating progressive large scale movements in blocky rock systems.” *ISRM Symposium*, Nancy, France, 129-136.

Cundall, P.A. (1989). “Numerical experiments on localization in frictional materials.” *Ingenieur-Archiv*, 59: 148-159.

Cundall, P.A., and Strack, O.D.L. (1979). “A discrete numerical model for granular assemblies.” *Géotechnique*, 29(1): 47-65.

Deresiewicz, H. (1958). “Mechanics of granular matter.” *Advances in Applied Mechanics*, 5: 233-306.

Desrues, J., and Chambon, R. (2002). “Shear band analysis and shear moduli calibration.” *International Journal of Solids and Structures*, 39: 3757-3776.

Desrues, J., Chambon, R., Mokni, M., and Mazerolle, F. (1996). “Void ratio evolution inside shear bands in triaxial sand specimens studied by computed tomography.” *Géotechnique*, 46(3): 529-546.

Desrues, J., Lanier, J., and Stutz, P. (1985). “Localization of the deformation in tests on sand sample.” *Engng. Fract. Mecha.*, 21: 909-921.

Drescher, A., Vardoulakis, I., and Han, C. (1990). “A biaxial apparatus for testing soils.” *Geotechnical Testing Journal*, 13(3): 226-234.

Duncan, J.M., and Seed, H.B. (1966). “Strength variation along failure surfaces in clay.” *Journal of the Soil Mechanics and Foundations Division*, ASCE, 92(SM6): 81-104.

Dlmekati, A., and El Shamy, U. (2010). “A practical co-simulation approach for multiscale analysis of geotechnical systems.” *Computers and Geotechnics*, 37: 494-503.

Evans, T.M. (2005). “Microscale physical and numerical investigations of shear banding in granular soils.” Ph.D Thesis, Georgia Institute of Technology, Atlanta.

Evans, T.M., and Frost, J.D. (2010). “Multiscale investigation of shear bands in sand: Physical and numerical experiments.” *Int. J. Numer. Anal. Methods Geomech.*

Fiala, J.C., and Harris, K.M.. (2001). “Extending unbiased stereology of brain ultrastructure to three-dimensional volumes.” *Journal of the American Medical Informatics Association*, 8(1): 1-16.

Finno, R.J., Harris, W.W., Mooney, M.A., and Viggiani, G. (1996). “Strain localization and undrained steady state of sand.” *Journal of Geotechnical Engineering*, ASCE, 122(6): 462-473.

Frost, J.D., Evans, T.M. (2009). “Membrane effects in biaxial compression tests.” *Journal of Geotechnical and Geoenvironmental Engineering*, 135(7): 986-991.

Frost, J.D., and Jang, D.J. (2000). “Evolution of sand microstructure during shear.” *Journal of Geotechnical and Geoenvironmental Engineering*, ASCE, 126(2): 116-230.

Frost, J.D., and Kuo, C.Y. (1996). “Automated determination of the distribution of local void ratio from digital images.” *Geotechnical Testing Journal*, 19(2): 107-117.

Frost, J.D., and Park, J.Y. (2003). “A critical assessment of the moist tamping technique.” *J. Geotechnical Testing*, 26(1): 57-70.

Fakhimi, A. (2009). “A hybrid discrete-finite element model for numerical simulation of geomaterials.” *Computers and Geotechnics*, 36: 386-395.

Griffiths, D.V., and Lane, P.A. (1999). “Slope stability analysis by finite elements.” *Géotechnique*, 49(3): 387-403.

Hall, S.A., Bornert, M., Desrues, J., Pannier, Y., Lenoir, N., Viggiani, G., and Besuelle, P. (2010). “Discrete and continuum analysis of localized deformation in sand using X-ray μCT and volumetric digital image correlation.” *Geotechnicque*, 60(5): 315-322.

Han, C., and Vardoulakis, I. (1991). “Plane-strain compression experiments on water-saturated fine-grained sand.” *Geotéchnique*, 41(1): 49-78.

Hasan, A., and Alshibli, K.A. (2010). “Experimental assessment of 3D particle-to-particle interaction within sheared sand using synchrotron microtomography.” *Geotéchnique*, 60(5): 369-379.

Hoffpauir, B.K., Pope, B.A., and Spirou, G.A. (2007). “Serial sectioning and electron microscopy of large tissue volumes for 3D analysis and reconstruction: a case study of the calyx of Held.” *Nature Protocols*, 2: 9-22.

Huang, Z.Y., Yang, Z.X., and Wang, Z.Y. (2008). “Discrete element modeling of sand behavior in a biaxial shear test.” *Journal of Zhejiang University – Science A*, 9(9): 1176-1183.

Ibrahim, A.A., and Kagawa, T. (1991). “Microscopic measurement of sand fabric from cyclic tests causing liquefaction.” *Geotechnical Testing Journal*, 14(4): 371-382.

Itasca Consulting Group. (2008). “PFC3D: Particle Flow Code in Three Dimensions.” Version 4.0.

Iwashita, K., and Oda, M. (1998). “Rolling resistance at contacts in simulation of shear band development by DEM.” *Journal of Engineering Mecahnics,* ASCE, 124(3): 285-292.

Jongerius, A., Schoonderbeek, D., and Jager, A. (1972). “The application of the Quantimet 720 in soil micromorphometry.” *The Microscope*, 20: 243-254.

Kaneko, K., Terada, K., Kyoya, T., and Kishino, Y. (2003). "Global-local analysis of granular media in quasi-static equilibrium." *International of Solids and Structures*, 40: 4043-4069.

Kjellman, W. (1936). "Report on an apparatus for consummate investigation of mechanical properties of soils." *Proceedings of 1st International Conference on Soil Mechanics and Foundation Engineering*, Vol. I, 16-20.

Kneafsev, T.J., Tomutsa, L., Moridis, G.J., Seol, Y., Freifeld, B.M., Taylor, C.E., and Gupta, A. (2007). "Methane hydrate formation and dissociation in a partially saturated core-scale sand sample." *Journal of Petroleum Science and Engineering*, 56(1-3): 108-126.

Kuhn, M.R. (1999). "Structured deformation in granular materials." *Mechanics of Materials*, 31(6):407-429.

Kuo, C.Y., and Frost, J.D. (1995). "Quantifying the fabric of granular materials – an image analysis approach." *Research Report No. GIT-CEE/GEO-95-1*, School of Civil and Environmental Engineering, Georgia Institute of Technology.

Kuo, C.Y., Frost, J.D., and Chameau, J.L. (1998). "Image analysis determination of stereology based fabric tensors." *Géotechnique*, 48(4): 515-525.

Lee, K.L. (1970). "Comparison of plane strain and triaxial tests on sand." *Journal of the Soil Mechanics and Foundation Division*, ASCE, 96(3):901-923.

Lee, S.W. (1998). "Influence of surface topography on interface strength and counterface soil structure." Ph.D Thesis, Georgia Institute of Technology, Atlanta.

Li, M.S., Ghosh, S., Rouns, T.N., Weiland, H., Richmond, O., and Hunt, W. (1998). "Serial sectioning method in the construction of 3-D microstructures for particle-reinforced MMCs." *Materials Characterization*, 41: 81-95.

Lindquist, W.B. (1999). "3DMA General Users Manual." State University of New York, Stony Brook.

Lindquist, W.B., Lee, S.M., Coker, D.A., Jones, K.W., and Spanne, P. (1996). "Medial axis analysis of void structure in three-dimensional tomographic images of porous media." *Journal of Geophysical Research*, 101(B4): 8297-8310.

Liyanapathirana, J., Carter, J.P., and Airey, D.W. (2005). "Numerical modeling of nonhomogeneous behavior of structured soils during triaxial tests." *International Journal of Geomechanics*, 5(1): 10-23.

Lobo-Guerrero, S., and Vallejo, L.E. (2007). "Influence of pile shape and pile interaction on the crushable behavior of granular materials around driven piles: DEM analyses." *Granular Matter*, 7: 241-250.

Macari-Pasqualino, E.J., Runesson, K., and Sture, S. (1994). "Response prediction of granular materials at low effective stresses."*Journal of Geotechnical Engineering*, 120(7): 1252-1268.

Mahmood, Z., and Iwashita, K. (2010). "Influence of inherent anisotropy on mechanical behavior of granular materials based on DEM simulations." *Int. J. Numer. Anal. Meth. Geomech.*, 34: 795-819.

Maynar, M.J.M., and Rodríguez, L.E.M. (2005). "Discrete numerical model for analysis of earth pressure balance tunnel excavation." *Journal of Geotechnical and Geoenvironmental Engineering*, ASCE, 131(10): 1234-1242.

Michelland, S., Schiborr, B., Coster, M., Mordike, B.L., and Chermant, J.L. (1989). "Size distribution of granular materials from unthresholded image." *Journal of Microscopy*, 156(3):303-311.

Ngan-Tillard, D.J.M., Cheng, X.H., Van Nes, J., and Zitha, P.L.J. (2005). "Application of x-ray computed tomography to cone penetration tests in sands." *Geotechnical Special Publication, Geo-Frontiers 2005*, 130-142: 2393-2404.

Ni, Q., Powrie, W., Zhang, X., and Harkness, R. (2000). "Effect of particle properties on soil behaviour: 3-D numerical modeling of shearbox tests." *Numerical Methods in Geotechnical Engineering - GeoDenver 2000, ASCE*: 58-70.

O'Sullivan, C., Bray, J.D., Riemer, M. (2002). "Influence of particle shape and surface friction variability on response of rod-shaped particulate media." *Journal of Engineering Mechanics*, ASCE, 128(11): 1182-1192.

O'Sullivan, C., and Cui, L. (2009). "Micromechanics of granular material response during load reversals: combined DEM and experimental study." *Power Technology*, 193: 289-302.

Oda, M. (1976). “Fabrics and their effects on the deformation behavior of sand.” Special Issue, Department of Foundation Engineering, Faculty of Engineering, Saitama University, Japan.

Oda, M., Takemura, T., and Takahashi, M. (2004). “Microstructure in shear band observed by microfocus X-ray computed tomography.” *Géotechnique*, 54(8): 539-542.

Otani, J., Mukunoki, T., and Obara, Y. (2000). “Application of X-ray CT method for characterization of failure in soils.” *Soils and Foundations*, 40: 111-118.

Peric, D., Runesson, K., and Sture, S. (1992). “Evaluation of plastic bifurcation for plane strain versus axisymmetry.” *Journal of Engineering Mechanics*, 118(3): 512-524.

Powrie, W., Ni, Q., Harkness, R., and Zhang, X. (2005). “Numerical modeling of plane strain tests on sands using a particulate approach.” *Géotechnique*, 55(4): 297-306.

Proctor, D.C., and Barton, R.R. (1974). “Measurements of the angle of interparticle friction.” *Géotechnique*, 24(4): 581-604.

Rechenmacher, A.L. (2005). “Grain-scale processes governing shear band initiation and evoluation in sands.” *Journal of the Mechanics and Physics of Solids*, 54:22-45.

Rechenmacher, A.L., Abedi, S., and Chupin, O. (2010). “Evolution of force chains in shear bands in sands.” *Géotechnique*, 60(5):343-351.

Rechenmacher, A.L., and Finno, R.J. (2004). “Digital image correlation to evaluate shear banding in dilative sands.” *Geotechnical Testing Journal*, 27(1): 13-22.

Rhines, F.N., and Craig, K.R. (1976). “Measurement of average grain volume and topological parameters by serial sectioning analysis.” *Metallurgical and Materials Transactions A*, 7(11): 1729-1734.

Rothenburg, L., and Bathurst, R.J. (1992). “Micromechanical features of granular assemblies with planar elliptical particles.” *Géotechnique*, 42(1): 79-95.

Santamarina, J.C., Klein, K.A., and Fam, M.A. (2001). Soils and Waves. John Wiley and Sons, West Sussex, England.

Salot, C., Gotteland, P., and Villard. (2009). “Influence of relative density on granular behavior: DEM simulations of triaxial tests.” *Granular Matter*, 11: 221-236.

Seo, H., Basu, D., Prezzi, M., and Salgado, R. (2009). “Load-settlement response of rectangular and circular piles in multilayered soil.” *Journal of Geotechnical and Geoenvironmental Engineering*, ASCE, 135(3): 420-430.

Sheng, D., Westerberg, B., Mattsson, H., and Axelsson, K. (1997). “Effects of end restraint and strain rate in triaxial tests.” *Computers and Geotechnics*, 21(3) : 163-182.

Shi, B., Murakami, Y., Wu, Z., Chen, J., and Inyang, H. (1999). “Monitoring of internal failure evolution in soils using computerization X-ray tomography.” *Engineering Geology*, 54: 321-328.

Shoda, D., Kawabata, T., Uchida, K., Numata, A., and Motoyama, H. (2009). “Distinct element analysis for group piles subjected to vertical loading.” *Proceedings of the International Offshore and Polar Engineering conference*, 274-279.

Singh, H., and Gokhale, A.M. (2005). “Visualization of three-dimensional microstructures.” *Materials Characterization*, 54: 21-29.

Sun, D.A., Huang, W.X., and Yao, Y.P. (2008). “An experimental study of failure and softening in sand under three-dimensional stress condition.” *Granular Matter*, 10: 187-195.

Tannant, D.D., and Wang, C. (2002). “PFC model of wedge penetration into oil sands.” *Geotechnical Special Publication No. 117: Discrete Element Methods, Numerical Modeling of Discontinua*, Santa Fe, NM: 311-316.

Tatsuoka, F., Sakamoto, M., Kawamura, T., and Fukushima, S. (1990). “Strength and deformation characteristics of sand in plane strain compression at extremely low pressures.” *Soil and Foundations*, 26(1): 65-84.

Tewari, A., and Gokhale, A.M. (2000). “Application of three-dimensional digital image processing for reconstruction of microstructural volume from serial sections.” *Materials Charaterization*, 44: 259-269.

Thomas, P.A., and Bray, J.D. (1999). "Capturing nonspherical shape of granular media with disk clusters." *Journal of Geotechnical and Geoenvironmental Engineering*, ASCE, 125(3): 169-178.

Thomson, P.R., and Wong, R.C.K. (2008). "Specimen nonuniformities in water-pluviated and moist-tamped sands under undrained triaxial compression and extension." *Canadian Geotechnical Journal*, 45(7): 936-956.

Thornton, C. (2000). "Numerical simulations of deviatoric shear deformation of granular media." *Géotechnique*, 50(1): 43-53.

Tordesillas, A., Muthuswamy, M., and Walsh, S.D.C.. (2008). "Mesoscale measures of nonaffine deformation in dense granular assemblies." *Journal of Engineering Mechanics, ASCE*, 134(12): 1095-1113.

Vardakos, S.S., Gutierrez, M.S., and Barton, N.R. (2007). "Back-analysis of Shimizu Tunnel No.3 by distinct element modeling." *Tunelling and Underground Space Technology*, 22: 401-413.

Vardoulakis, I. (1979). "Bifurcation analysis of the triaxial test on sand samples." *Acta Mech.*, 32: 35-54.

Vardoulakis, I. (1980). "Shear band inclination and shear modulous of sand in biaxial tests." *Int. J. Numer. Anal. Methods Geomech.*, 4: 103-119.

Viggiani, G., and Hall, S.A. (2008). "Full-field measurements, a new tool for laboratory experimental geomechanics." *Proceedings of Is-Atlanta 2008: Deformational Characteristics of Geomaterials*, Vol. 1, 3-26.

Wang, J., and Gutierrez, N. (2010), "Discrete element simulations of direct shear specimen scale effects." *Géotechnique*, 60(5): 395-409.

Wang, M., Bai, X., and Frost, J.D. (2010). "Influence of initial water content on the collapsibility of loess." *Experimental and Applied Modeling of Unsaturated Soils – Proceedings of GeoShanghai 2010*, GSP 202: 60-68.

Wang, Q., and Lade, P.V. (2001). "Shear banding in true triaxial tests and its effect on failure in sand." *Journal of Engineering Mechanics*, 127(8):754-761.

Wang, Y.H., and Leung, S.C. (2008). “A particulate-scale investigation of cemented sand behavior.” *Canadian Geotechnical Journal*, 45: 29-44.

Yan, W.M. (2009). “Fabric evolution in a numerical direct shear test.” *Computers and Geotechnics*, 36: 597-603.

Yang, C.T. (2002). “Boundary condition and inherent stratigraphic effects on microstructure evolution in sand specimens.” Ph.D Thesis, Georgia Institute of Technology, Atlanta.

Yang, X. (2005). “Three-dimensional characterization of inherent and induced sand microstructure.” Ph.D Thesis, Georgia Institute of Technology, Atlanta.

Yudhbir and Abedinzadeh, R. (1991). “Quantification of particle shape and angularity using the image analyzer.” *Geotechnical Testing Journal*, 14(3): 296-308.

Zhao, X.L., and Evans, T.M. (2009). “Discrete simulations of laboratory loading conditions.” *International Journal of Geomechanics*, ASCE, 9(4): 169-178.